

Coordination chemistry of actinides and fission products (lanthanides and molybdenum) with
neutral or acidic phosphine oxide ligands

A Dissertation

presented to

the Faculty of the Graduate School
at the University of Missouri-Columbia

In Partial Fulfillment

of the Requirements for the Degree

Doctor of Philosophy

by

Andrew Thomas Breshears

Dr. Justin R. Walensky, Dissertation Supervisor

May 2017

Portions of Chapter 1: © Copyright by De Gruyter 2015

Portions of Chapter 2: © Copyright by American Chemical Society 2016

Portions of Appendix B: © Copyright by Pergamon 2015

All other material: © Copyright by Andrew T. Breshears 2013-2017

All Rights Reserved

The undersigned, appointed by the Dean of the Graduate School, have examined the dissertation entitled

Coordination chemistry of actinides and fission products (lanthanides and molybdenum)
with neutral or acidic phosphine oxide ligands

presented by Andrew T. Breshears,

a candidate for the degree of doctor of philosophy of Chemistry,

and hereby certify that, in their opinion, it is worthy of acceptance.

Professor Justin R. Walensky, Advisor

Dr. Artem V. Gelis, Outside Mentor

Professor Silvia S. Jurisson

Professor J. David Robertson

Professor William H. Miller

I dedicate this thesis and the work that brought it to fruition to my God. As well as to my loving and ever supportive wife, Katherine, and to my twin daughters Olivia Grace, Madeliene Jane and your little brother in heaven John Marie.

ACKNOWLEDGEMENTS

I thank God for the gifts he's given me and for his providence in my life.

I would like to thank my immediate family for their support. My Wife and kids, Parents and Parent-In-Laws for their direction and encouragement. Without you all, I would not be the man I am today.

I would like to thank my Grandparent-in-laws, who have adopted me as one of their own and have mentored me in my career choice in science.

I am and will always be indebted to my advisor, Justin Walensky, for giving me an academic second chance. I am also indebted to my mentor at Argonne, Art Gelis, who took me under his wing and has always put me and my family before all other objectives. These two men have been the giants on whose shoulders I have ridden, despite my unworthiness to do so.

I am forever grateful to those who have taught me the techniques of their trade. Specifically, Charles Barnes, Wei Wycoff, John Muntean, and Alex Brown.

My experience at Missouri would have been a thousand times harder if it wasn't for the strong friendships and support I received from within my group and the department. Thank you, Andrew Behrle, Morgan Moody, Ashley Dame, Andrew Lane, Matt Vollmer, Pokpong Rungthanapathsophon, Alex Myers, Michael Tarlton, Jeremy Essner, Adrian Laciak, Anahita Zare, and Travis Pemberton.

Special Thanks to my collaborators: Alex Brown (ANL), Brian Gullekson (OSU), Alena Paulenova (OSU), Gary Baker (UM), and Suzanne Bart (Purdue).

Finally, thank you to my committee members for their amazing support and guidance;
Silvia Jurisson, Dave Robertson, and Bill Miller.

TABLE OF CONTENTS

ACKNOWLEDGMENTS	ii
LIST OF ILLUSTRATIONS AND TABLES	vii
LIST OF COMMONLY USED ACRONYMS	xv
Chapter	
1. INTRODUCTION	1
2. CHAPTER 1: STRUCTURE AND SPECTROSCOPY OF URANYL AND THORIUM COMPLEXES WITH SUBSTITUTED PHOSPHINE OXIDE LIGANDS	16
Abstract	16
Scope of Impact.....	17
Introduction	17
Experimental	18
Results and Discussion.....	23
Conclusion.....	34
References	36
3. CHAPTER 2: EXTRACTION OF WATER AND SPECIATION OF TRIVALENT LANTHANIDES AND AMERICIUM IN ORGANOPHOSPHORUS EXTRACTANTS	39
Abstract	39
Scope of Impact.....	40
Introduction	40
Experimental	43
Results and Discussion.....	47
Conclusion.....	73
References	76

4. CHAPTER 3: PRELIMINARY STUDIES INTO EXTRACTION AND STRIPPING VALUES FOR MOLYBDENUM WITH ORGANOPHOSPHORUS EXTRACTING LIGANDS AND OXIME CONTAINING LIGANDS	81
Abstract	81
Scope of Impact.....	81
Introduction	82
Experimental	83
Results and Discussion.....	85
Conclusion.....	94
Future Work	94
References	96
5. CHAPTER 4: SYNTHESIS OF HEXAVALENT MOLYBDENUM FORMO-, ACETOHYDROXAMATES AND DEFEROXAMINE VIA LIQUID-LIQUID METAL PARTITIONING	98
Abstract	98
Scope of Impact.....	99
Introduction	99
Experimental	102
Results and Discussion.....	109
Conclusion.....	130
References	133

APPENDIX

1. APPENDIX A: POSSIBLE PROFITS FROM REPROCESSING OF SPENT FUEL FROM LWRS, TH-FBR, AND LMFBR VIA AQUEOUS REPROCESSING AND PYROPROCESSING.....	139
---	-----

2. APPENDIX B: SYNTHESIS, SPECTROSCOPY, ELECTROCHEMISTRY, AND COORDINATION CHEMISTRY OF SUBSTITUTED PHOSPHINE SULFIDES AND SELENIDES	164
VITA.....	204

LIST OF ILLUSTRATIONS

Figure	Page
1. Introduction-Scheme 1: LaF ₃ precipitation process for recovering plutonium from irradiated uranium.	3
2. Introduction-Scheme 2: Flow diagram for reprocessing at the Hanford site	4
3. Introduction-Scheme 3: Basic flow diagram of PUREX process	6
4. Introduction-Table 1: Overview of different advanced nuclear fuel cycles and the ligands used in the processes.....	9
5. Introduction-Figure 2: Illustration of ligands from Table 1: 2-ethylhexyl phosphonic acid mono-2-ethylhexyl ether (HEH[EHP]), Tetraaklyldiglycolamide, (TODGA or TEHDGA), Diethylenetriaminepentaacetic acid (DTPA), diisopropylcarbamoylmethyl (phenyloctyl)phosphine oxide (CMPO), bis-6,6'-benzo[1,2,4]triazin-3-yl-(2,2')bipyridine (BTBP), bis-2,6-benzo[1,2,4]triazin-3-yl-pyridine (BTP), 1,2-diaminocyclohexanetetraacetic acid (CDTA), Acetohydroxamic acid (AHA)...	10
6. Introduction-Figure 3: The process flow for two different advanced fuel cycles. TRUEX/TALSPEAK process and the ALSEP.	11
7. Chapter 1-Table 1: X-ray crystallography parameters for complexes 5-9.....	22
8. Chapter 1-Table 2: ³¹ P NMR chemical shifts for complexes 1-9.	25
9. Chapter 1- Table 3: Infrared stretching frequencies (cm ⁻¹) of phosphine oxide ligands, 1-4, uranyl, 5-8, and thorium complex, 9.	25
10. Chapter 1- Table 4: Structural parameters for complexes 5-8.	26
11. Chapter 1- Figure 1: Thermal ellipsoid plot of 5 shown at the 50% probability level.	27
12. Chapter 1- Figure 2: Thermal ellipsoid plot of 6 shown at the 50% probability level	28

13. Chapter 1- Figure 3: Thermal ellipsoid plot of 7 shown at the 50% probability level.	29
14. Chapter 1- Figure 4: Thermal ellipsoid plot of 8 shown at the 50% probability level.	30
15. Chapter 1- Figure 5: Thermal ellipsoid plot of 9 shown at the 50% probability level.	31
16. Chapter 1- Table 5: Selected bond distances (Å) and angles (°) for 9.	31
17. Chapter 1- Figure 6: Normalized UV-vis absorption spectra of phosphine oxide ligands 1-4 in THF.	33
18. Chapter 1-Figure 7: Normalized excitation (broken profiles) and emission spectra (solid lines) of aromatic phosphine oxide ligands 1-4 in THF at a concentration of 2×10^{-5} M.	34
19. Chapter 2-Figure 1: Organic phase cation exchange molecules: HDEHP and HEH[EHP].	41
20. Chapter 2-Figure 2: Neodymium UV-Vis spectra of varying metal concentrations in 0.2 M HDEHP, 0.5 M HDEHP, 1.0 M HDEHP, 1.5 M HDEHP, and 2.0 M HDEHP.	48
21. Chapter 2- Figure 3: UV-Vis spectra of Nd extracted into 1.5M HDEHP and diluted with non-preequilibrated and preequilibrated 1.5M HDEHP, 1.0M HDEHP and diluted with non-preequilibrated and preequilibrated 1.0M HDEHP, and 0.5M HDEHP and diluted with non-preequilibrated and preequilibrated 0.5M HDEHP.	49
22. Chapter 2- Figure 4: Nd extraction into 0.5 M HDEHP followed by titration with 2.0 M HDEHP, increasing HDEHP concentration.	50
23. Chapter 2- Figure 5: Water concentration of HDEHP organic phases following extraction of neodymium.	51
24. Chapter 2- Figure 6: UV-Vis spectrum of 29.3 mM Nd in 2.0 M HDEHP following extraction and subsequent desiccation.	52
25. Chapter 2- Figure 7: Fourier transformed k^3 -weighted XAFS and best fit of the Nd (10 mM) L_{3} -edge spectra in 0.2 M HDEHP and 2.0 M HDEHP in n-dodecane.	53

26. Chapter 2- Table 1: k^3 -weighted XAFS fit results for the L_3 -edge of 0.2 M HDEHP / 10 mM Nd 2.0 M HDEHP / 10 mM Nd, 2.0 M HDEHP / 10 mM Nd (diluted)...	54
.....	
27. Chapter 2- Figure 8: k^3 -Weighted XAFS data in k -space of the Nd (10 mM) L_3 -edge in 0.2 M HDEHP and 2.0 M HDEHP in n-dodecane.	55
28. Chapter 2- Figure 9: UV-Vis Spectra of Pr, Nd, Sm, Am, Ho, and Er following extraction into 0.2 M HDEHP and 2.0 M HDEHP	57
29. Chapter 2- Table 2: Water Concentration in Post-Extraction Organic Phases of Various f-Elements	57
30. Chapter 2- Figure 10: Neodymium UV-Vis spectra of varying metal concentrations in 0.5 M HEH[EHP] and 2.0 M HEH[EHP]	58
31. Chapter 2- Figure 11: Water concentration of HEH[EHP] organic phases following extraction of neodymium.....	59
32. Chapter 2- Figure 12: UV-Vis spectra of Pr, Nd, Sm, Am, Ho, and Er following extraction into 0.2 M HEH[EHP] and 2.0 M HEH[EHP]	60
33. Chapter 2- Figure 13: Steady-state fluorescent emission of Eu in HDEHP organic phases of variable concentration and of the sieve-treated 72 h and 4 month samples, D_2O contacted and H_2O re-contacted samples.	61
34. Chapter 2- Table 3: Lifetime fluorescence measurements of 30 mM Eu extracted into varying concentrations of HDEHP and after being treated with 3 Å molecular sieves	62
35. Chapter 2- Figure 14: lifetime measurements of Eu-HDEHP complexes in dodecane at 0.2 M HDEHP, 1.5 M HDEHP, 2.0 M HDEHP, 3.0 M HDEHP. Data includes sieve treated (72 hours and 4 months) samples, post-dried D_2O contacted samples and post-dried re-contacted H_2O samples	66
36. Chapter 2- Table 4: ΔG of formation from water coordination with organophosphorus ligand dimers.....	68
37. Chapter 2- Table 5: Mulliken Charge values for selected atoms in Organophosphorus dimers and water complexes.	68

38. Chapter 2- Figure 15: Optimized geometry of a HDEHP dimer with water interacting with the POH-OP hydrogen bond of the dimer.	69
39. Chapter 2- Figure 16: Geometry around the metal centers showing only the coordinating ligand oxygens and the oxygen from the water for clarity.....	70
40. Chapter 2- Table 6: Average lanthanide-oxygen and lanthanide-phosphorus distance for lanthanum, lutetium, 6-coordinate water outer sphere (OS) and 7-coordinate water inner sphere (IS) complexes	71
41. Chapter 2- Figure 17: Optimized geometries of waterless 6-coordinate Ln(HA ₂) ₃ , water coordinated, 7-coordinate, distorted face-capped, and 6-coordinate octahedral with water outer sphere. Listed are the energies associated with the change in free energy between the complexes listed above the energies given for La and Lu.....	72
42. Chapter 3- Figure 1: Skeletal structures, from left to right, of HDEHP, HEH[EHP], Cyanex 272 and diethyldithiophosphonic acid.....	86
43. Chapter 3- Figure 2: D _{M0} values and evaluation of performance of commercially available organophosphorus extracting agents.	87
44. Chapter 3- Figure 3: Skeletal structures of diisopropyl dioxophosphinic acid, diisopropyl dithiophosphinic acid, and diisopropyl diselenophosphinic acid.....	88
45. Chapter 3- Figure 4: D values of molybdenum extraction from a 3 M nitric acid using 0.5 M diisopropyl dichalcogenide phosphinic acid in dodecane..	88
46. Chapter 3- Figure 5: D values for solutions mixed on the vortex mixer for different lengths of time.	89
47. Chapter 3- Figure 6: D values for extraction of different concentrations of molybdenum into a 0.5 M HEH[EHP]/dodecane organic phase.....	90
48. Chapter 3- Figure 7: Skeletal structures of formo-, aceto-, and benzylhydroxamic acids and hydroxamates.....	91
49. Chapter 3- Figure 8: D values of aceto-, formo-, and benzylhydroxamic acids stripping 0.05 M molybdenum from a 0.5 M HEH[EHP] organic phase.....	91
50. Chapter 3- Figure 9: Lawesson's rearrangement of acetohydroxamic acid (AHA) to produce the desired acetothiohydroxamic acid (S-AHA).	92

51. Chapter 3- Figure 10: Comparison of the D value performance of acetohydroxamic acid, versus the carbonyl substituted acetothiohydroxamic acid and the acetoselenohydroxamic acid.....	92
52. Chapter 3- Figure 11: Skeletal structures of alpha-benzoin oxime, acetone oxime, and acetoamidoxime.	93
53. Chapter 3- Figure 12: D values for 1.0 M stripping solutions containing acetohydroxamic acid (AHA), acetoamidoxime, acetone oxime, hydroxyl amine and alpha-benzoin oxime.....	94
54. Chapter 4- Figure 1: liquid-liquid solvent extraction method for synthesizing various Mo complexes.....	101
55. Chapter 4- Figure 2: The skeletal structures of the ligands, their names and abbreviations used in Chapter 4.	102
56. Chapter 4- Table 1: Crystal parameters for Mo-AHA and Mo-FHA.....	106
57. Chapter 4- Table 2: IR stretching frequencies of interest from HEH[EHP], $\text{KMoO}_3(\text{IO}_3)$ and $\text{MoO}_2(\text{NO}_3)_2\text{HEH}[\text{EHP}]_2$	110
58. Chapter 4- Figure 3: Optimized theoretical geometry of $\text{MoO}_2(\text{NO}_3)_2(\text{HEH}[\text{EHP}])_2$	112
59. Chapter 4- Figure 4: k^3 -Weighted Molybdenum <i>K</i> -edge XAFS <i>R</i> -space of $\text{MoO}_2(\text{NO}_3)_2\text{HEH}[\text{EHP}]_2$ solution.....	113
60. Chapter 4- Table 3: Structural parameters of $\text{MoO}_2(\text{NO}_3)_2\text{HEH}[\text{EHP}]_2$ determined from XAFS and from the DFT minimized structure	114
61. Chapter 4- Figure 5: Thermal ellipsoid plot of Mo-FHA, Mo-AHA, shown at the 50% probability level and skeletal structure of Mo-AHA and Mo-FHA.....	115
62. Chapter 4- Table 4: Bond lengths (Å) and angles (deg) of Mo-FHA and Mo-AHA compared with Mo-BHA (molybdenyl bisbenzohydroxamate) and Mo-PAHA (molybdenyl bisphenylacetylhydroxamate). Included is the bond length results of the DFT optimized structure of Mo-AHA.	116
63. Chapter 4- Table 5: IR stretching frequencies (cm^{-1}) of acetohydroxamic acid, Mo-DFO, Mo-AHA, and Mo-FHA.	118

64. Chapter 4- Figure 6: Extinction coefficient profiles of Mo-AHA, Mo-FHA and Mo-DFO.	119
65. Chapter 4- Figure 7: ^{95}Mo NMR spectra of Mo-FHA, Mo-AHA and Mo-DFO. 1M Na_2MoO_4 in D_2O was used as an internal standard.	120
66. Chapter 4- Figure 8: Numbering scheme of the hydroxamate sites on deferoxamine.	121
67. Chapter 4- Figure 9: Optimized structures of 1:1 molybdenyl:deferoxamine in different coordination motifs.	122
68. Chapter 4- Table 6: Selected bond lengths and bond angles of optimized structures, 1:1 and 3:2 molybdenum to deferoxamine. Change in free energy between the different coordination complexes is listed at the bottom of the table.	123
69. Chapter 4- Figure 10: Optimized structures of the 3:2 molybdenyl to deferoxamine complexes	124
70. Chapter 4- Figure 11: The skeletal structure of the most stable 1:1 and 3:2 Mo to DFO complex.	124
71. Chapter 4- Figure 12: Mass spectrum of the DFO stripping solution post stripping of Molybdenum for the HEH[EHP]/n-dodecane organic phase.	126
72. Chapter 4- Figure 13: k^3 -Weighted molybdenum K -edge XAFS of Mo-AHA and Mo-DFO solution in n-dodecane.	128
73. Chapter 4- Table 7: Structural parameters of Mo-AHA, Mo-DFO determined from XAFS.	128
74. Chapter 4- Figure 14: R -space spectra of Mo-DFO with and without carbon potentials.	130
75. Appendix A- Table 1: Mass of fission products present in spent nuclear fuel as a function of moles per gigawatt-thermal per year.	142
76. Appendix A- Figure 1: Basic flow diagram of PUREX process.	145
77. Appendix A- Figure 2: Fission Product recovery in a pyroprocessing diagram.	147

78. Appendix A- Table 2: Market prices of each fission product element as of early February, 2017.....	150
79. Appendix A- Table 3: Total possible profit from fission products assuming 100% recovery of each product.	151
80. Appendix A- Table 4: Final discharge from a reactor after decaying for 10, 30, 50 or 100 years.	153
81. Appendix B- Figure 1: Examples of known triarylphosphine chalcogenide compounds.....	166
82. Appendix B- Table 1: X-ray crystallographic data for complexes 1-8.	177
83. Appendix B- Table 2: X-ray crystallographic data for complexes 9 and 10.....	178
84. Appendix B- Table 3: ^{31}P NMR chemical shifts for 1-10.....	180
85. Appendix B- Table 4: ^{77}Se NMR spectroscopy resonances for Se containing compounds, 5-8 and 10.....	181
86. Appendix B- Table 5: IR stretching frequency (cm^{-1}) complexes 1-10.....	182
87. Appendix B- Figure 2: Normalized absorbance (broken profiles) and fluorescence emission (solid curves) spectra of 1 and 5, 2 and 6, 4 and 8.....	184
88. Appendix B- Figure 3: Normalized absorbance spectra (broken profiles) and fluorescence emission spectra (solid profiles) of the anthracenyl phosphine complexes 3 and 7 measured in toluene.	185
89. Appendix B- Figure 4: Representative cyclic voltammogram of PPh_2Ar , Ar = 1-pyrenyl, displaying irreversible one-electron oxidation wave at a positive potential with scan rate at 250 mVs^{-1}	186
90. Appendix B- Table 6: Reduction potentials (V vs Fc/Fc^+) of PPh_2Ar , at room temperature in THF.	187
91. Appendix B- Figure 5: Representative cyclic voltammogram of PPh_2Ar , Ar = 1-pyrenyl, displaying reversible one electron reduction of pyrene with scan rate dependence in THF.....	187
92. Appendix B- Table 7: Selected bonds lengths and angles of complexes 1-4.	188

93. Appendix B- Table 8: Selected bonds lengths and angles of complexes 5-8.	188
94. Appendix B- Table 9: Selected bonds lengths and angles of complexes 9 and 10.	189
95. Appendix B- Figure 6: Thermal ellipsoid plot of 1 and 5 shown at the 50% probability level.....	189
96. Appendix B- Figure 7: Thermal ellipsoid plot of 2 and 6 shown at the 50% probability level.....	190
97. Appendix B- Figure 8: Thermal ellipsoid plot of 3 and 7 shown at the 50% probability level. 3 oriented to show the 3°-degree bend in the anthracenyl ring, while 5 oriented to show the 5°-degree bend in the anthracenyl ring.	191
98. Appendix B- Figure 9: Thermal ellipsoid plot of 4 (left) and 8 (right) shown at the 50% probability level.	192
99. Appendix B- Figure 10: Thermal ellipsoid plot of 9 at 50% probability level.	192
100. Appendix B- Figure 11: Thermal ellipsoid of 10 at 50% probability level.	193
101. Appendix B- Table 10: Complexes with a 9-anthracenyl substituent on a triarylphosphine and the deviation from planarity that is observed.	194
102. Appendix B- Figure 12: Comparison of the anthracenyl strain in the optimized structures of unoxidized diphenylanthracenylphosphine; 3; 7	196
103. Appendix B- Figure 13: NICS(1) values of unoxidized and oxidized phosphines, 1- 8.	196

LIST OF FREQUENTLY USED ACRONYMS

Met Lab	Metallurgical Laboratory, University of Chicago, Chicago, IL
PUREX	Plutonium Uranium Extraction Process
REDOX	Reduction-Oxidation Process
UREX	Uranium Extraction Process
THOREX	Thorium Extraction Process
TRUEX	Transuranic Extraction Process
DIAMEX	Diamide Extraction process
DOE	Department of Energy
EU	European Union
FP	Fission Product(s)
ALSEP	Actinide Lanthanide Separation process
TALSPEAK	(Trivalent Actinide – Lanthanide Separation by Phosphorus Reagent Extraction from Aqueous Komplexes)
DIDPA	Diisododecylphosphoric acid process
SANEX	Selective Actinide Extraction Process
TRUSPEAK	Transuranic Separation by Phosphorus Reagent Extraction from Aqueous Komplexes
EXAm	Extraction process for Americium
GANEX	Group Actinide Extraction Process

CEA.....	French abbreviation for the Atomic Energy Commission
CHALMEX.....	Chalmers University Extraction Process
CMPO	diisopropylcarbamoylmethyl (phenyloctyl)phosphine oxide
TBP	tributyl phosphate
TODGA.....	Tetraoctyldiglycolamide
DTPA	Diethylenetriaminepentaacetic acid
BTBP.....	bis-6,6'-benzo[1,2,4]triazin-3-yl-(2,2')bipyridine
TEHDGA	Tetra-2-ethylhexyldiglycolamide
HDEHP	Di-2-ethylhexyl phosphoric acid
HEH[EHP]	2-ethylhexyl phosphonic acid mono-2-ethylhexyl ether
BTP	bis-2,6-benzo[1,2,4]triazin-3-yl-pyridine
AHA.....	Acetohydroxamic Acid
FHA.....	Formohydroxamic Acid
BHA	Benzylhydroxamic Acid
HA.....	Hydroxamic Acid
CDTA.....	1,2-diaminocyclohexanetetraacetic acid
PAH.....	Polyaromatic Hydrocarbon
MOX	Mixed-Oxide fuel (PuO ₂ and UO ₂)
SNM.....	Sensitive Nuclear Materials
PPM.....	Parts Per Million
THF.....	Tetrahydrofuran
Naph.....	Naphthyl

Anth.....	Anthracenyl
Phenan.....	Phenanthrenyl
Py	Pyrenyl
NRC	US Nuclear Regulatory Commission
TRF.....	Time-Resolved Fluorescence
DFT.....	Density Functional Theory
(E)XAFS	(Extended) X-ray Absorption Fine Structure
UNF.....	Used Nuclear Fuel
SANS	Small Angle Neutron Scattering
EDTA.....	Ethylenediaminetetraacetic acid
DGA.....	Diglycolamide
UFF.....	Universal Force-Field Calculation
CN.....	Coordination number
IS/OS.....	Inner Sphere/Outer Sphere
ABO	Alpha Benzoinoxime
DFO.....	Deferoxamine (synonyms: Desferoxamine, Desferrioxamine, DFOA, DFOB)
FTIR.....	Fourier Transform Infra-Red Spectroscopy
MM2	Molecular Mechanics 2 calculation
ESI+MS	Electrospray ionization mass spectrometry
ROI.....	Return on Investment
MWD/kg.....	Mega-watts (thermal) days per kilogram
MeV	Million Electron Volts

JENDL	Japanese Evaluated Nuclear Data Library
GWt (MWth).....	Gigawatt thermal (Megawatt thermal)
LWR.....	Light Water Reactor
PWR.....	Pressurized Light Water Reactor
BWR	Boiling Light Water Reactor
LMFBR.....	Liquid Metal Fast Breeder Reactor
LLW	Low-Level Waste
MW	Mixed Waste
kWh.....	Kilowatt hour
LEU.....	Low enriched uranium
GWd/tHM	Gigawatt days per ton of heavy metal
NORM.....	Naturally occurring radioactive material
mTHM/yr	metric ton of heavy metal per year (reprocessing unit)
CV.....	Cyclic Voltammetry
NICS(1).....	Nucleus Independent Chemical Shift (at 1 Å)

Introduction

The original intent for nuclear fuel reprocessing flowsheets and processes were to isolate fissile plutonium for use as the core of nuclear weapons.¹⁻² This purpose was set into motion during the early part of the 1900's. In early 1938, the Joliot-Curies in Paris announced that they had made a new transuranic element by transmuting uranium with neutrons, but that the new element behaved much like barium during separation. Repeating the experiment, Otto Hahn, Lise Mietner and Fritz Strassman found that there were many new radioactive elements after the same experiment and that one fraction behaved like barium, another like cerium. Lise Mietner, by the summer of 1938, fled to Sweden and was unable to see the experiment to its finish. However, Strassman confirmed and finished the experimental results by late 1938, which Hahn had Mietner's nephew, Otto Frisch, deliver the news. During the Christmas period of 1938, Mietner and Frisch worked out that the uranium nucleus was being fractured or "fissioned" apart. During this fissioning, a lot of energy is released per reaction on a scale never before seen.³⁻⁴ Mietner then leaked the results to Niels Bohr who was in Sweden with her at the time. Bohr then spread word of the results to physicists in the United States that took merely weeks to confirm the results. The confirmation that uranium does fission and that it releases so much energy during each event became the basis of the atomic bomb.³

While in 1932, Enrico Fermi had claimed that he had created elements 93 and 94, but as he did not separate and confirm that the elements had been created it was not until 1940 that Edwin McMillan was able to separate out neptunium (93) from the uranium target that had been irradiated with protons at Berkeley's 60" cyclotron.⁵ However, neptunium beta decays to plutonium and the separation of the two was achieved by Wahl and

Seaborg a year later due to the difficulty of isolating Pu from Np. After this, the race was on for creating enough fissile material for a nuclear weapon in both America under the Manhattan Project and in Germany under the Wilhelm Institute.

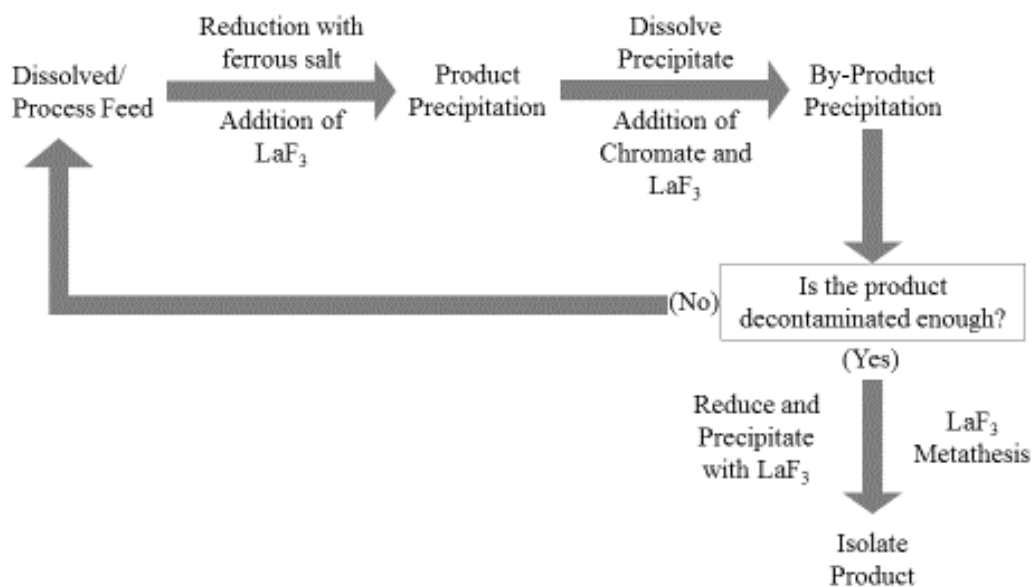
Before the start of World War II, Edgar Singer, who controlled the uranium ore from the Sinolobwe mine operated by Union Miniere, had moved a vast amount of pitchblende to the United States via export/import regulation with Standard Oil.¹ This greatly hampered the German effort to acquire the Belgian stockpile, since there was only a small amount left which did not bolster the pre-existing German reserve and much of what was left of the European stock. Due to this lack of uranium ore, enriching in U-235 was pursued but not with substantial backing by the government or other scientists. Instead, the Germans decided to focus on production of plutonium using a heavy water moderated reactor. However, by 1942, much of the government support had been diverted to other pressing war issues. Ultimately, the Germans never got to a point in the project in which plutonium was produced and isolated.³ Thus, we can surmise that the only nuclear fuel reprocessing was done through the Manhattan project.

As stated earlier, Singer's actions to move most of Union Miniere's uranium ore to the United States gave the US military effort a lead on the Germans. Not only was there enough material by S-1 committee's estimation to enrich to >90% U-235, sufficient for a fissile weapon, but also enough material to build multiple reactors to breed plutonium.⁶ However, much of this effort concerning reprocessing would have been possible if it was not for the McMillan, Seaborg and Thompson groups.

The original reprocessing flow sheet for recovering Np and Pu from irradiated uranium is shown in Scheme 1. This original scheme is called the lanthanum fluoride

process. This was used by McMillan to isolate Np. Later, Seaborg's group was able to isolate Pu from Np by using a stronger oxidizing agent that allowed for Pu to stay soluble while the by-products were precipitated.⁵

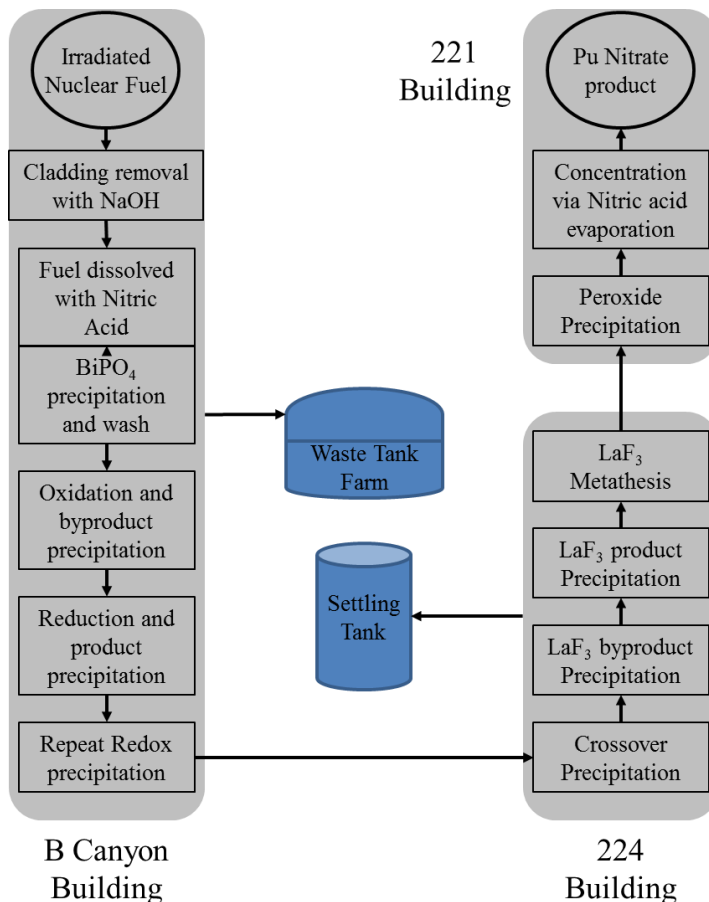
Scheme 1: LaF₃ precipitation process for recovering plutonium from irradiated uranium.



Up until the end of 1942, the lanthanum fluoride process was considered by the S-1 committee for all reprocessing operations. However, the process had two major flaws when scaling up. First, the LaF₃ precipitate tends to be gelatinous and, on a large scale, difficult to work with. Second, the fluoride was very corrosive and resulted in needing to change industrial chemical infrastructure on a regular basis. However, this was alleviated by S. G. Thompson, a former classmate of Seaborg, who took up Seaborg's offer to leave Standard Oil and join the Met Lab in Chicago. In early December of 1942, Thompson tried the first experiment of using bismuth phosphate as a carrier for Pu. He found that it produced a pure batch of Pu with a recovery rate of 80%. Others in the group continued to work on the process and could increase the recovery to 94% within a week's worth of trials and that it matched or was better than the decontamination factor for LaF₃. By the

time the process was implemented on a pilot plant scale, the process had been fine tuned to recover 98% of the plutonium. The key differences between the bismuth phosphate carrier and LaF_3 carrier was that nitric acid could be used in the feed and that the reducing agent could be changed to sodium nitrite. However, a final concentration step of LaF_3 was still necessary. As Seaborg said later, “There really is no discernable difference between the lanthanum fluoride and bismuth phosphate process other than what carrier was used”.⁵ The S-1 committee decided in May of 1943 to switch the Tennessee X-10 pilot plant from LaF_3 to bismuth phosphate and to build the two 200 area canyons at Hanford strictly with the bismuth phosphate process in mind. The scheme for reprocessing at the 200 area canyons is shown in Scheme 2.⁵⁻⁷

Scheme 2: Flow diagram for reprocessing at the Hanford site.

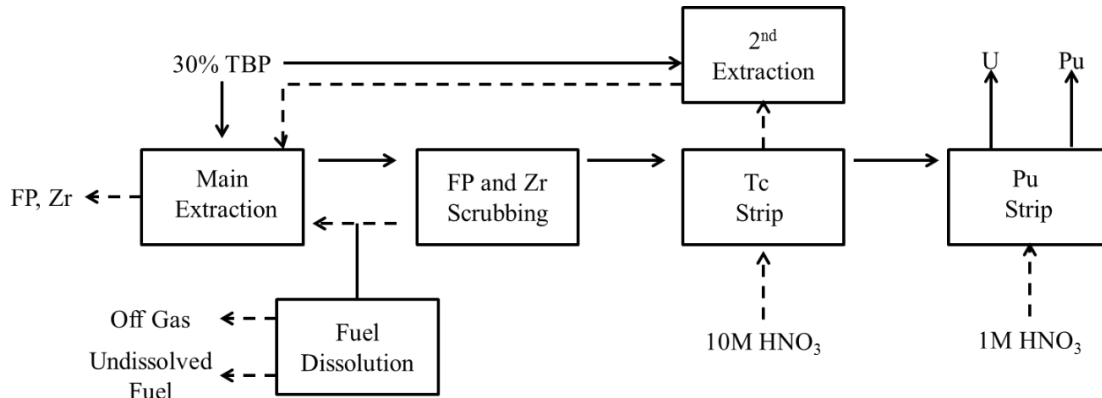


It was not until 1952 that the Bismuth Phosphate process was replaced by the liquid-liquid extraction processes of REDOX and PUREX. PUREX became favored over REDOX because of the possibility of explosions of reacted hexone in REDOX waste. The PUREX process and its variants are still widely employed into the present.^{5,7}

While until this point in history actinide separation processes have been utilized to separate weapons material, its use took on a peaceful purpose. Since the creation of Chicago Pile-4 (also known as Experimental Breeder Reactor-1) in 1951, the nuclear fuel cycle has been a promising example of using nuclear physics for peaceful civilian energy needs. This agenda was cemented into international policy by president D. Eisenhower with the “Atoms for Peace” speech given to the UN General Assembly in late 1953.⁸

As already mentioned, by this time Bismuth Phosphate had been replaced with PUREX. The issue with Bismuth Phosphate was that uranium that had not been fissioned or transmuted during its residence time in a reactor was discarded and could still be utilized. For this reason, the PUREX process was invented to conserve the uranium (Scheme 3). PUREX has led to other processes that could be used, depending on the situation or desired product streams. These other processes are THOREX, UREX, UREX+, TRUEX, and DIAMEX, just to name a few.⁹ These processes are all called solvent extraction processes because they use immiscible solvents and ligands to facilitate extraction or stripping of target elements. However, solvent extraction is only one of many different processes. Other processes include co-precipitation (BiPO_4), ion exchange, and pyroprocessing.¹⁰ In comparison with these other processes, solvent extraction has the highest mass through-put and allows for additional separations via tuning ligand extraction or stripping ligand sets, making it preferable to the others.

Scheme 3: Basic flow diagram of PUREX process



However, in the 60 years since the “Atoms for Peace” speech, nuclear fuel reprocessing has had a turbulent period in the United States. Civilian separation of plutonium was banned indefinitely with executive order 987, while in the next year, all civilian reprocessing was halted. In 1981, this policy was overturned but without fiscal incentives the restarting of civilian reprocessing of spent nuclear fuel was never executed.¹¹

Since then the national solution to the accumulation and storage of spent fuel assemblies has been to investigate and create a site for long term storage. The original Nuclear Waste Act set forth possible sites in the basalt formations of Richland, WA, the granite formations of Yucca Mountain in Nevada, and the salt caves of Northern Texas. In an amendment to the original act, the other sites were taken out of the act and the sole site being considered was Yucca Mountain and later was scuttled.¹²⁻¹³ Currently, the only approved policy for keeping nuclear spent fuel is in temporary storage at nuclear reactors.

Due to the long wait time for many of the minor actinides and fission products, DOE and various member states of the EU have decided to investigate partitioning and transmutation.¹⁴ Use of advanced nuclear fuel cycles allow for partitioning of various elements and transmutation would be taking various products from the advanced nuclear fuel cycle and burning them in a reactor or transmuting them into shorter lived products.

Upon viewing the historical issues with spent fuel storage and reprocessing, there are three major issues and the goals to correct them. They are:

- 1) Since nuclear materials in spent fuel can be diverted to create weapons of mass destruction/disruption, the solution would be to create robust processes or measures for monitoring nuclear materials.
- 2) Accumulation of large amounts of long-lived, highly radiotoxic material post U/Pu separation. The goal would be to create and optimize an advanced nuclear fuel cycle that would allow for further segregation of products in spent fuel. This would allow for smaller storage needs, better management of long-lived waste, and the mitigation of large volumes of spent material.
- 3) There is a lack of economic incentive to engage the private sector in nuclear reprocessing. The best way to solve this issue would be to investigate the possible fiscal incentives that would make reprocessing affordable and profitable for investors and thus create a market for reprocessing nuclear fuel.

In achieving goal 1, the use of forensic markers within nuclear fuel reprocessing lends itself to proving both a reliable marker and allows for an *in-situ* monitoring capability. As

uranyl nitrate and plutonium nitrate are major species in post-dissolver spent fuel and the major issue with nuclear security, these species are of interest to monitor.

Phosphine oxide ligands are ubiquitous in actinide separation chemistry and nuclear fuel reprocessing flowsheets. The previously mentioned PUREX process and many of its daughter processes use tributylphosphate as an extraction ligand.

Thus, in Chapter 1, I investigate fluorescent ligands of triarylphosphine oxide that would both model and possibly become a fluorescent marker of the resulting actinide nitrate phosphate complexes inherent in the PUREX process.

In achieving goal 2, it was appropriate to collaborate with Argonne National Lab which has been investigating advanced nuclear fuel cycles, such as the ALSEP process. Advanced nuclear fuel cycles can be summarized into one of 5 categories; Co-extracting trivalent actinides and lanthanides, partitioning trivalent actinides only, processes separating trivalent actinides from lanthanides, processes separating americium from curium, and processes co-separating all transuranic elements. An abbreviated list of the different solvent extraction processes is given in Table 1. The major processes of each different category, their main attributes and the ligands used in them are also listed. The ligands are shown in Figure 2 for reference.

At its core, ALSEP combines the functionality of TRUEX and TALSPEAK processes, see Figure 3.¹⁵ The ALSEP process was created by Drs. Gelis and Lumetta to separate non-f-element fission products, lanthanide fission products that are abundant in spent nuclear fuel and transuranics which, come from neutron induced transmutation of uranium and plutonium.

Table 1: Overview of different advanced nuclear fuel cycles and the ligands used in the processes.

Co-extraction of trivalent actinides and lanthanides		
Process	Overview	Ligands used
TRUEX	Used after UREX+ to separate out Pu, Am, Cm and Ln	CMPO, tributylphosphate (TBP)
DIAMEX	Co-extracts Ln and An present in PUREX raffinate	Malonamide, ethylenediamine triacetic acid
ARTIST	Separates out both U, Pu, TRU, Ln and fission products	Branched alkyl monoamides, TODGA, N-donor ligand
Processes to partition only trivalent actinides		
DIDPA	Separates HLW into four groups: TRU, platinum group, Sr-Cs, remaining elements	Diisodecylphosphoric acid, DTPA
Processes partitioning trivalent actinides from lanthanides		
SANEX	SANEX and its variations are meant to selectively extract trivalent actinides (An) from lanthanides (Ln) in a DIAMEX raffinate	BTBP, TODGA, BTP
TALSPEAK	Aims to separate minor actinides from Ln in TRUEX or UREX raffinate.	Di(2-ethylhexyl)phosphoric acid (HDEHP), DTPA
TRUSPEAK	Combines TRUEX and TALSPEAK to handle fission products as well as separate Ln and An	HDEHP, CMPO
ALSEP	Process to supplant TRUEX-TALSPEAK co-process by separating fission products from Ln and minor actinides in UREX or COEX raffinate	HEH[EHP], TODGA, DTPA
Processes separating americium from curium or from high-level waste (HLW)		
EXAm	Process for selectively extracting americium from PUREX raffinate	Malonamide, HDEHP, TEDGA, ethylenediamine triacetic acid
Processes to co-separate all transuranic elements		
GANEX U-only	Process to remove the bulk of uranium from high-level waste	Monoamide
CAE GANEX	Based on the DIAMEX-SANEX process. Process to extract all transuranic elements from the GANEX U-only raffinate in one product	Malonamide, HDEHP
Euro GANEX	Process to co-separate all transuranic elements from GANEX U-only	TODGA, Malonamide, CDTA, AHA, BTP
CHALMEX	Process for co-separating all transuranic elements from GANEX U-only	BTP, TBP, monoamide

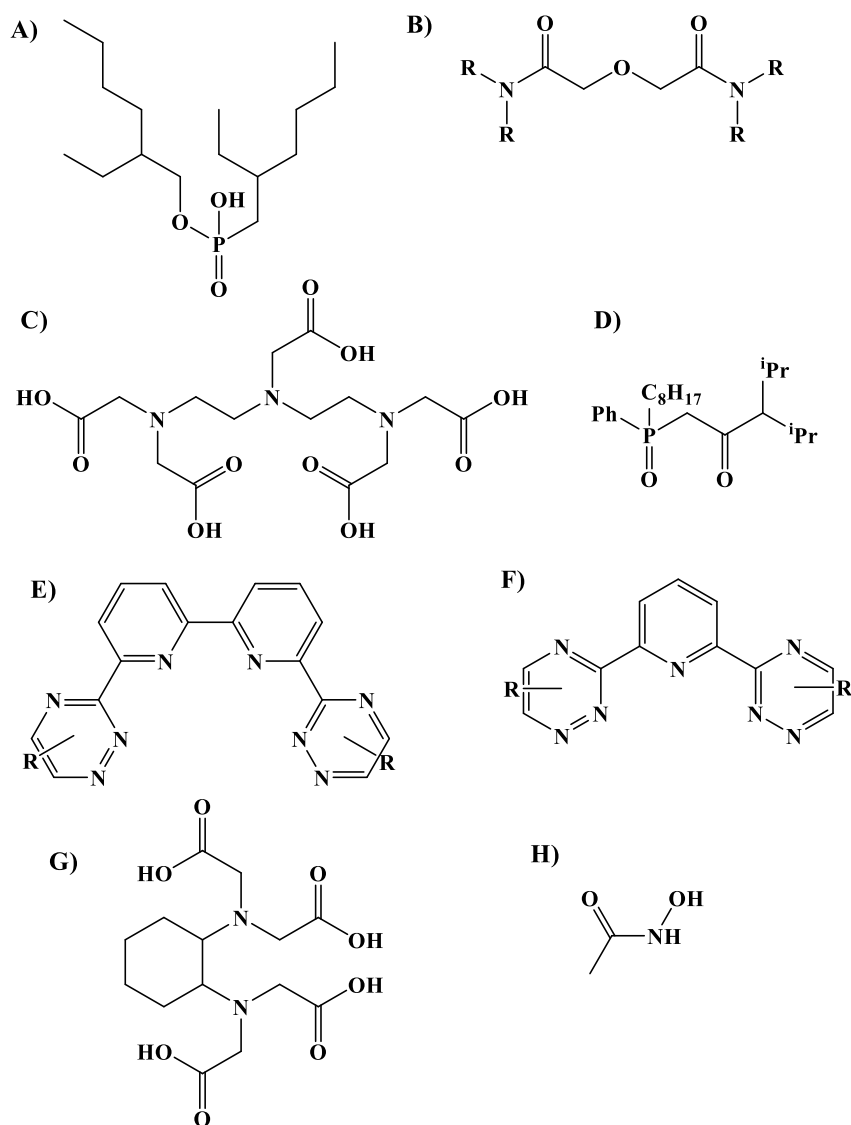


Figure 2: A) 2-ethylhexyl phosphonic acid mono-2-ethylhexyl ether (HEH[EHP]), B) Tetraalkyldiglycolamide, where R can be n-octyl or 2-ethylhexyl (TODGA or TEHDGA) C) Diethylenetriaminepentaacetic acid (DTPA), D) diisopropylcarbamoylmethyl (phenyloctyl)phosphine oxide (CMPO), E) bis-6,6'-benzo[1,2,4]triazin-3-yl-(2,2')bipyridine (BTBP), where R can be any functional group, F) bis-2,6-benzo[1,2,4]triazin-3-yl-pyridine (BTP), where R can be any functional group, G) 1,2-diaminocyclohexanetetraacetic acid (CDTA), H) Acetohydroxamic acid (AHA)

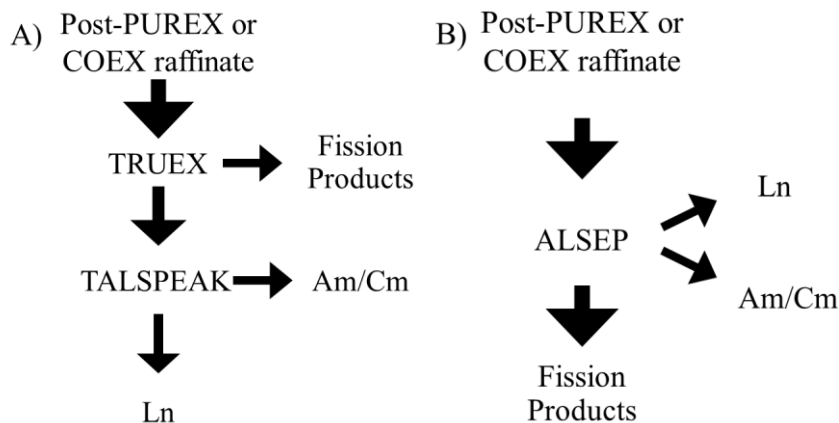


Figure 3: The process flow for two different advanced fuel cycles. A) TRUEX/TALSPEAK process in which two different processes separate fission products, minor actinides and lanthanides at each stage. B) The ALSEP process in which lanthanides, minor actinides and fission products are all separated from each other in one process.

Within the ALSEP process an organophosphorous acid such as 2-ethylhexylphosphonic acid mono-2-ethylhexyl ester (HEH[EHP], Figure 2A) and a diglycolamide such as tetraoctyldiglycolamide or tetra-2-ethylhexyldiglycolamide (Figure 2B) are used to extract the f-elements from the spent fuel stream, thus the lanthanides and minor actinides are in the extracted organic phase leaving all other non-f-element fission products in the aqueous raffinate. From the f-element loaded HEH[EHP]/TRDGA organic phase the lanthanides can be stripped into a fresh aqueous phase that has diethylenetriaminepentaacetic acid (DTPA), leaving the minor fission products in the organic phase to be stripped at a different step. Thus, the ALSEP process allows for major separation of lanthanides, minor actinides and fission products.

In ALSEP's extracted organic phase, lanthanide and minor actinide complexation by organophosphoric extractants is still a subject of investigation. There have been multiple interpretations as to their coordination and the state of the extraction ligands within the

organic phase. Traditionally, the interpretation has been that trivalent actinides and lanthanides are coordinated with three mono-deprotonated dimers of the phosphoric acid or $H(A)_2^-$ where A is the deprotonated phosphate. Contrary to this, other alternative species have been proposed ranging from bridging phosphates between metal centers to slight changes to the traditional tris-dimer coordination.¹⁶⁻²⁰ Due to this wide range of different coordination environments, I investigated the effects of ligand concentration on the coordination environment around lanthanides in Chapter 2 and the apparent change in coordination chemistry of lanthanides due to water-ligand concentration induced change in the organic phase.

Additionally, other fission products have been known to accumulate within the process, which then affects the distribution value, D, of various elements negatively. The fission products that are significant actors during separation processes are Ru, Mo, and Zr.¹⁰ Specifically for ALSEP, Mo accumulates and eventually changes both its D value within different stages of the process, as well as effects the D values of other elements is molybdenum. In most reprocessing, molybdenum is in the form of the dicationic molybdenyl ion (MoO_2^{2+}) due to the low pH and oxidizing nitric acid environment. Due to the hard acid and oxophilic nature of the molybdenyl ion, its chemistry is very similar to uranyl. Thus, in investigating the extraction and stripping behavior of molybdenum in the ALSEP process, I investigate the coordination chemistry of molybdenum with organophosphoric acid and hydroxamic acids in Chapter 3. While in Chapter 4, the kinetics and D values for molybdenum extraction and stripping using different organophosphoric acids and hydroxamic acids is examined.

Finally, in achieving goal 3, I look at current fiscal outlines and proposals for nuclear fuel reprocessing facilities. Current proposals only look at the cost of building and staffing a U/Pu recovery plant with or without the capability of creating MOX fuel. However, in many of these cost analysis proposals and papers, the financial recovery through selling of recovered U/Pu as reactor fuel is not proposed.²¹⁻²⁴ Moreover, advanced nuclear fuel cycles allow recovery of potential fuel materials valuable to sell, but would give the ability to implement additional processes to recover other valuable resources created through fission. Specifically of value would be recovery of lanthanides, group 9, 10 and 11 precious metals or other rare, high demand, elements. There would also be the profit that could be realized in recovery and selling medical isotopes, even though the resulting process would be most likely be significantly different and time critical. In Appendix A, I investigate the possible set up, cost and ultimately profitability from reprocessing spent nuclear fuel via recovery of high value elements.

References:

1. Zoellner, T., *Uranium : war, energy, and the rock that shaped the world*. Viking: New York, 2009.
2. Rhodes, R., *The making of the atomic bomb*. Simon & Schuster: New York, NY, 2012.
3. Irving, D. J. C., *The virus house*. Kimber: London, 1967.
4. Nelson, C., *The age of radiance : the epic rise and dramatic fall of the atomic era*. 2014.
5. Seaborg, G. T.; Kathren, R. L.; Gough, J. B.; Benefiel, G. T., *The plutonium story : the journals of professor Glenn T. Seaborg, 1939-1946*. Battelle Press: Columbus, 1994.
6. Nichols, K. D., *The road to Trinity*. Morrow: New York, 1987.
7. *Plutonium Handbook*. 2. 2. Gordon and Breach: New York, 1967.
8. Chernus, I., *Eisenhower's atoms for peace*. Texas A & M University Press: College Station, 2002.
9. Loveland, W. D.; Morrissey, D. J.; Seaborg, G. T., *Modern nuclear chemistry*. Wiley-Interscience: Hoboken, N.J., 2006.
10. Nash, K. L.; Madic, C.; Mathur, J. N.; Lacquement, J., Actinide Separation Science and Technology. In *The Chemistry of the Actinide and Transactinide Elements*, Morss, L. R.; Edelstein, N. M.; Fuger, J., Eds. Springer Netherlands: Dordrecht, 2006; pp 2622-2798.
11. Thompson, K. W., *Presidents and arms control : process, procedures, and problems*. University Press of America ; Miller Center, University of Virginia: Charlottesville, 1997.
12. Till, C. E.; Chang, Y. I., *Plentiful energy : the story of the integral fast reactor, the complex history of a simple reactor technology, with emphasis on its scientific basis for non-specialists*. Amazon Publishing: United States, 2011.
13. D'Agata, J., *About a mountain*. W.W. Norton: New York, 2010.
14. Joly, P.; Boo, E. *ROADMAP: Actinide separation processes 2015*; SACSESS: 2016; p 77.
15. Gelis, A. V.; Lumetta, G. J., Actinide Lanthanide Separation Process- ALSEP. *Ind. & Eng. Chem. Res.* **2014**, *53*, 1624-1631.

16. Braley, J. C.; Grimes, T. S.; Nash, K. L., Alternatives to HDEHP and DTPA for Simplified TALSPEAK Separations. *Ind. & Eng. Chem. Res.* **2012**, *51*, 629-638.
17. Peppard, D. F.; Mason, G. W.; Maier, J. L.; Driscoll, W. J., Fractional Extraction of the Lanthanides as their Di-alkyl Orthophosphates. *J. Inorg. Nucl. Chem.* **1957**, *4*, 334-343.
18. Grimes, T. S.; Tian, G.; Rao, L.; Nash, K. L., Optical Spectroscopy Study of Organic-Phase Lanthanide Complexes in the TALSPEAK Separations Process. *Inorg. Chem* **2012**, *51*, 6299-6307.
19. Marie, C.; Hiscox, B.; Nash, K. L., Characterization of HDEHP-lanthanide Complexes Formed in a Non-Polar Organic Phase Using ³¹P NMR and ESI-MS. *Dalton Trans* **2012**, *41*, 1054-1064.
20. Gannaz, B.; Antonio, M. R.; Chiarizia, R.; Hill, C.; Cote, G., Structural Study of Trivalent Lanthanide and Actinide Complexes Formed Upon Solvent Extraction. *Dalton Trans.* **2006**, 4553-4562.
21. Bunn, M., Hui Zhang, Li Kang *The Cost of Reprocessing in China. Cambridge, Mass.: Report for Project on Managing the Atom, Belfer Center for Science and International Affairs, Harvard Kennedy School,*; January, 2016.
22. Schneider, E. A.; Deinert, M. R.; Cady, K. B., Cost analysis of the US spent nuclear fuel reprocessing facility. *Energy Econ.* **2009**, *31* (5), 627-634.
23. Choi, S.; Nam, H. O.; Ko, W. I., Environmental life cycle risk modeling of nuclear waste recycling systems. *Energy* **2016**, *112*, 836-851.
24. *Nuclear proliferation and civilian nuclear power. Report of the Nonproliferation Alternative Systems Assessment Program. Volume IX. Reactor and fuel cycle description;* DOE/NE-0001/9F; TRN: 80-011296 United States 10.2172/5413513 DOE NE English ; Department of Energy, Washington, DC (USA). Assistant Secretary for Nuclear Energy: 1980.

Chapter 1: Structure and Spectroscopy of Uranyl and Thorium Complexes with Substituted Phosphine Oxide

Ligands[†]

[†] This chapter is based on a manuscript that was submitted to and accepted by

Radiochimica Acta. The DOI is: 10.1515/ract-2014-2295 and can be cited as:

Breshears, A. T.; Barnes, C. L.; Wagle, D. V.; Baker, G. A.; Takase, M. K.; Walensky, J.

R., Structure and spectroscopy of uranyl and thorium complexes with substituted phosphine oxide ligands. *Radiochim. Acta*, **2015**; *103*, 49.

Abstract

Phosphine oxide ligands are important in the chemistry of the nuclear fuel cycle. Herein is reported the synthesis and characterization of a series of phosphine oxide ligands with polycyclic aromatic hydrocarbon (PAH) groups to enhance the spectroscopic features of uranyl, UO_2^{2+} , and to make detection more efficient. Complexation of OPPh_2R , $\text{R} = \text{C}_{10}\text{H}_7$ (naphthyl); C_{14}H_9 (phenanthrenyl); C_{14}H_9 (anthracenyl); and C_{16}H_9 (pyrenyl), to $\text{UO}_2(\text{NO}_3)_2$ afforded the eight-coordinate complexes, $\text{UO}_2(\text{NO}_3)_2(\text{OPPh}_2\text{R})_2$. An eleven-coordinate complex, $\text{Th}(\text{NO}_3)_4[\text{OPPh}_2(\text{C}_{14}\text{H}_9)]_3$, $\text{C}_{14}\text{H}_9 = \text{phenanthrenyl}$, was structurally characterized, and was found to be the first thorium compound isolated with three phosphine oxide ligands bound. The phosphine oxide ligands were not fluorescent but the anthracenyl-substituted ligand showed broad, approximately 50 nm red-shifted emission relative to typical anthracene, making this ligand set a possibility for use in detection. The synthesis and spectroscopy of the uranyl and thorium complexes are presented.

Scope of Impact

The work presented in this chapter as in context with the current state of knowledge for the field presents a new understanding of ligand design for sensing sensitive nuclear material (SNM). This work adds to that knowledge by demonstrating that the use of a fluorescent marker, normally easily identified and quantified on its own, with uranyl and thorium does not have the desired effect of aiding detection of said material. However, within the body of work presented in this chapter is the phenomenon of an unexpected red shift in the fluorescence profile of the anthracenyl diphenyl phosphine oxide. This unexpected change is explored in greater detail in Appendix B.

Introduction

With the increasing population of the world comes a rise in energy consumption, which requires diverse solutions. All indications are that nuclear power will remain an important player for many years. However, the advancement of nuclear energy has the consequence of overlooking the production of nuclear weapons and, to combat this, new methods for sensing actinides in complex matrices need to be developed. Uranyl nitrate, $\text{UO}_2(\text{NO}_3)_2$, is the major species throughout the nuclear fuel cycle and therefore there is interest in investigating how to exploit the properties of UO_2^{2+} to enhance its detection. One prominent feature of UO_2^{2+} is its phosphorescence; however, in general, it is quite weak, and our approach was to attempt to amplify this property.

Phosphine oxide ligands are ubiquitous in actinide chemistry. For example, tributyl phosphate (TBP), $\text{OP}(\text{O}^i\text{Bu})_3$, is used in the PUREX and other processes to extract uranyl into the organic phase. Due to this, many phosphine oxide ligands have been reported to coordinate to actinyl complexes. For example, $\text{AnO}_2(\text{NO}_3)_2(\text{OPPh}_3)_2$, An = U, Np¹, Pu²,

$\text{AnO}_2\text{Cl}_2(\text{OPPh}_3)_2$, $\text{An} = \text{U}^3$, Np^1 and $\text{UO}_2(\text{O}_2\text{CCH}_3)_2(\text{OPPh}_3)_2$ ⁴ have been reported. However, to my knowledge, uranyl complexes with phosphine ligands bearing polycyclic aromatic hydrocarbons (PAHs) have not been reported. The rationale for using these ligands was to enhance the spectroscopic properties of uranyl and use a phosphine oxide ligand that would be more robust than TBP to radiolysis.⁵ Herein, we report the synthesis, characterization, and spectroscopy of uranyl nitrate complexes with phosphine oxide ligands bearing a PAH, $\text{UO}_2(\text{NO}_3)_2(\text{OPPh}_2\text{Ar})$, $\text{Ar} =$ naphthyl, anthracenyl, phenanthrenyl, and pyrenyl.

Experimental

All reactions were conducted in air unless otherwise specified. $\text{UO}_2(\text{NO}_3)_2(\text{H}_2\text{O})_6$ was used as is from legacy stock. All other chemicals were purchased (Aldrich) at 95% or higher purity and used as received. All ^1H , ^{13}C , and ^{31}P NMR data were obtained on a 250 MHz ARX, 300 MHz DRX or 500 MHz DRX Bruker spectrometer. ^1H NMR shifts were referenced internally to the residual protio impurities at δ 5.32 ppm (CDHCl_2). ^{13}C NMR shifts were referenced internally to the residual peaks at δ 53.52 ppm (CD_2Cl_2). ^{31}P NMR spectra were externally referenced to 0.00 ppm with 85% H_3PO_4 in D_2O . Infrared spectra were recorded from KBr pellets on a Perkin-Elmer Spectrum One FT-IR spectrometer. Absorbance spectra were obtained using a Varian Cary 50 Bio UV-Vis spectrophotometer and luminescence spectra were acquired on a Varian Cary Eclipse fluorimeter. Elemental analyses were performed by Atlantic Microlab, Inc. (Norcross, GA).

Caution! Depleted uranium (> 99.274% U^{238}) primarily emits an alpha particle at 4.2 MeV with a half-life of 4.468 billion years. Although common

glassware and PPE are sufficient to shield from the alpha emission, depleted uranium should only be handled in a controlled environment by those who are sufficiently trained and qualified in radiation safety.

Synthesis of phosphines and phosphine oxides, 1-4. Phosphines $P(C_6H_5)_2(C_{10}H_7)(C_{10}H_7 = \text{naphthyl})$,⁶ $P(C_6H_5)_2(C_{14}H_9)(C_{14}H_9 = \text{phenanthrenyl})$, $P(C_6H_5)_2(C_{14}H_9)(C_{14}H_9 = \text{anthracenyl})$, and $P(C_6H_5)_2(C_{16}H_9)(C_{16}H_9 = \text{pyrenyl})$,⁷ and phosphine oxides, $OP(C_6H_5)_2(C_{10}H_7)(C_{10}H_7 = \text{naphthyl})$, **1**, $OP(C_6H_5)_2(C_{14}H_9)(C_{14}H_9 = \text{phenanthrenyl})$, **2**, $OP(C_6H_5)_2(C_{14}H_9)(C_{14}H_9 = \text{anthracenyl})$, **3**, and $OP(C_6H_5)_2(C_{16}H_9)(C_{16}H_9 = \text{pyrenyl})$, **4** were synthesized according to literature procedures.⁸

$UO_2(NO_3)_2[OP(C_6H_5)_2(C_{10}H_7)]_2$, 5. A 20 mL scintillation vial was charged with $UO_2(NO_3)_2(H_2O)_6$ (100 mg, 0.199 mmol) and 10 mL of THF was aliquoted into the vial. **1** (171 mg, 0.521 mmol) was added to the mixture and then stirred for 2 h. The solvent was reduced under vacuum to one-fifth of the original volume and the compound was then placed in a freezer at 0 °C overnight to yield a pale orange solid (245 mg, 90%). ¹H NMR (CD_2Cl_2 , 500 MHz, 21 °C): δ 6.9-7.8 (m, 20H), 7.1-8.5 ppm (m, 14H) ppm. ¹³C NMR (CD_2Cl_2 , 125 MHz, 21 °C): δ 124.3 (naph), 126.5 (naph), 127.2 (Ph), 127.5 (naph), 128.7 (Ph), 128.9 (naph), 129.6 (Ph), 131.0 (naph), 132.0 (naph), 132.7 (naph), 133.3 (naph), 133.5 (Ph), 133.8 (naph), 134.0 (naph) ppm. ³¹P NMR (CD_2Cl_2 , 101 MHz, 21 °C): δ 52.08 ppm. IR (KBr, cm^{-1}): 1548 (s, N=O), 1495 (s, C=C), 1474 (s), 1296 (s, NO₃), 1124 (s, P=O), 1079 (s, P-O), 1024 (w), 935 (s, U=O), 832 (w), 806 (m), 776 (m, =C-H), 753 (w), 727 (w), 558 (m), 543 (s), 505 (w). Anal. Calcd for $C_{44}H_{34}N_2O_{10}P_2U$: C, 50.30%; H, 3.25%; N, 2.67%. Found: C, 50.18%; H, 3.52%; N, 2.65%.

UO₂(NO₃)₂[OP(C₆H₅)₂(C₁₄H₉)]₂, 6. A 20 mL scintillation vial was charged with UO₂(NO₃)₂(H₂O)₆ (100 mg, 0.199 mmol) and 10 mL of THF dispensed into the vial. **2** (176 mg, 0.465 mmol) was added to the mixture and then stirred for 2 h. The solvent was reduced in vacuo to one-fifth of the original volume and then placed in a freezer at 0 °C overnight to yield a pale green-yellow solid (274 mg, 99%). ¹H NMR (CD₂Cl₂, 500 MHz, 21°C): δ 7.11-7.29 (m, 4H, Ph), 7.43-7.56 (m, 8H, Ph), 7.53-7.68 (m, 8H, Ph), 7.74-7.84 (m, 4H, phenan), 7.81-7.94 (m, 2H, phenan), 8.35-8.41 (m, 4H, phenan), 8.63-8.74 (m, 4H, phenan), 8.76-8.81 (m, 4H, phenan) ppm. ¹³C NMR (CD₂Cl₂, 125 MHz, 21°C): δ 123.0 (phenan), 123.53 (phenan), 127.4 (Ph), 127.5 (phenan), 128.1 (Ph), 129.0 (phenan), 129.1 (phenan), 129.6 (phenan), 130.1 (Ph), 130.2 (phenan), 130.3 (phenan), 131.2 (phenan), 131.4 (phenan), 132.3 (phenan), 132.4 (Ph), 132.8 (phenan), 133.7 (phenan), 137.1 (phenan) ppm. ³¹P NMR (CD₂Cl₂, 101 MHz, 21°C): δ 49.13 ppm. IR (KBr, cm⁻¹): 3061 (m), 2974 (m), 2869 (m), 1612 (w), 1588 (m), 1521 (s, N=O), 1438 (s, C=C), 1384 (m), 1285 (s, NO₃), 1197 (w), 1134 (s, P=O), 1089 (s, P-O), 1035 (m), 998 (w), 963 (m), 930 (s, U=O), 904 (w), 859 (w), 811 (w), 748 (s, =C-H), 721 (s), 696 (s), 610 (m), 572 (s), 531 (s), 517 (m). Anal. Calcd for C₅₂H₃₈N₂O₁₀P₂U: C, 54.27%; H, 3.33%; N, 2.43%. Found: C, 53.18%; H, 3.67%; N, 2.40%.

UO₂(NO₃)₂[OP(C₆H₅)₂(C₁₄H₉)]₂, 7. A 20 mL scintillation vial was charged with UO₂(NO₃)₂(H₂O)₆ (100 mg, 0.199 mmol) and 10 mL of THF was dispensed into the vial. **3** (171 mg, 0.452 mmol) was added to the mixture and then stirred for 2 h. The solvent was reduced in vacuo to one-fifth of the original volume and the complex was placed in a freezer at 0 °C overnight to yield a pale yellow solid (262 mg, 96%). ¹H NMR (CD₂Cl₂, 500 MHz, 21°C): δ 6.99 (d, 8H, Ph, ¹J_{H-H} = 7 Hz), 7.14 ppm (t, 4H, Ph, ¹J_{H-H} = 7 Hz),

7.4-7.6 ppm (m, 8H, anth), 7.82-7.90 ppm (m, 8H, Ph), 8.0-8.2 (m, 8H, anth) 8.47 (s, 2H, anth) ppm. ^{13}C NMR (CD_2Cl_2 , 125 MHz, 21°C): δ 125.4 (Ph), 126.8 (anth), 129.2 (Ph), 129.7 (anth), 131.7 (anth), 131.8 (Ph), 132.0 (anth), 134.5 (anth), 135.0 (Ph), 135.5 (anth), 135.9 (anth), 136.7 (anth) ppm. ^{31}P NMR (CD_2Cl_2 , 101 MHz, 21°C): δ 48.19 ppm. IR (KBr, cm^{-1}): 3064 (w), 1619 (w), 1517 (s, N=O), 1438 (s, C=C), 1384 (w), 1284 (s, NO_3), 1125 (s, P=O), 1083 (s, P-O), 1034 (w), 935 (s, U=O), 844 (w), 824 (w), 756 (w), 737 (m, =C-H), 697 (m), 563 (w), 530 (m). Anal. Calcd for $\text{C}_{52}\text{H}_{38}\text{N}_2\text{O}_{10}\text{P}_2\text{U}$: C, 54.27%; H, 3.33%; N, 2.43%. Found: C, 53.46%; H, 3.28%; N, 2.38%.

$\text{UO}_2(\text{NO}_3)_2[\text{OP}(\text{C}_6\text{H}_5)_2(\text{C}_{16}\text{H}_9)]_2$, **8.** A 20 mL scintillation vial was charged with $\text{UO}_2(\text{NO}_3)_2(\text{H}_2\text{O})_6$ (100 mg, 0.199 mmol) and 10 mL of THF was dispensed into the vial. **4** (176 mg, 0.438 mmol) was added to the mixture and then stirred for 2 h. The solvent was reduced in vacuo to one-fifth of the original volume and the complex placed in a freezer at 0 °C overnight to yield a pale green-yellow solid (274 mg, 99%). ^1H NMR (CD_2Cl_2 , 500 MHz, 21°C): δ 8.92 (d, 4H, Py, $^1J_{\text{H-H}} = 9.5$ Hz), 8.25 (m, 8H), 8.08 (m, 8H), 7.79-7.46 (m, 18H) ppm. ^{13}C NMR (CD_2Cl_2 , 125 MHz, 21°C): δ 123.7 (py), 125.0 (py), 125.2 (Ph), 125.7 (py), 126.2 (Ph), 126.4 (py), 126.5 (py), 126.6 (py), 127.2 (py), 128.7 (Ph), 129.9 (py), 130.4 (py), 130.7 (Ph), 131.3 (py), 132.0 (py), 132.1 (py), 132.2 (py), 133.0 (py), 133.8 (py), 134.3 (py) ppm. ^{31}P NMR (CD_2Cl_2 , 101 MHz, 21°C): δ 51.21 ppm. IR (KBr, cm^{-1}): 3049 (w), 2963 (w), 2852 (w), 1626 (w), 1591 (w), 1519 (s, N=O sym str.), 1437 (m), 1384 (s), 1280 (s, asym. str. NO_3), 1208 (w), 1138 (s, P=O str.), 1097 (s, P-O), 1029 (m), 999 (w), 971 (w), 933 (s, U=O), 928 (m), 856 (m), 824 (w), 753 (w), 726 (w), 692 (m), 551 (m), 528 (m), 504 (w). Anal. Calcd for $\text{C}_{52}\text{H}_{38}\text{N}_2\text{O}_{10}\text{P}_2\text{U}$: C, 54.27%; H, 3.33%; N, 2.43%. Found: C, 53.18%; H, 3.67%; N, 2.40%.

Th(NO₃)₄[OP(C₆H₅)₂(C₁₄H₉)₃, 9. A 20 mL scintillation vial was charged with Th(NO₃)₄(H₂O)₄ (100 mg, 0.181 mmol) and 10 mL of THF was dispensed into the vial. **2** (301 mg, 0.795 mmol) was added to the stirring solution and overnight turned a deep red color. The solvent was removed in vacuo to one-fifth of the original volume, and the complex was placed in the freezer at 0 °C to yield a light-yellow powder and polycrystalline beads. The beads were recrystallized out of a concentrated solution of benzene to produce yellow crystalline product of **9** (150 mg, 50% yield). ¹H NMR (CD₂Cl₂, 300 MHz, 21°C): δ 8.84 (d, 6H, ¹J_{H-H} = 8 Hz), 8.32 (bs, 3H), 7.99-7.89 (m, 7H), 7.85-7.73 (m, 20H), 7.62-7.45 (m, 12H), 7.41-7.24 (m, 9H) ppm. ¹³C NMR (CD₂Cl₂, 75 MHz, 21°C): δ 123.8 (phenan), 124.3 (Ph), 126.3 (phenan), 128.3 (phenan), 128.5 (Ph), 129.1 (phenan), 129.2 (phenan), 130.0 (Ph), 130.2 (phenan), 130.5 (phenan), 131.1 (phenan), 131.5 (phenan), 131.8 (phenan), 133.4 (phenan), 133.6 (phenan), 134.3 (phenan), 139.0 (Ph), 140.0 (phenan) ppm. ³¹P NMR (CD₂Cl₂, 101 MHz, 21°C): δ 44.9 ppm. IR (KBr, cm⁻¹): 3057(w), 1506 (s, N=O), 1438 (s, O-N str.), 1384 (s, P-C), 1299 (s, asym. str. NO₃), 1127 (s, P=O str.), 1082 (s, P-O str.), 1028(m), 961(w), 810(w), 748(w), 724(s), 693(m), 620(m), 572(m), 533(s, Th-O), 499(m). Anal. Calcd for C₅₂H₃₈N₂O₁₀P₂U: C, 58.00 %; H, 3.56 %; N, 3.47%. Found: C, 57.31%; H, 3.80%; N, 3.55%.

Crystallographic Data Collection and Structure Determinations. The selected single crystal was mounted on a nylon cryoloop using viscous hydrocarbon oil. X-ray data collection was performed at 173(2) or 100(2) K. The X-ray data were collected on a Bruker CCD diffractometer with monochromated Mo-K α radiation ($\lambda = 0.71073 \text{ \AA}$). The data collection and processing utilized Bruker Apex2 suite of programs.⁹ The structures

were solved using direct methods and refined by full-matrix least-squares methods on F^2 using Bruker SHELEX-97 program.¹⁰ All non-hydrogen atoms were refined with anisotropic displacement parameters. All hydrogen atoms were added on idealized positions and not allowed to vary. Thermal ellipsoid plots were prepared by using X-seed with 50% of probability displacements for non-hydrogen atoms.¹¹ Crystal data and details for data collection for complexes **5-9** are provided in Table 1, and significant bond distances and angles are gathered in Tables 4 and 5.

Table 1: X-ray crystallography parameters for complexes **5-9**.

	5	6	7	8	9
CCDC Deposit Number	1005324	1005321	1005323	1005325	1005322
Empirical Formula	C ₄₄ H ₃₄ N ₂ O ₁₀ P ₂ U	C ₅₂ H ₃₈ N ₂ O ₁₀ P ₂ U	C ₅₂ H ₃₈ N ₂ O ₁₀ P ₂ U	C ₅₆ H ₃₈ N ₂ O ₁₀ P ₂ U	C ₉₉ H ₇₈ N ₄ O ₁₅ P ₃ Th ₁
Formula weight (g/mol)	1050.70	1150.80	1150.80	1202.87	1888.6
Crystal Habit, color	Needle, Pale green	Prism, Pale green yellow	Block, Pale yellow	Prism, Pale green yellow	Prism, Yellow
Temperature (K)	100(2)	173(2)	173(2)	173(2)	100(2)
Space group	<i>P</i> 1	<i>P</i> -1	<i>P</i> 2 ₁ / <i>c</i>	<i>P</i> -1	<i>P</i> -1
Crystal system	<i>Triclinic P</i>	<i>Triclinic P</i>	<i>Monoclinic P</i>	<i>Triclinic P</i>	<i>Triclinic P</i>
Volume (Å ³)	2023.31 (6)	1635.5(3)	2288.57(4)	1307.35 (3)	4207.65(5)
<i>a</i> (Å)	9.4887(15)	9.0855(10)	14.383(8)	9.014(2)	12.7596(9)
<i>b</i> (Å)	10.8116(17)	9.7152(10)	9.735(5)	12.511(3)	14.0268(10)
<i>c</i> (Å)	20.710(3)	16.3826(18)	17.526(9)	13.168(3)	25.5719(19)
α (°)	102.658(3)	73.856(1)	90.00	109.143(3)	89.984(1)
β (°)	91.102(3)	82.960(1)	111.156(6)	105.180(3)	84.026(10)
γ (°)	101.955(3)	80.505(1)	90.00	98.700(3)	67.700(1)
<i>Z</i>	2	1	2	1	2
Calculated density (Mg/m ³)	1.725	1.575	1.670	1.614	1.491
Absorption coefficient (mm ⁻¹)	4.153	3.10	3.68	3.23	1.90
Final R indices [I > 2 σ (I)]	R1 = 0.0305 wR2 = 0.0619	R1 = 0.020 wR2 = 0.052	R1 = 0.030 wR2 = 0.067	R1 = 0.033 wR2 = 0.066	R1 = 0.030 wR2 = 0.066

Results and Discussion

Synthesis and Spectroscopy. The phosphine oxide ligands, **1-4**, were readily prepared as previously reported.⁸ Reaction of two equivalents of the phosphine oxide ligands with

$\text{UO}_2(\text{NO}_3)_2(\text{H}_2\text{O})_6$ in THF yielded new products as discerned by ^{31}P NMR spectroscopy, Table 2. The phenanthrenyl-substituted phosphine oxide ligand, $\text{OPPh}_2(\text{C}_{14}\text{H}_9)$, **2**, also coordinates to the thorium metal center when reacted with $\text{Th}(\text{NO}_3)_4(\text{H}_2\text{O})_4$, Table 2. The ligand, **2**, was chosen due to its propensity to form isolable products which could be readily characterized by X-ray diffraction analysis. The uranyl complexes were found to be soluble in THF and CH_2Cl_2 but only sparingly soluble in arene solvents, while **9** was more soluble in toluene. The ^1H , ^{13}C , and ^{31}P NMR spectra for each uranyl complex showed only one set of aryl and phosphorus resonances indicating a symmetric coordination environment. Coordination of the phosphine oxide to uranyl leads to a downfield shift in the ^{31}P NMR spectrum. This can be attributed to less electron density on the phosphorus atom due to the actinide metal center siphoning electron density from the oxide, which then removes more from phosphorus. There does not seem to be an apparent trend as a function of ^{31}P NMR chemical shift versus ligand electron withdrawing strength. The ^{31}P NMR spectrum of **9** showed a broad resonance at 44.9 ppm, which is unusual for a diamagnetic species. This was attributed to fluxional behavior of the phosphine oxide ligand in solution with two or three ligands coordinated to thorium.

In accordance with the ^{31}P NMR chemical shifts indicative of less electron density on the phosphorus atoms and weakening of the P-O bond, the infrared spectra of uranyl complexes, **5-8**, have a corresponding red shift of the P-O stretching frequency, Table 3. For example, in free $\text{OPPh}_2(\text{C}_{16}\text{H}_9)$, **4**, a stretch at 1171 cm^{-1} is observed and is located at 1138 cm^{-1} in $\text{UO}_2(\text{NO}_3)_2[\text{OPPh}_2(\text{C}_{16}\text{H}_9)]_2$, **8**.

Table 2: ^{31}P NMR chemical shifts for complexes **1-9**.

Compound	³¹ P NMR Chemical Shift (ppm)
1	31.5
2	31.8
3	34.6
4	32.0
5	52.1
6	48.2
7	49.1
8	51.2
9	44.9

Table 3: Infrared stretching frequencies (cm⁻¹) of phosphine oxide ligands, **1-4**, uranyl, **5-8**, and thorium complex, **9**.

Bond stretching frequency (cm ⁻¹)	1	2	3	4	5	6	7	8	9
$\nu(\text{U}=\text{O})_{\text{asym}}$	-	-	-	-	935	935	930	930	-
$\nu(\text{P}=\text{O})$	1182	1187	1179	1171	1124	1124	1134	1138	1127

X-ray Crystallography Analysis

Single crystal X-ray diffraction analysis of complexes **5-9** was performed to examine their structural features. The structure of **5**, Figure 1, exhibits a seven-coordinate complex with *C*₁ symmetry with one of the nitrate ligands coordinating κ^1 -(O) instead of κ^2 -(O,O). The uncoordinated oxygen atom (O9) on the nitrate has a hydrogen bond, 2.378 Å, with the closest hydrogen on an adjacent naphthyl ring (H39), Figure 1A. Due to the

κ^1 -(O) bonding of the nitrate ligand, there is a contraction of that U-O bond from 2.4813(3) to 2.3720(3) Å. The remaining uncoordinated oxygen (O10) also hydrogen bonds with a hydrogen atom (H8) on the adjacent naphthyl ring at 2.671 Å, Figure 1A. However, this effect is only observed in the solid state as the ^1H NMR spectrum of **5** indicates that the complex exhibits C_{2v} symmetry.

Table 4: Structural parameters for complexes **5-8**.

Bond distance (Å)/angle (°)	5	6	7	8
U1-O (oxo)	1.7694(2)	1.7661(17)	1.757(3)	1.765(3)
U1-O (nitrate)	2.3720(3)	2.5179(18)	2.527(3)	2.520(3)
U1-O (nitrate)	2.4813(3)	2.5406(18)	2.546(3)	2.532(2)
U1-O (OPPh ₂ Ar)	2.3035(2)	2.3627(16)	2.370(3)	2.343(2)
PI-O4	1.5108(2)	1.5066(17)	1.511(3)	1.502(2)
O-U1-O (uranyl)	175.11(3)	180.00(4)	180.0	180.0

Complexes **6-8** are all eight-coordinate $\text{UO}_2(\text{NO}_3)_2(\text{OPPh}_2\text{Ar})_2$ complexes. The U-O (phosphine oxide) bond lengths of 2.3627(16), 2.370(3), and 2.343(2) Å for **6**, Figure 2, **7**, Figure 3, and **8**, Figure 4, respectively, are nearly identical to 2.35-2.36 Å in $\text{UO}_2(\text{NO}_3)_2(\text{OPPh}_3)_2$. Given the bond distances and angles compare well to previously reported uranyl complexes of the form $\text{UO}_2(\text{NO}_3)_2(\text{OPR}_3)_2$,^{1, 12-25} this suggests that PAH substituted phosphine oxides do not significantly affect the sigma donation to the uranium metal center. Another feature in all four complexes is that the PAH is positioned to not sterically interfere, thus even the pyrenyl derivative displays an identical structure to the phenanthrenyl and anthracenyl. One feature that warrants mention is a small $\sim 3^\circ$ twist from planarity in the anthracenyl ring in **7**, Figure 3. The naphthyl, phenanthrenyl, and pyrenyl are all planar and this twist in the anthracenyl ring may have a consequence on the fluorescence spectrum.

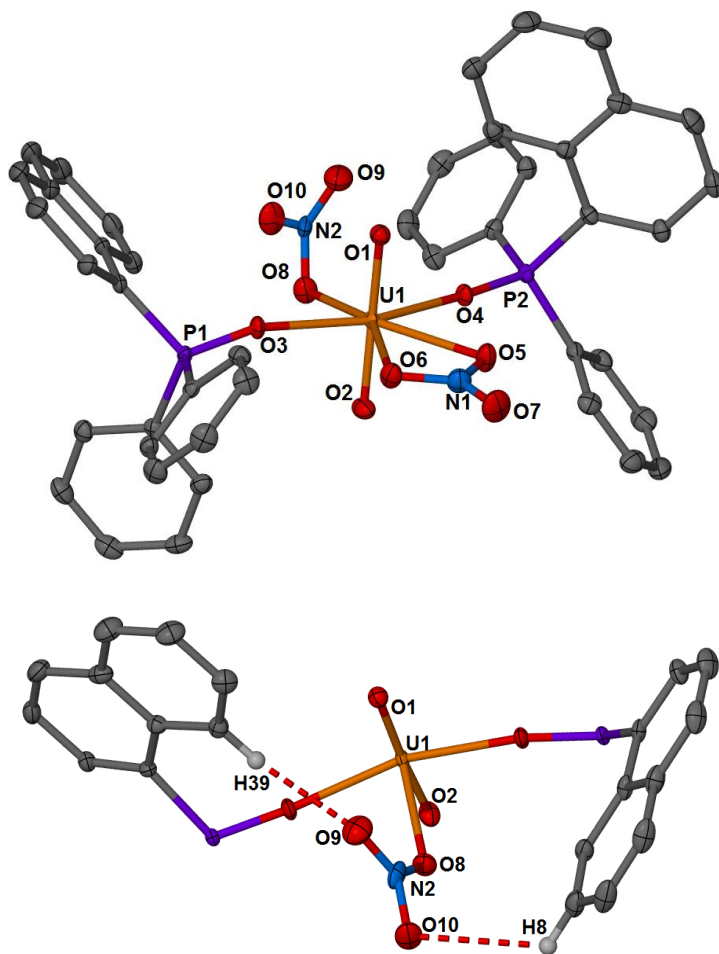


Figure 1: (Top) Thermal ellipsoid plot of **5** shown at the 50% probability level. Hydrogen atoms and solvent molecules have been removed for clarity. (Bottom) Thermal ellipsoid plot of **5** with phenyl rings and $\kappa^2(\text{O},\text{O})$ nitrate removed. Dotted lines between H39 and O9 (2.378 Å) as well as H8 and O10 (2.671 Å) have been added to highlight hydrogen bonding.

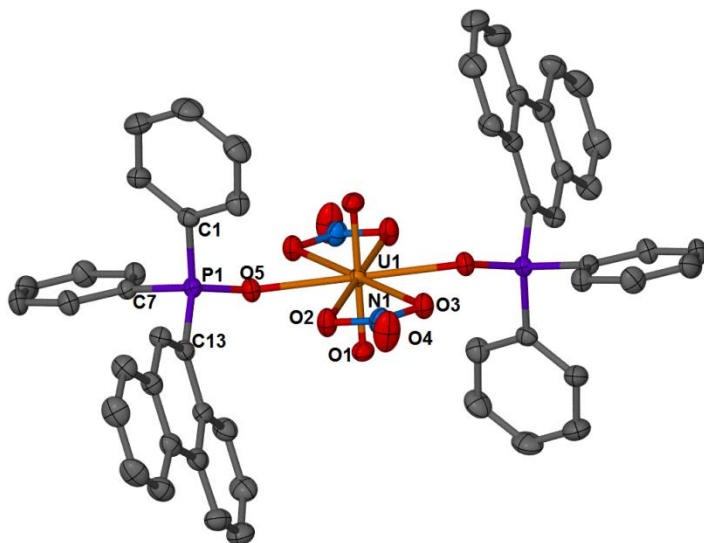


Figure 2: Thermal ellipsoid plot of **6** shown at the 50% probability level. Hydrogen atoms and solvent molecules have been removed for clarity.

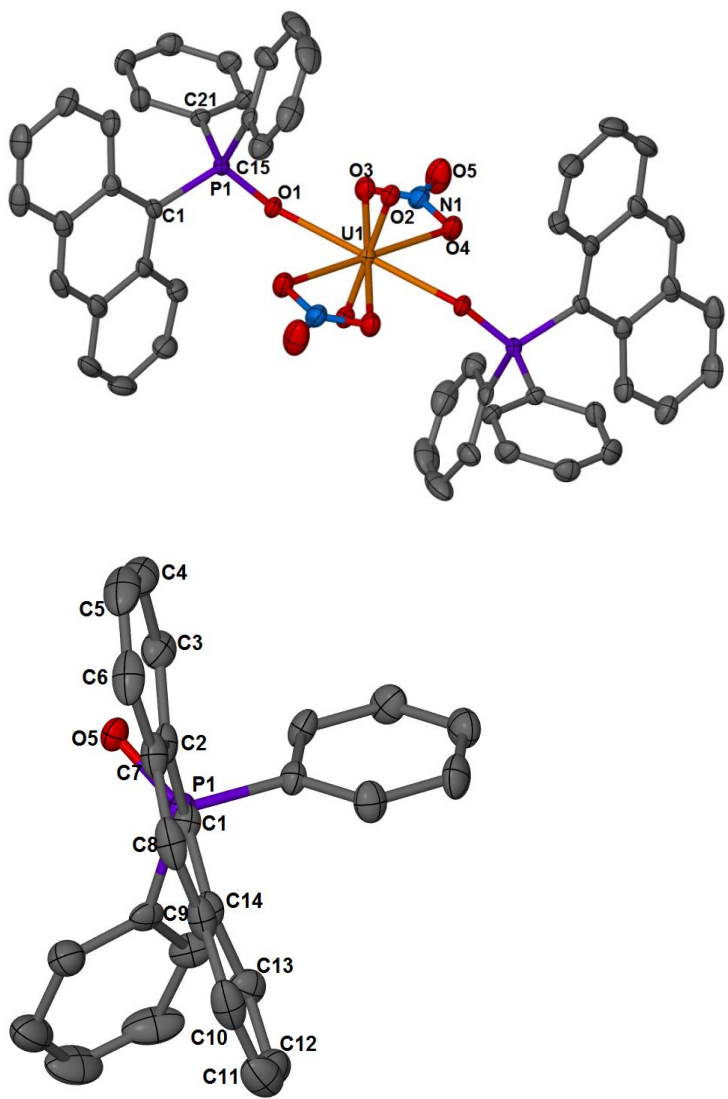


Figure 3: (Top) Thermal ellipsoid plot of **7** shown at the 50% probability level. Hydrogen atoms and solvent molecules have been removed for clarity. (Bottom) Twist in anthracenyl ligand from planarity is shown.

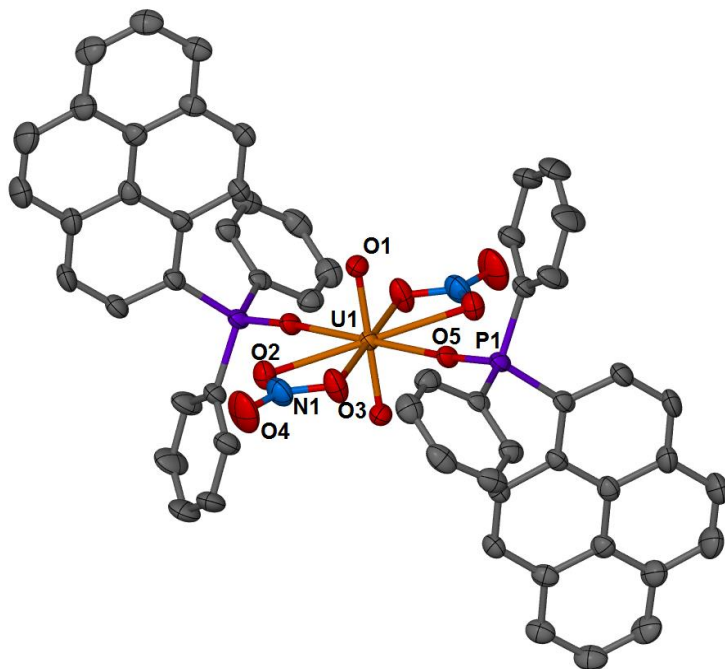


Figure 4: Thermal ellipsoid plot of **8** shown at the 50% probability level. Hydrogen atoms and solvent molecules have been removed for clarity.

Building on the success with uranyl led to also examining the coordination of **2** with $\text{Th}(\text{NO}_3)_4$. The solid-state structure of **9** revealed an eleven-coordinate complex with $\text{Th}(\text{NO}_3)_4$ and three $\text{OPPh}_2(\text{C}_{14}\text{H}_9)$ ligands coordinated, Figure 5. While NMR spectroscopy has observed thorium complexes with three coordinated phosphine oxide ligands,²⁶⁻²⁷ this appears to be the first isolated structure. As previously mentioned, the ^{31}P NMR spectrum of **9** showed a broad resonance and this is most likely due to the fluxional behavior of one of the phosphine oxide ligands associating and dissociating from the thorium center. This increased coordination number also has the effect of forcing a pair of the nitrates to be nonlinear and angle towards the coordination site of the single phosphine oxide, with an N-Th-N angle of 149.40° . However, the thorium-oxygen

bond lengths of the nitrate ligands in **9** of 2.39 to 2.41 Å compare well to those of 2.31-2.35 Å in $\text{Th}(\text{NO}_3)_4(\text{OPMe}_3)_2$ and 2.33-2.35 Å $\text{Th}(\text{NO}_3)_4(\text{OPPh}_3)_2$.

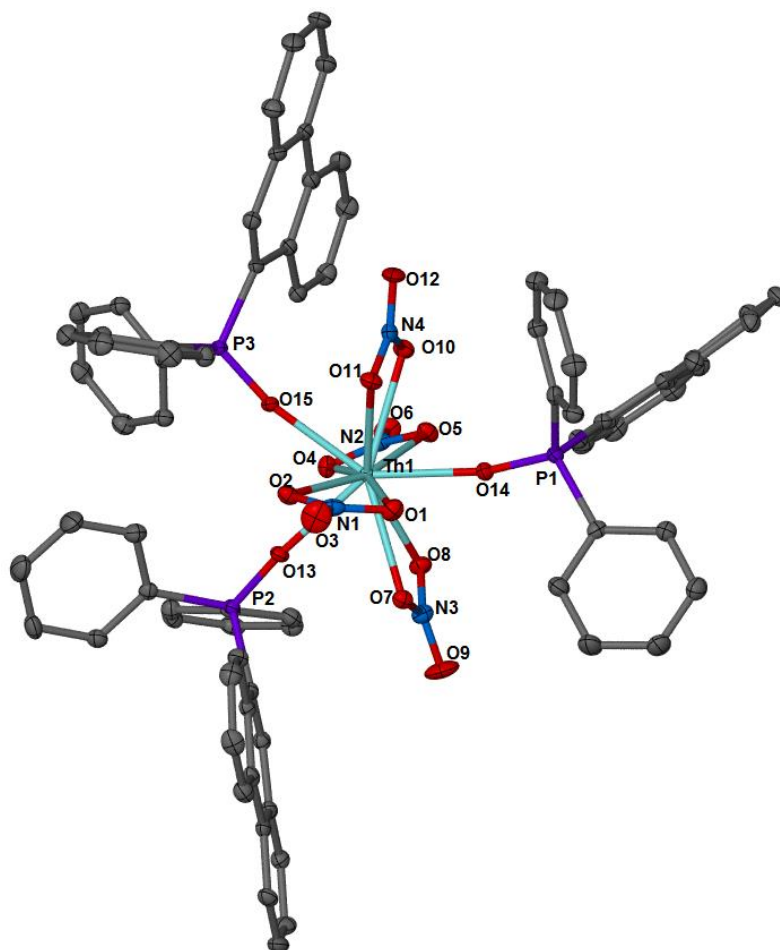


Figure 5: Thermal ellipsoid plot of **9** shown at the 50% probability level. Hydrogen atoms and solvent molecules have been removed for clarity.

Table 5: Selected bond distances (Å) and angles (°) for **9**.

Bond distance (Å)/angle (°)	9
Th-O1 (nitrate)	2.6293(18)
Th-O2 (nitrate)	2.5600(18)
Th-O4 (nitrate)	2.6109(18)
Th-O5 (nitrate)	2.5973(18)
Th-O7 (nitrate)	2.6268(18)
Th-O8 (nitrate)	2.5866(19)
Th-O10 (nitrate)	2.6098(18)
Th-O11 (nitrate)	2.5925(18)

Th-O13 (OPPh ₂ Ar)	2.4108(17)
Th-O14 (OPPh ₂ Ar)	2.3914(17)
Th-O15 (OPPh ₂ Ar)	2.3954(17)
P2-O13	1.5053(18)
P1-O14	1.5161(18)
P3-O15	1.5116(18)
O-Th-O (phosphines)	140.28(6) 142.31(6) 77.41(6)
N-Th-N (nonlinear nitrates)	149.40(6)

Optical Spectroscopy

The electronic absorbance spectra for the aromatic phosphine oxide ligands **1–4** in THF are provided in Figure 6 and accord well with the absorbance profiles expected for the parent PAH compounds. The corresponding fluorescence excitation and emission spectra are shown in Figure 7. Consistent with an earlier report, the phosphines were observed to be non-fluorescent.⁸ The order of the emission intensities for their oxides, however, is **4** > **3** >> **2** >> **1** with ligands **1–3** showing relative intensities of roughly 2.4%, 11, and 51%, respectively, when compared to the intensity from the 1-pyrenyl ligand **4**. Interestingly, the emission observed from the 9-anthryl phosphine oxide ligand **3** is structureless and red-shifted by *ca.* 50 nm relative to typical anthracene monomer emission, which shows vibronic character. This was, in fact, also seen in earlier work from Akasaka et al.,⁸ but was not specifically mentioned. Broad, red-shifted emission from PAHs is frequently associated with excited-state dimer (excimer) formation, however this seems an unlikely explanation for this photophysical behavior given that the solutions are highly dilute where intermolecular association during the excited-state lifetime is unlikely. This red shift is tentatively attributed to the bending of the anthracene ring witnessed for this ligand in its uranyl complex (*vide supra*), however, at this point it is not clear if the same

non-planar geometry is assumed for the ring in the free phosphine oxide ligand. Further study into the cause of this photophysical phenomenon is covered in Appendix B. This shift represents a fundamental difference from the results for ligands **1**, **2** and **4** in which the emission appears typical of the monomer-type emission expected on the basis of the parent PAH.

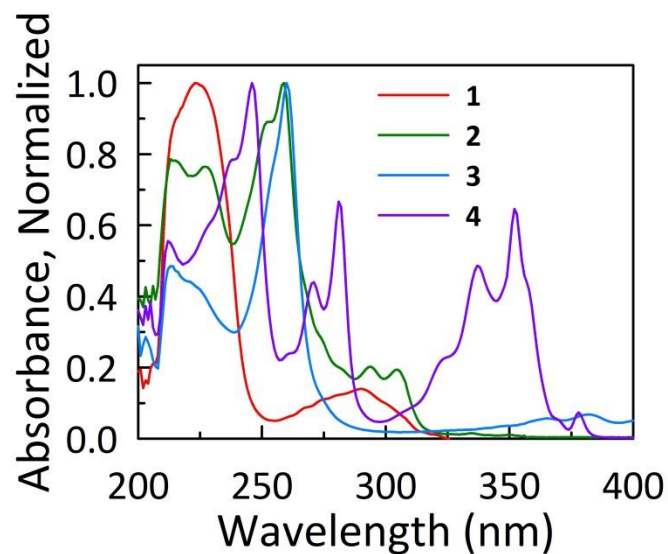


Figure 6: Normalized UV-vis absorption spectra of phosphine oxide ligands **1–4** in THF.

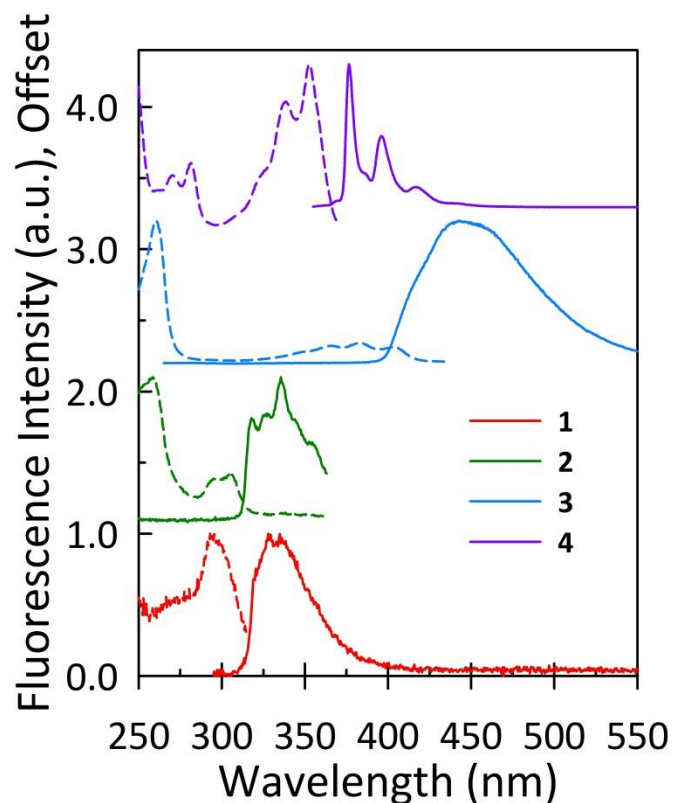


Figure 7: Normalized excitation (broken profiles) and emission spectra (solid lines) of aromatic phosphine oxide ligands **1–4** in THF at a concentration of 2×10^{-5} M. The emission and excitation wavelengths used to record these spectra were 320/290, 368/260, 440/260, and 377/337 nm for compounds **1**, **2**, **3**, and **4**, respectively.

The fluorescence spectra for the uranyl complexes, **5–8**, were also attempted in THF solution at mM concentrations, however, it was found that the phosphine oxide ligands dissociated at dilute concentration. This was verified by ^{31}P NMR spectroscopy of the 1 mM stock solution, which showed the presence of free ligand only. Thus, the fluorescence profile was identical to that of the free ligand and the spectroscopy of the uranyl complexes could not be satisfactorily obtained.

Conclusion

Novel triaryl phosphine oxide ligands have been synthesized and characterized through ^1H , ^{13}C , and ^{31}P NMR as well as IR, UV-Vis, and fluorescence spectroscopy where one of the aryl substituents is a polycyclic aromatic hydrocarbon. Two ligands coordinate to $\text{UO}_2(\text{NO}_3)_2$ to form eight-coordinate complexes, which were characterized by X-ray crystallography. In addition, for the first time three phosphine oxide ligands were structurally observed to bind to $\text{Th}(\text{NO}_3)_4$ to produce an eleven-coordinate species. The fluorescence spectrum of the anthracenyl-substituted phosphine oxide ligand showed no vibronic coupling and was red-shift approximately 50 nm from free anthracene, providing possible opportunities for detection.

Acknowledgments.

I would like to thank Durgesh Wagle and Dr. Gary Baker for their help in collecting the fluorescence spectroscopy data. I would also like to thank Drs. Michael Takase and Charles Barnes for assisting in collection of the single crystal x-ray diffraction structures and their work to complete and format the CIF files for publication.

This material is based upon work supported by the U.S. Department of Homeland Security under Grant Award Number, 2012-DN-130-NF0001-02. The views and conclusions contained in this document are those of the authors and should not be interpreted as necessarily representing the official policies, either expressed or implied, of the U.S. Department of Homeland Security. We also acknowledge the Nuclear Regulatory Commission (NRC) Faculty Development Award for financial support.

References

1. Alcock, N. W.; Roberts, M. M.; Brown, D., Actinide structural studies. Part 1. Crystal and molecular structures of dinitratodioxobis(triphenylphosphine oxide)neptunium(VI), dinitratodioxobis(triphenylphosphine oxide)uranium(VI), and dichlorodioxo-(triphenylphosphine oxide)neptunium(VI). *J. Chem. Soc., Dalton Trans.* **1982**, (1), 25-31.
2. Charushnikova, I. A.; Krot, N. N.; Starikova, Z. A., Crystal structure of a complex of Pu(VI) nitrate with triphenylphosphine oxide, $[\text{PuO}_2(\text{NO}_3)_2(\text{OP}(\text{C}_6\text{H}_5)_3)_2]$. *Radiochem.* **2007**, *49* (6), 561-564.
3. Bombieri, G.; Forsellini, E.; Day, J. P.; Azeez, W. I., Crystal and molecular structure of dichlorodioxobis(triphenylphosphine oxide)uranium(VI). *J. Chem. Soc., Dalton Trans.* **1978**, (6), 677-680.
4. Panattoni, C.; Graziani, R.; Bandoli, G.; Zarli, B.; Bombieri, G., Chemistry of the uranyl group. II. Preparation and properties of triphenylphosphine oxide and triphenylarsine oxide complexes of uranyl acetate and the structure of $(\text{UO}_2(\text{CH}_3\text{COO})_2(\text{C}_6\text{H}_5)_3\text{PO})_2$. *Inorg. Chem.* **1969**, *8* (2), 320-325.
5. Gillens, A.; Powell, B., Rapid quantification of TBP and TBP degradation product ratios by FTIR-ATR. *J. Radioanal. Nucl. Chem.* **2013**, *296* (2), 859-868.
6. Allen, D. V.; Venkataraman, D., Copper-Catalyzed Synthesis of Unsymmetrical Triarylphosphines. *JOC* **2003**, *68* (11), 4590-4593.
7. Arrigo, L. M.; Galenas, M.; Bassil, D. B.; Tucker, S. A.; Kannan, R.; Katti, K. V.; Barnes, C. L.; Jurisson, S. S., Fluorescent phosphinimine as possible precursor to an anionic and fluorescent sensor for Tc-99. *Radiochim. Acta* **2008**, *96* (12), 835-844.
8. Akasaka, K.; Suzuki, T.; Ohru, H.; Meguro, H., Study on Aromatic Phosphines for Novel Fluorometry of Hydroperoxides (I) -Synthesis and Spectral Properties of Diphenyl Aryl Phosphines and Their Oxides. *Anal. Lett.* **1987**, *20* (5), 731-745.
9. Apex II suite, B. A. L., 2006, Madison, WS.
10. Sheldrick, G., A short history of SHELX. *Acta Cryst. A* **2008**, *64* (1), 112-122.
11. Barbour, L. J., X-Seed – A Software Tool for Supramolecular Crystallography. *J. Supramol. Chem.*, **2001**, *1*, 189-191.
12. Matveeva, A. G.; Grigoriev, M. S.; Dvoryanchikova, T. K.; Matveev, S. V.; Safiulina, A. M.; Sinegribova, O. A.; Passechnik, M. P.; Godovikov, I. A.; Tatarinov, D. A.; Mironov, V. F.; Tananaev, I. G., Complexes of (2-methyl-4-oxopent-2-yl)diphenylphosphine oxide with uranyl and neodymium nitrates: synthesis and structures in the solid state and in solution. *Russ. Chem. Bull.* **2012**, *61* (2), 399-404.

13. Agostini, G.; Giacometti, G.; Clemente, D. A.; Vicentini, M., Crystal and molecular structure of uranyl nitrate trimethylphosphate. *Inorg. Chim. Acta* **1982**, 62 (0), 237-240.
14. Babecki, R.; Platt, A. W. G.; Tebby, J. C.; Fawcett, J.; Russell, D. R.; Little, R., The crystal and molecular structure of $\text{UO}_2(\text{NO}_3)_2[\text{Ph}_2\text{P}(\text{O})\text{CH}_2\text{C}(\text{O})\text{Ph}]_2$ and its role in the solvent extraction of the uranyl ion. *Polyhedron* **1989**, 8 (10), 1357-1360.
15. Burns, J. H., Solvent-extraction complexes of the uranyl ion. 1. Crystal and molecular structure of bis(nitrato)bis(tri-n-butylphosphine oxide)dioxouranium(VI). *Inorg. Chem.* **1981**, 20 (11), 3868-3871.
16. Burns, J. H.; Brown, G. M.; Ryan, R. R., Structure of dinitratodioxobis(triisobutyl phosphate)uranium(VI) at 139 K. *Acta Cryst. C* **1985**, 41 (10), 1446-1448.
17. Casellato, U.; Fregona, D.; Tamburini, S.; Vigato, P. A.; Graziani, R., Synthesis and characterization of uranyl(VI) and thorium(IV) complexes with phosphine oxides. The crystal structure of $\text{UO}_2(\text{NO}_3)_2(\text{NO}_2\text{-C}_6\text{H}_4\text{Ph}_2\text{PO})_2$. *Inorg. Chim. Acta* **1985**, 110 (1), 41-46.
18. Charpin, P.; Lance, M.; Soulie, E.; Vigner, D., Structure du dinitratodioxobis(triamide hexamethylphosphorique)uranium(VI), $[\text{UO}_2(\text{NO}_3)_2(\text{C}_6\text{H}_{18}\text{N}_3\text{OP})_2]$. *Acta Cryst. C* **1985**, 41 (6), 884-886.
19. Conary, G. S.; Duesler, E. N.; Paine, R. T., Coordination chemistry of 2-diethylphosphonato-4,6-dipiperidino-1,3,5-triazine with uranyl nitrate. *Inorg. Chim. Acta* **1988**, 145 (1), 149-156.
20. Cromer, D. T.; Ryan, R. R.; Karthikeyan, S.; Paine, R. T., Structural studies of uranyl complexes of diphenyl-dimethylaminosulfonylmethyl phosphine oxide and diisopropyl-tolylsulfinylmethyl phosphonate ligands. *Inorg. Chim. Acta* **1990**, 172 (2), 165-172.
21. de Aquino, A. R.; Bombieri, G.; Isolani, P. C.; Vicentini, G.; Zukerman-Schpector, J., Characterization, luminescence and crystal structure of uranyl nitrate complexes with diphenyl-N-ethylphosphine amide and tripiperidinephosphine oxide. *Inorg. Chim. Acta* **2000**, 306 (1), 101-105.
22. Henderson, W.; Leach, M. T.; Nicholson, B. K.; Wilkins, A. L.; Hoye, P. A. T., Uranyl nitrate complexes of camphene-derived organophosphorus ligands, and the X-ray crystal structure of $[\text{UO}_2(\text{NO}_3)_2(\text{RPO}_3\text{Me}_2)_2]$ (R=endo-8-camphanyl). *Polyhedron* **1998**, 17 (21), 3747-3752.
23. Kanellakopulos, B.; Dernberger, E.; Maier, R.; Nuber, B.; Stammli, H.-G.; Ziegler, M. L., Molekülstruktur und Ladungsverteilung. IV1) Elektrisches Dipolmoment von 1:2-Addukten des Uranyl-nitrats mit Trialkylphosphaten. Die Kristallstruktur von

$\text{UO}_2(\text{TEP})_2(\text{NO}_3)_2$ und $\text{Bis}[(\mu\text{-diethylphosphato-O—O'})\text{nitrato}(\text{triethyl-phosphato})\text{-dioxouran(VI)}]$, $\{\text{UO}_2\}[(\text{EtO})_2\text{PO}_2](\text{EtO})_3\text{PO}](\text{NO}_3)_2$. *Z. Anorg. Allg. Chem.* **1993**, 619 (3), 593-600.

24. Karthikeyan, S.; Ryan, R. R.; Paine, R. T., Synthesis and coordination properties of (sulfinylmethyl)phosphonates and (sulfonylmethyl)phosphonates. Crystal and molecular structure determinations for $\text{UO}_2(\text{NO}_3)_2[(\text{iso-C}_3\text{H}_7\text{O})_2\text{P}(\text{O})\text{CH}_2\text{S}(\text{O})_2\text{C}_6\text{H}_{11}]_2$ and $\text{Gd}(\text{NO}_3)_3[(\text{iso-C}_3\text{H}_7\text{O})_2\text{P}(\text{O})\text{CH}_2\text{S}(\text{O})(\text{p-CH}_3\text{C}_6\text{H}_4)].\text{H}_2\text{O}$. *Inorg. Chem.* **1989**, 28 (14), 2783-2789.

25. Znovjyak, K. O.; Ovchynnikov, V. A.; Sliva, T. Y.; Shishkina, S. V.; Amirkhanov, V. M., $\text{Bis}(\text{N}\{-\text{bis}[\text{methyl}(\text{phenyl})\text{amino}]\text{phosphoryl}\}-2,2,2\text{-trichloroacetamide})\text{dinitratodioxidouranium(VI)}$. *Acta Cryst. E* **2010**, 66 (3), m306.

26. du Preez, J. G. H.; van Vuuren, C. P. J., The chemistry of uranium. Part XII. Nitrate complexes of uranium(IV) and thorium(IV). *J. Chem. Soc., Dalton Trans.* **1975**, (15), 1548-1552.

27. Bagnall, K. W.; Wakerley, M. W., Phosphine oxide complexes of thorium(IV), uranium(IV), neptunium(IV), and dioxouranium(VI) nitrates. *J. Chem. Soc., Dalton Trans.* **1974**, (8), 889-895.

Chapter 2: Extraction of Water and Speciation of Trivalent Lanthanides and Americium in Organophosphorus Extractants[†]

[†]This chapter is based on a manuscript that was submitted to and accepted by *Inorganic Chemistry*. The DOI is: 10.1021/acs.inorgchem.6b01756 and can be cited as:

Gullekson, B. J.; Breshears, A. T.; Brown, M. A.; Essner, J. B.; Baker, G. A.; Walensky, J. R.; Paulenova, A.; Gelis, A. V., Extraction of Water and Speciation of Trivalent Lanthanides and Americium in Organophosphorus Extractants. *Inorg. Chem.* **2016**, *55* (24), 12675-12685.

Abstract

Complexes of the trivalent lanthanides and americium with di-2-ethylhexyl phosphoric acid (HDEHP) in an aliphatic diluent were probed with UV-Vis, X-ray Absorption Fine Structure (XAFS), and Time-Resolved Fluorescence (TRF) spectroscopy, while water concentration was determined by Karl Fischer titrations. The work in this chapter focuses on the change in the Nd hypersensitive UV-Vis absorbance region in relation to the pseudo-octahedral Nd environment when coordinated with three HDEHP dimers. In contrast to recently reported interpretations, the work herein establishes that while impurities influence this electronic transition band, high water content can cause the distortion of the pseudo-octahedral symmetry of the six-coordinated Nd, resembling the reported spectra of seven-coordinated Nd compounds. Extended X-ray Absorption Fine Structure (EXAFS) analysis of the Nd in high concentration HDEHP solutions also points to an increase in the coordination number from 6 to 7. Spectral behavior of other lanthanides (Pr, Ho, Sm, Er)

and Am(III) as a function of the HDEHP concentration suggests that the water coordination with the metal likely depends on the metal's effective charge. Fluorescence data using lifetime studies, excitation and emission spectra support the inclusion of water in the Eu coordination sphere. Further, the role of the effective charge was confirmed by comparison of Gibbs free energies of 6 and 7 coordinate La-HDEHP-H₂O and Lu-HDEHP-H₂O complexes using Density Functional Theory. In contrast, HEH[EHP], the phosphonic acid analog of HDEHP, exhibits a smaller capacity for water, and the electronic absorption spectra of Nd or Am appear to be unchanged, although the Pr spectra show a noticeable change in intensity as a function of water content. Electronic absorption extinction coefficients of Am(III), Nd(III), Pr(III), Sm(III), Er(III) and Ho(III) as a function of the HDEHP concentration are reported for the first time.

Scope of Impact

Presented in this chapter is an investigation of the change in the hyperfine UV-Vis spectral region of neodymium and other lanthanides. According to present knowledge in this field, the only reason there should be a change in the hyperfine spectrum would be if there is a change in the coordination environment. In the literature, it was assumed that if the hyperfine region changed while using only HDEHP, then the change had to come from an impurity, such as mono-2-ethylhexyl phosphate. However, in this work, it was found that the purity was not the only reason for a change in the hyperfine region, but that water could also co-extract and cause a change in the coordination environment and thus a change in the hyperfine region of the neodymium.

Introduction

Organophosphoric cation exchange extractants have been widely employed as a means of partitioning metals in solvent extraction processes and analytical chromatographic techniques. HDEHP in particular has been used in separation of uranium, lanthanides, and transition metals in post-leaching extraction, and in separation of transuranics in the nuclear fuel cycle.¹⁻³ HDEHP is used in the TALSPEAK process as a means of separating trivalent minor actinides from fission produced lanthanides in Used Nuclear Fuel (UNF).^{4,5} In recent years, advances have focused on combining TALSPEAK with other process steps to simplify separations or through the use of analogous extractants, such as 2-Ethylhexyl phosphonic acid mono-2-ethylhexyl ester (HEH[EHP], Figure 1B) to improve process operations.⁶⁻⁸

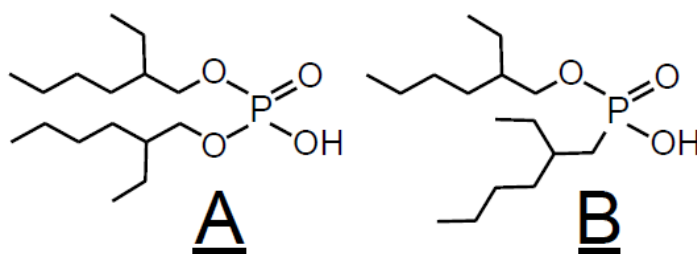


Figure 1: Organic phase cation exchange molecules: (A) HDEHP and (B) HEH[EHP]

Metal complexation in the HDEHP organic phases remain a subject of investigation, with multiple interpretations as to the nature of organophosphoric extractant coordination to the metal center. The traditional interpretation of trivalent actinide and lanthanide speciation following extraction has been metal coordination with three mono-deprotonated dimers of HDEHP in the form $M(HA_2)_3$, where “A” represents the DEHP anion and “H” represents the acid proton, however, several alternate species have been proposed.^{9,10} Pseudo-octahedral coordination of the metal in highly symmetrical systems

have been suggested through investigations with time resolved laser fluorescence spectroscopy (TRLFS) and Extended X-ray Absorption Fine Structure (EXAFS) of similar systems, however differences in experimental conditions prompt further studies.^{11,12}

UV-Vis-NIR spectroscopy of f-elements has been used to identify the types of complexes that these metals form with various ligands.^{13,14} Certain electronic transitions are hypersensitive to symmetry and electronic field strength of the metals, such as the $^4I_{9/2} \rightarrow ^4G_{5/2}, ^2G_{7/2}$ transition of neodymium, the $^4I_{9/2} \rightarrow ^2H_{9/2}, ^4F_{5/2}$ transition of holmium, and the $^4I_{15/2} \rightarrow ^2H_{11/2}$ transition of erbium. Several other trivalent f-elements, such as praseodymium ($^3H_4 \rightarrow ^3P_2, ^1I_6, ^3P_1, ^3P_0$) and americium ($^7F_0 \rightarrow ^5L_6$), have absorption bands in the visible region.¹⁴ Jensen, *et. al.* reported multiple means of organic Nd complexation in HDEHP using Small Angle Neutron Scattering (SANS) coupled with UV-Vis-NIR spectroscopy, with $Nd(HA_2)_3$ present at high HDEHP concentration and low metal loading, and a bridged, two metal species of the type $Nd_2(DEHP)_6$ reported at low HDEHP concentration and high metal loading.¹⁵ Alternately, using x-ray single crystal scattering of Nd dimethyl phosphate compounds and UV-Vis spectroscopic results, the coordination of Nd in HDEHP organic phases has been found to exist as a pseudo-octahedral coordination environment independent of metal loading percentage, and the changes in speciation at low HDEHP concentration were a result of impurities in the cation exchange extractant.¹⁶

A recent study pointed out that the differences in the 570 to 583 nm absorption ratio were due to the impurity, mono-2-ethylhexyl phosphate, in HDEHP and left no question as to whether other causes affect this ratio. Indeed, it was recently found that the 570 to 583 nm absorption ratio did change, even with the lack of an impurity.¹⁷ It has been noted that aqueous species such as water and lactate can co-extract with metals into the organic

phase.¹⁰ These co-extracted species, if bound to the inner coordination sphere of the metal could produce an effect on the hyperfine regions of Nd UV-Vis spectrum. This would also influence process monitoring, which relies on these electronic transitions.¹⁸ This investigation seeks to identify the source of metal coordination changes in different concentration HDEHP containing organic phases in order to improve understanding of how metals coordinate to HDEHP and HEH[EHP] under different organic phase conditions.

Experimental Methods

UV-Vis Spectroscopy and Karl Fischer Water Determination

Organic solutions were prepared by mass from purified cation exchange ligand stocks. HDEHP (J.T. Baker, 98%) was purified by the copper precipitation purification technique with slight modifications. Precipitation of Cu[DEHP]₂ out of diethyl ether was carried out 3 times. Between each precipitation, after washing with acetone, the product was dried for 2 hours with a stream of dry nitrogen. The dissolving of Cu[DEHP]₂ in diethyl ether was allowed to proceed over 1 hr to ensure all of the precipitate was dissolved. After converting Cu[DEHP]₂ back to CuSO₄ and HDEHP, the organic phase was washed five times (20 mL per wash) with deionized water (D.I. H₂O) to ensure that there was no sulfuric acid remnant in the organic phase. HDEHP was concentrated by removing the solvent in vacuo on a Schlenk line with a 25 mmHg vacuum, while the HDEHP-diethyl ether flask was heated to 90 °C. The purity of HDEHP was >99.95% as confirmed by both ³¹P NMR spectroscopy and acid-base titration in 80% methanol-water mixture.¹⁹ HEH[EHP] (Yick-Vic Chemicals & Pharmaceuticals, 97%) was purified using the copper precipitation purification technique to >99.95% purity as confirmed by ³¹P NMR spectroscopy and by measuring the density.¹⁹ Each extractant was dissolved in n-dodecane (Acros Organics 99+%), used as

delivered. Lanthanide chlorides were individually prepared by dissolving Nd_2O_3 (Sigma Aldrich, 99.9%), $\text{Pr}(\text{NO}_3)_3$ (Alfa Aesar, 99.9%), $\text{Sm}(\text{NO}_3)_3$ (Sigma Aldrich, 99.9%), Er_2O_3 (Sigma Aldrich, >99.9%) and Ho_2O_3 (Sigma Aldrich, >99.9%) in concentrated HCl (Macron, ACS grade) and evaporated. Aqueous solutions were then prepared by dissolving in a HCl solution (Macron, ACS grade) with the final solution measured to be pH 2.80 +/- 0.05 as checked with an Orion 8165 BNWP pH electrode. Metal concentrations were determined by EDTA titrations with xylenol orange as an indicator.²⁰ Americium chloride was prepared similarly through conversion of an in-house ^{243}Am stock solution purified using a DGA column (Eichrom) by dissolution in concentrated HCl and subsequent evaporation, followed by dissolution in HCl at pH 2.80. The concentration was determined through LSC counting on a Perkin Elmer Tricarb 3180 with alpha/beta discrimination. All aqueous solutions were prepared with D.I. H_2O (Millipore, 18.1 $\text{M}\Omega\cdot\text{cm}$).

Solvent extraction was performed by contacting equal volumes of organic and aqueous phases for 10 minutes using a vortex mixer followed by centrifugation at 3000 rpm for 5 minutes or until phase separation. UV-Vis-NIR spectra of the post extraction organic phases were collected on a Cary 6000i UV-Vis-NIR spectrometer with a jacketed cell held at 20 °C. Water concentration in the organic phases was determined by volumetric Karl Fischer titrations on a Mettler Toledo DL58 auto titrator with each sample measured in duplicate.²⁰ Distribution ratios of the lanthanides were determined using a colorimetric technique with Arsenazo III at pH 9 buffered by triethanolamine and compared to a calibration curve.²¹ Distribution ratios of ^{243}Am were determined through LSC alpha counting using Tri-Carb 2910 (Perkin Elmer) with an alpha-beta discriminator to prevent the interference from the beta-emitting ^{239}Np daughter radioisotope. Water was removed

from post-metal extraction organic phases with 3 Å molecular sieves heated for at least 5 hours at 225 °C at 15 kPa.

EXAFS Procedure

Neodymium was extracted into the HDEHP phase (*n*-dodecane diluent) from a pH ~3 chloride solution. The organic layers were separated and transferred to a modified 4.5 mL cuvette with an epoxied Kapton window. The cell window was oriented at a 45-degree angle with respect to the incident beam, while the detector was nominally positioned at 90° with respect to the incident beam in the horizontal plane. X-ray absorption fine structure (XAFS) spectra were measured on the Materials Research Collaborative Access Team (MRCAT) insertion device beam line 10-ID at Argonne National Laboratory's Advanced Photon Source (APS). The energy was selected with a cryogenic Si (111) double-crystal monochromator. The scan mode was continuous scanning with undulator tracking. Harmonic rejection was accomplished with a Rh-coated mirror, while energy calibration was with the Fe K edge of a metallic Fe foil (7110.75 eV).²² No further calibration or alignment of the scans was performed; the average shift within a series of scans for each sample was less than 0.02 eV. The Nd L₃ edge (6208 eV) was probed in fluorescence mode using a gas ionization chamber and Soller slits with a vanadium filter.²³ The data is comprised of the average of four or more scans and was treated using *Athena* and *Artemis* software packages.^{24,25}

Time-Resolved Fluorescence Spectroscopy Procedure

An aqueous europium stock (30.0 mM) in pH 2.80 HCl was prepared from europium nitrate hexahydrate (Alfa Aesar, 99.9%) and extracted into HDEHP, 1:1 organic to aqueous by volume, 4 mL sample size. Molecular sieves (Sigma Aldrich, 3 Å pore size) were dried for

16-20 h at 200 °C prior to use. Approximately 20 dry sieve beads were added to each sample and the samples were stored in the dark for 24 h, after which fluorescence lifetime measurements were conducted. This procedure was repeated two additional times with the addition of new sieve beads, after which the fluorescence lifetime was measured.

Steady-state fluorescence measurements were collected on a HORIBA Jobin Yvon Fluorolog®-3 spectrofluorometer exciting at 464 nm and monitoring the emission from 474 - 800 nm. Due to the long-lived nature of the Eu-complexes' lifetimes, the time-resolved measurements were obtained on a Varian Cary Eclipse Fluorometer with a 464 nm excitation wavelength and monitoring the emission of the hypersensitive electric-dipole transition $^5D_0 \rightarrow ^7F_2$ (605–620 nm, specifically at 610 nm). The individual lifetime measurements were an average of 100 scans in which the Xe flash lamp was flashed 50 times per scan with delay and gate times of 0.001 ms and 0.01 ms, respectively. All measurements were conducted at ambient temperature using 1 cm quartz cuvettes.

1.4 mL of the dried organic phase were contacted with 1.4 mL of D₂O, rapidly vortexed for one minute, and then centrifuged at 5000 rpm for 5 min to separate the phases. The organic phase was then pipetted out and stored in the dark for 24 hours. After storage, the excitation, emission spectra, and lifetimes were collected. The same process was repeated with H₂O for both reproducibility of Eu extraction and comparison with the D₂O spectras. All the experimental parameters for the steady-state and lifetime collections remained the same as above.

Computational details

The electronic structure of (HDEHP)₂(H₂O), (HEH[EHP])₂(H₂O), (Cyanex272)₂H₂O, M(H(DEHP)₂)₃, M(H₂O)(H(DEHP)₂)₃ (water inner sphere), and M(H(DEHP)₂)₃•H₂O

(water outer sphere), where M= La, Lu, were examined using the Gaussian09 D.01 software suite.²⁶ GaussView 5.0.9 was used to draw molecular structures and write Gaussian09 input files.²⁷ The 2-ethylhexyl alkyl groups of dimers were truncated to 2-methylpropyl. Initially, the metal HDEHP complexes alkyl groups were truncated to methyl and after the preliminary optimization and frequency calculations were expanded to the full 2-ethylhexyl alkyl chains and re-optimized. Starting geometries were initially optimized using UFF force field calculations native to the Gaussian09 suite. Density functional theory was performed at the Becke-3 exchange and Lee-Yang-Parr correlation functional (B3LYP) level of theory.²⁸⁻³⁰ Full geometry optimizations were performed and stationary points were determined to be global minima using analytical frequency calculations. The Stuttgart/Dresden triple- ζ basis set was used to model lanthanum and lutetium.^{31,32} While the Pople double- ζ quality basis set, 6-31G(d,p), was used for all non-lanthanide atoms.^{33,34}

Experimental Results and Discussion

Neodymium Speciation in HDEHP Organic Phases

Aqueous phase neodymium solutions between 1.3 mM Nd and 29.3 mM Nd were extracted into 0.2 –2.0 M HDEHP solution in n-dodecane. UV-Vis spectra were taken for each post-extraction organic phase with the absorption bands of the $^4I_{9/2} \rightarrow ^4G_{5/2}, ^2G_{7/2}$ electronic transition shown in Figure 2. The spectral characteristics remain constant with changes in metal concentration, but shift with respect to HDEHP concentration.

At low HDEHP concentrations, the spectra resemble those of a pseudo-octahedron, containing the characteristic 6 absorption bands (570, 575, 583, 590, 598, 605 nm) with the 570 nm band (A_{570}) being the most prominent absorption.¹⁶ This type of absorbance has been previously identified as representative of polymeric speciation in the

organic phase.^{15,16} With an increase in HDEHP concentration however, A_{570} is seen to decrease while the absorption band at 583 nm (A_{583}) is seen to increase. This is consistent with an increase in the coordination number of the metal complex to a seven-coordinate species.¹³

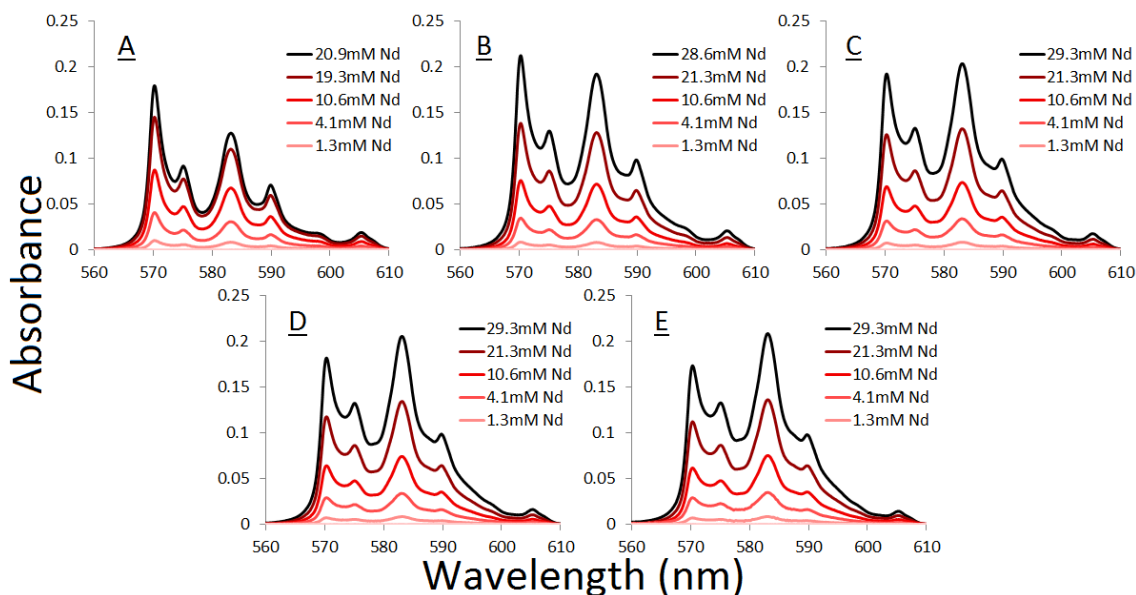


Figure 2: Neodymium UV-Vis spectra of varying metal concentrations in (A) 0.2 M HDEHP, (B) 0.5 M HDEHP, (C) 1.0 M HDEHP, (D) 1.5 M HDEHP, and (E) 2.0 M HDEHP

Dilution of Nd loaded organic phases of higher HDEHP concentration with non-pre-equilibrated solutions of the same HDEHP concentration resulted in a substantial shift of the UV-Vis spectra, whereas dilution with pre-equilibrated organic phases resulted in no spectral change (Figure 3). Upon dilution, A_{570} was seen to increase and A_{583} was seen to decrease, suggesting a decrease in the coordination number.¹³

Furthermore, when Nd is extracted into a 0.5 M HDEHP organic phase and the HDEHP concentration is increased via titration of a higher HDEHP concentration organic phase, no shift in the spectrum is seen, as shown in Figure 4.

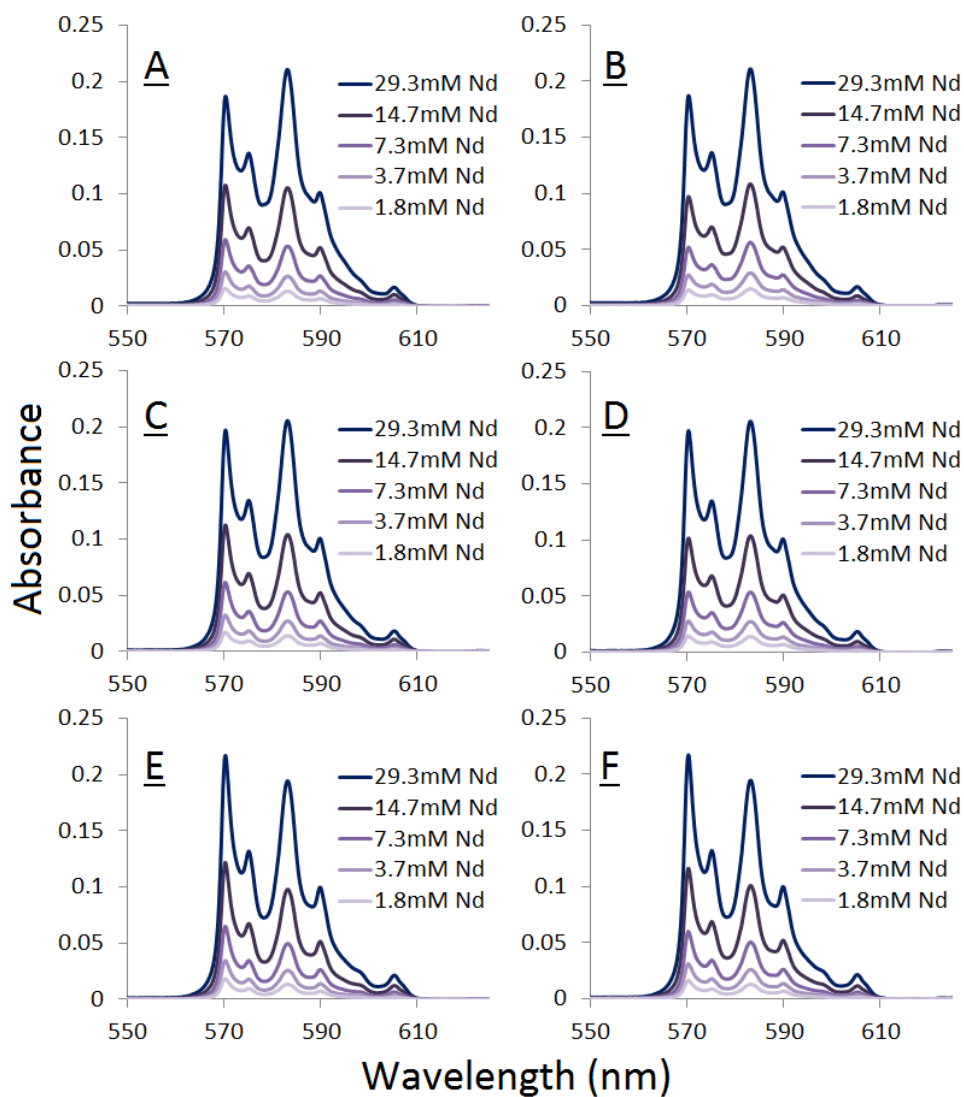


Figure 3: UV-Vis spectra of Nd extracted into 1.5 M HDEHP and diluted with non-preequilibrated (A) and pre-equilibrated (B) 1.5 M HDEHP, 1.0 M HDEHP and diluted with non-preequilibrated (C) and pre-equilibrated (D) 1.0 M HDEHP, and 0.5 M HDEHP and diluted with non-preequilibrated (E) and pre-equilibrated (F) 0.5 M HDEHP

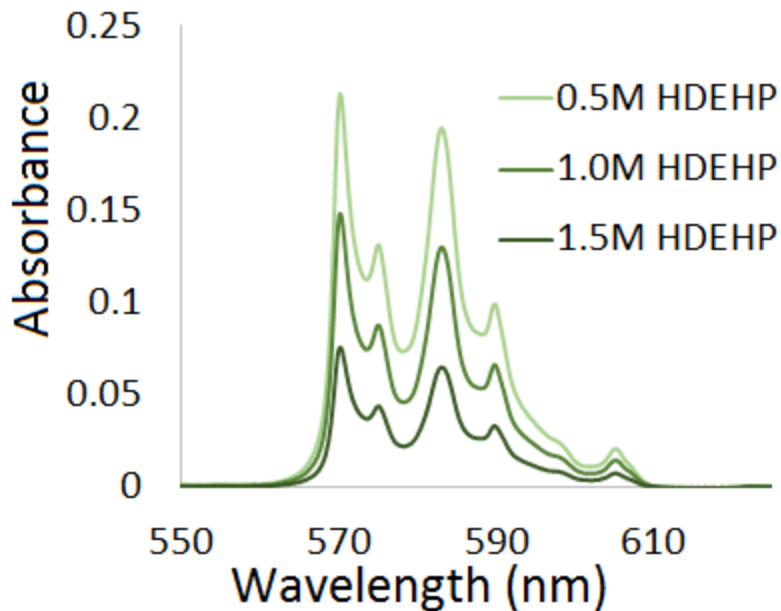


Figure 4: Nd extraction into 0.5 M HDEHP followed by titration with 2.0 M HDEHP, increasing HDEHP concentration

This behavior also alludes to the presence of an alternate extracted species that may be causing changes in the metal complexation in these organic phases. The water concentration in post-extraction organic phases was determined by Karl Fischer titrations, as shown in Figure 5 as a function of pre-extraction aqueous phase metal concentration for each HDEHP concentration. Increasing the organic phase HDEHP concentration results in appreciable increases in the extracted water concentration, however, the metal concentration in the ranges studied have little to no effect on the extraction of water. Given the significant excess of ligand relative to metal concentration, these results suggest that the ligand is the primary vehicle for loading the significant quantities of water into the organic phase.

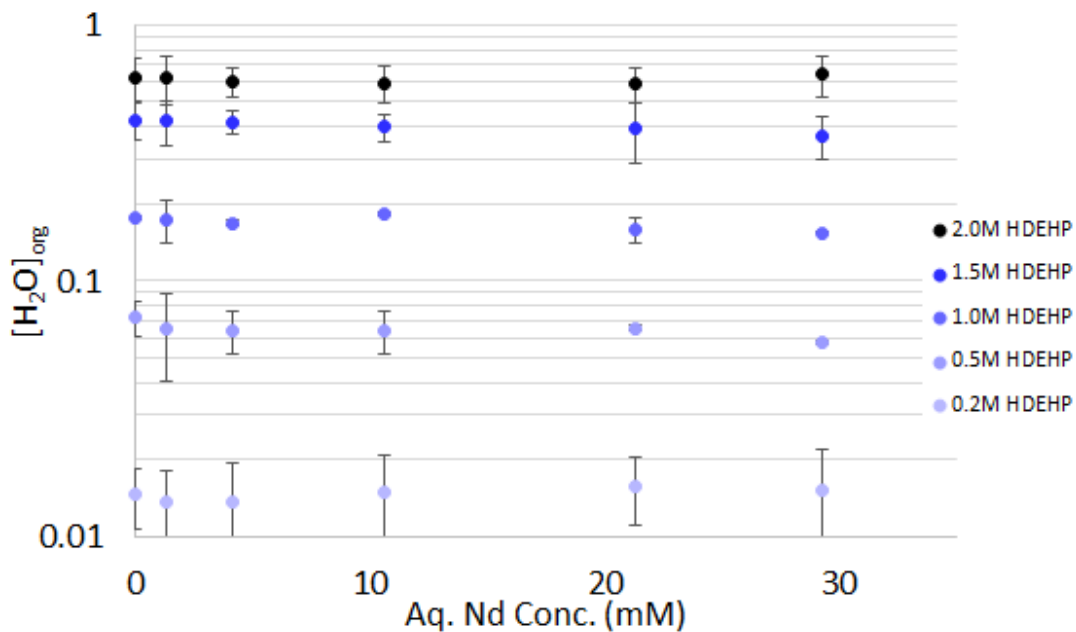


Figure 5: Water concentration of HDEHP organic phases following extraction of neodymium

To relate organic phase water content to metal speciation, 29.3 mM Nd was extracted into a 2.0 M HDEHP organic phase and was then dried over 3 Å molecular sieves for two, 3 day periods. UV-Vis spectra were collected and water was determined using Karl Fischer titrations after extraction and each drying step. The UV-Vis spectra are shown in Figure 6. As seen, the spectra shift significantly upon water removal with A_{570} increasing and A_{583} decreasing, similar to the spectra of lower HDEHP concentration organic phases. This suggests that the speciation changes of neodymium in HDEHP organic phases are largely a result of water co-extracted to the organic phase. Furthermore, the nature of the spectral shift indicates that the coordination number of the metal in the organic phase may be decreasing as water is removed.¹³

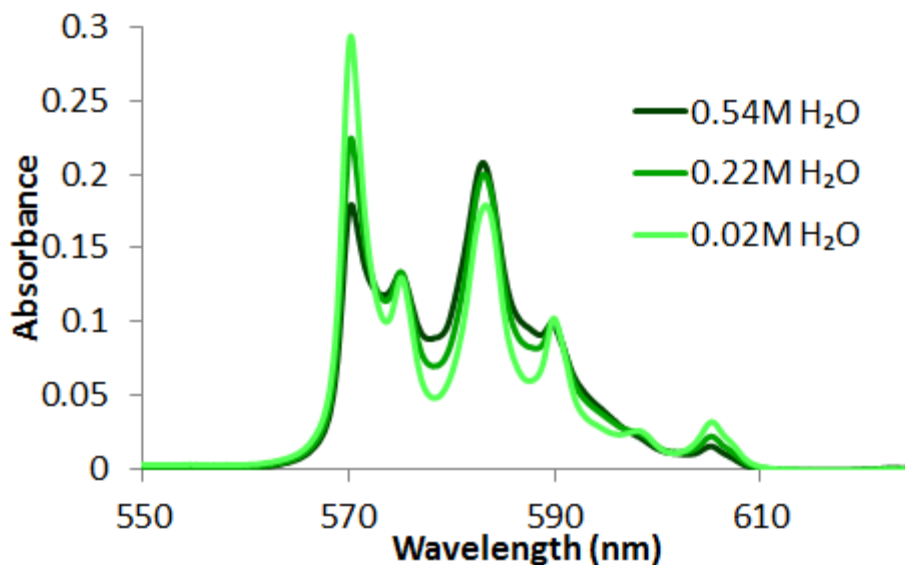


Figure 6: UV-Vis spectrum of 29.3 mM Nd in 2.0 M HDEHP following extraction and subsequent desiccation

Metal Coordinate Structure of Nd in HDEHP Organic Phases

The interpretations of the Fourier-Transform (FT) of the XAFS spectra primarily focus on the two most substantial peaks in Figure 7. They correspond to the nearby oxygen and phosphorous scattering paths at 1.9 Å and 3.4 Å (uncorrected for phase-shift), respectively. To resolve any differences between the two spectra, all parameters were fixed including S_0^2 (a generally accepted value of 0.9 was employed based on previous studies that probed Nd in identical or very similar solvents¹³), pre- and post-edge reduction, k -range (2–11 Å⁻¹), R -range (1–6 Å), and the input FEFF8.00 file. The input file was comprised of a two-shell model (O: 2.3 Å and P: 3.9 Å); multiple scatter paths did not aid the fit statistics. The variables allowed to refine were bond distances (R), Debye-Waller factors (σ^2), the change in edge energy (ΔE_0), and the oxygen coordination number CN.

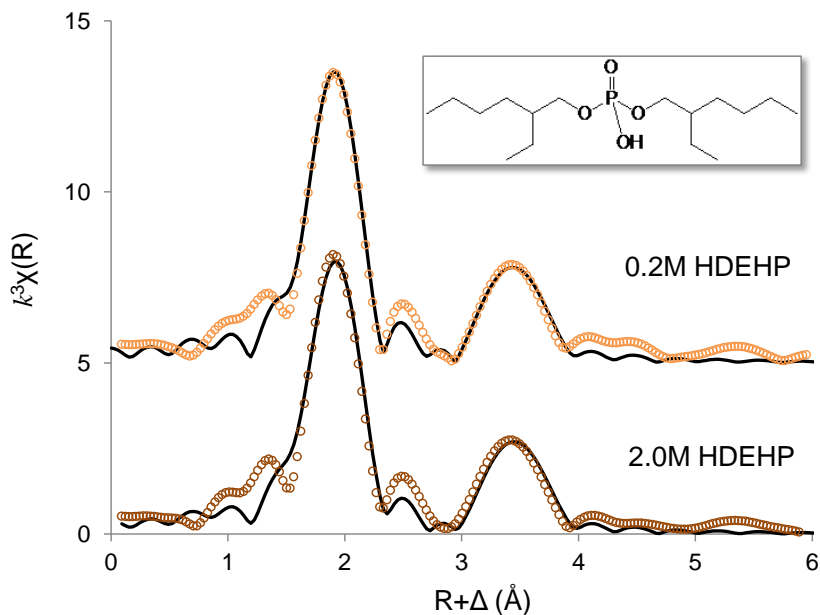


Figure 7: Fourier transformed k^3 -weighted XAFS and best fit of the Nd (10 mM) L_3 -edge spectra in 0.2 M HDEHP (offset by +5) and 2.0 M HDEHP in n-dodecane. Circles represent experimental data; solid lines represent the model fit.

The results are consistent with conventional x-ray absorption interpretations of Ln-coordinated organophosphorus extractants, which have thus far accepted a general coordination chemistry of $6 \times O$ and $6 \times P$ at approximately 2.3 \AA and 3.8 \AA , respectively.^{12,35,36} The assumption that $S_0^2 = 0.9$ affects all fits equally and therefore the differences in the coordination number with statistical uncertainties are reliable. Nonetheless, the conclusions are not dependent on the exact value of S_0^2 . The relative magnitude of the CNs is useful, since the actual S_0^2 is presumed to be identical between such similar coordination environments. However, the inherent uncertainties in resolving CNs by XAFS are known.³⁷ The CN for the P-shell was fixed at 6.0 since it is unlikely that anything other than a three-dimer HDEHP complex is coordinated (separate refinements yielded CNs of approximately 6.0–6.3). From the results listed in Table 1, one can

recognize a larger CN for the 2.0 M HDEHP data. Targeting the extra source of oxygen scatter by XAFS proved to be inconclusive considering only one or two water molecules may be sufficient to disrupt the symmetry of three HDEHP dimers coordinated to the metal. However, simultaneously varying all other parameters such as S_0^2 and the input files always resulted in a more oxygen populated environment for the 2.0 M HDEHP solution than for 0.2 M. In a separate set of experiments, a 2.0 M HDEHP solution containing 100 mM Nd was diluted to 10 mM Nd with fresh 2.0 M HDEHP in order to analyze the effects of diluting the extracted water. This solution was analyzed in the same manner and the results (listed in Table 1 as 2.0 M-diluted) reveal a coordination environment more similar to that of 0.2 M HDEHP. Though the CN results support the initial claims that water may be coordinating to the Nd-(DEHP)₃(HDEHP)₃ complex at higher [HDEHP], the reality is that the two CN values are only marginally statistically different. In fact, the only parameters correlated to the oxygen neighbors that are statistically different (albeit 1- σ uncertainty) are the radial distances. For a better interpretation of those results requires further investigation of the k -space.

Table 1: k^3 -weighted XAFS fit results for the L₃-edge of 0.2 M HDEHP / 10 mM Nd (R-factor = 0.019), 2.0 M HDEHP / 10 mM Nd (R-factor = 0.026), 2.0 M HDEHP / 10 mM Nd (diluted) (R-factor = 0.020) solutions in n-dodecane (uncertainty: 1- σ).

[HDEHP]	Potential	$R / \text{\AA}$	CN	$\sigma^2 \times 10^{-3} / \text{\AA}^{-1}$	$\Delta E_0 / \text{eV}$
0.2M	O	2.346 ± 0.008	6.3 ± 0.4	5 ± 1	4.2 ± 0.5
	P	3.88 ± 0.01	6 ^a	7 ± 2	
2.0M	O	2.362 ± 0.006	7.0 ± 0.3	7 ± 1	4.1 ± 0.4
	P	3.89 ± 0.01	6 ^a	8 ± 1	
2.0M -diluted	O	2.352 ± 0.007	6.5 ± 0.3	6 ± 1	4.2 ± 0.4
	P	3.88 ± 0.01	6 ^a	7 ± 1	

^a Fixed parameter

When considering the classic XAFS equation the pre-factor describes a slowly-varying amplitude envelope that, for these samples, emphasizes the contribution of the Nd-O scattering path at low- k . The oscillatory term $\sin[2kR+\delta(k)]$ will reflect small shifts in the phase for small shifts in bond length.³⁸ Though it is certain that the P-shell and multiple scattering potentials could also contribute some spectral shift in k -space, the nature of low k are usually long wavelengths in which contributions typically sum in phase.³⁸ Assuming equal phase-shifts and only considering a one-shell scattering potential, the sin term will generally shift $\chi(k)$ oscillations to even lower k for slightly larger distance scattering paths. With a sharp contrasted view, this is exactly what one sees in Figure 8, as the k -space shows a slight shift to lower k for the 2.0 M HDEHP sample. The 2.0 M HDEHP data, when refined, resulted in an average Nd-O path length that is approximately 0.02 Å longer than for 0.2 M HDEHP.

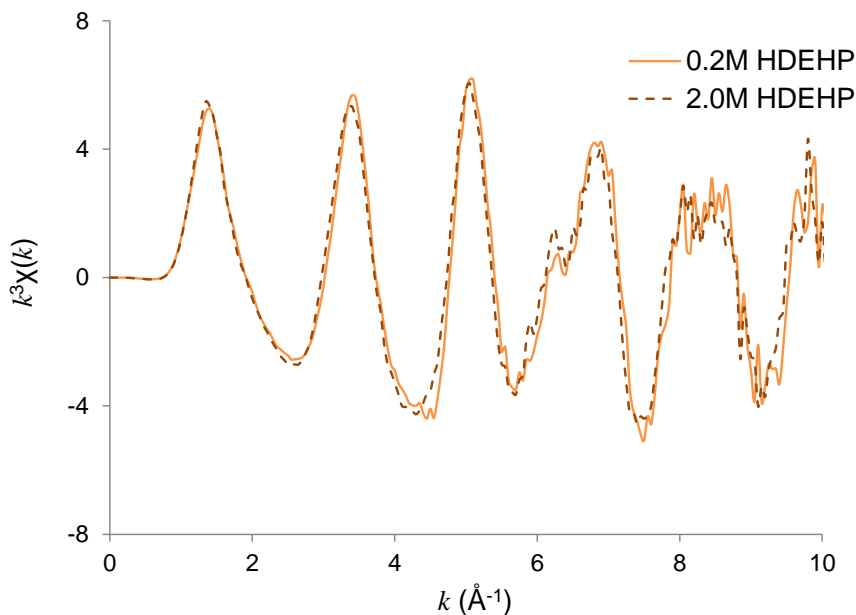


Figure 8: k^3 -Weighted XAFS data in k -space of the Nd (10 mM) L_3 -edge in 0.2 M HDEHP and 2.0 M HDEHP in n-dodecane.

The hypothesis formulated as to why the average Nd-O bond length is slightly larger in 2.0 M HDEHP is two-fold: either the XAFS is picking up the alleged water molecules coordinated to the outer-sphere of the Nd (assumably 2.49 Å based on aqueous Nd(III) XAFS analysis) or the water is coordinated to the HDEHP dimers which is stretching the HDEHP Nd-O path lengths.³⁹ An additional Nd-O at 2.49 Å is consistent with the observed results since a path at that distance would increase the average Nd-O bond length and σ^2 given no other changes to the inner-sphere coordination environment. Though the XAFS results are not entirely sufficient in pin-pointing the components responsible for altering the electronic spectra, the statistically larger Nd-O bond lengths and the higher oxygen CN support the claims that an additional source of oxygen – alongside the six HDEHP molecules – is within the metal’s local environment in 2.0 M HDEHP.

Other f-Elements in HDEHP Organic Phases

To understand the effects of water extraction into HDEHP organic phases on other f-elements and as a function of radii, spectra were collected at low (0.2 M) and high (2.0 M) HDEHP concentration after extraction of 17.7 mM Pr, 0.3 mM Am, 29.8 mM Sm, 12.9 mM Ho, and 14.4 mM Er. The water concentration in the post-extraction organic phases as determined by Karl Fischer titration for Pr and Ho are comparable to that of Nd as shown in Table 2. As the Karl Fischer titration is a destructive technique, water extraction testing was not performed for the americium extraction. The spectra of the $^3H_4 \rightarrow ^3P_2, ^1I_6, ^3P_1, ^3P_0$ transitions of praseodymium, the $^7F_0 \rightarrow ^5L_6$ transition of americium, the $^4I_{9/2} \rightarrow ^2H_{9/2}, ^4F_{5/2}$ transition of holmium, $^6H_{5/2} \rightarrow ^6P_{7/2}, ^4D_{1/2}, ^4F_{9/2}$ transition of samarium, and the $^4I_{15/2} \rightarrow$

$^4H_{11/2}$ transition of erbium along with the $^4I_{9/2} \rightarrow ^4G_{5/2}, ^2G_{7/2}$ transition of neodymium are shown in Figure 9, and corrected for metal concentration.⁴⁰⁻⁴²

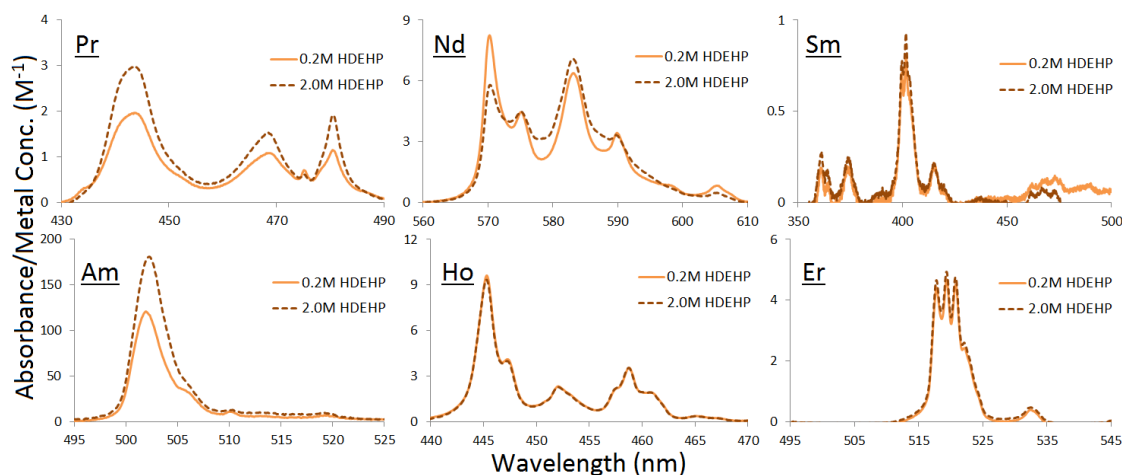


Figure 9: UV-Vis Spectra of Praseodymium, Neodymium, Samarium, Americium, Holmium, and Erbium following extraction into 0.2 M HDEHP (solid line) and 2.0 M HDEHP (dashed line)

Table 2: Water Concentration in Post-Extraction Organic Phases of Various f-Elements

	Pr	Sm	Ho	Er
2.0 M HDEHP	0.590 +/- 0.021	0.521 +/- 0.116	0.569 +/- 0.054	0.539 +/- 0.022
0.2 M HDEHP	0.020 +/- 0.001	0.013 +/- 0.002	0.011 +/- 0.001	0.009 +/- 0.001
2.0 M HEH[EHP]	0.319 +/- 0.007	0.308 +/- 0.028	0.322 +/- 0.011	0.318 +/- 0.007

When varying the HDEHP concentration, the spectrum shifts significantly for Pr and Am, while the spectral shift of Sm is present but is much subtler. However, the spectra remain constant for Ho and Er. Furthermore, the absorbances of Pr and Am increased, while Sm decreased, with an increase in HDEHP concentration and the resulting increase in water concentration. This suggests that, with an increase in water concentration, the symmetry of the metal complexes is perturbed allowing for parity changes not otherwise

allowed by the Laporte selection rule.⁴³ These changes in the light lanthanide spectra indicate metal speciation changes, however the constant spectra for the hypersensitive regions of holmium and erbium suggest that water might be less likely to coordinate with the metal center due to the lanthanide contraction.

f-Element Speciation in HEH[EHP] Organic Phases

The spectra of Nd between 1.4 mM and 29.3 mM in 2.0 M HEH[EHP] and 0.5 M HEH[EHP] are shown in Figure 10, while Karl Fischer determination of organic phase water are shown in Figure 11. The concentration of water extracted to HEH[EHP] organic phases is similarly flat across the range of metals extracted, however the water extraction ability of HEH[EHP] is significantly lower. The UV-Vis spectra of Nd in HEH[EHP] organic phases are constant with differing concentrations of HEH[EHP] however, indicating that water does not coordinate with Nd in the HEH[EHP] organic phases.

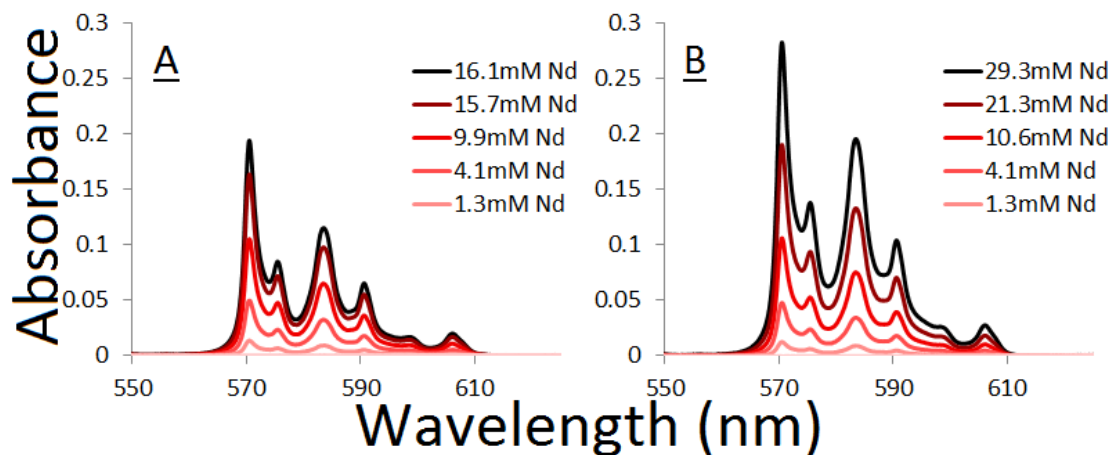


Figure 10: Neodymium UV-Vis spectra of varying metal concentrations in (A) 0.5 M HEH[EHP] and (B) 2.0 M HEH[EHP]

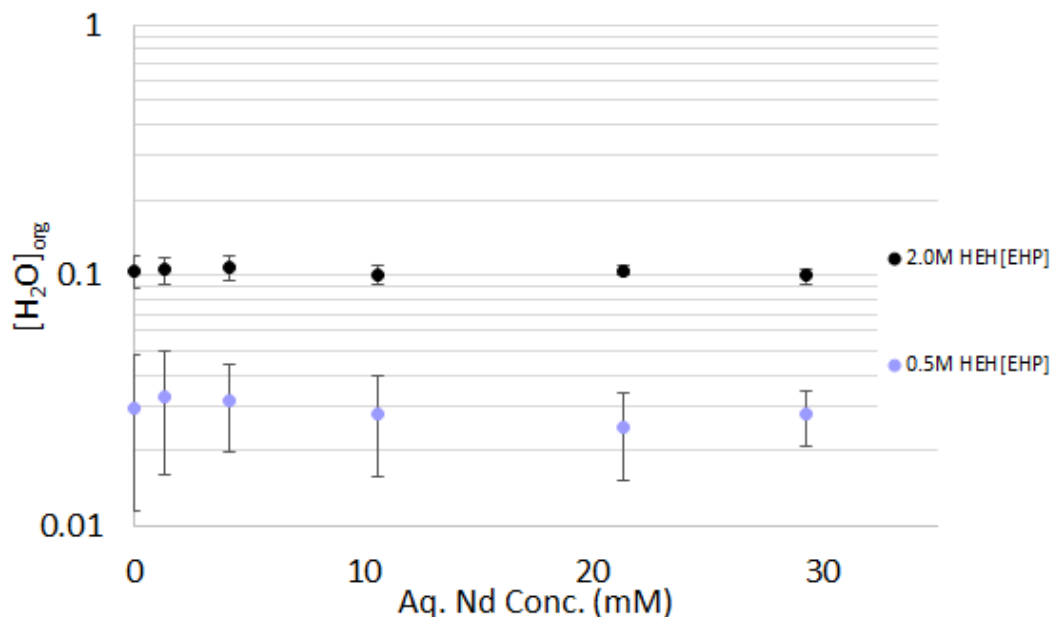


Figure 11: Water concentration of HEH[EHP] organic phases following extraction of neodymium

Like the HDEHP investigation, 17.7 mM Pr, 0.3 mM Am, 13.6 mM Sm, 12.9 mM Ho, and 14.4 mM Er were extracted into 0.2 M and 2.0 M HEH[EHP] with UV-Vis spectra collected of the post-extraction organic phases and compared to the Nd spectra, shown in Figure 12. The water concentration in 2.0 M HEH[EHP] is shown in Table 2, while the water concentration in 0.2 M HEH[EHP] was too low to be accurately quantified. Praseodymium showed a similar increase in absorbance intensity compared to the HDEHP spectra, possibly indicating a change in the metal complex symmetry. All other metals however show the same metal corrected spectra, regardless of HEH[EHP] concentration. Furthermore, americium shows much lower absorbance intensity when bonded with HEH[EHP] than when bonded with HDEHP, possibly indicating greater complex symmetry. This data suggests that while the lightest lanthanides may have different metal complexation environments based on HEH[EHP] concentration, lanthanides above

neodymium (as well as americium) are not affected by the extractant concentration, and subsequent differences in the water concentration.

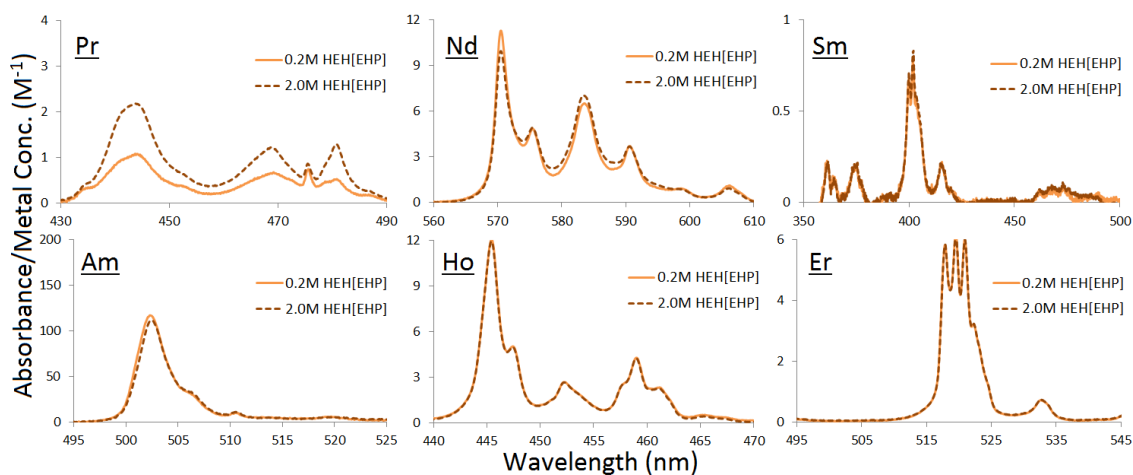


Figure 12: UV-Vis spectra of praseodymium, neodymium, samarium, americium, holmium, and erbium following extraction into 0.2 M HEH[EHP] (solid line) and 2.0 M HEH[EHP] (dashed line)

Fluorescence Results and Discussion

Emission spectra of the organic phases following extraction of 30 mM Eu^{3+} using various concentrations of HDEHP are provided in Figure 13A. As the HDEHP concentration increased, the emission intensities of the $^5\text{D}_0 \rightarrow ^7\text{F}_1$ (590 nm) and $^5\text{D}_0 \rightarrow ^7\text{F}_2$ (608 and 618 nm) transitions systematically decreased, which indicates that the inner coordination sphere of Eu^{3+} is affected by the increased chelator concentration. This systematic decrease is further highlighted in Figure 13B, where $F_{200 \text{ mM}}$ represents the fluorescence of the 0.2 M HDEHP complex and F represents the fluorescence of the higher HDEHP concentrations at the wavelengths indicated. The emission intensities decrease with increasing extractant concentration in roughly a linear fashion between HDEHP concentrations of 0.2 – 2.0 M but deviate at 3.0 M.

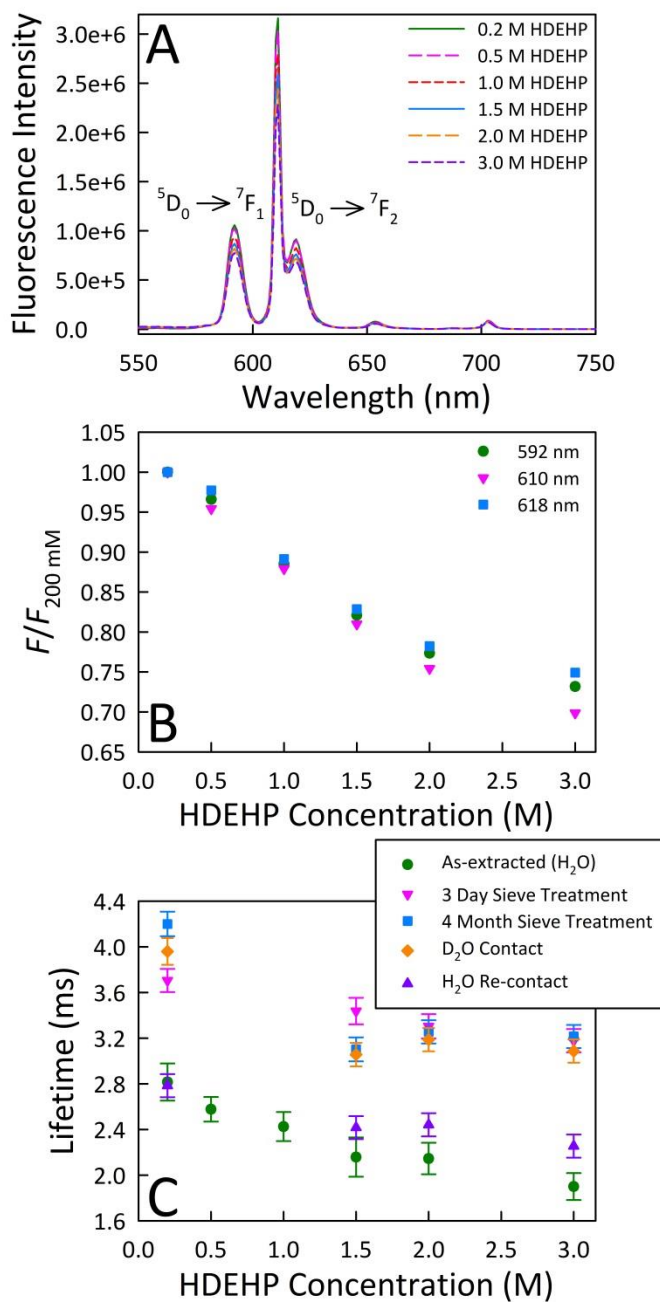


Figure 13: (A) Steady-state fluorescent emission of Eu in HDEHP organic phases of variable concentration, (B) Ratio of the emission of the higher HDEHP concentrations to the emission arising from the 0.2 M HDEHP complex (C) Calculated lifetimes of the as-extracted samples, the sieve-treated 72 h and 4 month samples, D₂O contacted and H₂O re-contacted samples.

To elucidate whether the changes in the Eu^{3+} inner coordination sphere are due solely to the increasing ligand concentration or due to the presence of water within the inner sphere, lifetime (τ) measurements were conducted on the freshly extracted Eu-HDEHP samples (Figure 13C). Similar to the steady-state emission intensities, the lifetimes for the HDEHP/ Eu^{3+} complexes linearly decreased as the HDEHP concentration increased suggesting that the Eu^{3+} inner coordination sphere may have water inclusion. The initial linear decrease in the lifetimes of the as-extracted samples is believed to arise from water coordination to the metal inner coordination sphere at higher concentrations of HDEHP, resulting in a shorter fluorophore lifetime. The inclusion of water within the inner coordination sphere of Eu^{3+} does result in a substantial decrease in the fluorescence lifetime from the typical ms regime to sub-ms lifetimes with just one coordinated water molecule producing fluorescence decay rates (k_{obs}) of 1300 s^{-1} ($\tau = 769 \text{ }\mu\text{s}$) and 900 s^{-1} if only a single O-H of water was allowed to cause quenching.¹¹

All decays were fit to a 3 parameter, single exponential decay function ($y = y_0 + ae^{-bx}$) with the resultant decay rates and calculated fluorescence lifetimes provided in Table 3. The lifetime of the 0.2 M HDEHP, Eu-extracted sample, matches a previously reported lifetime of $\sim 333 \text{ s}^{-1}$.⁴⁴ The hydration numbers were calculated using the equation, $N_{\text{H}_2\text{O}} = 1.05 \times 10^{-3} \cdot k_{\text{obs}}(\text{Eu}) - 0.44$, previously used by Grimes *et al.*¹¹ However, many of the K_{obs} present for the species constitute an imaginary number of waters (less than 0), thus further studies with both molecular sieves and D_2O were investigated.

Table 3: Lifetime fluorescence measurements of 30 mM Eu extracted into varying concentrations of HDEHP and after being treated with 3 Å molecular sieves

As-Extracted

HDEHP Conc. (M)	k_{obs} (s^{-1})	τ (ms)
0.2	355 ± 8	2.81 ± 0.16
0.5	388 ± 1	2.58 ± 0.11
1.0	413 ± 21	2.42 ± 0.13
1.5	465 ± 36	2.16 ± 0.17
2.0	466 ± 8	2.15 ± 0.14
3.0	526 ± 5	1.90 ± 0.12

24 h Sieve Treatment

HDEHP Conc. (M)	k_{obs} (s^{-1})	τ (ms)
0.2	283 ± 1	3.53 ± 0.11
1.5	391 ± 1	2.56 ± 0.10
2.0	454 ± 1	2.20 ± 0.11
3.0	533 ± 3	1.88 ± 0.11

48 h Sieve Treatment

HDEHP Conc. (M)	k_{obs} (s^{-1})	τ (ms)
0.2	271 ± 1	3.69 ± 0.11
1.5	297 ± 0	3.37 ± 0.10
2.0	329 ± 0	3.04 ± 0.10
3.0	315 ± 0	3.18 ± 0.10

72 h Sieve Treatment

HDEHP Conc. (M)	k_{obs} (s^{-1})	τ (ms)
0.2	270 ± 0	3.71 ± 0.10
1.5	291 ± 1	3.44 ± 0.12
2.0	303 ± 1	3.30 ± 0.11
3.0	315 ± 0	3.18 ± 0.10

4 month Sieve Treatment

HDEHP Conc. (M)	k_{obs} (s^{-1})	τ (ms)
0.2	238 ± 0	4.20 ± 0.11
1.5	322 ± 1	3.10 ± 0.11
2.0	307 ± 0	3.26 ± 0.10
3.0	311 ± 0	3.21 ± 0.10

D₂O Contact

HDEHP Conc. (M)	k_{obs} (s^{-1})	τ (ms)
0.2	253 ± 1	3.96 ± 0.12
1.5	327 ± 0	3.06 ± 0.10
2.0	314 ± 0	3.19 ± 0.10
3.0	324 ± 0	3.09 ± 0.10

H₂O Re-contact

HDEHP Conc. (M)	k_{obs} (s^{-1})	τ (ms)
0.2	359 ± 0	2.78 ± 0.10
1.5	414 ± 0	2.42 ± 0.10
2.0	410 ± 0	2.44 ± 0.10
3.0	444 ± 0	2.25 ± 0.10

To determine the extent of water coordinated within the inner sphere, select samples were treated with 3 Å molecular sieves to dehydrate the post extraction organic phases. Fresh sieves (~20 beads) were added to the samples every 24 h, after which fluorescence lifetimes were collected. As shown in Figure 13C (pink triangle), after a 72 h sieve treatment, the lifetimes of the samples all drastically increased to above 3 ms (3.1 – 3.7 ms), with the lifetime of the 3 M HDEHP sample rising by more than 2-fold. Within the first 24 h sieve treatment, the fluorescent lifetimes for the 0.2 and 1.5 M HDEHP concentrations increased by over 0.4 ms while the 2.0 and 3.0 M samples showed little to no increase (see Table 3), likely due to the polarity and viscosity of these solutions, which inhibits diffusion and thus the subsequent dehydration of the inner sphere.

A third 24 h sieve treatment (totaling 72 h) to ensure total dehydration produced a marginal increase in the fluorescence lifetimes indicating that the samples were, for the most part, fully dehydrated. The overall 32 – 67% increase in the lifetimes clearly reveals that water is indeed inducing a change to the inner coordination sphere of Eu^{3+} , with the possibility of water being directly coordinated to the metal in the inner sphere. The trend of decreasing lifetime with increasing HDEHP concentrations is still apparent, suggesting some potential ligand contribution to the observed lifetime differences. The samples were then left on the sieves for 4 months. The emission spectra and lifetimes were nominally the same as the data for the 72 h sieve treatment, indicating sample longevity.

To further investigate potential ligand contributions and as a control to H_2O inclusion in the inner sphere of Eu, dried samples were contacted with 99.9% D_2O . Due to

the isotopic difference between deuterium and hydrogen, energy states available for vibronic quenching are not available. This will allow for comparison of both the D₂O contacted Eu lifetimes and the H₂O contacted lifetimes. However, the donor property of the oxygen atom in heavy or normal water does not change and will still allow for the formation of a 7-coordinate complex. The fluorescence lifetimes will be different between the heavy and light water, but the excitation and emission spectra should be the same. This will contrast with the completely dried samples as it should have no available water, heavy or light, to form a 7-coordinate complex.

The fluorescence lifetimes showed that between the dried and D₂O contacted sample, there was no change in lifetimes (see Figure 13C). However, upon contacting dried samples with H₂O the lifetime shortened to the original sample lifetimes. Using both the H₂O and D₂O lifetimes, Choppin's equation for H₂O versus D₂O coordination could be used, $n=A(K_{\text{obs}(\text{H}_2\text{O})} - K_{\text{obs}(\text{D}_2\text{O})})$, where n is the number of inner sphere waters and K_{obs} is the lifetime in milliseconds, and A is a fixed constant (1.05).⁴⁵ This eliminated the problem with the first hydration equation of having negative waters in the inner sphere, resulting in a calculated inner sphere hydration of ~0.25 waters. This is still lower than expected, but that reason and discussion is given later. It was observed that the emission spectra for both D₂O and H₂O were very similar, showing a decrease in the 610 to 618 nm ratio (see Figure 13). The excitation profile, monitoring the 610 nm emission feature, for both the H₂O and D₂O also showed the same resonances and subsequent decrease in sensitivity as concentrations of water increased relative to the dried samples (see Figure 14).

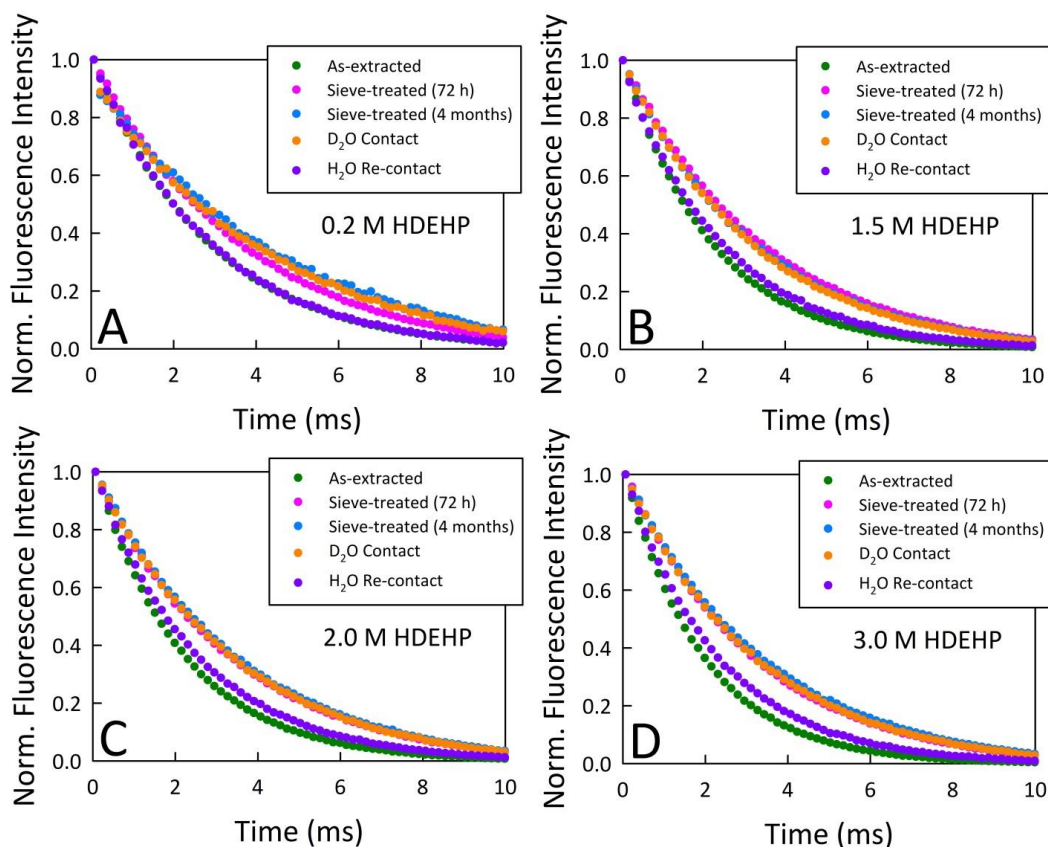


Figure 14: lifetime measurements of Eu-HDEHP complexes in dodecane at A) 0.2 M HDEHP, B) 1.5 M HDEHP, C) 2.0 M HDEHP, D) 3.0 M HDEHP. Norm. stands for normalized. Data includes sieve treated (72 hours and 4 months) samples, post-dried D₂O contacted samples and post-dried re-contacted H₂O samples.

In a past study, the 589 nm excitation feature was used to determine if multiple species were existing in solution.⁴⁴ The excitation feature at 589 nm showed an increase in full width at half maximum as water concentration increased in the organic phase compared to the sieve dried samples. This suggests that another, albeit not very large concentration of, species is being formed as water concentration increases.

In other water inner sphere Eu fluorescence investigations, the assumption is that the hydration equations and especially the constants would be the same for most major species of the same metal center.^{11,45,46} However, with a ligand like HDEHP in dodecane

which is capable of forming multiple hydrogen bonds, the energy of an O-H stretch would decrease as oxygen from HDEHP creates a hydrogen bond with water, thus there would be a reduced effective quenching mode for water to quench Eu fluorescence. Further investigation into the lifetimes and actual hydration of lanthanides in the presence of partially hydrophilic organic ligands utilizing high fidelity instrumentation and more stringent control on hydration is warranted.

Computational Discussion

UV-Vis and TRFS results prompted investigation of the electronic structure of both the dimers and the metal complexes using Density Functional Theory (DFT). Previous investigations of hydrogen bonding using DFT has shown trends amenable to those seen in other f-element coordination complexes.⁴⁷ It has been previously demonstrated however that DFT, B3LYP/6-311g**, can over emphasize hydrogen bonding induced changes in geometry and enthalpies of formation for complexes.⁴⁸ Thus the focus is on the trend for these complexes and not on the quantitative energy results, however, the calculations were carried out at the highest level of theory with the full ligands rather than truncated alkyl chains as has been justified by previous studies.^{49,50}

As was observed with Karl Fischer titration of HDEHP and HEH[EHP] shown in Figures 5 and 11 and by Nash *et al.*, DFT calculations suggest that HDEHP more effectively extracts water into the organic phase than HEH[EHP] or Cyanex272. The overall trend of water extraction into the organic phase is HDEHP>>HEH[EHP]>Cyanex272 (see Table 4).⁸ Examining the change in Mulliken charge for the phosphorus and the oxygen atoms that make up the 8-member ring of the dimer, the values do not significantly change when water coordinates to the dimer (see

Table 5). This supports the idea that while the oxo- and hydroxyl- group that interact with water or a metal ion do not change in charge and extracting character, the dipole and overall nature of the charge around the phosphorous does change. This also provides HDEHP with greater interfacial character, allowing for more effective extraction of polar atoms such as metal ions or water than HEH[EHP] or Cyanex272.

Table 4: ΔG of formation from water coordination with organophosphorus ligand dimers

Species	ΔG (kcal/mol)
$(\text{HDEHP})_2 \rightarrow (\text{HDEHP})_2\text{H}_2\text{O}$	-2.39
$(\text{HEH}[\text{EHP}])_2 \rightarrow (\text{HEH}[\text{EHP}])_2\text{H}_2\text{O}$	-1.03
$(\text{Cyanex}272)_2 \rightarrow (\text{Cyanex})_2\text{H}_2\text{O}$	0.00

Table 5: Mullikan Charge values for selected atoms in Organophosphorus dimers and water complexes

Species	P	O (POH)	O (P=O)	O (H ₂ O)
$(\text{HDEHP})_2$	1.23	-0.17	-0.66	-
$(\text{HDEHP})_2\text{H}_2\text{O}$	1.16	-0.23	-0.66	0.04
$(\text{HEH}[\text{EHP}])_2$	1.16	-0.21	-0.66	-
$(\text{HEH}[\text{EHP}])_2\text{H}_2\text{O}$	1.16	-0.23	-0.66	0.04
$(\text{Cyanex}272)_2$	1.08	-0.23	-0.67	-
$(\text{Cyanex})_2\text{H}_2\text{O}$	1.08	-0.23	-0.67	-0.62
H ₂ O	-	-	-	-0.62

Also of note is the apparent change in point group of water. The water moiety that is participating in hydrogen bonding with the organophosphorus dimer appears to lose its C_{2v} geometry and take on C_{3v} geometry (see Figure 15).

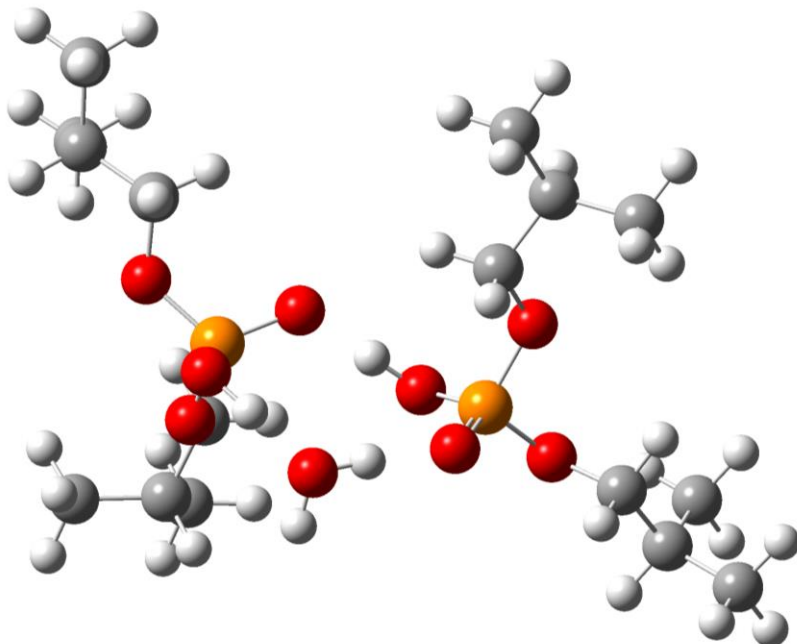


Figure 15: Optimized geometry of a HDEHP dimer with water interacting with the POH-OP hydrogen bond of the dimer.

Even more important to the investigation is how water interaction influences metal-ligand coordination. UV-Vis, EXAFS and fluorescence data suggest that there are two possible modes of interaction for water that would have an effect on the metal coordination dependent f-orbital electronic transitions. Either water will be outer sphere and interact with the hydrogen bond of the coordinated HDEHP dimer, or it will coordinate inner sphere with the lanthanide ion. The different geometries found for both coordination environments are shown in Figure 16. As shown in Figure 16, geometrically, the association of water will either not change the pseudo-octahedral environment of the water free complex with water in the outer sphere or water will coordinate in the inner sphere and create a 7-coordinate, distorted face-capped octahedron or very strained pseudo-pentagonal bipyramidal geometry.

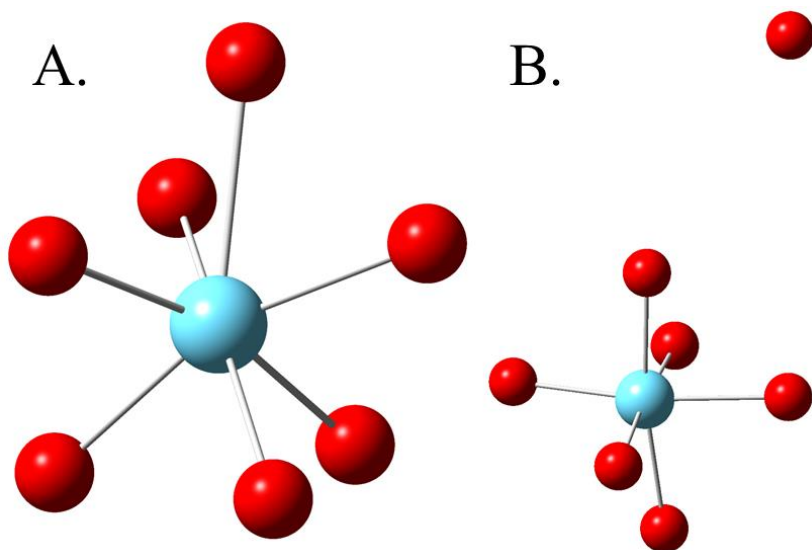


Figure 16: Geometry around the metal centers showing only the coordinating ligand oxygens and the oxygen from the water for clarity. A. The optimized $\text{Ln}(\text{H}(\text{DEHP})_2)_3 (\text{H}_2\text{O})$ with water coordinated inner sphere creating the pseudo face-capped octahedral geometry. B. The optimized geometry of $\text{Ln}(\text{H}(\text{DEHP})_2)_3 (\text{H}_2\text{O})$ with water outer sphere hydrogen bonding with the $\text{H}(\text{DEHP})_2$ dimer.

The geometries of the 6-coordinate complex with water in the outer sphere closely resemble that of the 6-coordinate complex without water, while the 7-coordinate structure does have some elongation in the metal oxygen bonds. The average bond distances and metal-phosphorus distances for the La and Lu complexes are shown in Table 6. When lanthanide contraction is considered, the values from geometry calculations (Table 6) agree well with the EXAFS data (Table 1). This gives credence to the hypothesis that when larger atomic radii lanthanides become 7-coordinate with an inner sphere water, the change in average bond distance is negligible and is within the standard deviation of both DFT calculations and EXAFS.

Table 6: Average lanthanide-oxygen and lanthanide-phosphorus distance for lanthanum, lutetium, 6-coordinate water outer sphere (OS) and 7-coordinate water inner sphere (IS) complexes. Ln-O deviation is high because of the slightly longer La-OH₂ bond length from dative interaction (~0.15 Å). While the Lu-OH₂ bond is ~0.4 Å further than the other Lu-O bond lengths.

Complex	Ln-O Average Å (Std. Dev)	Ln-P Average Å (Std. Dev)
La(H(HDEHP) ₂) ₃ (H ₂ O) IS	2.487 (0.090)	3.883 (0.088)
La(H(HDEHP) ₂) ₃ (H ₂ O) OS	2.427 (0.060)	3.880 (0.053)
Lu(H(HDEHP) ₂) ₃ (H ₂ O) IS	2.270 (0.159)	3.640 (0.061)
Lu(H(HDEHP) ₂) ₃ (H ₂ O) OS	2.218 (0.049)	3.632 (0.064)

The difference in energies between the two coordination complexes is highlighted in Figure 17. One sees that for La, the 7-coordinate structure with inner sphere water coordination is energetically favorable by 5.6 kcal/mol and the outer sphere coordination of water is unfavorable by 6.3 kcal/mol compared to the non-hydrated species. Overall, this trend suggests that the coordination of water to the La metal center is favorable to either outer sphere water or no water coordination. This matches observations for the lighter lanthanides in which an increase in water concentration does change the hyperfine regions of the absorption and emission spectra.

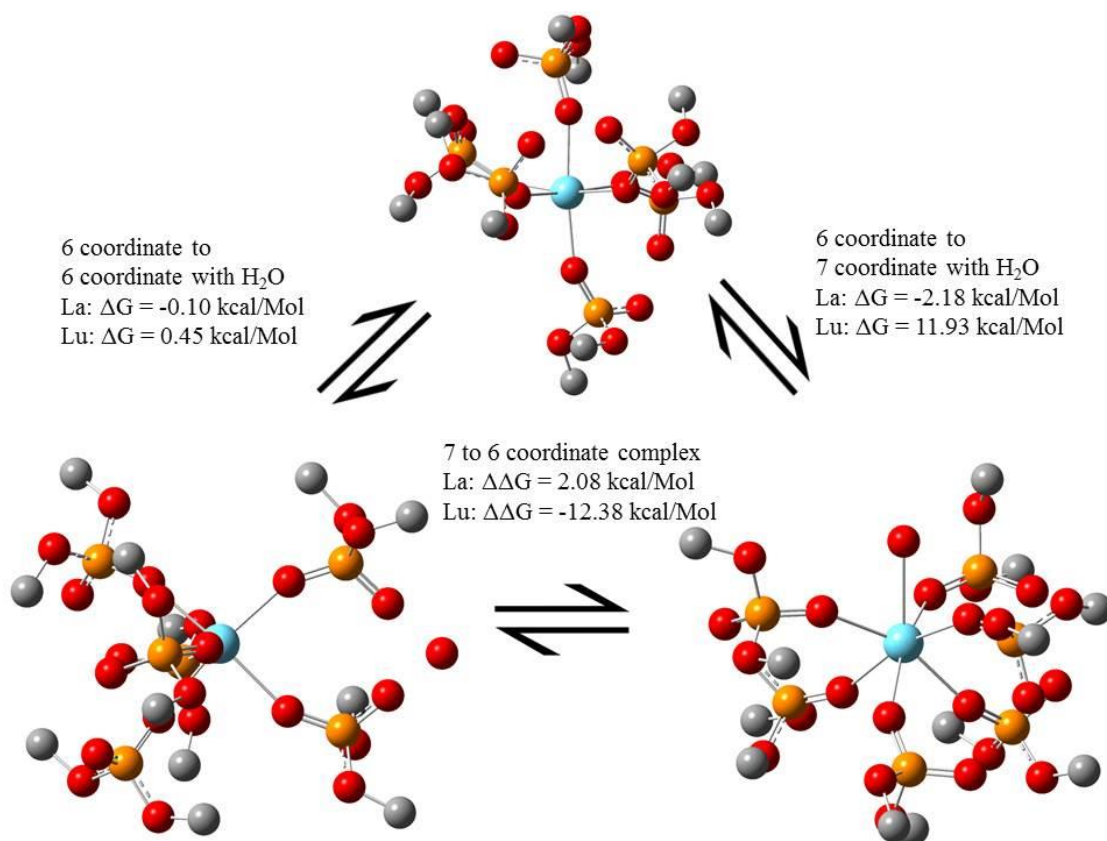


Figure 17: Optimized geometries of waterless 6-coordinate Ln(HA₂)₃ [Top Center], water coordinated, 7-coordinate, distorted face-capped octahedron [Bottom Right], and 6-coordinate octahedral with water outer sphere [Bottom Left]. Listed are the energies associated with the change in free energy between the complexes listed above the energies given for La and Lu.

When investigating the Lu coordination complex the free energy profile is very different. Hydration of the complex, either outer or inner sphere, is energetically unfavorable by 6.8 and 13.31 kcal/mol, respectively. This is also in line with the observed water influence on hyperfine regions becoming less prevalent with smaller radii lanthanides. However, the DFT results for Lu suggest that while outer sphere hydration is preferred over inner sphere coordination of water, both are energetically unfavorable

compared to the un-hydrated 6 coordinate complex. As both metal centers are singlets, have the same ligand set, the ligand is not truncated and the same geometries for 6 and 7 coordination geometries, and the only plausible difference between the effect on the calculations is the size of the metal ionic radius.

As the Gibbs free energy is a direct correlation to the equilibria of complexes in solution, Le Chatelier's principle would also have an effect on the observed species in solution. As water concentration in the organic phase is a function of organophosphorus ligand concentration and the type of organophosphorus ligand, it would hold that lower ligand concentration would not have a high enough water concentration to allow a 7-coordinate complexes to be observed, as previously seen.¹⁶ However, as ligand concentration is increased, water concentration is also increased, pushing the equilibrium to a higher observable concentration of 7-coordinate water inner sphere complex to be formed, also previously observed.^{15,17}

Conclusion

UV-Vis, XAFS, TRFLS spectroscopies, Karl Fischer titrations, and DFT calculations of various lanthanides and americium extracted by HDEHP in n-dodecane led to insight into changes in metal coordination with HDEHP concentrations ranging from 0.2 M HDEHP to 2.0 M HDEHP. It was found that water was concomitant to metal extraction by the ligand, which resulted in a change in the electronic spectrum. Due to the size of the f-element radius, the effect that water had on the spectrum was due to the equilibrium for forming the 7-coordinate species, which included water in the inner coordination sphere of the extracted metal. This equilibrium is entirely dominated by the radii as smaller radii lanthanides did not show the same propensity for changes in the hyperfine region UV-Vis

and XAFS spectra. Thus, it suggests that for Am and the larger lanthanides (such as the first Ln tetrad), water forms a 7-coordinate species of $\text{Ln}(\text{H}(\text{EDHP})_2)_3(\text{H}_2\text{O})$, which resembles a distorted face-capped octahedron. In comparison, metals extracted into HEH[EHP] in n-dodecane showed a lowered ability for the extraction of water to the organic phase, and for the ability to form the inner coordination sphere water complex except with the lightest lanthanides.

Acknowledgments

I would like to acknowledge Drs. Brian Gullekson and Alena Paulenova for their contribution of the americium UV-Vis spectrum and the Karl Fischer titration data. I would like to acknowledge Drs. Jeremy Kropf and M. Alex Brown for their work on Nd XAFS. Finally, I would like to acknowledge Jeremy Essner and Dr. Gary Baker for their TRFS spectroscopy work with europium.

This chapter has been created in using data and equipment owned by UChicago Argonne, LLC, Operator of Argonne National Laboratory (“Argonne”). Argonne, a U.S. Department of Energy Office of Science laboratory, is operated under Contract No. DE-AC02-06CH11357. The U.S. Government retains for itself, and others acting on its behalf, a paid-up nonexclusive, irrevocable worldwide license in said chapter to reproduce, prepare derivative works, distribute copies to the public, and perform publicly and display publicly, by or on behalf of the Government.

This work was funded by the Department of Energy – Office of Nuclear Energy, Sigma Team for Advanced Actinide Recover, and Nuclear Energy University Program award No. DE-NE0000720. The computation for this work was performed on the high performance computing infrastructure provided by Research Computing Support Services

at the University of Missouri, Columbia, MO. This work was prepared by The Curators of the University of Missouri under award #NRC-HQ-15-G-0036, from the Office of the Chief Human Capital Officer of the Nuclear Regulatory Commission. The statements, findings, conclusions, and recommendations are those of the author(s) and do not necessarily reflect the view of the Outreach and Recruitment Branch or the US Nuclear Regulatory Commission.

References

1. Rengan, K.; Meyer, R. A.; Hahn, R. L.; National Research, C.; Committee on, N.; Radiochemistry; National Research, C.; Board on Chemical, S.; Technology; National Research, C.; Commission on Physical Sciences, M.; Applications *Ultrafast chemical separations*; National Academy Press: Washington, D.C., 1993.
2. Moyer, B. A. *Proceedings of ISEC 2008, International Solvent Extraction Conference - Solvent Extraction: Fundamentals to Industrial Applications*, 2008.
3. Rydberg, J.; Musikas, C.; Choppin Gregory, R. *Principles and practices of solvent extraction*; M. Dekker: New York, 1992.
4. Nilsson, M.; Nash, K. L., Review Article: A Review of the Development and Operational Characteristics of the TALSPEAK Process., *Solv. Ext. and Ion Exch* **2007**, *25*, 665-701.
5. Weaver, B.; Kappelmann, F. A. *TALSPEAK: A New Method of Separating Americium and Curium from the Lanthanides by Extraction from an Aqueous Solution of an Aminopolyacetic Acid Complex with a Monoacidic Organophosphate or Phosphonate*; ORNL-3559, 1964.
6. Lumetta, G. J.; Gelis, A. V.; Braley, J. C.; Carter, J. C.; Pittman, J. W.; Warner, M. G.; Vandegrift, G. F., The TRUSPEAK concept: Combining CMPO and HDEHP for Separating Trivalent Lanthanides from the Transuranic Elements. *Solv. Ext. and Ion Exch.* **2013**, *31*, 223-236.
7. Gelis, A. V.; Lumetta, G. J., Actinide Lanthanide Separation Process—ALSEP. *Ind. & Eng. Chem. Res.* **2014**, *53*, 1624-1631.
8. Braley, J. C.; Grimes, T. S.; Nash, K. L., Alternatives to HDEHP and DTPA for Simplified TALSPEAK Separations., *Ind. & Eng. Chem. Res.* **2012**, *51*, 629-638.
9. Peppard, D. F.; Mason, G. W.; Maier, J. L.; Driscoll, W. J., *J. Inorg. Nucl. Chem.* **1957**, *4*, 334-343.
10. Marie, C.; Hiscox, B.; Nash, K. L., Characterization of HDEHP-lanthanide complexes formed in a non-polar organic phase using ^{31}P NMR and ESI-MS, *Dalton Trans.* **2012**, *41*, 1054-1064.
11. Grimes, T. S.; Tian, G.; Rao, L.; Nash, K. L., Optical Spectroscopy Study of Organic-Phase Lanthanide Complexes in the TALSPEAK Separations Process, *Inorg. Chem* **2012**, *51*, 6299-6307.

12. Gannaz, B.; Antonio, M. R.; Chiarizia, R. H., C.; Cote, G., Structural study of trivalent lanthanide and actinide complexes formed upon solvent extraction, *Dalton Trans.* **2006**, 38, 4553-4562.
13. Karraker, D. G., Hypersensitive transitions of six-, seven-, and eight-coordinate neodymium, holmium, and erbium chelates, *Inorg. Chem.* **1967**, 6, 1863-1868.
14. Cotton, S. *Lanthanide and Actinide Chemistry*; John Wiley & Sons: West Sussex, England, 2006.
15. Jensen, M. P.; Chiarizia, R.; Urban, V., Investigation of the aggregation of the neodymium complexes of dialkylphosphoric, -orthothiophosphinic, and -dithiophosphinic acids in toluene, *Solv. Ext. and Ion Exch.* **2007**, 19, 865-884.
16. Lumetta, G. J.; Sinkov, S. I.; Krause, J. A.; Sweet, L. E., Neodymium(III) Complexes of Dialkylphosphoric and Dialkylphosphonic Acids Relevant to Liquid-Liquid Extraction Systems, *Inorg. Chem.* **2016**, 55, 1633-1641.
17. Gullekson, B. J.; Gelis, A. V.; Paulenova, A., Trans-Lanthanide Comparison of Metal Organic Complexes in an Actinide Lanthanide Partitioning System, *Global 2015*; Société Française d'Énergie Nucléaire: Paris, France: 2015, p 1647-1652.
18. Bryan, S. A.; Levitskaia Tatiana, G.; Johnsen, A. M.; Orton, C. R.; Peterson, J. M., Spectroscopic monitoring of spent nuclear fuel reprocessing streams: an evaluation of spent fuel solutions via Raman, visible, and near-infrared spectroscopy, *Radiochim. Acta* **2011**; 99, p 563-572.
19. Partridge, J. A.; Jensen, R. C., Purification of Di-(2-Ethylhexyl) Phosphoric Acid By Precipitation of Copper(II) Di-(2-Ethylhexyl)Phosphate, *J. Inorg. Nucl. Chem.* **1969**, 31, 2587-2589.
20. Harris, D. C. *Quantitative Chemical Analysis*; 8th Ed. ed.; W. H. Freeman and Company: New York, New York, 2010.
21. Fritz, J. S.; Richard, M. J.; Lane, W. J., Spectrophotometric Determination of Rare Earths, *Anal. Chem.* **1956**, 30, 1776-1779.
22. Kraft, S.; Stumpel, J.; Becker, K.; Kuetsgens, U., High Resolution X-Ray Absorption Spectroscopy with Absolute Energy Calibration for the Determination of Absorption Edge Energies., *Tev. Sci. Instrum.*, **1996**, 67, 681-687.
23. Center for X-ray Optics and Advanced Light Source, X-ray Data Booklet, Lawrence Berkeley National Laboratory, CA, October 2009.
24. Newville, M.; IFEFFIT: Interactive XAFS Analysis and FEFF Fitting., *J. Synch. Rad.*, **2001**, 8, 322-324.

25. Ravel, B.; Newville, M., ATHENA, ARTEMIS, HEPHAESTUS: Data Analysis for X-Ray Absorption Spectroscopy Using IFEFFIT., *J. Synch. Rad.* **2005**, *12*, 537-547
26. Frisch, M. J. T., G. W.; Schlegel, H. B.; Scuseria, G. E.; Robb, M. A.; Cheeseman, J. R.; Scalmani, G.; Barone, V.; Mennucci, B.; Petersson, G. A.; Nakatsuji, H.; Caricato, M.; Li, X.; Hratchian, H. P.; Izmaylov, A. F.; Bloino, J.; Zheng, G.; Sonnenberg, J. L.; Hada, M.; Ehara, M.; Toyota, K.; Fukuda, R.; Hasegawa, J.; Ishida, M.; Nakajima, T.; Honda, Y.; Kitao, O.; Nakai, H.; Vreven, T.; Montgomery Jr., J. A.; Peralta, J. E.; Ogliaro, F.; Bearpark, M. J.; Heyd, J.; Brothers, E. N.; Kudin, K. N.; Staroverov, V. N.; Kobayashi, R.; Normand, J.; Raghavachari, K.; Rendell, A. P.; Burant, J. C.; Iyengar, S. S.; Tomasi, J.; Cossi, M.; Rega, N.; Millam, N. J.; Klene, M.; Knox, J. E.; Cross, J. B.; Bakken, V.; Adamo, C.; Jaramillo, J.; Gomperts, R.; Stratmann, R. E.; Yazyev, O.; Austin, A. J.; Cammi, R.; Pomelli, C.; Ochterski, J. W.; Martin, R. L.; Morokuma, K.; Zakrzewski, V. G.; Voth, G. A.; Salvador, P.; Dannenberg, J. J.; Dapprich, S.; Daniels, A. D.; Farkas, Ö.; Foresman, J. B.; Ortiz, J. V.; Cioslowski, J.; Fox, D. J.; ; Gaussian, Inc.: Wallingford CT, 2009
27. Dennington, R. K., T.; Millam, J.; ; 5 ed.; Semichem Inc.: Shawnee Mission, KS, 2009
28. Stephens, P.J.,; Devlin F.J.; Chabalowski, C.F.; Frisch, M.J., Ab Initio Calculations of Vibrational Absorption and Circular Dichroism Spectra Using Density Functional Force Fields. *J. Phys. Chem.*, **1994**, *98*, 11623-11627.
29. Becke, A.D., Density-functional thermochemistry. III. The role of exact exchange, *J. Chem. Phys.*, **1993**, *98*, 5848-5652
30. Lee, C.; Yang, W.; Parr, R.G.; Development of the Colle-Salvetti Correlation-Energy Formula into a Functional of the Electron Density. *Phys. Rev. B.*, **1998**, *37*, 785-789
31. Bergner, A.; Dolg M.; Kuchle, W.; Stoll, H.; PreuB, H. Ab Initio Energy-Adjusted Pseudopotentials for Elements of Groups 13-17, *Mole. Phys.*, **1993**, *97*, 5852
32. Dolg, M.; Stoll, H.; Preuss, H.; Energy-adjusted ab initio pseudopotentials for the rare earth elements, *J. Phys. Chem.*, **1989**, *90*, 1730-1734
33. Hariharan, P. C.; Pople, J. A.,; The influence of Polarization Functions on Molecular Orbital Hydrogenation Energies. *Theor. Chim. Acta.*, **1973**, *28*, 213-222.
34. Francl, M. M.,; Pietro, W. J.; Hehre, W. J.; Binkley, J. S.; Gordon, M. S.; DeFress, D. J.; Pople, J. A.; Self-consistent molecular orbital methods. XXIII. A polarization-type basis set for second-row elements., *J. Chem. Phys.*, **1982**, *77*, 3654-3665

35. Jensen, M. P.; Bond, A. H.; Comparison of Covalency in the Complexes of Trivalent Actinide and Lanthanide Cations. *J. Am. Chem. Soc.*, **2002**, *124*, 9870-9877
36. Cocalia, V. A.; Jensen, M. P.; Holbrey, J. D.; Spear, S. K.; Stepinski, D. C.; Rogers, R. D.; Identical Extraction Behavior and Coordination of Trivalent or Hexavalent f-Element cations Using Ionic Liquid and Molecular Solvents. *Dalton Trans.*, **2006**, 4553-4562
37. Ravel, B.; Kelly, S. D.; The Difficult Chore of Measuring Coordination by EXAFS. *AIP Conf. Proc.*, **2007**, *882*, 150-152
38. Bunker, G.; Introduction to XAFS, Cambridge University Press, NY, 2010, pg. 130.
39. Brown, M. A.; Kropt, A. J.; Paulenova, A.; Gelis, A. V.; Aqueous Complexation of Citrate with Neodymium(III) and Americium(III): a Study by Potentiometry, Absorption Spectrophotometry, Microcalorimetry, and XAFS. *Dalton Trans.*, **2014**, 6446-6454.
40. Morss, L. R.; Endelstein, N. M.; Fuger, J.; *The Chemistry of the Actinide and Transactinide Elements*, 4th Ed.; Springer: Dordrecht, Netherlands, 2010.
41. Wang, N.; Jiang, W.; Xu, X.; Si, Z.; Bai, H.; Tian, C.; Visible Absorption Spectra of the 4f Electron Transitions of Neodymium, Praseodymium, Holmium, and Erbium Complexes with Fleroxacin and their Analytical Application. *Anal. Sci.*, **2002**, *18*, 591-594
42. Henrie, D. E.; Fellows, R. L.; Choppin, G. R.; Hypersensitivity in the Electronic Transitions of Lanthanides and Actinide Complexes. *Coord. Chem. Rev.*, **1976**, *18*, 199-224
43. Atkins, P.; Overton, T.; Rourke, J.; Weller, M.; Armstrong, F.; Hagerman, M.; *Shriver & Atkins' Chemistry*, 5th Ed.; W.H. Freeman & Company: New York, NY, 2010.
44. Beitz, J. V.; Sullivan, J. C., Laser-induced fluorescence studies of europium extractant complexes in organic phases, *J. Less-Common Met.*, **1989**, *148*, 159-166.
45. Choppin, G. R.; Peterman, D. R., Applications of lanthanide luminescence spectroscopy to solution studies of coordination chemistry, *Coord. Chem. Rev.*, **1998**, *174*, 283-299.
46. Tian, G.; Martin, L. R.; Rau, L.; Complexation of Lactate with Neodymium(III) and Europium(III) at Variable Temperatures: Studies by Potentiometry, Microcalorimetry, Optical Absorption, and Luminescence Spectroscopy. *Inorg. Chem.*, **2010**, *49*, 10598-10605.

47. Luo, J.; Wang, C. -Z.; Lan, J. -H.; Wu, Q. -Y.; Zhao, Y. -L.; Chai, Z. -F.; Nie, C. -M.; Shi, W. -Q.; Theoretical Studies on the AnO_2^{n+} (An = U, Np; n = 1,2) Complexes with Di-(2-ethylhexyl)phosphoric Acid. *Dalton Trans.*, **2015**, 44, 3227-3236
48. Breshears, A. T.; Behrle, A. C.; Barnes, C. L.; Laber, C. H.; Baker, G. A.; Walensky, J. R.; Synthesis, Spectroscopy, Electrochemistry, and Coordination Chemistry of Substituted Phosphine Sulfides and Selenides. *Polyhedron*, **2015**, 100, 333-343
49. Comba, P.; Gloe, K.; Inoue, K.; Gruger, T.; Stephan, H.; Yoshizuka, K., Molecular Mechanics Calculations and the Metal Ion Selective Extraction of Lanthanoids. *Inorg. Chem.*, **1998**, 37, 3310-3315.
50. Sella, C.; Nortier, P.; Bauer, D.; A Molecular Modelling Study about the Influence of the Structure of Alkyl Chains of Dialkyl Phosphoric Acids on Liquid-Liquid Lanthanide(III) Extraction. *Solv. Extr. Ion Exch.*, **1997**, 15, 931-960.

Chapter 3: Preliminary studies into extraction and stripping values for molybdenum with organophosphorus extracting ligands and oxime containing ligands

Abstract

High loading of molybdenum within advanced nuclear fuel cycles prompted investigation of K_D values for various extracting and stripping ligands. Herein, forward extraction capability was investigated for acidic organophosphorus ligands from high molar nitric acid. Additionally, experiments to investigate the ability of oxime functional group containing organic ligands to strip molybdenum from the acidic organophosphorus ligand organic phase were pursued. From this limited work, it was found that the extracting agents HDEHP and HEH[EHP] were the most efficient organophosphorus extractants of molybdenum. Stripping Mo from HDEHP and HEH[EHP] was found to be the most efficient for hydroxamic acid. However, other oxime moieties possess similar efficiencies as hydroxamic acid. It was found that exchanging oxygen for other softer chalcogenides in both steps greatly degrade the efficiency of the parent ligand.

Scope of Impact

This chapter affects current knowledge due to focusing on acidic extractants operated at very high concentrations of HNO_3 . To the best of my knowledge, the literature has focused either on extraction of molybdenyl at very low pH with TBP from HCl or the use of acidic organophosphorus ligands at dilute acid conditions ($\text{pH} > 1$). As for stripping, the use of oxime ligands has focused on either non-alkyl hydroxamates, or oximes specifically for the analytical determination of molybdenum (α -benzoin oxime).

Oximes show propensity for stripping and especially in relation to one another has not been explored.

Introduction

In its radioactive and stable isotopic forms, molybdenum is a focal element among the nuclear industries and developing nuclear technologies. ^{99}Mo is arguably the most important isotope in nuclear medicine, and its daughter $^{99\text{m}}\text{Tc}$ is used to diagnose a large percentage of heart diseases and cancers worldwide every year, making the current supply shortage of $^{99}\text{Mo}/^{99\text{m}}\text{Tc}$ an ongoing, high-priority situation.¹ With regards to nuclear power generation, Mo is an abundant fission product of ^{235}U that constitutes roughly 12% of the atoms per fission product pair, or 3.35 parts per thousand and 10% by weight of spent nuclear fuel pre- and post-PUREX processes, respectively.²⁻³ Since the Mo concentration in aged fuel is substantial, it appreciably impacts aqueous nuclear fuel reprocessing flowsheets.⁴ Various forms of chemical treatments for new separation technologies that may also complement the existing technologies are essential to isolate molybdenum.

Liquid-liquid extraction and acetohydroxamic acid (AHA) are familiar tools in nuclear fuel reprocessing flowsheets.⁵ Acetohydroxamic acid is a water soluble, weak acid ($\text{p}K_{\text{a}} \approx 9.0$) that is used to strip, reduce, and separate Pu(IV) from a metal-loaded solution of tri-*n*-butyl phosphate (TBP) and U(VI).⁶ We recently discovered that AHA can effectively strip Mo(VI) from an organophosphoric/phosphinic/phosphonic acidic extractant.⁷ Furthermore, Mo(VI) can be extracted by the aforementioned extractants from a mildly concentrated solution of nitric acid – a feature that is unusual, considering that this class of extractants typically targets metals in the pH region of 2-5. These unique

combinations of extraction, stripping, and liquid-liquid treatment of Mo in solution have crafted a new recovery concept for molybdenum in nitric acid solutions.⁷

While most reprocessing schemes use a combination of acidic and neutral ligand, such as ALSEP using HEH[EHP] and DGA, our focus is on the acidic ligand for this process. Thus our work herein examines the efficiency of high acid concentration separation and stripping of molybdenum for the sake of application to advanced nuclear fuel reprocessing schemes and recovery for medical isotopes.

Experimental

Unless otherwise noted, all materials were purchased at 95% purity or better (Sigma-Aldrich, St. Louis, MO) and were used as received. HEH[EHP] was purchased at 95% purity (Yick-Vic Chemicals and Pharmaceuticals, Hong Kong, China), Cyanex 272 and 572 were purchased at 85% purity (Cyanex Solvay Co., Newark, NJ). HEH[EHP] was further purified by previously reported methods.⁸ HDEHP was purchased at 98% purity (Sigma-Aldrich, St. Louis, MO) and was purified by the copper hydroxide process reported previously.⁹ Water was distilled and further purified by a Merck Millipore Simplicity system to produce 18.2 M Ω deionized water. An acidic 0.5 M MoO₂²⁺ solution was made by dissolving 0.025 mol of Na₂MoO₄·2H₂O in 50 mL of 4.0 M nitric acid and vortexed until a clear, light yellow solution was obtained.

Synthesis of the diisopropyl dichalcogenide phosphinic acids was performed according to previous literature procedures.¹⁰ Formohydroxamic acid, HFHA, was synthesized according to the previously published procedure and was recrystallized out of boiling ethyl acetate twice.¹¹ All chalcogenide hydroxamic acids, ketoximes and amidoximes that could not be purchased via Sigma-Aldrich were synthesized by slight

modifications to previously reported procedures where only the starting material was varied.¹²

Procedure for determining D values

Unless otherwise noted, all mixing was 1:1 by volume of organic to aqueous solution, and the two phases in a glass centrifuge tube were contacted via a vortex mixer for 120 s and centrifuged at 3000 rpm for 120 s to separate the two phases. The bulk of the phases were separated via transfer pipet; care was taken to not remove solution close to the interface, and were placed in separate centrifuge tubes.

The distribution ratios were determined by using ⁹⁹Mo tracer that was then counted on a Perkins-Elmer 1480 automatic gamma counter with a NaI(Tl) detector at the 740 keV line. If cold Mo was used without a radiotracer, aqueous solutions containing molybdenum were determined by mass via the alpha-benzoin oxime precipitation method as previously reported.¹³ Post precipitation of the molybdenum alpha-benzoin oxime complex (Mo-ABO) was followed by centrifugation at 3000 rpm for 10 min. The supernatant was decanted and the precipitate was washed using DI water, suspended and re-centrifuged three times. After the final wash and centrifugation, the samples were left overnight in an oven set to 70°C to evaporate all remaining water in the sample. The samples were then allowed to equilibrate to ambient temperature before being weighed on a five-place balance.

For the radioactive tracer experiments, aliquots were taken of the organic and aqueous samples and were counted on the NaI gamma detector. Total counts were always 10,000 or greater to reduce the error of the counting experiments. The D value for Mo was determined as follows:

$$D_{Mo} = \frac{\frac{Total\ counts}{Count\ time * V}_{org}}{\frac{Total\ counts}{Count\ time * V}_{aq}} \quad (1)$$

For non-radiotracer experiments where bulk molybdenum was used, stock aqueous solution and the post extraction or stripping aqueous sample was used in the alpha-benzoin oxime precipitation. The D value for the non-radiotracer experiments was determined as follows:

$$D_{Mo} = \frac{\frac{Mass\ Mo-ABO}{V}_{stock} - \frac{Mass\ Mo-ABO}{V}_{aq}}{\frac{Mass\ Mo-ABO}{V}_{aq}} \quad (2)$$

Where for both equation 1 and 2, V is volume of the aliquoted sample.

Results and Discussion

Extraction studies

First, experiments focused on extraction of Mo with commercially available organophosphorus ligands to find the most effective extractant. These ligands hold up well under radiolysis (radiolysis work was done by Idaho National Lab and is not yet reported) and were chosen for the experiments. Experiments used di-2-ethylhexyl phosphoric acid (HDEHP), 2-ethylhexyl phosphonic acid mono-2-ethylhexyl ether (HEH[EHP]), di-2-ethylhexyl phosphinic acid (Cyanex 272), commercially available mixture of HEH[EHP] and Cyanex 272 (Cyanex 572), and diethyl dithiophosphonic acid for extraction. For reference, the skeletal structures of these commercially available ligands are shown in Figure 1.

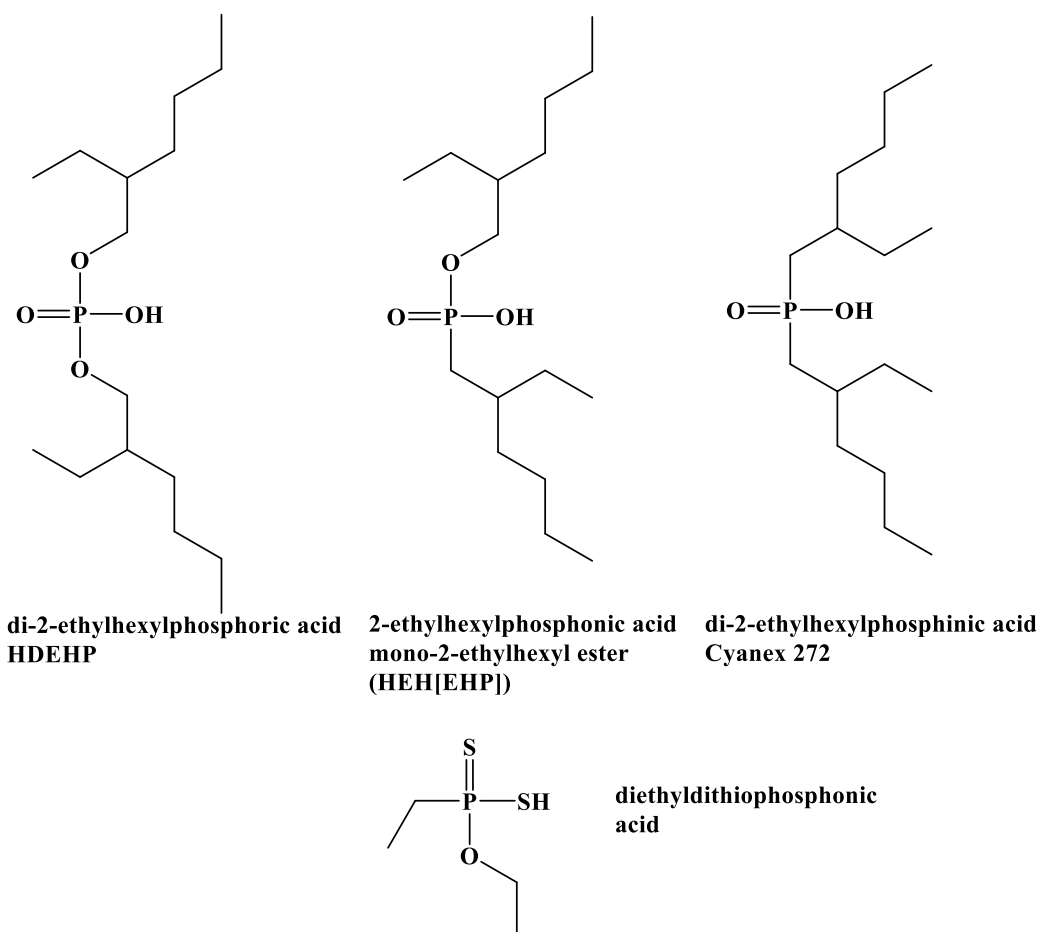


Figure 1: Skeletal structures, from left to right, of HDEHP, HEH[EHP], Cyanex 272 and diethyldithiophosphonic acid.

The lower pKa extracting agents, HDEHP and HEH[EHP], had the highest D values with D_{M_0} being greater than 1, while the Cyanex family was not as effective. Extraction with diethyl dithiophosphonic acid resulted in a D_{M_0} below 0.1. The comparison of D values for each of these ligands are shown in Figure 2.

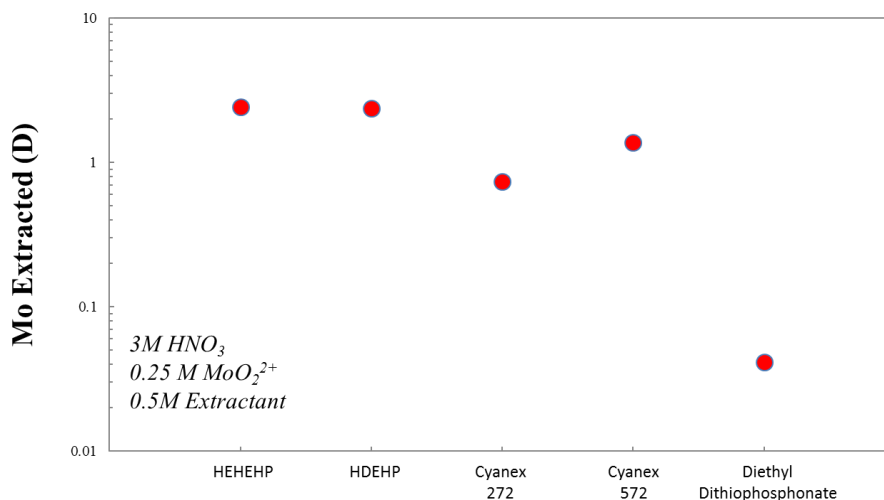


Figure 2: D_{Mo} values and evaluation of performance of commercially available organophosphorus extracting agents. Error bars were omitted for clarity. ($n = 3$; $\sigma = 0.32$ for HEH[EHP], 0.28 for HDEHP, 0.41 for Cyanex 272, 0.38 for Cyanex 272, 0.08 for diethyl dithiophosphonate)

However, there were two problems with comparing diethyldithiophosphonic acid to the other ligands in this group. First, the alkyl substituents are ethyls not 2-ethylhexyls. Second, there was a mixture of both oxygen and thiols, which would have a mixed effect on the extraction of Mo. Due to interest in finding how only the chalcogen substituents change D values, ligands were synthesized to only vary in the chalcogen substituents of the phosphorus without incorporating a difference in alkyl group or having a mixed chalcogen system. The ligands synthesized were bis(isopropyl) phosphinic acids with either dioxo, dithio, or diseleno as the chalcogen substituent. These ligands are shown in their skeletal structures in Figure 3. A 0.5 M solution of each ligand was made in n-dodecane and contacted with the 3 M nitric acid molybdenum aqueous stock. The resulting D_{Mo} values are shown in Figure 4.

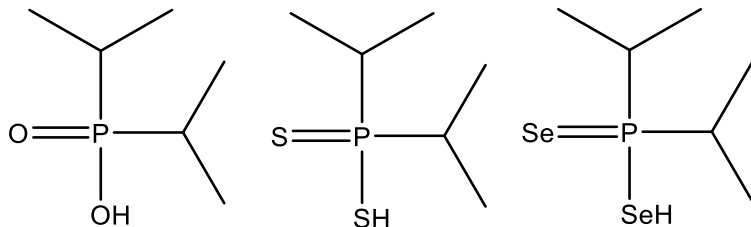


Figure 3: From left to right, bis(isopropyl) dioxophosphinic acid, bis(isopropyl) dithiophosphinic acid, and bis(isopropyl) diselenophosphinic acid.

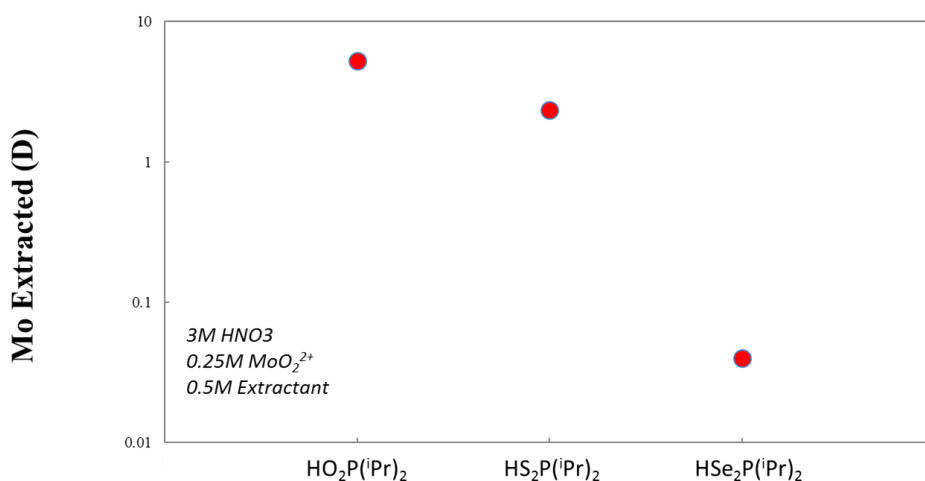


Figure 4: D values of molybdenum extraction from a 3 M nitric acid using 0.5 M bis(isopropyl) dichalcogenide phosphinic acid in dodecane. The chalcogenides, from left to right: oxygen, sulfur and selenium. Error bars were omitted for clarity. ($n = 3$; $\sigma = 1.8$ for $\text{HO}_2\text{P}(\text{iPr})_2$, 1.5 for $\text{HS}_2\text{P}(\text{iPr})_2$, and 0.11 for $\text{HSe}_2\text{P}(\text{iPr})_2$)

The oxido phosphinic acid had the highest D_{Mo} value of 4, with the sulfido having a value of 2. The worst performing phosphinic acid was the selenido with a D_{Mo} value of 0.05. This trend reflected the softness, or charge divided by ionic radius, of the chalcogen substituents. Due to the hexavalent oxidation state of Mo in high concentration nitric acid, this trend was expected, following hard-soft interaction rules.¹⁴

After the chalcogen phosphinic acid experiment confirmed that oxygen is the optimal substituent, further work was performed to optimize extraction of molybdenum by HEH[EHP] and HDEHP. The focus of the work was directed to HEH[EHP] due to observations that HDEHP retained too much Mo and Mo would degrade to Mo blue. Mo blue is a complex ion formation of Mo +4 and +6 in the presence of phosphates.¹⁵ HEH[EHP] was found to be stable in comparison with HDEHP on the same time scale. A mixing time optimization experiment produced the results shown in Figure 5. The two phases were close to achieving equilibrium by 45 s, while their values do not change significantly after 90 s of mixing. Peak loading of Mo in HEH[EHP] was also an important variable needing investigation. Different mM concentrations of Mo in 3 M nitric acid, containing a ⁹⁹Mo tracer, were extracted to find the optimum loading for Mo into HEH[EHP] (Figure 6).

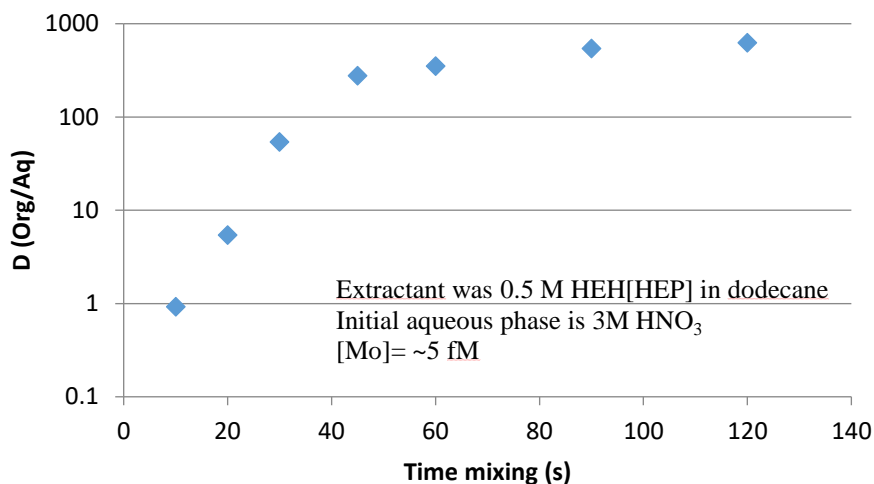


Figure 5: D values for solutions mixed on the vortex mixer for different lengths of time.

Error bars were omitted for clarity. (n = 4, 0.2% < σ < 1.02%)

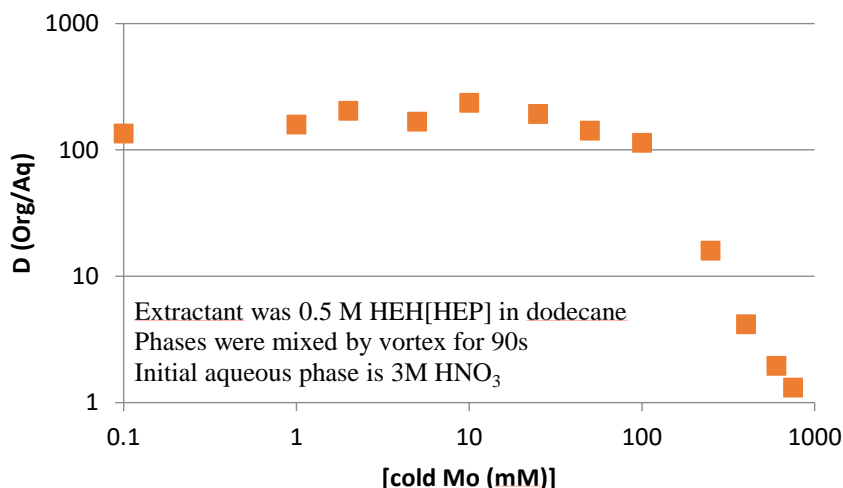


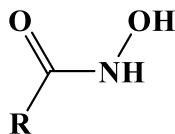
Figure 6: D values for extraction of different concentrations of molybdenum into a 0.5 M HEH[EHP]/dodecane organic phase. Error bars were omitted for clarity. ($n = 3$, $0.4\% < \sigma < 1.23\%$)

From Figure 6, it appeared that for 0.5 M HEH[EHP] in dodecane, the maximum concentration for was 100 mM Mo to achieve quantitative extraction. Having finished the optimization experiments of the extraction of molybdenum by HEH[EHP], the next step was to investigate stripping of molybdenum from the HEH[EHP] organic phase.

Mo stripping studies

Various oxime ligands were investigated as possible high-efficiency molybdenum stripping ligands. First, due to their ubiquitous nature in nuclear reprocessing technology, hydroxamic acids with functional groups of formo-, aceto- and benzyl- were compared; see Figure 7 for skeletal structures. Due to their universal use in reprocessing technology, radiolysis was not a factor in our studies. In stripping performance, the hydroxamic acids were comparable to one another with acetohydroxamic acid having a D value of about 0.002, benzylhydroxamic acid and formohydroxamic acid having a D value of about

0.004, see Figure 8. As opposed to the D values for extraction, where a higher D value was desirable, a lower D value for stripping means greater efficiency.

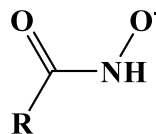


Hydroxamic Acid, where:

R= H; Formohydroxamic Acid (HFHA)

R= CH₃; Acetohydroxamic Acid (HAHA)

R= C₆H₅; Benzylhydroxamic acid (HBHA)



Hydroxamates, where:

R= H; Formohydroxamate (FHA)

R= CH₃; Acetohydroxamate (AHA)

R= C₆H₅; Benzylhydroxamate (BHA)

Figure 7: Skeletal structures of formo-, aceto-, and benzylhydroxamic acids and hydroxamates.

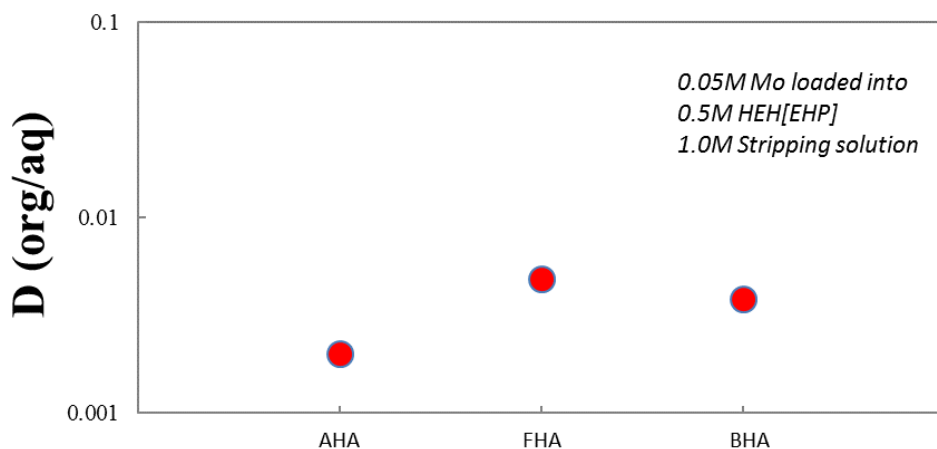


Figure 8: D values of aceto-, formo-, and benzylhydroxamic acids stripping 0.05 M molybdenum from a 0.5 M HEH[EHP] organic phase. Error bars were omitted for clarity. (n = 3, σ = 0.013 for AHA, 0.025 for FHA, and 0.012 for BHA)

Due to a difference in efficiency of 0.2% of total molybdenum, note that the hydroxamates were equally efficient at stripping molybdenum. Due to interest in hard and soft donor interaction with high oxidation state metals (MoO₂²⁺, UO₂²⁺), acetohydroxamic acid was subjected to Lawesson's or Woollin's rearrangement to

convert the carbonyl into a thiocarbonyl or selenocarbonyl, respectively. The rearrangement reactions are shown in Figure 9.

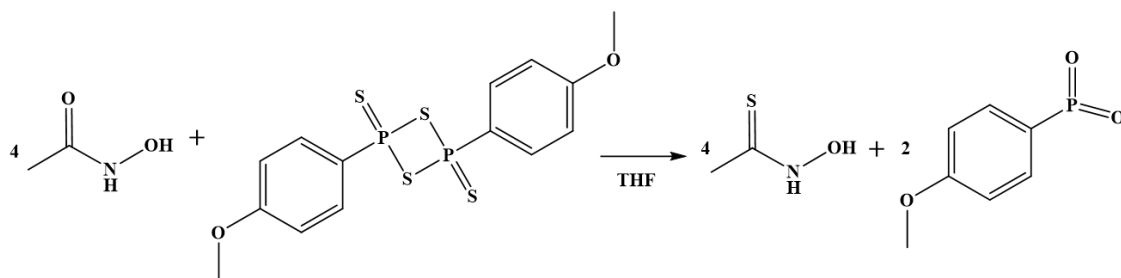


Figure 9: Lawesson's rearrangement of acetohydroxamic acid (AHA) to produce the desired acetothiohydroxamic acid (S-AHA).

After isolating the desired hydroxamic acid in high purity (>98%), the solutions were made from the hydroxamic acids at a concentration of 1.0 M and were immediately used to extract Mo, see Figure 10. The same trend that was observed for the chalcogenide substituent phosphinic acids was observed for the stripping of molybdenum. This furthermore reinforces the idea that molybdenum prefers ligands bearing harder donors.

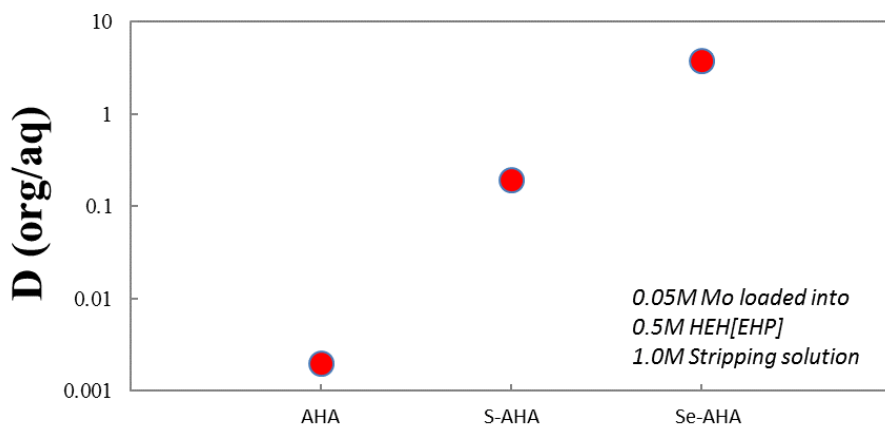


Figure 10: Comparison of the D value performance of acetohydroxamic acid, versus the carbonyl substituted acetothiohydroxamic acid and the acetoselenohydroxamic acid. Error bars omitted for clarity. ($n = 3$, $\sigma = 0.015$ for AHA, 0.25 for S-AHA, and 2.83 for Se-AHA)

However, there was a secondary issue in using the chalcogen bearing hydroxamic acids. The chalcogenide hydroxamic acids tended to undergo hydrolysis within days instead of months. This rendered a mixture of monothioacetic acid and acetic acid. It is likely the thioacetic acid underwent further oxidation to form acetic acid. Due to this degradation of the chalcogenide ligands, regardless of the D values, the use of chalcogenide substituted hydroxamates would be unadvisable for separations flowsheets.

Since hydroxamic acids are a subgroup of organic compounds called oximes, the performance of other oximes was investigated for stripping molybdenum from HEH[EHP]. 1.0 M solutions of acetohydroxamic acid, acetoamidoxime, acetone oxime, hydroxylamine, and alpha-benzoin oxime (ABO) were made and their performance in terms of D_{Mo} values were recorded; see Figure 11 for skeletal structures and Figure 12 for D values. Acetohydroxamic acid was found to be the most efficient stripping ligand with the lowest D_{Mo} value of 0.002, with all but hydroxylamine coming close in D values. Immediately upon mixing, the hydroxylamine and alpha-benzoin oxime created powders in the aqueous stripping phase which was undesirable for reprocessing technology.

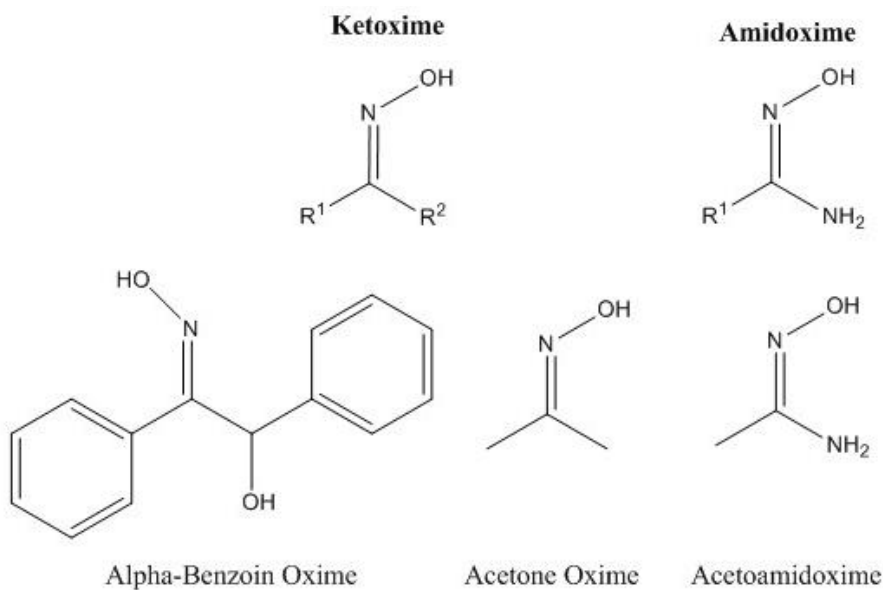


Figure 11: Skeletal structures of alpha-benzoin oxime, acetone oxime, and acetoamidoxime.

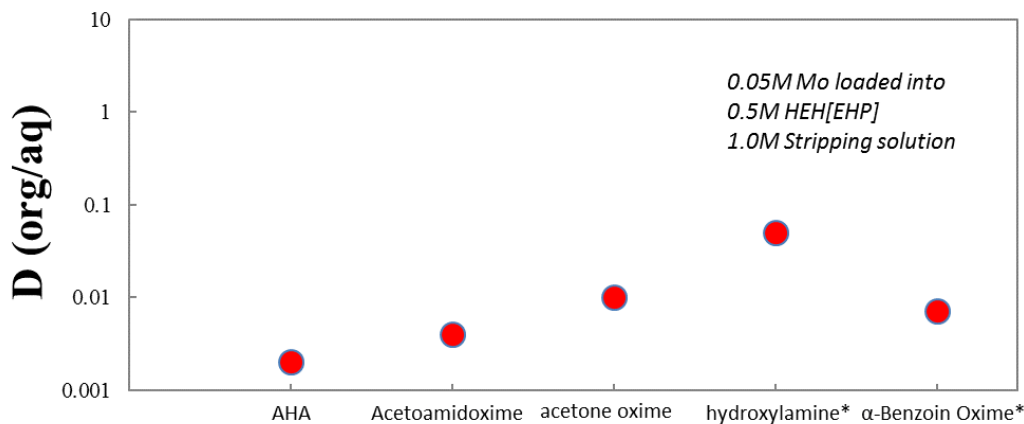


Figure 12: D values for 1.0 M stripping solutions containing acetohydroxamic acid (AHA), acetoamidoxime, acetone oxime, hydroxyl amine and alpha-benzoin oxime. The asterisk denotes solutions that immediately formed powders upon contact with the molybdenum containing HEH[EHP] organic phase. Error bars omitted for clarity. (n = 3, 18.9% < σ < 25.9%)

Conclusion

It was found that the harder chalcogen, oxygen, was the most efficient at complexing and partitioning molybdenum. While the softer chalcogenides had a drastic effect on the performance of ligands, organophosphorus extracting ligands HDEHP and HEH[EHP] were the most efficient at extracting Mo. For stripping ligands, the oxime ligands performed similarly, with a greater efficiency shown by the hydroxamic acids and amidoxime ligands.

Future Work

During the writing of this work, additional experiments are ongoing to explore the kinetics and thermodynamics of the extraction and stripping chemistry in greater detail.

To facilitate this, a microfluidics set up is being employed to achieve greater accuracy. This set up has been successfully employed by our group for other reprocessing technologies.

Additionally, further work with different substituents of the oxime moieties is also underway to investigate how changing the ligand affects efficiency. Future investigation will also focus on acid concentration dependence, nitrate dependence, stripping aqueous phase loading and efficiency of stripping from different organophosphorus ligands.

Acknowledgments

This chapter would not have been possible without the mentorship of Dr. M. Alex Brown, who taught me the fundamental lab technique to obtain the results presented. Dr. Brown, Dr. Gelis and Dr. Walensky were also integral in writing this chapter.

This work was funded by the Department of Energy – Office of Nuclear Energy, Sigma Team separations of minor actinides. I would also like to thank the MU Fellowship in Radiochemistry Program for financial support. The MU Fellowship in Radiochemistry Program is supported by a grant to the The Curators of the University of Missouri under award #NRC-HQ-15-G-0036, from the Office of the Chief Human Capital Officer of the Nuclear Regulatory Commission. Any statements, findings, conclusions, and recommendations are those of the author(s) and do not necessarily reflect the view of the Outreach and Recruitment Branch or the US Nuclear Regulatory Commission.

References

1. Service, R. F., Scrambling to Close the Isotope Gap. *Science* **2011**, *331* (6015), 277-279.
2. Benedict, M.; Pigford, T. H.; Levi, H. W., *Nuclear chemical engineering*. McGraw-Hill: New York, 1981.
3. Choppin, G. R.; Choppin, G. R.; Liljenzin, J.-O.; Rydberg, J., *Radiochemistry and nuclear chemistry*. Butterworth-Heinemann: Woburn, MA, 2002.
4. Gelis, A. V.; Lumetta, G. J., Actinide Lanthanide Separation Process—ALSEP. *Ind. Eng. Chem. Res.* **2014**, *53* (4), 1624-1631.
5. Taylor, R. J.; May, I.; Wallwork, A. L.; Denniss, I. S.; Hill, N. J.; Galkin, B. Y.; Zilberman, B. Y.; Fedorov, Y. S., The applications of formo- and aceto-hydroxamic acids in nuclear fuel reprocessing. *J. Alloys Compd.* **1998**, *271–273*, 534-537.
6. Tkac, P.; Paulenova, A., The Effect of Acetohydroxamic Acid on Extraction and Speciation of Plutonium. *Sep. Sci. Technol.* **2008**, *43* (9-10), 2670-2683.
7. Gelis, A. V.; Brown, M. A. Patent Pending.
8. Hu, Z.; Pan, Y.; Ma, W.; Fu, X., Purification of organophosphorus acid extractants. *Solvent Ext. Ion Exch.* **1995**, *13*, 965.
9. Partridge, J. A.; Jensen, R. C., Purification of di-(2-ethylhexyl)phosphoric acid by precipitation of copper(II) di-(2-ethylhexyl)phosphate. *J. Inorg. Nuc. Chem.* **1969**, *31* (8), 2587-2589.
10. Behrle, A. C.; Kerridge, A.; Walensky, J. R., Dithio- and Diselenophosphinate Thorium(IV) and Uranium(IV) Complexes: Molecular and Electronic Structures, Spectroscopy, and Transmetalation Reactivity. *Inorg. Chem.* **2015**, *54* (24), 11625-11636.
11. Fishbein, W. N.; Daly, J.; Streeter, C. L., Preparation and some properties of stable and carbon-14 and tritium-labeled short-chain aliphatic hydroxamic acids. *Anal. Biochem.* **1969**, *28*, 13-24.
12. Smith, M. B.; March, J., *March's Advanced Organic Chemistry: Reactions, Mechanisms, and Structure*. Wiley: 2007.
13. Elwell, W. T.; Wood, D. F., *Analytical chemistry of molybdenum and tungsten*. Pergamon Pr.: Oxford [usw.], Braunschweig, 1971.
14. Atkins, P. W. A. P. W., *Shriver & Atkins inorganic chemistry*. Oxford University Press ; W.H. Freeman and Co.: Oxford; New York; New York, 2006.

15. Murphy, J.; Riley, J. P., A Single-Solution Method for the Determination of Soluble Phosphate in Sea Water. *J. Marine Bio. Assoc. UK* **1958**, 37 (1), 9-14.

Chapter 4: Synthesis of hexavalent molybdenum formo-, acetohydroxamates and deferoxamine via liquid-liquid metal partitioning

Abstract

A new method of crystal growth and synthesis based on liquid-liquid partitioning is reported that allows for isolation and characterization of molybdenyl bisformohydroxamate (**Mo-FHA**), molybdenyl bisacetohydroxamate (**Mo-AHA**), and trimolybdenyl bisdeferoxamine (**Mo-DFO**) for the first time. When an immiscible organic phase is loaded with molybdenum, the metal can be stripped into an aqueous phase containing the ligand of interest. Crystal growth occurs in the aqueous phase near the interface. This novel approach affords shorter crystal growth time (hourly timeframe). All three Mo complexes were characterized in solution via FTIR, NMR, UV-Vis, and XAFS, while Mo-AHA and Mo-FHA structures were resolved by single crystal X-ray diffraction. Using the molybdenyl hydroxamate structural information, the speciation of Mo in a siderophore complex (Mo-DFO) was determined via complimentary spectroscopic methods and was confirmed by DFT calculations. ESI-MS confirmed that a Mo-deferoxamine complex of 1:1 metal to ligand complex exists in solution. The Mo solution speciation in the precursor organic phase, $\text{MoO}_2(\text{NO}_3)_2\text{HEH}[\text{EHP}]_2$ (where HEH[EHP] is 2-ethylhexylphosphonic acid mono-2-ethylhexyl ester) was characterized via FTIR, DFT and XAFS, and reported.

Scope of Impact

The work presented herein establishes a new method of Mo crystal growth, as well as, the crystal structures of new molybdenyl bisalkylhydroxamate crystal structures. While crystals of molybdenyl deferoxamine were isolated, they did not prove useful during investigation with a single crystal x-ray diffractometer. Due to this, solution spectroscopy, mass spectrometry and DFT were utilized to establish the most likely coordination number and environment of deferoxamine around molybdenum in aqueous solution. This contributes to the current state of knowledge as it gives a definitive coordination environment for a molybdenyl deferoxamine complex.

Introduction

Solvent extraction or liquid-liquid distribution applies two immiscible solvents to facilitate separation for a third soluble component (or *solute*), which is distributed between the two solvents. The partitioning of the solute (often times a metal ion, M) can be quantified in the form of a distribution ratio, which is typically the ratio of organic to aqueous concentrations, or $D_M = [M]_{\text{org}} / [M]_{\text{aq}}$.¹ The variables that govern the distribution of the targeted solute are numerous, but a constraint is that the phases are solution-based and all components are soluble. Insoluble components are generally unwanted in solvent extraction technologies.² However, experiments herein uncovered a liquid-liquid pathway that yielded single crystals of several molybdenum compounds. More importantly, the compounds could not be synthesized to the extent of our abilities by conventional crystallization methods such as slow evaporation and solvent dependent recrystallization.

The liquid-liquid technique mobilizes hexavalent molybdenum between phases by tuning the extraction nature via the forward and back-extraction. The difference between this method and other liquid-liquid crystallization methods is that the solute achieves equilibrium between phases and is not reliant on volatile alcohols or salting agents to a phase to achieve crystal growth.³⁻⁷ Extensive heating (conventionally applied in crystal engineering) cannot be tolerated with some ligands, e.g. small hydroxamic acids, on account of their tendency to hydrolyze and degrade to their acetate moieties.

One of the immiscible phases is a phosphonic acid extractant, such as 2-ethylhexylphosphonic acid mono-2-ethylhexyl ester (HEH[EHP]), in a hydrocarbon solvent that can effectively extract metal ions from acidic solutions. Subsequently, the metal-loaded organic solvent can be removed and contacted with a fresh aqueous matrix containing the ligand, such as acetohydroxamate (AHA). Though the analyte's coordination environment changes between phases, the 6+ valence remains; a schematic is shown in Figure 1 and the abbreviations for the moieties and their skeletal structures are shown in Figure 2. Once the metal achieves equilibrium in the final aqueous solution, interfacial currents promote crystallization when the phases are left unperturbed. The interfacial currents occur due to the interaction and microsolvation of the polar HEH[EHP] with molybdenyl ion and water.⁸⁻⁹ Crystal growth occurs close to the liquid-liquid interface after a brief period.

Hydroxamic acids are biologically relevant ligands that have influenced nearly four decades of fundamental iron, molybdenum, and vanadium coordination complexes in solid state and solution chemistry.¹⁰⁻¹⁴ Specifically, relevant to cellular and plant biology, molybdenum(VI) is incorporated into a cell via the molybdate transporter

protein.¹⁵ Cellular molybdate transport allows for biological acid-base and redox chemistry to take place without the formation of competing polyoxometalates.¹⁶ The formation of polyoxometalates makes isolation of various metal-ligand complexes very difficult in a laboratory practice. Thus, noticeably absent from literature are Mo(VI) crystals with formohydroxamate (FHA), acetohydroxamate (AHA) and deferoxamine (DFO).

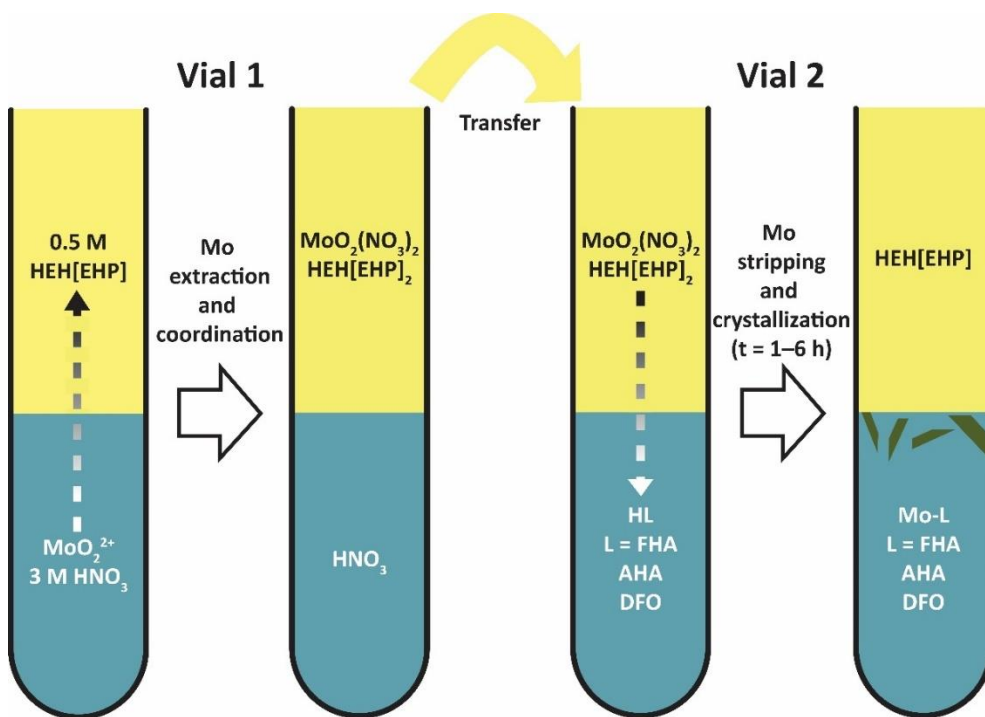


Figure 1: liquid-liquid solvent extraction method for synthesizing various Mo complexes. From left to right- MoO_2^{2+} is extracted from an acidic aqueous solution using 2-ethylhexylphosphonic acid mono-2-ethylhexyl ester (HEH[EHP]), in dodecane. The $\text{MoO}_2(\text{NO}_3)_2\text{HEH}[\text{EHP}]_2$ complex is added to a new vial with an aqueous solution of the desired ligand. The ligand strips the MoO_2^{2+} from the organic phase and when left in contact for several hours, the crystals form near the interface.

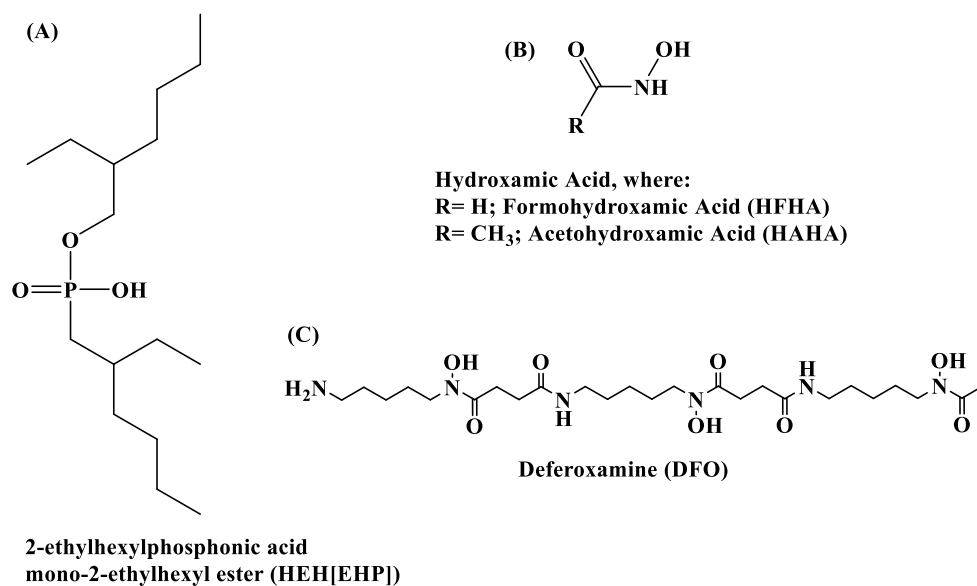


Figure 2: The skeletal structures of the ligands, their names and abbreviations used in this work. Where (A) is HEH[EHP], (B) is generic hydroxamic acid moiety, (C) is Deferoxamine (synonyms: desferoxamine, desferrioxamine, DFOA, DFOB).

Though the solution equilibria of molybdenyl bisacetohydroxamate has been characterized,¹⁷ searching for crystal structures and related coordination chemistry properties have come up shorthanded. The lack of coordination chemistry involving AHA and FHA in metal complexes is also surprising considering their role in nuclear fuel reprocessing technologies that treat appreciable concentrations of Mo.¹⁸⁻²³

Experimental

Unless otherwise noted, all materials were purchased (Sigma-Aldrich, St. Louis, MO) at 95% purity or better and used as received. HEH[EHP] was purchased at 95% purity (Yick-Vic Chemicals and Pharmaceuticals, Hong Kong, China) and was further purified by previously reported methods.²⁴ Water was distilled and further purified by a Merck Millipore Simplicity system to produce 18.2 MΩ deionized water. An acidic 0.5 M MoO₂²⁺ solution was made by dissolving 0.025 mol of Na₂MoO₄·2H₂O in 50 mL of 4.0

M nitric acid and vortexed until a clear, light yellow solution was obtained. Formohydroxamic acid, HFHA, was synthesized according to previously published procedure.²⁵ In addition, HFHA was recrystallized twice out of boiling ethyl acetate.

¹H, ³¹P and ⁹⁵Mo NMR spectra were obtained on a 500 MHz ESB Bruker spectrometer. Heavy water (D₂O) or deuterated toluene (C₇D₈) (Sigma-Aldrich) were used as received. ¹H NMR spectroscopy was referenced *in situ* to the residual protio impurity of the solvent at 4.79 ppm for heavy water and 2.08 for deuterated toluene (C₇D₇H). ³¹P NMR spectroscopy was referenced externally to 85% H₃PO₄ in D₂O at 0.00 ppm. ⁹⁵Mo NMR spectroscopy was referenced externally to 1.0 M Na₂MoO₄ in D₂O, calibrated to 0.00 ppm. ¹⁷O NMR spectroscopy was referenced internally to D₂O at 0.00 ppm. Infrared spectra were collected using a smart iTR diamond press on a Thermo Nicolet 6700 FT-IR averaging 64 scans at a resolution of 2 cm⁻¹, unless otherwise stated. IR background scans were of air for crystalline products, DI water if product was in aqueous phase, or of *n*-dodecane if product was in the organic phase. Absorbance spectra were obtained on a Varian Cary 50 Bio UV-vis spectrophotometer. Elemental analysis was performed by Atlantic Microlab, Inc. (Norcross, GA).

MoO₂(NO₃)₂(HEH[EHP])₂

In a 10-mL glass centrifuge tube, 0.5 M HEH[EHP] in *n*-dodecane was contacted once with a 3 M HNO₃, 0.5 M MoO₂²⁺ solution (see general experimental for Mo nitric acid solution). A Genie 2 Vortex mixer, set at the maximum mixing intensity of 3200 rpm, was used for all solvent extraction experiments. The **MoO₂(NO₃)₂(HEH[EHP])₂** yield was 92% with respect to HEH[EHP], confirmed by precipitation of residual Mo in the aqueous phase by alpha benzoin oxime; due to the affinity of the complex for dodecane,

the product was not isolable in pure form. ^1H NMR (C_7D_8 , 500 MHz): δ 6.98 (1H, bs), 4.0-4.8 (2H, m), 0.7-2.5 (37 H, m). $^{31}\text{P}\{^1\text{H}\}$ NMR (dodecane, 202 MHz): δ 34.44 ($^2J_{\text{P-Mo}} = 450$ Hz (broad), $^2J_{\text{P-}^{97}\text{Mo}} = 450$ Hz (broad)). IR (organic solution, cm^{-1}): 2965 (w, CH st.), 2877 (w), 1670 (w, NO_3 asym st.), 1460 (w, ethylhexyl CH_2 wag), 1402 (w, CH_2 scissoring), 1379 (w, NO st.), 1160 (w, P=O st.), 1060 (br. s, P-O-C st and POH st overlapped), 949 (m, Mo=O st), 920 (m, Mo=O st.), 867 (br. m, free NO_3 wag), 822 (m, alkyl scissor), 766 (br. w, alkyl wag.).

Mo-AHA, $\text{MoO}_2(\text{acetohydroxamate})_2$

The molybdenum containing organic phase, $\text{MoO}_2(\text{NO}_3)_2\text{HEH}[\text{EHP}]_2$ from the previous section, was contacted 1:1 v:v with a 1.0 M acetohydroxamic acid solution in DI water in a 10 mL glass centrifuge tube. The solution was vortexed for 30 seconds, centrifuged at 3000 rpm for 30 seconds and then the two phases stayed contacted overnight. Green blocks of X-ray diffraction quality crystals ($\sim 0.25 \text{ mm}^3$) of **Mo-AHA** formed close to the interface of the organic and aqueous phases (84% yield in isolable crystalline form). ^1H NMR (D_2O , 500 MHz): δ 1.80 (1H, singlet), 1.76 (3H, singlet). ^{95}Mo NMR (D_2O , 32 MHz): δ 140.3. IR (crystal, cm^{-1}): 3163 (m, NH st.), 3100 (m, CH st.), 3029 (m, CH st.), 2924 (m), 2852 (m), 1602 (s, C=O), 1516 (s, NCO wag.), 1426 (s, $\text{CH}_3\text{C}=\text{O}$), 1388 (s, $\text{CH}_3\text{C}=\text{O}$), 1329 (br. m, NH wag), 1106 (s, N-O st.), 1046 (w), 1036 (w), 1001 (s, AHA out of plane bend), 936 (s, Mo=O), 915 (w), 901 (s, Mo=O), 748 (br. m), 674 (s). Anal. Calc. for $\text{C}_4\text{H}_{12}\text{MoN}_2\text{O}_6$: C, 17.15; H, 4.32; N, 10.00%. Found: C, 17.15; H, 4.33; N, 9.99%.

Mo-FHA, $\text{MoO}_2(\text{formohydroxamate})_2$

Mo-FHA was synthesized analogously to **Mo-AHA**, but formohydroxamic acid was used instead of acetohydroxamic acid. Green needle-like crystals suitable for X-ray diffraction formed close to the interface of the organic and aqueous phases (80% yield in isolable crystalline form). ^1H NMR (D_2O , 500 MHz): δ 7.45 (1H, singlet), 1.76 (1H, br. singlet). ^{95}Mo NMR (D_2O , 32 MHz): δ 148.5. IR (crystal, cm^{-1}): 3172 (m, NH st.), 3012 (w), 2911 (w), 1558 (s, C=O), 1516 (s, NCO wag.), 1471 (s, HC=O), 1369 (w, HC=O), 1305 (m, NH wag), 1221 (m), 1019 (w), 896 (s, Mo=O), 868 (s, Mo=O), 671 (br. m). Anal. Calc. for $\text{C}_2\text{H}_4\text{MoN}_2\text{O}_6$: C, 9.69; H, 1.63; N, 11.29%. Found: C, 9.66; H, 1.69; N, 11.27%.

Mo-DFO, $\text{Mo}_3\text{O}_6(\text{deferoxamate})_2$,

Mo-DFO was synthesized analogously to **Mo-AHA**, but a 0.1 M solution of deferoxamine mesylate salt was used instead of acetohydroxamic acid. Deferoxamine in literature is synonymous with desferoxamine, desferrioxamine, DFO, DFOA, and DFOB. The 0.1 M solution was prepared by weighting out 0.6568 grams into a Class A 10 ml volumetric flask, then adding 0.1012 grams of triethanolamine and addition of DI H_2O to the 10 mL mark. Green octahedron-like crystals formed close to the interface of the organic and aqueous phases but were of poor diffraction quality. Isolable yield was 15% with respect to the deferoxamine ligand. ^1H NMR (D_2O , 500 MHz): δ 3.67-3.55 (8 H, multiplet), 3.150 (4 H, quartet, $J = 7.5$ Hz), 2.968 (4 H, triplet, $J = 7.5$ Hz), 2.768 (6 H, doublet, $J = 9$ Hz), 2.469 (4 H, triplet, $J = 7$ Hz), 2.083 (2 H, singlet) 1.70-1.55 (8 H, multiplet), 1.52-1.43 (4 H, multiplet), 1.40-1.22 (6 H, multiplet), 1.153 (4 H, triplet, $J = 7.5$ Hz). ^{95}Mo NMR (D_2O , 32 MHz): δ 128.29. ^{17}O NMR (D_2O , 67 MHz): δ 902, 685. IR (crystal, cm^{-1}): 3308 (m, OH st.) 3096 (m, NH_2 st.), 2928 (m, NH stretch), 2857 (m,

CH₂ stretch), 1624 (s, C=O), 1565 (s, C=O), 1427 (m, NCO wag.), 1270 (w), 1162 (br. S, C-N st.), 1102 (m), 1043 (s), 930 (s, M=O), 894 (s, M=O), 777 (m), 730 (m). Anal. Calc. for C₆₄H₁₄₆Mo₃N₁₄O₂₈S₂ [(MoO₂)₃(Deferoxamine)₃(HNEt₃Mesylate)₂]: C, 40.21; H, 7.70; N, 10.26%. Found: C, 40.71; H, 7.79; N, 10.33%.

Single crystal x-ray diffraction experiments

The selected single crystals were mounted on a nylon cryoloop, oil or epoxy was not used. X-ray data collection was performed at 100(2) K. The x-ray data were collected on a Bruker CCD diffractometer with monochromated Mo-K α radiation ($\lambda = 0.71073 \text{ \AA}$). The data collection and processing utilized Bruker Apex2 suite of programs.²⁶ The structures were solved using direct methods and refined by full-matrix least-squares methods on F^2 using Bruker SHELX-97 program.²⁷ All non-hydrogen atoms were refined with anisotropic displacement parameters. All hydrogen atoms were added on idealized positions and not allowed to vary. The Fourier map of the electron density was scrutinized for evidence of a proton on the hydroxyl oxygen, but none was found. Thermal ellipsoid plots were prepared by using X-seed with 50% of probability displacements for non-hydrogen atoms.²⁸ The crystal parameters for **MoO₂(formohydroxamate)₂** and **MoO₂(acetohydroxamate)₂** are presented in Table 1.

Table 1: Crystal parameters for **Mo-AHA** and **Mo-FHA**

	Mo-AHA	Mo-FHA
CCDC Deposit Number	1418854	1448475
Empirical Formula	C ₄ H ₈ Mo ₁ N ₂ O ₆	C ₂ H ₄ Mo ₁ N ₂ O ₆
Formula weight (g/mol)	276.06	248.01
Crystal Habit, color	Prism, Yellow	Needle, Yellow
Temperature (K)	100(2)	100(2)

Space group	<i>P2₁/c</i>	<i>Fdd2</i>
Crystal system	<i>Monoclinic P</i>	<i>Orthorhombic F</i>
Volume (Å ³)	834.3(8)	1281.5(6)
<i>a</i> (Å)	6.565(4)	11.808(3)
<i>b</i> (Å)	9.626(5)	19.137(6)
<i>c</i> (Å)	13.270(7)	5.6711(16)
α (°)	90.0	90.0
β (°)	95.757(5)	90.0
γ (°)	90.0	90.0
<i>Z</i>	4	8
Calculated density (Mg/m ³)	2.98	2.571
Absorption coefficient (mm ⁻¹)	1.58	2.035
Final R indices [<i>I</i> > 2 σ (<i>I</i>)]	R1 = 0.026 wR2 = 0.068	R1 = 0.010 wR2 = 0.027

Computational details

MoO₂(NO₃)₂(HEH[EHP])₂, Mo₂O₄(acetohydroxamate)₂, molybdenyl(HDesferoxamine) and Mo₃O₆(Deferoxamine)₂ were examined using MM2 calculations native to the Chem3D program to find initial starting geometries. Each of the MM2 geometries was then inputted into the Gaussian09 suite of software for examining their electronic structure.²⁹ The 2-ethylhexyl alkyl groups of HEH[EHP] were truncated to ethyl alkyl groups to conserve computational resources. Density functional theory was performed at the B3LYP (Becke-3 exchange and Lee-Yang-Parr correlation functional) level of theory.³⁰⁻³² Full geometry optimizations were performed and stationary points were determined to be global minima using analytical frequency calculations. The

Stuttgart/Dresden triple zeta basis set was used to model molybdenum.³³⁻³⁴ While the Pople double- ζ quality basis set, 6-31G(d,p), was used for all non-metal atoms.³⁵⁻³⁶

Electrospray Ionization Mass Spectrometry

Molybdenum deferoxamine samples were prepared as previously stated with slight modification; the samples were made without use of the sacrificial base (trimethylamine) to ensure no additional fragmentations were introduced during ESI sample introduction to the MS. Post extraction the samples created a third phase, which disappeared after the samples sat overnight before removing the aqueous layer. An Agilent 1260 Infinity high-performance liquid chromatograph equipped with a quad pump (G1311B), an autosampler (G1329B) and a quadrupole mass spectrometer ESI detector (6120; MSD) running in continuous positive mode was used. The aqueous sample was diluted by a factor of 10 using HPLC-grade water (Sigma-Aldrich). The mobile phase was HPLC-grade water at 25 °C, which was fed directly into the MSD. The pumping speed was either 0.25 mL/min (run 1) or 0.1 mL/min (run 2). 1 μ L of the diluted stock solution was injected into the detector using the autosampler. The fragmentation voltage of the MSD was 70 V.

XAFS

Samples were prepared via the solvent extraction method as explained previously, and were investigated on the beam line within 24 hours of sample synthesis. Samples were irradiated in a spectrophotometric cuvette that contained a Kapton-covered window. XAFS measurements were made on the insertion device beam line of the Materials Research Collaborative Access Team (MRCAT) at the Advanced Photon Source, Argonne National Laboratory. The X-ray energy was selected with a liquid nitrogen

cooled, double-crystal Si(111) monochromator and a platinum-coated mirror was used for harmonic rejection. Data were collected in transmission in step scan mode. The scan mode was continuous scanning with undulator tracking. Harmonic rejection was accomplished with a Rh-coated mirror, while energy calibration was with the Fe K edge of a metallic Fe foil (7110.75 eV).³⁷ No further calibration or alignment of the scans was performed; the average shift within a series of scans for each sample was less than 0.02 eV. The Mo K-edge (20,000 eV) was probed in absorbance mode.³⁸ The spectra were processed and modelled using Athena and Artemis software, respectively.³⁹⁻⁴⁰

Results and Discussion

It was crucial to investigate the molybdenum speciation in the organic phase—the precursor in the hydroxamate complexes and crystal growth experiments. Molybdenum exhibits a relatively wide range of valence states, extraction complexes, and solution equilibria. Since the target species was molybdenyl with hydroxamates, we verified that the extracting solvent was simply a vehicle for molybdenyl outside of an aqueous matrix and that no other valence was present. IR, NMR, XAFS spectroscopies and DFT calculations characterized this step.

Next, liquid-liquid crystallization was used to grow single crystals and determine the structures of **Mo-AHA** and **Mo-FHA**. However, **Mo-DFO** crystals did not result in a usable crystal structure. Therefore, comparison of DFO with the hydroxamate complexes was carried out using solution based spectroscopy in order to derive a possible coordination environment.

Characterization of MoO₂(NO₃)₂HEH[EHP]₂ in the organic phase

Cyanex 272 and di-2-ethylhexyl phosphoric acid were also tried in place of HEH[EHP]. However, Cyanex 272 did not produce crystals upon the stripping step and while crystals did form with di-2-ethylhexyl phosphoric acid, it was a strong enough ligand to compete with crystal formation reducing the yield. Hence HEH[EHP] was found to be the optimal organophosphorus extraction ligand and thus was characterized.

IR and NMR spectroscopy

In the $\text{MoO}_2(\text{NO}_3)_2\text{HEH}[\text{EHP}]_2$ IR spectra, Table 2, the metal-oxido stretching frequencies and subsequent red shifting of the phosphoryl stretch verify metal-ligand coordination by HEH[EHP]. The molybdenum-oxido stretches were identified due to their similarity to another ionic molybdenum complex.⁴¹ Observed was a relatively small red shift in the P-OH stretch indicating that the P-O bond is not being weakened to the same extent as the P=O. This suggests that the HEH[EHP] is still protonated and acting as a neutral donor, otherwise, the two stretching frequencies would be indistinguishable due to the delocalization over the O-P-O atoms. There are absorptions assigned to bound (1379 cm^{-1}) and free nitrate (1670, 867 cm^{-1}).⁴²

Table 2: IR stretching frequencies of interest from HEH[EHP], $\text{KMoO}_3(\text{IO}_3)$ and $\text{MoO}_2(\text{NO}_3)_2\text{HEH}[\text{EHP}]_2$

	HEH[EHP] (cm^{-1})	$\text{KMoO}_3(\text{IO}_3)$ (cm^{-1})	$\text{MoO}_2(\text{NO}_3)_2\text{HEH}[\text{EHP}]_2$ (cm^{-1})
M-O1	-	931, 916	949, 920
P=O stretch	1196	-	1160
P-OH	1036	-	1020 broad
NO_3^-	-	-	1670, 1379, 867

^1H , ^{31}P and ^{95}Mo NMR spectroscopy further characterized the $\text{MoO}_2(\text{NO}_3)_2\text{HEH}[\text{EHP}]_2$ complex. The ^1H NMR spectrum exhibits a broad resonance, assigned to the hydroxyl group, shifted upfield to 6.98 ppm. ^{31}P NMR spectrum shows both coordinated and free ligand phosphorus peaks. Coordinated HEH[EHP] was downfield at 34.44 ppm from the free ligand and had broad satellites 450 Hz from the resonance, which indicated spin-spin coupling with both ^{95}Mo and ^{97}Mo . The broad satellites most likely reflect the asymmetry and the coupling with ^{31}P nuclei. No resonances were observed in the ^{95}Mo trials. We reason that due to the phosphorus spin coupling, low symmetry and ligand exchange, the ^{95}Mo resonance is NMR silent.

DFT Calculations

Initially, various four coordinate tetrahedral and six coordinate octahedral MoO_2^{2+} , nitrate, and HEH[EHP] complexes were optimized. Overall, the tetrahedral optimized geometries were not as low in free energy as the octahedral structures. In comparing the octahedral optimized structures, the IR data allowed us to rule out all but two possible starting geometries, a MoO_2^{2+} with either 4 HEH[EHP] moieties or MoO_2^{2+} bound to two nitrates and two HEH[EHP] moieties. Consequently, $\text{MoO}_2(\text{NO}_3)_2(\text{HEH}[\text{EHP}])_2$ is lower in energy by 9 kJ/mol. This complex is illustrated in Figure 3 with relevant bond lengths of the coordination sphere given in Table 3.

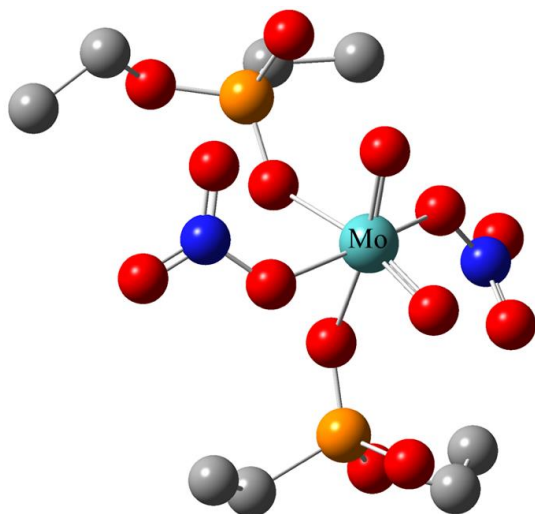


Figure 3: Optimized theoretical geometry of $\text{MoO}_2(\text{NO}_3)_2(\text{HEH}[\text{EHP}])_2$. HEH[EHP] has been truncated to ethyl chains.

X-ray Absorption Fluorescence Spectroscopy

The K -edge $k^3\chi(k)$ XAFS, Fourier-Transform (FT), and best fits for $\text{MoO}_2(\text{NO}_3)_2\text{HEH}[\text{EHP}]_2$ are provided in Figure 4. The coordination numbers, calculated path lengths and Debye-Waller factors are listed in Table 3. Treating the axial oxygens as a standard, the amplitude reduction factor was fixed at $S_0^2 = 0.94$, which gave the most resilient values of $N_{\text{yl}} = 2$ for separate refinements of Mo in mineral acids; the same fixed value was applied to the $\text{MoO}_2(\text{NO}_3)_2\text{HEH}[\text{EHP}]_2$. The data were refined within a k -window of $3.0 - 15.8 \text{ \AA}^{-1}$ and an R-range of $1.15 - 4 \text{ \AA}$. The potentials included Mo-O, Mo-N, Mo-C, and Mo-P; multiple scattering was not considered as single-scattered potentials were sufficient. The dominant signal in each case is the peak shown around 1.2 \AA (uncorrected for phase-shift), which corresponds to Mo-O pathways. Beyond this intense peak are much weaker signals that are attributed to Mo-N, or Mo-P. Organo-phosphorous extractants (such as HDEHP, HEH[EHP], or Cyanex 272) are primarily suited to extract cations from weakly acidic solutions, thus literature is mainly targeted at M-O and M-P pathways in the manner of a proton-exchange and subsequent

coordination environment.⁴³ Considering that the Mo was extracted into HEH[EHP] from 3 M HNO₃, the data was treated with a solvation-type approach, which rules out the proton-exchange mechanism and includes charge-balancing counter-ions such as nitrate, as also considered with the DFT results. Additionally, when analyzing M(VI)O₂ elements by XAFS, there will be more than one M-O pathway which can sometimes be visually distinct within the spectra, such as uranyl-HDEHP (di-2-ethylhexyl phosphoric acid).⁴⁴ This was not the case when analyzing **MoO₂(NO₃)₂HEH[EHP]₂** as seen by the solo Mo-O signal.

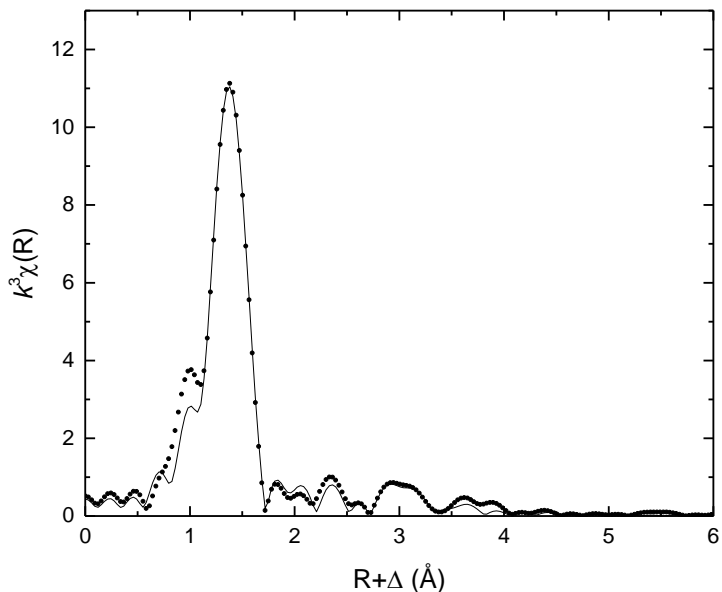


Figure 4: k^3 -Weighted Molybdenum K -edge XAFS R-space of **MoO₂(NO₃)₂HEH[EHP]₂** solution. The points represent the experimental data; the solid line represents the model fit.

Table 3: Structural parameters of **MoO₂(NO₃)₂HEH[EHP]₂** (R -factor = 0.003) determined from XAFS and from the DFT minimized structure. The amplitude reduction factor, S_0^2 , was fixed at 0.94 (2σ uncertainty). CN : coordination number; R : radial distance; σ^2 : Debye-Waller factor; E_0 : change in absorption edge.

	R (Å)	$\sigma^2 \times 10^{-3}$ (Å ²)	ΔE_0	DFT Results (Å)
<i>MoO₂(NO₃)₂HEH[EHP]₂ (CN = 2)</i>				
Mo-O ₁	1.708 ± 0.006	1.2 ± 0.8	5.7 ± 2.4	1.717
Mo-O ₂	2.03 ± 0.01	3 ± 2		2.047
Mo-O ₃	2.19 ± 0.02	6 ± 2		2.211
Mo-N	3.30 ± 0.06	2 ± 4		3.050
Mo-P	3.31 ± 0.04	5 ± 4		3.463

The best fit to the dominant Mo-O peak was obtained with three separate doubly-degenerate Mo-O paths corresponding to the oxido ligands, an oxygen from nitrate, and the phosphonyl oxygen from HEH[EHP]; the results are listed in Table 3. Omitting any one of these pathways appreciably worsened the R-factor statistics. Multiple M-O pathways deconvoluted through XAFS are not unusual even when calculated to be over a tenth of an angstrom apart.⁴⁵ Beyond the combined Mo-O peaks are subtle features that are just above the noise level, which fit Mo-N and Mo-P pathways. The Mo-N and Mo-P path lengths are representative of being outer sphere and coordinated through their respective oxygens.

The underlining goal in analyzing and interpreting **MoO₂(NO₃)₂HEH[EHP]₂**, however, was to validate that the immiscible HEH[EHP] bulk served as a vehicle for molybdenyl and a precursor for Mo-hydroxamates. Therefore, all the techniques used for Mo characterization in the organic phase point to the conclusion that Mo exists as a molybdenyl ion, coordinated with two nitrate ions and two organophosphorus ligands. The HEH[EHP] ligand is not acting as an acidic extractant in this case, but rather as a neutral extractant, which partitions Mo through a solvation mechanism. This finding is critical for the following steps of the Mo crystal synthesis as the Mo preserves its molybdenyl moiety throughout the process.

Crystal structures of Mo-FHA and Mo-AHA

As previously stated, single crystals of **Mo-AHA** and **Mo-FHA** formed close to the interface of the organic and aqueous phases in the reaction vial in a matter of hours. Other crystal growth methods, such as evaporation or cooling of a concentrated solution required a time scale of days and ultimately resulted in the degradation of **Mo-AHA** and **Mo-FHA**. Using the bi-phasic method, single crystals of XRD quality were examined, elucidating the coordination environments illustrated in Figure 5 and bond lengths and angles are given in Table 4.

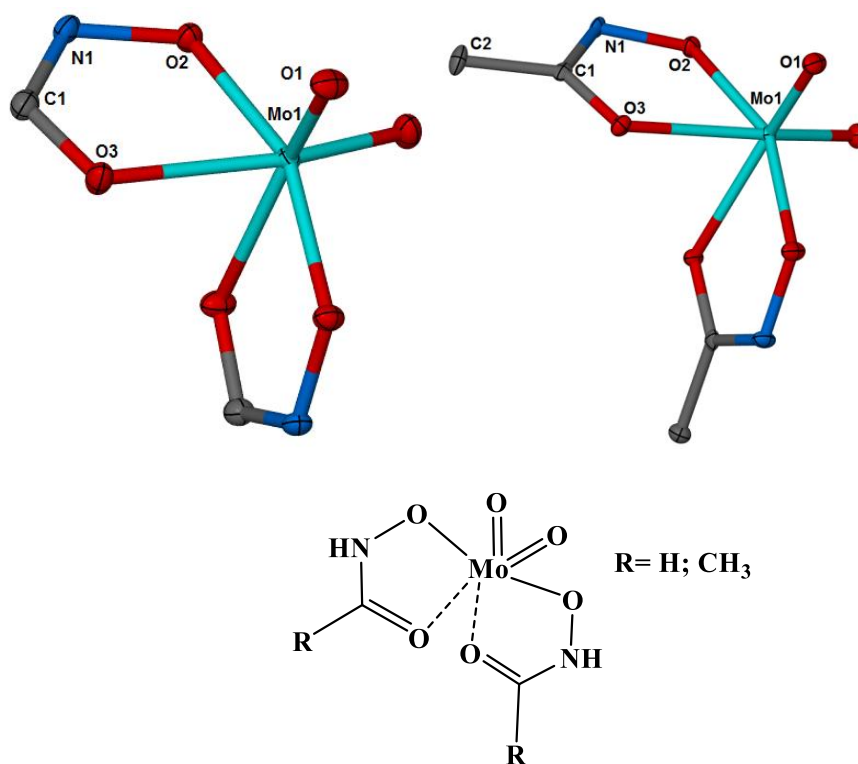


Figure 5: Thermal ellipsoid plot of **Mo-FHA** (Top left), **Mo-AHA** (Top Right), shown at the 50% probability level. Skeletal structure of **Mo-AHA** and **Mo-FHA** (bottom center) is shown for comparison. For clarity, hydrogen atoms have been omitted from the crystal structures.

A comparison of the structures of **Mo-FHA** and **Mo-AHA** shows no substantive differences. The only differences come in the interaction of the carbonyl with the metal

center and the C-O bond. The AHA carbonyl bond is longer than in FHA by 0.013 Å. The interaction between the carbonyl oxygen and the metal center is also affected. The M-O₃ bond is 0.023 Å longer for the AHA than the FHA complex. Comparing these results with other molybdenum(VI) hydroxamate complexes demonstrates the effects of the carbonyl substituent. There is a clear electron effect of the R group going from aceto to formo to the more electron withdrawing benzo (BHA) or phenylacetyl (PAHA) carbonyl substituents resulting in a longer distance from the oxygen to metal center.

Table 4: Bond lengths (Å) and angles (deg) of **Mo-FHA** and **Mo-AHA** compared with **Mo-BHA** (molybdenyl bisbenzohydroxamate) and **Mo-PAHA** (molybdenyl bisphenylacetylhydroxamate). Included is the bond length results of the DFT optimized structure of **Mo-AHA**.

	Mo-AHA	Mo-FHA	Mo-BHA ⁴⁶	Mo-PAHA ⁴⁷	Mo-AHA DFT results
M-O ₁	1.708(2)	1.7087(19)	1.704	1.689(14)	1.709
M-O ₂	2.011(2)	2.0031(19)	1.994	1.990(12)	2.033
M-O ₃	2.214(2)	2.191(2)	2.153	2.245(12)	2.308
O ₁ -Mo-O _{1'}	104.66(10)	104.71(14)	103.51	105.53(8)	105.75
O ₂ -Mo-O _{2'}	156.00(8)	157.56(11)	155.93	152.87(5)	153.25
O ₁ -Mo-O _{3'}	159.94(8)	159.15(9)	160.70	160.73(6)	160.31
C ₁ -N ₁	1.307(4)	1.297(3)	1.316	1.298(2)	1.328
C ₁ -O ₃	1.284(3)	1.271(3)	1.262	1.267(18)	1.258
N ₁ -O ₂	1.375(3)	1.371(3)	1.386	1.366(19)	1.366

Interestingly, a mixed ligand crystal structure of molybdenyl hydroxamate/hydroximate by Nicholas *et al.* was synthesized.⁴⁸ However, there was no isolation of a bisacetohydroxamate complex. There was only the isolation of a white powder after oxidation. This resulting white powder, when compared to our yellow-green molybdenum acetohydroxamate complex, is more reticent of colorless HAHA or MoO₃, confirming the novelty of our bi-phasic system for forming complexed and facilitating crystal growth.

DFT calculations of **Mo-AHA** were also pursued. Due to our crystal structures and those from literature, initial geometries were modeled to be the same.^{46, 48-54} The final minimized structures' bond lengths of interest are in Table 4 and the DFT geometry matches that of the crystal structure in Figure 5. The crystal structure's bond lengths and angles confirm the optimized DFT structure, lending credence to using DFT optimization to find the coordination environment of other molybdenum hydroxamate complexes.

Crystals of Mo-DFO

The biphasic approach that resulted in **Mo-AHA** crystals was also applied to solutions of DFO. Crystals of **Mo-DFO** were observed at the interface much like Mo-FHA and Mo-AHA, however, they could not be treated in the same manner. Crystal growth was sporadic and was reproducible in approximately 30% of the trials. Their formation was found to be dependent on the final pH of the aqueous stripping solution and needed to be treated with a base capable of binding the mesylate salt to prevent interaction with the ligand and metal center. When crystal growth did occur, crystals did not polarize light and show mosaicism when interrogating with a single crystal x-ray diffractometer. However, the crystals appeared to be single and of octahedral shape. Considering these

complications, molybdenum deferoxamine aqueous solutions were investigated via DFT and solution spectroscopy, most notably XAFS, to identify the coordination environment of the molybdenum metal center. The solution spectroscopy of molybdenum hydroxamate complexes, especially **Mo-AHA**, and investigation via XAFS were used to compare and resolve the coordination environment of the **Mo-DFO** complex.

Spectroscopic and DFT studies of Mo-FHA, Mo-AHA and Mo-DFO

IR, NMR, UV-Vis spectroscopy

Each of the metal-hydroxamate complexes' IR spectra show the metal-oxido stretches as well as the subsequent red shift of the amide, carbonyl and nitrosyl functional groups as electron density is donated to the metal center. These changes in the IR spectra support the idea that the molybdenyl hydroxamate complex is present in Mo-DFO. Table 5 gives comparative stretching frequencies of the metal complexes, as well as acetohydroxamic acid for comparison.

Table 5: IR stretching frequencies (cm^{-1}) of acetohydroxamic acid, **Mo-DFO**, **Mo-AHA**, and **Mo-FHA**.

(cm^{-1})	HAHA	Mo-AHA	Mo-FHA	Mo-DFO
M-O1	-	936, 901	896, 871	930, 894
C1-N1	1547	1516	1516	1506
C1=O3	1619	1602	1558	1624, 1565
N1-O2	1136	1106	1104	1102

Additionally, complex formation can be interrogated with use of UV-Vis spectroscopy. For **Mo-AHA** and **Mo-FHA**, an absorbance band is present around 250 nm (Figure 6). The UV-vis absorbance for **Mo-DFO** on the other hand has two peaks, one as a shoulder

at ~250 nm and a larger peak at ~325 nm. This matches previous reports of molybdenum deferoxamine complexes via UV-Vis spectroscopy.⁵⁵ It was determined that there was only one species formed but we did not go further to identify the complex. While the same type of band is seen between AHA, FHA and DFO at 250 nm, further investigation with other techniques, such as NMR, are needed to compare metal and ligand environments.

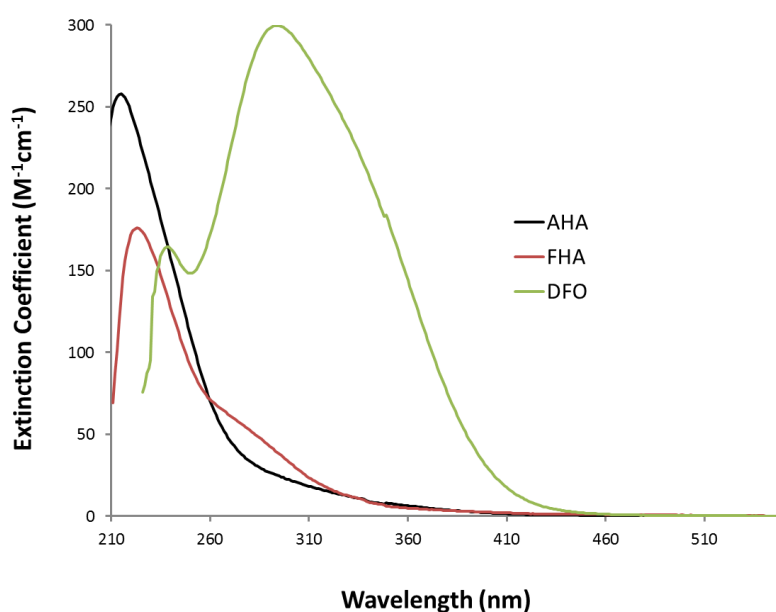


Figure 6: Extinction coefficient profiles of Mo-AHA, Mo-FHA and Mo-DFO

The ¹H NMR spectrum of **Mo-AHA** showed an up field shift of the amine proton to 1.80 ppm and the methyl proton resonance was slightly shifted downfield to 1.76 ppm. While the ⁹⁵Mo resonance was observed at 140.3 ppm, downfield from the initial 0.5 M MoO₂²⁺ solution resonance at -63.1 ppm. The **Mo-FHA** ¹H NMR spectrum showed the amine proton to be at 1.76 ppm and the formic proton was slightly shifted up field to 7.45 ppm from the formic proton resonance of the protonated hydroxamic acid at 7.80 ppm.⁵⁶

The ^{95}Mo resonance was observed at 148.5 ppm, which is ~8 ppm downfield from **Mo-AHA**.

In comparison, the ^{95}Mo NMR resonance for **Mo-DFO** appears at 128 ppm, which is farther up field than both **Mo-FHA** and **Mo-AHA**. As DFO contains a longer alkyl chain than either aceto- or formohydroxamate, it can be reasoned that this could increase electron donation to the metal center causing the upfield shift. However, the shift in resonance in comparing the complexes is not substantial enough to warrant other major differences in structure. This suggests that the coordination around the molybdenyl metal center is approximately the same in each complex (FHA, AHA, DFO), see Figure 7. The proton resonance of **Mo-DFO** shows a slight red shift in the methyl proton and in the alpha CH_2 groups closest to the hydroxamate site bonded through the amine, however, the rest of the proton resonances are relatively unaffected.

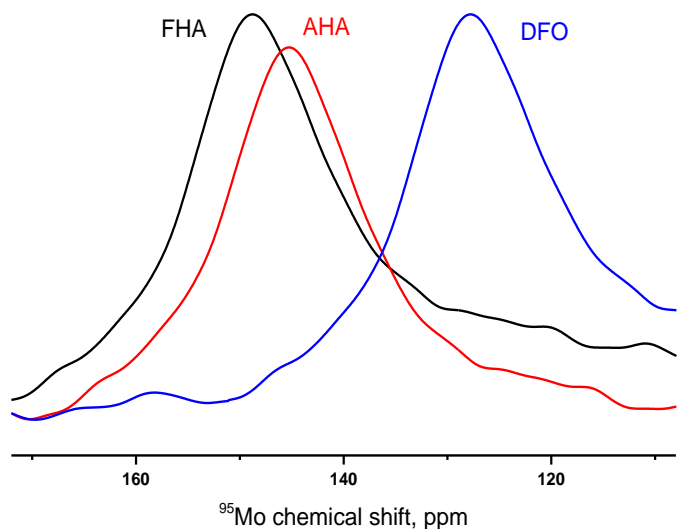


Figure 7: ^{95}Mo NMR spectra of **Mo-FHA**, **Mo-AHA** and **Mo-DFO**. 1M Na_2MoO_4 in D_2O was used as an internal standard.

While IR, NMR and UV-Vis spectroscopy identified that the complexes were formed, use of DFT and XAFS was needed to identify actual bond lengths and coordination sphere around the molybdenum in solution.

DFT Calculations of Mo-DFO

With success in obtaining a DFT structure that matched crystal structures for other molybdenum hydroxamates, our focus was given to possible coordination environments of deferoxamine around molybdenyl. Relatively high loading of the organic phase with $\text{MoO}_2(\text{NO}_3)_2 \cdot \text{HEH}[\text{EHP}]_2$ compared to the concentration of DFO in the aqueous phase, see experimental, meant that there would be only two possible metal to ligand ratios, a 1:1 or a 2:3 Mo:DFO coordination environment. The 1:1 coordination would be either a 1,2, 1,3 coordination or possibly a dimer with 2 molybdenum and 2 DFO molecules coordinated in a 1,3',3,1' fashion; prime denotes the hydroxamate site of a second DFO molecule, see Figure 8 for numbering scheme of DFO. All three structures were created and optimized, with each model illustrated in Figure 9. Using the sum of free energy from the frequency calculation, it was found that the most likely minimum energy structure is the 1,3',3,1' dimer coordination of Mo by 7.74 kcal/mol with the 1,3 monomer being close in energy by 3.47 kcal/mol, see Table 6. The relevant bond lengths are given in Table 6 and agree with both our previous molybdenyl hydroxamate DFT results and their crystal structures previously shown.

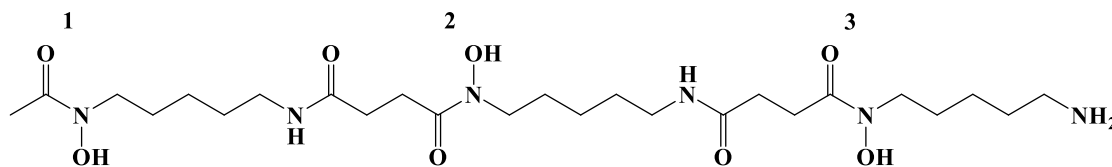


Figure 8: Numbering scheme of the hydroxamate sites on deferoxamine

The second possible coordination scheme would be two deferoxamines bonding to three molybdenum. There could either be a 1,3',2,2',3,1' motif like that of an alpha helical structure or a 1,3,2,2',3',1' binding motif, illustrated in Figure 10. Both structures were optimized and their bond lengths are given in Table 6. The free energy results in the frequency calculations showed that the non-helical structure was favored by 14 kcal/mol. The molecular skeletal structures of the 1:1 and 3:2 species that were deemed most thermodynamically stable via DFT are shown in Figure 11.

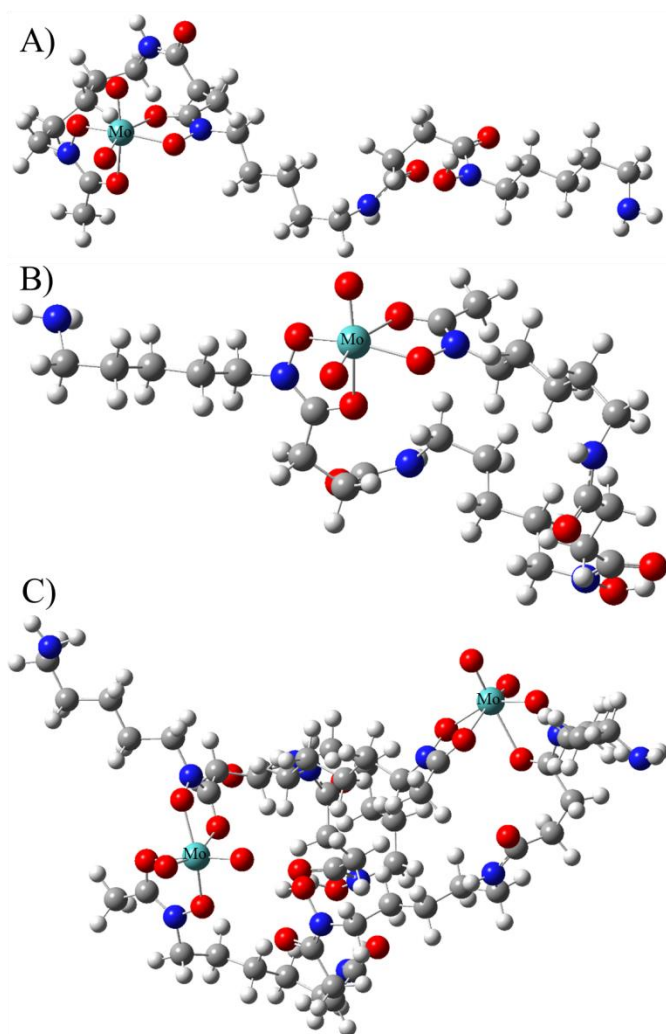


Figure 9: Optimized structures of 1:1 molybdenyl:deferoxamine in different coordination motifs. A) 1,2-MoDFO, B) 1,3-MoDFO, C) the dimer form, 1,3',3,1'-Mo₂DFO₂

Table 6: Selected bond lengths and bond angles of optimized structures, 1:1 and 3:2 molybdenum to deferoxamine. Change in free energy between the different coordination complexes is listed at the bottom of the table. The highest energy conformers are arbitrarily set to 0 for ease of comparison.

(Averages, Å, °)	1,2-MoDFO	1,3-MoDFO	1,3',3,1'-Mo₂DFO₂	1,3,2,2',1',3'-Mo₃DFO₂	1,3',2,2',3,1'-Mo₃DFO₂ (helix)
Mo-O _{oxido}	1.711	1.711	1.711	1.714	1.717
Mo-O _{hydroxyl}	2.030	2.026	2.024	2.028	2.068
Mo-O _{carbonyl}	2.286	2.288	2.271	2.268	2.218
O-Mo-O _{oxidos}	105.51	105.58	104.90	105.35	104.28
O-Mo-O _{hydroxides}	153.22	151.86	150.55	152.91	150.05
O-Mo-O _{oxido-carbonyl}	159.49	160.44	160.25	159.68	159.86
C-N	1.332	1.333	1.343	1.332	1.333
C-O	1.262	1.262	1.263	1.265	1.262
N-O	1.376	1.376	1.376	1.376	1.376
$\Delta\Delta G$ (kcal/mol)	0	-3.47	-7.74	-14.86	0

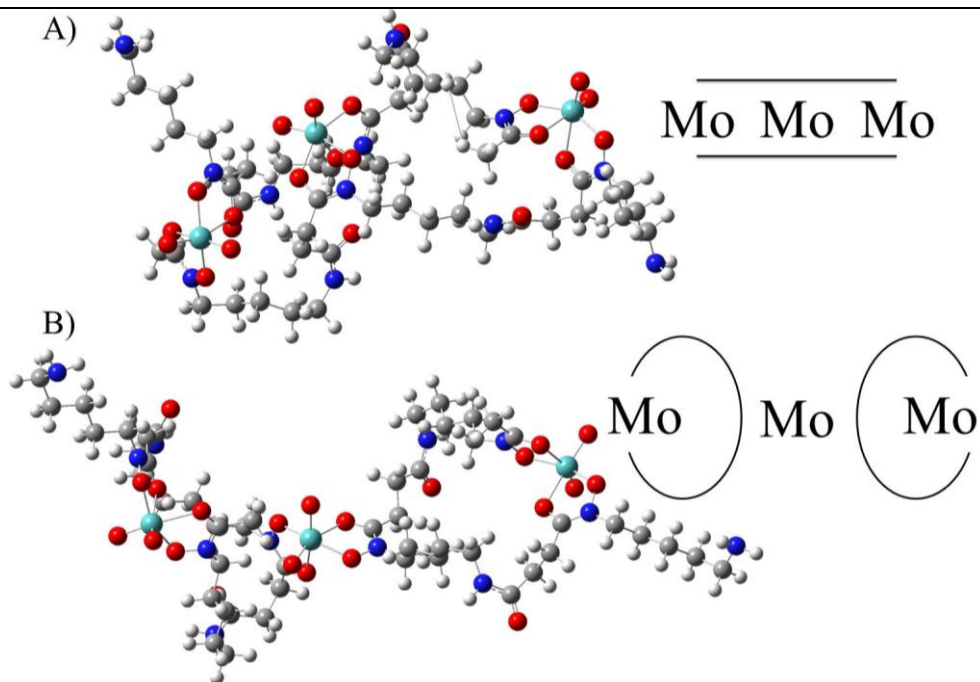


Figure 10: Optimized structures of the 3:2 molybdenyl to deferoxamine complexes. A) The helix like 1,3',2,2',3,1'-Mo₃DFO₂ as opposed to B) the bidentate 1,3,2,2',1',3'-Mo₃DFO₂.

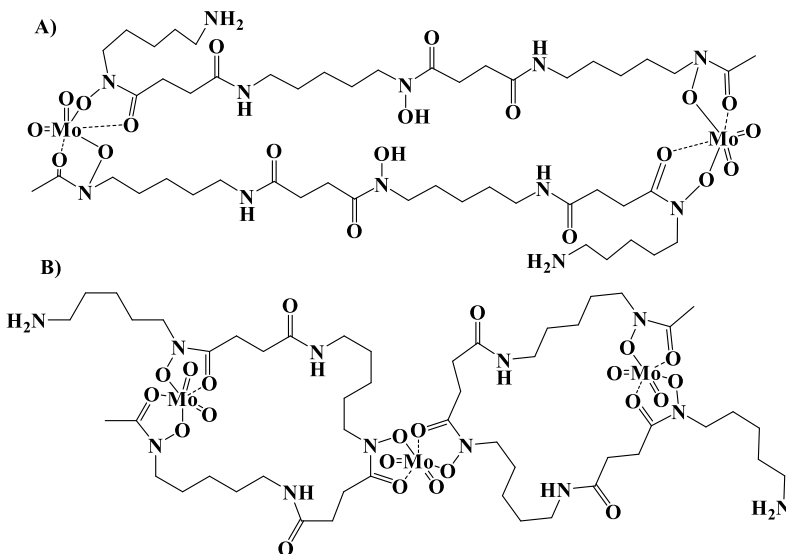


Figure 11: The skeletal structure of the 1:1 Mo to DFO dimer is shown, A, which was found to be the most 1:1 moiety stable by 4.27 kcal/mol. While B shows the skeletal structure of the most stable 3:2 Mo to DFO complex.

However, while computation gives us the most probable structure, XAFS is necessary to compare **Mo-AHA** and **Mo-DFO** to confirm the actual structure.

Electrospray Ionization Mass Spectrometry of the Mo-DFO solution

Due to the possible multiple bonding motifs that are available to deferoxamine in the presence of molybdenum, ESI-MS was employed to determine which binding mode is present, 1:1 or 3:2, and which conformer of the binding mode is present in solution.

The data for the mass spectrometry was run at a flow rate of 250 $\mu\text{L}/\text{min}$. The data showed that our highest m/z peak was at 1413, see Figure 12. As this was the highest m/z peak, there is either little possibility that a 3:2 Mo:DFO species (expected mass of 2,061

with fragment populating the > 1450 m/z range) is actually synthesized in solution or the complex is so weakly bound that ionization decomposes it rather than causing fragmentation to the DFO first. Other high m/z peaks were found at 1230, 1124, and 1002. These m/z peaks have less than 0.3% of the intensity compared to the 561 m/z peak at 100% intensity. The only peak at this range that could be fitted with high confidence was the m/z peak of 1230. This peak is best modeled as a molybdenyl that is bound to two deprotonated DFOs with the loss of a water via charge rearrangement at an oxime group to give off water. Other examples of oximes undergoing charge rearrangement to displace water has been well documented.⁵⁷ Interestingly, m/z peak of 1413 is higher than that of a Mo:DFO dimer (expected mass of 1374) but was not fit to any plausible models.

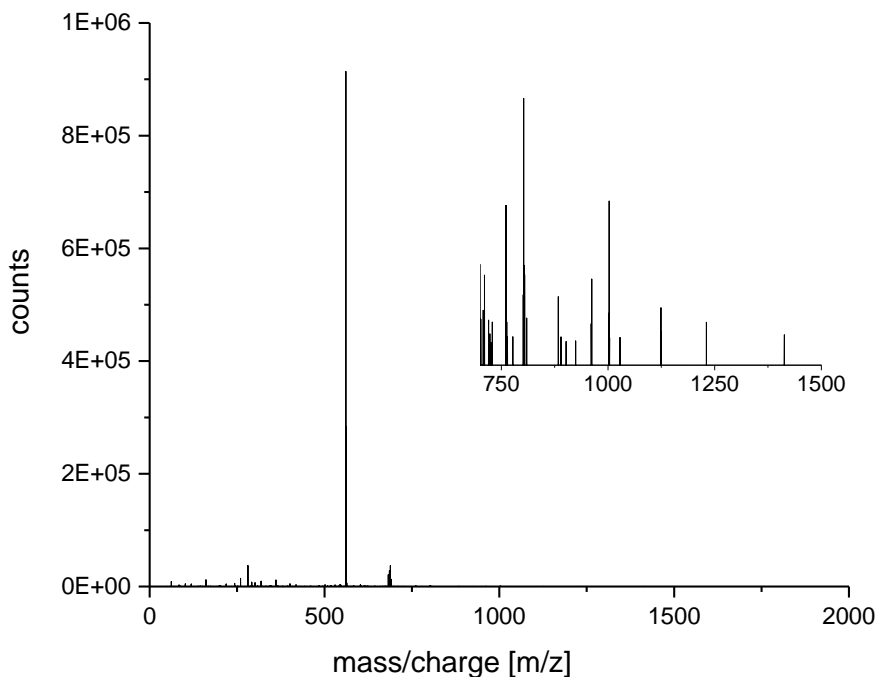


Figure 12: Mass spectrum of the DFO stripping solution post stripping of Molybdenum for the HEH[EHP]/n-dodecane organic phase.

The most telling peak with a m/z below 1002 is the m/z peak at 688 of an intensity of 4.06%, corresponds to that of $\text{MoO}_2\text{DFOH}^+$, confirming that there is a 1:1 molybdenum to deferoxamine complex being formed in solution. The 688 m/z could also be a double cationic charge on a Mo:DFO dimer, but without the ability to do tandem mass spectrometry, this is solely speculation. There is also the DFOH^+ at m/z of 561 being the highest intensity peak. This most likely corresponds to one of two possibilities, either the ESI is causing a fragmentation that causes Mo to lose DFO or there is enough free ligand in solution that the DFOH^+ species is the most prevalent. While theoretically ionization could cause degradation of the Mo-DFO species to molybdenum and deferoxamine H^+ , the small yield of Mo-DFO product (see experimental) suggests that this affect is probably small and that free ligand makes up the bulk of these counts. DFOH_2^{2+} is also present in the ESI-MS at 281 m/z . In fact, most peaks below a m/z of 561 could be accounted for as either a form of molybdenum as molybdic acid, molybdenum trioxide, or as a degradation product of DFO, which has been well characterized elsewhere.⁵⁸

Due to the lack of m/z detected above 1450, the dominance of the data by uncomplexed ligand, and the detection of the m/z of 688 corresponding to a 1:1 Mo:DFO complex, it is with high confidence that we believe that only the 1:1 complex is formed in solution and is most likely a 1,3-molybdenyl deferoxamine complex or a form of a Mo-DFO dimer.

X-ray Absorption Fluorescence Spectroscopy of Mo-AHA and Mo-DFO in solution

The K -edge $k^3\chi(k)$ XAFS, Fourier-Transform (FT), and best fits for **Mo-AHA** and **Mo-DFO** are provided in Figure 13. The coordination numbers, calculated path lengths and Debye-Waller factors are listed in Table 7. The potentials included Mo-O, Mo-N, and

Mo-C with selected multiple scatter pathways depending on the spectra. The dominant signal in each case is the peak shown around 1.2 Å (uncorrected for phase-shift), which corresponds to Mo-O pathways. Beyond this intense peak are much weaker signals that are attributed to Mo-N, Mo-C, or both, and possibly multiple scatter pathways. The Mo-N and Mo-C path lengths are considered of the same nature as the Mo-P and Mo-N path lengths seen with $\text{MoO}_2(\text{NO}_3)_2(\text{HEH}[\text{EHP}])_2$ and are outer sphere.

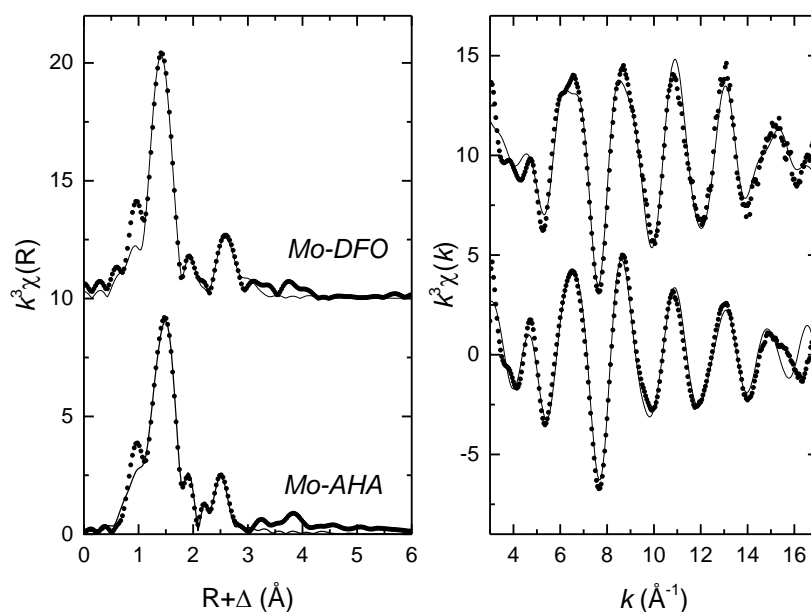


Figure 13: k^3 -Weighted molybdenum K-edge XAFS of **Mo-AHA** (bottom) and **Mo-DFO** (top) solution in n-dodecane. The points represent the experimental data; the solid line represents the model fit. The Mo-DFO spectra are shifted +10.

Table 7: Structural parameters of Mo-AHA (R-factor = 0.035), Mo-DFO (R-factor = 0.032) determined from XAFS. The amplitude reduction factor, S_0^2 , was fixed at 0.94 and the uncertainty is reported as 2σ . CN: coordination number; R: radial distance; σ^2 : Debye-Waller factor; E_0 : change in absorption edge.

R (Å)	$\sigma^2 \times 10^{-3}$ (Å ²)	ΔE_0
---------	---	--------------

<i>Mo-AHA (CN = 2)</i>			
Mo-O ₁	1.70 ± 0.01	3 ± 1	9.6 ± 3.4
Mo-O ₂	1.99 ± 0.01	0.5 ± 1	
Mo-O ₃	2.12 ± 0.02	1 ± 1	
Mo-C	2.90 ± 0.04	3 ± 4	
Mo-N	3.3 ± 0.1	9 ± 10	
<i>Mo-DFO (CN = 2; CN_C = 7)</i>			
Mo-O ₁	1.69 ± 0.01	1 ± 1	7.8 ± 7.6
Mo-O ₂	1.99 ± 0.02	1 ± 2	
Mo-O ₃	2.15 ± 0.02	5 ± 4	
Mo-N	2.92 ± 0.04	1 ± 4	
Mo-C	3.36 ± 0.08	9 ± 10	

The **Mo-AHA** *R*-spectra resemble many similarities to **MoO₂(NO₃)₂HEH[EHP]₂** with regards to multiple Mo-O pathways concealed within the dominant peak. The data were best reproduced with three distinct Mo-O interactions and Mo-N/Mo-C pathways. The first, Mo-O₁, represents the oxido ligands where the bond lengths of 1.7 Å are within the experimental uncertainty of the **Mo-AHA** single crystal XRD results. The second and third oxygen pathways represent the de-protonated hydroxyl and carbonyl groups, respectively. Overall, the XAFS results are in good agreement with the crystal structure of **Mo-AHA** except for some discrepancy between the carbon and nitrogen pathways. The signal at approximately 2.5 Å (uncorrected) is a combination of the two single-scatter paths. Based on XAFS, the Mo-N pathway is 3.3 Å from the Mo center whereas the carbon pathway was nearly 0.4 Å shorter. The crystal diffraction results are, however, swapped. It is not unreasonable to assume that the XAFS signal could confuse the signals since both pathways scatter off of a lower Z potential. Multiple refinements that individually varied a C or N pathway usually worsened the *R*-factor, but the better statistical fits were obtained by coordinating two potentials approximately 2.9 Å and 3.3 Å from the Mo absorption edge.

The **Mo-DFO** data R - and k -space are shown in Figure 13. First, and in very similar fashion to **Mo-AHA**, three Mo-oxygen interactions were concealed within the dominant peak. The potentials were also interpreted in the same manner as **Mo-AHA** with near identical results. The first striking difference between the two spectra was the significant contributions from carbon atoms in **Mo-DFO**. Visually, the distinction can be seen by the signal at 2.5 Å (uncorrected). Our fit was reasonably reproduced by fixing CN_C to seven and the effect of omitting carbon (Figure 14). This assumption, however, inherits uncertainties given that it is highly unlikely that the carbon atoms will scatter the signal to give the same results. One DFO molecule contains 25 carbon atoms and estimating the coordination geometry of each with respects to the Mo center would be exhaustive and high-risk. Nonetheless, the larger contribution of carbon scattering – relative to AHA – is the unique feature that separates the two ligands while simultaneously drawing the conclusion that DFO coordinates to Mo primarily through the hydroxamate sites.

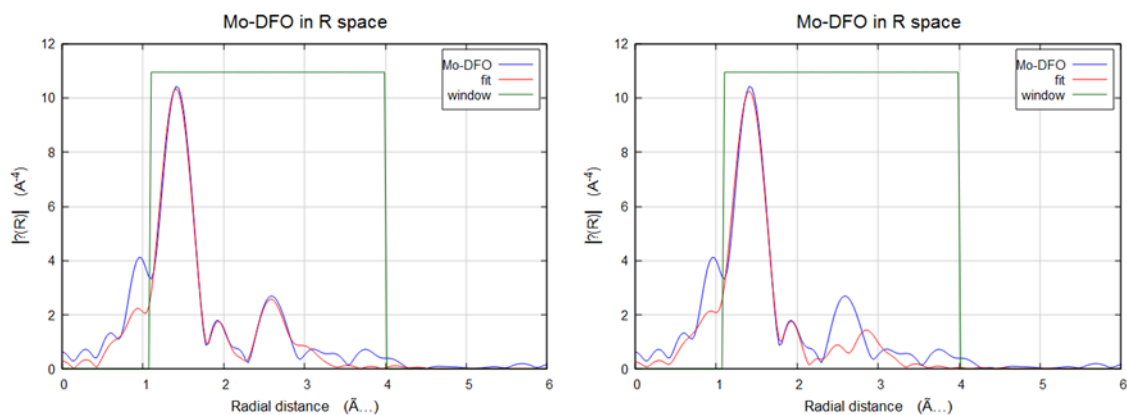


Figure 14: R-space spectra of **Mo-DFO** with (left) and without (right) carbon potentials.

Thus, examining the XAFS data in concordance with the UV-Vis, IR and NMR spectroscopy, supported by DFT calculations, gives a highly probable structure for a

molybdenum complex with a siderophore. This structure is then reinforced by comparing it to the experimental data of **Mo-FHA** and **Mo-AHA**, including single crystal XRD structures of the complexes. There is a high confidence that when DFO binds to molybdenum, it takes on the complex structure seen in Figure 9A or 11A.

Conclusion

Using HEH[EHP] in a hydrocarbon diluent as an extracting agent to deliver Mo(VI) provides a useful starting point for investigating older solution chemistry with new crystals. Examining the Mo extracted organic phase by IR, NMR spectroscopy, DFT and XAFS suggests that HEH[EHP] extracts Mo as $\text{MoO}_2(\text{NO}_3)_2$ and deprotonation of HEH[EHP] is not required.

Contacting $\text{MoO}_2(\text{NO}_3)_2\text{HEH[EHP]}_2$ with aqueous solutions of hydroxamic acids results in a new method for complex synthesis and for crystal growth at the interface- **Mo-AHA** and **Mo-FHA** crystal structures were determined via this method. However, crystals of **Mo-DFO** were unsuitable for XRD and required various spectroscopic techniques to report its coordination chemistry.

In particular, to study the speciation of **Mo-DFO**, IR, NMR, and UV-Vis spectroscopy were used to verify MoO_2^{2+} complexation. DFT calculations found the lowest energy complex and the most probable coordination environment of DFO around molybdenum. XAFS spectra of **Mo-AHA** and **Mo-DFO** were nearly identical with respects to the active oxygen bonds, suggesting that **Mo-DFO** coordination is in the same fashion as **Mo-AHA** via bonding with the carbonyl and nitrosyl oxygens, complementing our DFT results. Thus, the most probable structure of **Mo-DFO** in solution is either a 1,3-molybdenyl deferoxamine or a dimolybdenyl bisdeferoxamine complex.

Acknowledgments

I would like to thank Dr. M. Alex Brown for his coordination, collection, and modeling of the XAFS spectra. As well as his tireless help in editing and preparing this chapter. Ira Bloom was a vital part for his willingness and timely collection of the ESI mass spectrometry data. I would also like to thank, Charles Barnes, for assisting in collection of the single crystal x-ray diffraction structures and their work to complete and format the CIF files for publication. I would also like to thank Mark Silvers and Professor Thomas Albrecht-Schmitt for their helpful discussion and direction on synthesizing formohydroxamic acid. As well as, thank Dr. John Muntean for his patience and assistance with NMR spectroscopy and Dr. R. Jeremy Kropf for assistance with XAFS.

The submitted manuscript has been created by UChicago Argonne, LLC, Operator of Argonne National Laboratory (“Argonne”). Argonne, a U.S. Department of Energy Office of Science laboratory, is operated under Contract No. DE-AC02-06CH11357. The U.S. Government retains for itself, and others acting on its behalf, a paid-up nonexclusive, irrevocable worldwide license in said article to reproduce, prepare derivative works, distribute copies to the public, and perform publicly and display publicly, by or on behalf of the Government.

This work was funded by the Department of Energy – Office of Nuclear Energy, Sigma Team separations of minor actinides.

This manuscript was prepared by The Curators of the University of Missouri under award #NRC-HQ-15-G-0036, from the Office of the Chief Human Capital Officer of the Nuclear Regulatory Commission. Any statements, findings, conclusions,

and recommendations are those of the author(s) and do not necessarily reflect the view of the Outreach and Recruitment Branch or the US Nuclear Regulatory Commission. The computational chemistry for this work was performed on the high-performance computing infrastructure provided by Research Computing Support Services at the University of Missouri, Columbia, MO.

References

1. Rydberg, J.; Musikas, C.; Choppin Gregory, R., *Principles and practices of solvent extraction*. M. Dekker: New York, 1992.
2. Schulz, W. W.; Burger, L. L.; Navratil, J. D., *Science and technology of tributyl phosphate. Volume III, Volume III*. CRC Press: Boca Raton, Fla., 1990.
3. Sathish, M.; Miyazawa, K. i., Selective precipitation of tubular-like short fullerene (C60) whiskers at liquid-liquid interface. *CrystEngComm* **2010**, *12* (12), 4146-4151.
4. Ray, D. R.; Kumar, A.; Reddy, S.; Sainkar, S. R.; Pavaskar, N. R.; Sastry, M., Morphology of BaSO₄ crystals grown at the liquid-liquid interface. *CrystEngComm* **2001**, *3* (45), 213-216.
5. Jia, X.; Yang, G.; Gao, P.-Y.; Liu, W.-G.; Pan, H.-B., One-pot controlled synthesis, magnetic properties and gas response of [small alpha]-Fe₂O₃ nanostructures prepared via a liquid-liquid interface solvothermal route. *CrystEngComm* **2016**.
6. Ali, M.; Rahaman, H.; Rahman, D. S.; Nath, S.; Ghosh, S. K., Water/n-heptane interface as a viable platform for the self-assembly of ZnO nanospheres to nanorods. *CrystEngComm* **2014**, *16* (33), 7696-7700.
7. Cheng, X.-L.; Jiang, J.-S.; Hu, M.; Mao, G.-Y.; Liu, Z.-W.; Zeng, Y.; Zhang, Q.-H., Liquid-liquid interface-assisted solvothermal synthesis of durian-like [small alpha]-Fe₂O₃ hollow spheres constructed by nano-polyhedrons. *CrystEngComm* **2012**, *14* (9), 3056-3062.
8. Ghadar, Y.; Parmar, P.; Samuels, A. C.; Clark, A. E., Solutes at the liquid:liquid phase boundary—Solubility and solvent conformational response alter interfacial microsolvation. *J. Chem. Phys.* **2015**, *142* (10), 104707.
9. Ghadar, Y.; Christensen, S. L.; Clark, A. E., Influence of aqueous ionic strength upon liquid:liquid interfacial structure and microsolvation. *Fluid Phase Equilib.* **2016**, *407*, 126-134.
10. Harris, W. R.; Carrano, C. J.; Raymond, K. N., Coordination chemistry of microbial iron transport compounds. 16. Isolation, characterization, and formation constants of ferric aerobactin. *J. Am. Chem. Soc.* **1979**, *101* (10), 2722-2727.
11. Ghosh, P.; Chakravorty, A., Molybdenum complexes. 3. Bis(hydroxamates) of dioxomolybdenum(VI) and their reactions: control of redox activity by substituent effects, protic equilibria, and oxaziridine formation. *Inorg. Chem.* **1983**, *22* (9), 1322-1327.

12. Fisher, D. C.; Barclay-Peet, S. J.; Balfe, C. A.; Raymond, K. N., Synthesis and characterization of vanadium(V) and -(IV) hydroxamate complexes. X-ray crystal structures of oxochlorobis(benzohydroxamato)vanadium(V) and oxoisopropoxo(N,N'-dihydroxy-N,N'-diisopropylheptanediamido)vanadium(V). *Inorg. Chem.* **1989**, 28 (24), 4399-4406.
13. Brown, D. A.; Bögge, H.; Coogan, R.; Doocey, D.; Kemp, T. J.; Müller, A.; Neumann, B., Oxygen Abstraction Reactions of N-Substituted Hydroxamic Acids with Molybdenum(V) and Vanadium(III) and -(IV) Compounds. *Inorg. Chem.* **1996**, 35 (6), 1674-1679.
14. Farkas, E.; Csoka, H.; Toth, I., New insights into the solution equilibrium of molybdenum(vi)-hydroxamate systems: ¹H and ¹⁷O NMR spectroscopic study of Mo(vi)-desferrioxamine B and Mo(vi)-monohydroxamic acid systems. *Dalton Trans.* **2003**, (8), 1645-1652.
15. Tejada-Jimenez, M.; Chamizo-Ampudia, A.; Galvan, A.; Fernandez, E.; Llamas, A., Molybdenum metabolism in plants. *Metallomics* **2013**, 5 (9), 1191-1203.
16. Sugimoto, H.; Sato, M.; Asano, K.; Suzuki, T.; Mieda, K.; Ogura, T.; Matsumoto, T.; Giles, L. J.; Pokhrel, A.; Kirk, M. L.; Itoh, S., A Model for the Active-Site Formation Process in DMSO Reductase Family Molybdenum Enzymes Involving Oxido-Alcoholato and Oxido-Thiolato Molybdenum(VI) Core Structures. *Inorg. Chem.* **2016**, 55 (4), 1542-1550.
17. Farkas, E.; Megyeri, K.; Somsák, L.; Kovács, L., Interaction between Mo(VI) and siderophore models in aqueous solution. *J. Inorg. Biochem.* **1998**, 70 (1), 41-47.
18. Koide, Y. U., M.Shosenji, H.Yamada, K., Studies of Collectors. X. Complexing Ability of Amino Hydroxamic Acid Ligands with Dioxouranium(VI) in Aqueous Solution. *Bull. Chem. Soc. Jpn.* **1989**, 62 (11), 3714-3715.
19. Taylor, R. J.; May, I.; Wallwork, A. L.; Denniss, I. S.; Hill, N. J.; Galkin, B. Y.; Zilberman, B. Y.; Fedorov, Y. S., The applications of formo- and aceto-hydroxamic acids in nuclear fuel reprocessing. *J. Alloys Compd.* **1998**, 271-273, 534-537.
20. Tkac, P.; Matteson, B.; Brusio, J.; Paulenova, A., Complexation of uranium(VI) with acetohydroxamic acid. *J. Radioanal. Nuc. Chem.* **2008**, 277 (1), 31-36.
21. Tkac, P.; Paulenova, A., The Effect of Acetohydroxamic Acid on Extraction and Speciation of Plutonium. *Sep. Sci. Technol.* **2008**, 43 (9-10), 2670-2683.
22. Silver, M. A.; Dorfner, W. L.; Cary, S. K.; Cross, J. N.; Lin, J.; Schelter, E. J.; Albrecht-Schmitt, T. E., Why Is Uranyl Formohydroxamate Red? *Inorg. Chem.* **2015**, 54 (11), 5280-5284.

23. John, S. G.; Ruggiero, C. E.; Hersman, L. E.; Tung, C.-S.; Neu, M. P., Siderophore Mediated Plutonium Accumulation by *Microbacterium flavescens* (JG-9). *Environ. Sci. Technol.* **2001**, *35* (14), 2942-2948.
24. Hu, Z.; Pan, Y.; Ma, W.; Fu, X., Purification of organophosphorus acid extractants. *Solvent Ext. Ion Exch.* **1995**, *13*, 965.
25. Fishbein, W. N.; Daly, J.; Streeter, C. L., Preparation and some properties of stable and carbon-14 and tritium-labeled short-chain aliphatic hydroxamic acids. *Anal. Biochem.* **1969**, *28*, 13-24.
26. Apex II suite, B. A. L., 2006, Madison, WS.
27. Sheldrick, G., *Acta Cryst. A* **2008**, *64*, 112.
28. Barbour, L. J., *J. Supramol. Chem.* **2001**, *1*, 189.
29. Frisch, M. J.; Trucks, G. W.; Schlegel, H. B.; Scuseria, G. E.; Robb, M. A.; Cheeseman, J. R.; Scalmani, G.; Barone, V.; Mennucci, B.; Petersson, G. A.; Nakatsuji, H.; Caricato, M.; Li, X.; Hratchian, H. P.; Izmaylov, A. F.; Bloino, J.; Zheng, G.; Sonnenberg, J. L.; Hada, M.; Ehara, M.; Toyota, K.; Fukuda, R.; Hasegawa, J.; Ishida, M.; Nakajima, T.; Honda, Y.; Kitao, O.; Nakai, H.; Vreven, T.; Montgomery Jr., J. A.; Peralta, J. E.; Ogliaro, F.; Bearpark, M. J.; Heyd, J.; Brothers, E. N.; Kudin, K. N.; Staroverov, V. N.; Kobayashi, R.; Normand, J.; Raghavachari, K.; Rendell, A. P.; Burant, J. C.; Iyengar, S. S.; Tomasi, J.; Cossi, M.; Rega, N.; Millam, N. J.; Klene, M.; Knox, J. E.; Cross, J. B.; Bakken, V.; Adamo, C.; Jaramillo, J.; Gomperts, R.; Stratmann, R. E.; Yazyev, O.; Austin, A. J.; Cammi, R.; Pomelli, C.; Ochterski, J. W.; Martin, R. L.; Morokuma, K.; Zakrzewski, V. G.; Voth, G. A.; Salvador, P.; Dannenberg, J. J.; Dapprich, S.; Daniels, A. D.; Farkas, Ö.; Foresman, J. B.; Ortiz, J. V.; Cioslowski, J.; Fox, D. J. *Gaussian 09*, Gaussian, Inc.: Wallingford, CT, USA, 2009.
30. Stephens, P. J.; Devlin, F. J.; Chabalowski, C. F.; Frisch, M. J., *J. Phys. Chem.* **1994**, *98*, 11623.
31. Becke, A. D., *J. Chem. Phys.* **1993**, *98*, 5648.
32. Lee, C.; Yang, W.; Parr, R. G., *Phys. Rev. B* **1988**, *37*, 785.
33. Bergner, A.; Dolg, M.; Küchle, W.; Stoll, H.; Preuß, H., Ab initio energy-adjusted pseudopotentials for elements of groups 13–17. *Mole. Phys.* **1993**, *80* (6), 1431-1441.
34. Dolg, M.; Stoll, H.; Preuss, H.; Pitzer, R. M., Relativistic and correlation effects for element 105 (hahnium, Ha): a comparative study of M and MO (M = Nb, Ta, Ha) using energy-adjusted ab initio pseudopotentials. *J. Phys. Chem.* **1993**, *97* (22), 5852-5859.

35. Hariharan, P. C.; Pople, J. A., *Theor. Chim. Acta* **1973**, 28, 213.
36. Francl, M. M.; Pietro, W. J.; Hehre, W. J.; Binkley, J. S.; Gordon, M. S.; DeFrees, D. J.; Pople, J. A., *J. Chem. Phys.* **1982**, 77, 3654.
37. Kraft, S.; Stümpel, J.; Becker, P.; Kuetgens, U., High resolution x-ray absorption spectroscopy with absolute energy calibration for the determination of absorption edge energies. *Rev. Sci. Instr.* **1996**, 67 (3), 681-687.
38. X-ray Data Booklet. Center for X-ray Optics and Advanced Light Source, X-ray Data Booklet, Lawrence Berkeley National Lab, CA, October, 2009.
39. Newville, M., IFEFFIT: Interactive XAFS Analysis and FEFF Fitting. . *J. Synch. Rad.* **2001**, 8, 322-324.
40. Ravel, B.; Newville, M., ATHENA, ARTEMIS, HEPHAESTUS: Data Analysis for X-ray Absorption Spectroscopy Using IFEFFIT. *J. Synch. Rad.* **2005**, 12, 537-541.
41. Sykora, R. E.; Ok, K. M.; Halasyamani, P. S.; Albrecht-Schmitt, T. E., Structural Modulation of Molybdenyl Iodate Architectures by Alkali Metal Cations in AMoO₃(IO₃) (A = K, Rb, Cs): A Facile Route to New Polar Materials with Large SHG Responses. *J. Am. Chem. Soc.* **2002**, 124 (9), 1951-1957.
42. Pretsch, E.; Bühlmann, P.; Badertscher, M., IR Spectroscopy. In *Structure Determination of Organic Compounds: Tables of Spectral Data*, Springer Berlin; Berlin, Heidelberg, 2009; pp 1-67.
43. Gannaz, B.; Antonio, M. R.; Chiarizia, R.; Hill, C.; Cote, G., Structural Study of Trivalent Lanthanide and Actinide Complexes Formed Upon Solvent Extraction. . *Dalton Trans.* **2006**, 4553-4562.
44. Cocalia, V. A.; Jensen, M. P.; Holbrey, J. D.; Spear, S. K.; Stepinski, D. C.; Rogers, R. D., Identical Extraction Behavior and Coordination of Trivalent or Hexavalent f-Element Cations Using Ionic Liquid and Molecular Solvents. *Dalton Trans.* **2005**, 1966-1971.
45. Skanthakumar, S.; Antonio, M. R.; Wilson, R. E.; Soderholm, L., The Curium Aqua Ion. *Inorg. Chem.* **2007**, 46 (9), 3485-3491.
46. Chatterjee, B., Donor properties of hydroxamic acids. *Coord. Chem. Rev.* **1978**, 26 (3), 281-303.
47. Paul, S. S.; Selim, M.; Saha, A.; Mukherjea, K. K., Synthesis and structural characterization of dioxomolybdenum and dioxotungsten hydroxamato complexes and their function in the protection of radiation induced DNA damage. *Dalton Trans.* **2014**, 43 (7), 2835-2848.

48. Lin, S. P.; Khan, M. A.; Nicholas, K. M., Unexpected formation of a novel mixed hydroxamato/hydroximato complex. *J. Chem. Soc., Chem. Commun.* **1994**, (21), 2425-2426.
49. Dutta, R. L.; Chatterjee, B., Molybdenum: Part III. Dioxo Molybdenum (VI) Complexes with Hydroxamic Acids. *J. Indian Chem. Soc.* **1967**, *44* (9), 780-786.
50. Kurzak, B.; Kozłowski, H.; Farkas, E., Hydroxamic and aminohydroxamic acids and their complexes with metal ions. *Coord. Chem. Rev.* **1992**, *114* (2), 169-200.
51. Wieghardt, K.; Holzbach, W.; Hofer, E.; Weiss, J., Complexes of (hydroxylamido-O,N)molybdenum(VI). Preparation and crystal structures of dicesium bis(benzohydroximato)-cis-dioxomolybdate(VI) hydrate and of (benzohydroxamato)(benzohydroximato)(N,N-dimethylhydroxylamido-O,N)oxomolybdenum(VI). *Inorg. Chem.* **1981**, *20* (2), 343-348.
52. Dzyuba, V. I.; Koval, L. I.; Bon, V. V.; Pekhnyo, V. I., Synthesis and structure of lipophilic dioxo-molybdenum (VI) bis(hydroxamato) complexes. *Polyhedron* **2010**, *29* (15), 2900-2906.
53. Farkas, E.; Csoka, H.; Bell, G.; A. Brown, D.; P. Cuffe, L.; J. Fitzpatrick, N.; K. Glass, W.; Errington, W.; J. Kemp, T., Oxygen versus nitrogen co-ordination in complexes of MoVI and hydroxamate derivatives of [small alpha]-amino acids: equilibrium, structural and theoretical studies. *J. Chem. Soc., Dalton Trans.*, **1999**, (16), 2789-2794.
54. Neu, M. P.; Matonic, J. H.; Ruggiero, C. E.; Scott, B. L., Structural Characterization of a Plutonium(IV) Siderophore Complex: Single-Crystal Structure of Pu-Desferrioxamine E. *Angew. Chem. Int. Ed.* **2000**, *39* (8), 1442-1444.
55. Farkas, E.; Csóka, H.; Micera, G.; Dessi, A., Copper(II), nickel(II), zinc(II), and molybdenum(VI) complexes of desferrioxamine B in aqueous solution. *J. Inorg. Biochem.* **1997**, *65* (4), 281-286.
56. Paviet-Hartmann, P. W., A.; Mausolf, E.; Campbell, K.; Poineau, F., Application of Formohydroxamic Acid in Nuclear Processing: Synthesis and Complexation With Technetium-99. In *18th International Conference on Nuclear Engineering*, Xi'an, China, 2010; Vol. 1, pp 387-391.
57. McLafferty, F. W.; Turecek, F., *Interpretation of mass spectra*. University Science Books: Sausalito, Calif., 1993.
58. Groenewold, G. S.; Van Stipdonk, M. J.; Gresham, G. L.; Chien, W.; Bulleigh, K.; Howard, A., Collision-induced dissociation tandem mass spectrometry of

desferrioxamine siderophore complexes from electrospray ionization of UO_2^{2+} , Fe^{3+} and Ca^{2+} solutions. *J. Mass Spectrom.* **2004**, 39 (7), 752-761.

Appendix A: Possible profits from reprocessing of spent fuel from LWRs, Th-FBR, and LMFBR via aqueous reprocessing and pyroprocessing

Abstract

This work explores the economic viability of recovering fission products to off-set the cost of reprocessing spent nuclear fuel. The calculations found that a few of the elements that make up the fission products had significant value and were produced in high enough quantity that a profit was possible. Both thermal and fast reactors were explored, with those reactors using either U-233, U-235, or Pu-239 as the fissile isotope in their fuel. This report revealed that a fast reactor with a Pu-239 fuel was the most advantageous for profit at 5.09 million dollars per metric ton of heavy metal that was reprocessed. This work also corrected for neutron absorption of fission products and decay for the case of a thermal reactor with U-235 fuel and found that it did influence the gross profit, decreasing it by 0.42 %.

Scope of Impact

This work supports the economic case for reprocessing. Until now, the economics of reprocessing focused on profit gained from recycling uranium and plutonium to be reused as fuel for reactors. However, with the abundance of uranium ore (primarily from foreign suppliers and MOX fuel from dismantled and blended down nuclear weapons) there was little monetary incentive to reprocess for the sake of reusing reactor fuel. This work instead focused on both the recovery of fissionable actinides for new reactor fuel

and the value of the fission product raffinate for industrial use given the current estimates for the cost of a new reprocessing facility and its operation.

Introduction

Off-setting the cost of reprocessing would be necessary if investment (private or public) was to be ascertained.¹ Domestic policy is aligned with the idea of reducing the waste footprint, the efficient utilization of scarce resources and pathways to a more diverse energy portfolio. However, the prices and the amount of capital needed to accomplish these goals could be prohibitive. If so, the free market would not support this policy since it becomes too exorbitant to pursue.²⁻⁵ Alternatively, if an off-setting cost or return on investment (ROI) could be realized, and if it is on par with the ROI of pursuing other technologies, then barriers to investment would be greatly reduced.⁵⁻⁶

This report examines the modeling of U and Pu recovery for use to offset the cost of new fuel in reactors. While fission products could be sold to offset the cost, only certain fission products would be viable due to the long residence time in spent fuel pools to allow for high activity isotopes to decay and to dissipate decay heat. This work focused on longer wait times (10 to 100 years) before attempting to recover fission products from spent fuel. This approach ruled out the harvesting of medical isotopes and other short-lived isotopes to offset costs and will not be examined in this report.⁷

Recovery of fissile material and fission products

This work assumed that the major fissile atoms in each fuel cycle are U-233, U-235 and Pu-239. While larger atomic mass transuranics are produced during high burn-up and are fissionable under high energy, high-flux conditions, they are not a significant contributor to fission events within the reactor.⁸ The transuranics are more likely to be

produced in thermal neutron flux reactors, with fissioning of those transuranics accounting for <4% for a burn-up of 40 MWD/kg and <15% for 70 MWD/kg.⁹ In fast reactors, the higher energy neutron flux reduced the amount of transuranic build up by increasing the probability of fission in transuranics.⁹ Thus, this work assumed that the fission yields were entirely from U-233, U-235 and Pu-239 in either a thermal or fast neutron reactor. The JENDL fission product files gave the fission product yield in atom percent of each fissile isotope in both thermal and fast neutron flux.¹⁰ Lamarsh stated in Chapter 3 of his textbook that the number of fissions per day per megawatt thermal was 2.7 times ten to the 21st (2.70×10^{21}).¹¹ Even with absorption of neutrons, no other neutron interactions are considered in the fission calculations since fission is the sole producer at full power reactor thermal energy. Each fission event produces two different fission product atoms. Three-body fission does occur but the probability was low and could be ignored for simplicity. Thus, this work assumed that each mole of fissioned atoms would produce two moles of fission products. As stated previously, energy released by the fission event was paramount, as this event produced the heat in a reactor, but this energy came from mass converting to energy. This energy was isotope dependent, but for the calculations of this paper, was assumed to be ~200 MeV per fission event. However, 200 MeV converted into mass is less than 0.1 amu and was negligible in calculating the total mass of fission products.¹² The atom percentage from the JENDL fission product data was multiplied by the moles of fission products to obtain the number of moles of each fission product produced. This was calculated and reported in Table 1 as moles of isotope produced as a function of moles per year per gigawatt-thermal.

Table 1: Mass of fission products present in spent nuclear fuel as a function of moles per gigawatt-thermal per year. Mass was calculated using the JENDL data multiplied by the moles of fission products from LaMarsh's *Introduction to Nuclear Engineering* (see previous paragraph).¹⁰⁻¹²

	U-233		U-235		Pu-239	
	Thermal mol/yr GWt	Fast mol/yr GWt	Thermal mol/yr GWt	Fast mol/yr GWt	Thermal mol/yr GWt	Fast mol/yr GWt
V	1.68E-15	1.31E-15	6.69E-16	1.45E-14	0.00E+00	1.18E-14
Cr	9.32E-11	7.62E-11	9.39E-11	1.47E-09	1.66E-11	3.25E-10
Mn	5.34E-08	5.56E-08	4.36E-08	5.04E-07	1.52E-08	1.96E-07
Fe	9.96E-06	1.10E-05	5.31E-06	4.34E-05	2.50E-06	2.46E-05
Co	1.99E-04	2.25E-04	5.16E-05	3.52E-04	5.61E-05	4.61E-04
Ni	7.13E-03	8.03E-03	1.04E-03	6.62E-03	1.20E-03	7.99E-03
Cu	5.98E-02	6.91E-02	1.34E-02	6.92E-02	1.05E-02	4.47E-02
Zn	8.36E-01	9.34E-01	4.04E-01	1.40E+00	1.27E-01	3.39E-01
Ga	3.15E+00	3.46E+00	2.69E+00	5.03E+00	8.67E-01	1.64E+00
Ge	2.26E+01	2.03E+01	1.79E+01	2.57E+01	6.97E+00	9.22E+00
As	6.53E+01	5.60E+01	4.83E+01	5.61E+01	2.18E+01	2.49E+01
Se	2.14E+02	2.22E+02	1.69E+02	2.01E+02	7.25E+01	7.71E+01
Br	3.84E+02	3.95E+02	3.23E+02	3.74E+02	1.32E+02	1.35E+02
Kr	9.96E+02	9.71E+02	8.49E+02	8.13E+02	2.82E+02	3.09E+02
Rb	1.19E+03	1.14E+03	1.12E+03	1.08E+03	4.35E+02	4.46E+02
Sr	1.75E+03	1.72E+03	1.71E+03	1.71E+03	8.13E+02	8.25E+02
Y	2.05E+03	2.00E+03	2.12E+03	2.13E+03	1.24E+03	1.23E+03
Zr	2.14E+03	2.09E+03	2.36E+03	2.36E+03	1.66E+03	1.65E+03
Nb	1.66E+03	1.65E+03	1.99E+03	2.01E+03	1.85E+03	1.86E+03
Mo	1.16E+03	1.20E+03	1.52E+03	1.55E+03	1.98E+03	1.98E+03
Tc	5.98E+02	6.56E+02	8.95E+02	9.18E+02	1.64E+03	1.66E+03
Ru	4.59E+02	5.27E+02	7.20E+02	7.50E+02	1.61E+03	1.63E+03
Rh	1.41E+02	1.74E+02	2.60E+02	3.00E+02	1.10E+03	1.06E+03
Pd	3.63E+01	6.57E+01	5.63E+01	8.42E+01	5.99E+02	5.76E+02
Ag	1.14E+01	3.11E+01	1.16E+01	2.77E+01	2.41E+02	2.22E+02
Cd	6.24E+00	2.34E+01	9.56E+00	1.43E+01	2.72E+01	3.95E+01
In	1.73E+01	2.84E+01	1.51E+01	3.65E+01	2.15E+01	3.07E+01
Sn	1.59E+02	2.14E+02	1.60E+02	2.32E+02	1.73E+02	2.00E+02
At	3.15E+02	3.81E+02	3.96E+02	4.47E+02	4.05E+02	4.10E+02
Te	8.75E+02	9.18E+02	9.83E+02	9.86E+02	9.50E+02	9.58E+02
I	1.13E+03	1.16E+03	1.27E+03	1.28E+03	1.35E+03	1.32E+03
Xe	1.75E+03	1.80E+03	1.94E+03	1.88E+03	1.92E+03	1.88E+03

Cs	1.34E+03	1.35E+03	1.54E+03	1.54E+03	1.40E+03	1.40E+03
Ba	1.94E+03	1.88E+03	2.04E+03	1.99E+03	1.78E+03	1.76E+03
La	1.35E+03	1.24E+03	1.41E+03	1.39E+03	1.11E+03	1.09E+03
Ce	1.30E+03	1.20E+03	1.34E+03	1.31E+03	1.08E+03	1.07E+03
Pr	9.02E+02	8.42E+02	9.90E+02	9.64E+02	8.20E+02	8.14E+02
Nd	7.07E+02	6.57E+02	8.13E+02	7.83E+02	6.93E+02	6.95E+02
Pm	1.05E+02	1.00E+02	1.40E+02	1.35E+02	1.76E+02	1.84E+02
Sm	1.05E+02	1.01E+02	1.40E+02	1.35E+02	1.82E+02	1.92E+02
Eu	1.50E+01	1.52E+01	2.05E+01	2.11E+01	5.00E+01	5.88E+01
Gd	1.43E+00	1.83E+00	1.89E+00	2.64E+00	1.45E+01	1.99E+01
Tb	3.35E-02	6.09E-02	3.65E-02	1.11E-01	9.53E-01	1.95E+00
Dy	4.69E-03	4.42E-03	3.64E-03	1.34E-02	2.83E-01	7.29E-01
Ho	3.49E-05	6.39E-05	5.38E-05	1.24E-04	7.27E-03	6.26E-02
Er	1.45E-05	2.65E-05	2.38E-05	5.10E-05	2.94E-03	3.42E-02
Tm	1.63E-07	3.03E-07	8.80E-07	2.15E-06	5.49E-05	9.53E-04
Yb	1.95E-08	3.40E-08	1.02E-07	2.80E-07	6.75E-06	1.09E-04
Lu	0.00E+00	8.28E-16	0.00E+00	0.00E+00	0.00E+00	2.24E-12

The profit from recovering the U and Pu for use as reactor fuel would be entirely dependent on the type of reactor from which the spent fuel was reprocessed and the amount of fuel reprocessed per GWt. Not every reactor has the same conversion or breeding coefficient. On average, LWRs have a conversion factor of less than one, while breeder reactors have a conversion factor of greater than one.¹² This work assumed that fuel reprocessed would have an average conversion factor of one. In addition, each reactor and its core design would have the greatest effect on the amount of fuel discharged and its burn-up. Previous DOE reports reported that on average, the discharge of spent fuel for an LWR and LMFBR is 4.5 and 2.85 metric tons of heavy metal per gigawatt-thermal, respectively.¹² This amount of spent fuel would dictate the total reprocessing mass flow needed for a reprocessing plant in terms of gigawatt thermals per year, e.g. how many reactors would be able to reprocess using a reprocessing plant and the total potential fuel and fission products recoverable by the same plant.

After fuel has been irradiated in a reactor, the fuel is removed and allowed to cool. After cooling for a sufficient amount time the fuel is reprocessed to recover U, Pu, other transuranics (TRU) and fission products (FP). The two overarching reprocessing techniques employed in spent fuel reprocessing are aqueous reprocessing and pyroprocessing. Aqueous reprocessing requires that the spent fuel be in a form that allows for nitric acid dissolution. The spent fuel that under goes this process is usually in the form of oxide fuel. Pyroprocessing requires that the spent fuel be in metallic form for electrorefining. Although each technique has a necessary input form, chemical conversion between the oxide fuel and metallic fuel or vice versa is simple and only requires an extra step before feeding the spent fuel into a reprocessing stream.¹³

For aqueous reprocessing, to access and isolate fission products, it is imperative to separate out the major mass contributions prior to reprocessing. In this case, the major mass contributors for uranium-based LWR spent fuel are uranium and plutonium. The major contributors for Th-U based light and heavy water converter or breeder fuel are uranium and thorium. To accomplish this for the U-Pu spent fuel, the PUREX process can be used to remove ~97% of starting spent fuel mass, leaving a lower mass of fission products and minor actinides which are subsequently sent to a different process. A simple PUREX flow diagram is shown in Figure 1.

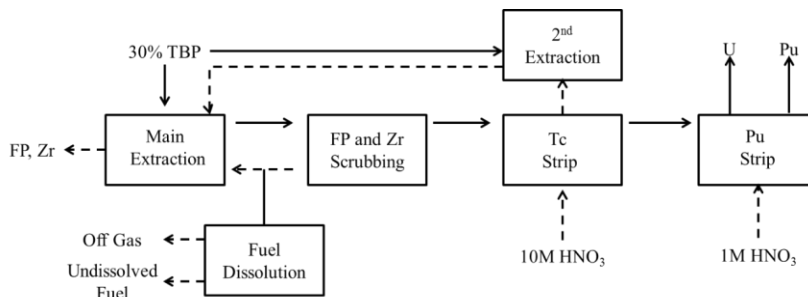


Figure 1: Basic flow diagram of PUREX process.

Th-U spent fuel could be reprocessed in a similar way to U-Pu spent fuel using the THOREX process, which removes Th and U while leaving a fission product stream. In most descriptions of the PUREX and THOREX fuel cycle, the fission products that were stripped from the extraction product were usually left to be transformed into a different waste form for storage in a repository.¹⁴ However, in this scenario, this stream of fission products would undergo further aqueous reprocessing to isolate and separate the desired fission products for recovery and trade on the free market.

The pyroprocessing technique facilitates the same separation of the large quantity of mass in the form of U, Pu and other transuranics from fission products, see Till and Chang's *Plentiful Energy*.¹⁰ In pyroprocessing, the spent metallic fuel is loaded into the electrorefiner and a current is passed through it with molten salts as the electrolyte. Uranium and transuranics plate out as a dendrite onto the cathode, while noble metal fission products and fuel-cladding stayed in the anode basket used to introduce the spent fuel into the electrorefiner. Fission products that dissolved in the molten salt were transported through a zeolite filter, where the soluble fission products were collected as chloride salts in the zeolite. After the electrorefining, the fission products in either metal or salt form underwent vitrification for long-term storage.

In this scenario of recovering the fission products, the noble metal fission products could be collected and dissolved in nitric acid after removal from the electrorefiner. The zeolite filters that have trapped the fission product salts could be dissolved in either hot alkaline solution or in hydrofluoric acid. The possible issue with alkaline dissolution is that many of the fission products and dissolved zeolite could become refractory oxides and hydroxides. The fission products not trapped with the

zeolite refractory oxide formation could be dissolved in nitric acid and treated much like the PUREX fission product stream. The hydrofluoric acid, fission-product, zeolite dissolution stream could be converted to a PUREX-like fission product stream by adding an alkali earth metal nitrate, i.e. $\text{Ba}(\text{NO}_3)_3$ or $\text{Ca}(\text{NO}_3)_3$. The HF would undergo double displacement forming nitric acid and insoluble barium or calcium salts, which could then be recovered as a solid from the aqueous stream. See Figure 2 for an overview of pyroprocessing and fission product recovery.

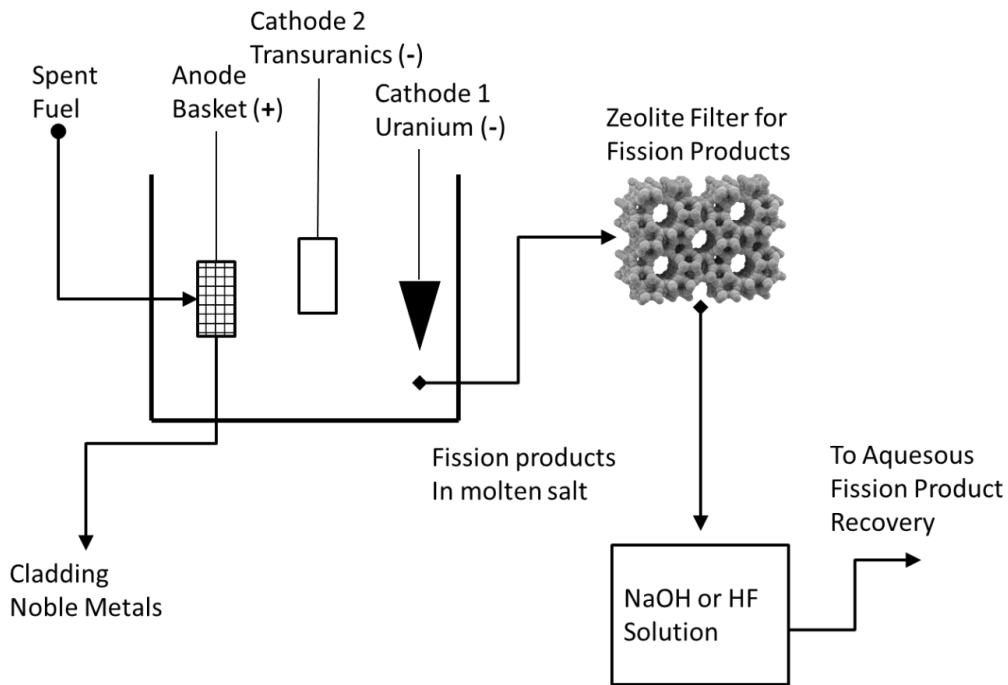


Figure 2: Fission Product recovery in a pyroprocessing diagram

Waste disposal cost and effect on profits

Due to the nature of reprocessing, waste would be produced and would need to be treated in the same manner as was done with spent fuel from nuclear power plants, or low-level or mixed wastes from the DOE national laboratories. Paying either the NRC or DOE to facilitate and control all spent waste would be a liability to those that reprocess.

There are three unknowns to deal with: the volume of the waste, nature of the waste, and the cost per unit volume charged by the NRC or DOE to dispose of the discharged waste.

The issue with the volume and the nature of waste is entirely impacted by the reprocessing scheme and technology used per unit of spent fuel reprocessed. Both factors vary widely between reprocessing schemes alone. For example, in the most recent SACSESS report, technologies such as TRUEX reported up to three times as much volume of waste as input.¹⁵ The report also showed that other technologies have a technical readiness level (TRL) so low that the volume of waste and its final designation (LLW, MW or TRU) was still unknown.

The cost per unit of waste depends entirely on whether the final recipient of the waste would be either the NRC or DOE. More than likely the final recipient would be the DOE, however, as of this writing the NRC collects the funds for civilian disposal of spent nuclear fuel and is in control of the repository. For the NRC, current cost for disposing of unwanted spent fuel is 1/10 cent per kWh of electricity produced. This would be problematic for a reprocessing plant where electricity production as a form of payment would be entirely too inaccurate to estimate the cost of disposal. This would open the possibility of power utilities paying the cost for the disposal of waste and the company in charge of reprocessing then pays for the spent fuel. Alternatively, power utility companies could eliminate their current waste costs by creating a new agreement between the reprocessing companies and the NRC. However, this would require rewriting of the law. If a law were passed, this might create a lack of uniformity on the monetary side of agreements between the individual power utilities and the reprocessing company complicates the ability to predict the final cost and the structure such an agreement might

take, since the addition of the NRC agreements to the current two parties' agreements makes it a complicated three-party agreement. Trying to predict the effects of such an agreement between the three parties and the cost to just one party would be entirely unpredictable.

However, using the current cost model of the DOE created an easier method to predict cost. Granted that the DOE handles cost of radioactive waste disposal solely from military and national laboratory sites and would not enter a civilian agreement. The DOE model for costs is straightforward and available to use in this work. Currently it costs a project \$37.20 per L to dispose of low-level waste (LLW), \$193.03 per L of mixed waste (MW) and transuranic waste (TRU), (March of 2017, Argonne National Lab). Using the SACSESS road map and if most reprocessing schemes match the TRUEX reprocessing scheme for waste, reprocessing would produce 2 L of LLW and 1 L of TRU per 1 L of feed. In this case, original ORNL documentation reported that 1 metric ton of spent fuel would dissolve in 3000 L of nitric acid dissolver solution.¹⁶⁻¹⁷ The dissolver solution was diluted with scrubbing steps in correlation of the fission product and transuranic containing raffinate from COEX. This addition of scrubbing steps gives a 1:2 correlation on dissolver solution to feed for advanced reprocessing. Thus, the volume of waste per metric ton of spent fuel would comprise of 12000 L of LLW and 6000 L of TRU waste, and the cost would be \$1,604,580 per metric ton of spent fuel using DOE standards for disposal cost. This method will be considered later when determining "average" profit for a reprocessing plant.

Expected returns from fissile material and isolation of the top three fission products

The total return from fission products would be a function of their market price and the amount produced (assuming a 100% recovery). The market prices are compiled for each possible fission product element and are listed in Table 2. Using Tables 1 and 2, the total possible return from recovery for each isotope were calculated and the results are listed in Table 3. The calculation results revealed that the most effective return could be made from recovering strontium, barium and lanthanide from fissile uranium based reactor fuel, and fissile plutonium based reactor fuel it was found that rhodium, palladium and barium would produce the most profit from the fission product stream.

Table 2: Market prices of each fission product element as of early February, 2017.

Market price		London Metal Exchange (Norm materials only, not priced for radioisotopes)		
Z	Name	Kg/Kmol	Price per Kg (2017 USD)	Form
23	Vanadium	50.94	19.33	Ferro Vanadium
24	Chromium	52	1.94	Ferro chrome
25	Manganese	54.94	1.65	Ingot
26	Iron	55.85	0.09	Metal pellets
27	Cobalt	58.93	26.72	Ingot
28	Nickel	58.69	10.31	Ingot
29	Copper	63.55	5.29	Ingot
30	Zinc	65.39	2.66	Ingot
31	Gallium	69.72	249	Ingot
32	Germanium	72.64	1670	Ingot
33	Arsenic	74.92	1.8	Powder
34	Selenium	78.96	0.56	Powder
35	Bromine	79.9	0.15	Liquid
36	Krypton	83.8	12.5	Gas
37	Rubidium	85.47	2440	Metal pellets
38	Strontium	87.62	7520	Dendritic pieces
39	Yttrium	88.91	1320	Powder
40	Zirconium	91.22	258	Ingot
41	Niobium	92.91	1680	Powder
42	Molybdenum	95.94	790	Ingot
43	Technetium	98	0	no available index
44	Ruthenium	101.07	1910.00	Ingot
45	Rhodium	102.91	30868.17	Ingot
46	Palladium	106.42	22845.66	Ingot

47	silver	107.87	621.22	Ingot
48	Cadmium	112.41	500	Ingot
49	Indium	114.82	540	Ingot
50	Tin	118.71	8.36	Ingot
51	Antimony	121.76	17.64	Ingot
52	Tellurium	127.6	235	Ingot
53	Iodine	126.9	43	Chips
54	Xenon	131.29	1200	Liquid
55	Cesium	132.91	3675	Ingot
56	Barium	137.33	7600	Ingot
57	Lanthanum	138.91	6000	Ingot
58	Cerium	140.11	1190	Ingot
59	Praseodymium	140.91	1000	Ingot
60	Neodymium	144.24	1284	Ingot
61	Promethium	145	0	no available index
62	Samarium	150.36	824	Ingot
63	Europium	151.96	26119	Ingot
64	Gadolinium	157.25	2045	Ingot
65	Terbium	158.93	6330	Ingot
66	Dysprosium	162.5	1019	Ingot
67	Holmium	164.93	5100	Ingot
68	Erbium	167.26	10100	Ingot
69	Thulium	168.93	19775	Ingot
70	Ytterbium	173.04	30400	Ingot
71	Lutetium	174.97	22200	Ingot

Table 3: Total possible profit from fission products assuming 100% recovery of each product. The three most profitable isotopes are highlighted for each fissile nucleus at each average spectrum.

Z	U-233		U-235		Pu-239	
	Thermal \$/yr GWt	Fast \$/yr GWt	Thermal \$/yr GWt	Fast \$/yr GWt	Thermal \$/yr GWt	Fast \$/yr GWt
V	1.66E-15	1.29E-15	6.59E-16	1.43E-14	0.00E+00	1.16E-14
Cr	9.40E-12	7.69E-12	9.47E-12	1.48E-10	1.67E-12	3.28E-11
Mn	4.84E-09	5.04E-09	3.95E-09	4.57E-08	1.37E-09	1.78E-08
Fe	4.81E-08	5.31E-08	2.57E-08	2.10E-07	1.21E-08	1.19E-07
Co	3.13E-04	3.54E-04	8.12E-05	5.54E-04	8.83E-05	7.26E-04
Ni	4.31E-03	4.86E-03	6.28E-04	4.01E-03	7.27E-04	4.83E-03
Cu	2.01E-02	2.33E-02	4.49E-03	2.33E-02	3.55E-03	1.50E-02

Zn	1.45E-01	1.63E-01	7.03E-02	2.44E-01	2.20E-02	5.89E-02
Ga	5.47E+01	6.00E+01	4.66E+01	8.73E+01	1.50E+01	2.85E+01
Ge	2.74E+03	2.46E+03	2.17E+03	3.12E+03	8.46E+02	1.12E+03
As	8.80E+00	7.55E+00	6.51E+00	7.57E+00	2.94E+00	3.36E+00
Se	9.44E+00	9.80E+00	7.47E+00	8.91E+00	3.21E+00	3.41E+00
Br	4.60E+00	4.73E+00	3.87E+00	4.48E+00	1.58E+00	1.62E+00
Kr	1.04E+03	1.02E+03	8.89E+02	8.51E+02	2.96E+02	3.24E+02
Rb	2.47E+05	2.37E+05	2.34E+05	2.26E+05	9.06E+04	9.30E+04
Sr	1.15E+06	1.13E+06	1.13E+06	1.12E+06	5.36E+05	5.44E+05
Y	2.40E+05	2.34E+05	2.49E+05	2.50E+05	1.46E+05	1.44E+05
Zr	5.04E+04	4.91E+04	5.55E+04	5.56E+04	3.91E+04	3.89E+04
Nb	2.60E+05	2.58E+05	3.10E+05	3.14E+05	2.89E+05	2.90E+05
Mo	8.77E+04	9.13E+04	1.15E+05	1.18E+05	1.50E+05	1.50E+05
Tc	0.00E+00	0.00E+00	0.00E+00	0.00E+00	0.00E+00	0.00E+00
Ru	8.85E+04	1.02E+05	1.39E+05	1.45E+05	3.11E+05	3.14E+05
Rh	4.48E+05	5.54E+05	8.27E+05	9.52E+05	3.50E+06	3.38E+06
Pd	8.83E+04	1.60E+05	1.37E+05	2.05E+05	1.46E+06	1.40E+06
Ag	7.66E+02	2.08E+03	7.78E+02	1.86E+03	1.62E+04	1.49E+04
Cd	3.51E+02	1.32E+03	5.37E+02	8.05E+02	1.53E+03	2.22E+03
In	1.07E+03	1.76E+03	9.33E+02	2.27E+03	1.34E+03	1.91E+03
Sn	1.58E+02	2.12E+02	1.59E+02	2.30E+02	1.72E+02	1.98E+02
At	6.76E+02	8.17E+02	8.50E+02	9.60E+02	8.71E+02	8.81E+02
Te	2.62E+04	2.75E+04	2.95E+04	2.96E+04	2.85E+04	2.87E+04
I	6.16E+03	6.34E+03	6.92E+03	6.99E+03	7.39E+03	7.21E+03
Xe	2.75E+05	2.84E+05	3.06E+05	2.96E+05	3.02E+05	2.97E+05
Cs	6.56E+05	6.60E+05	7.53E+05	7.54E+05	6.85E+05	6.86E+05
Ba	2.03E+06	1.97E+06	2.13E+06	2.07E+06	1.86E+06	1.84E+06
La	1.13E+06	1.03E+06	1.18E+06	1.16E+06	9.24E+05	9.08E+05
Ce	2.16E+05	2.00E+05	2.23E+05	2.18E+05	1.79E+05	1.79E+05
Pr	1.27E+05	1.19E+05	1.39E+05	1.36E+05	1.16E+05	1.15E+05
Nd	1.31E+05	1.22E+05	1.51E+05	1.45E+05	1.28E+05	1.29E+05
Pm	0.00E+00	0.00E+00	0.00E+00	0.00E+00	0.00E+00	0.00E+00
Sm	1.31E+04	1.25E+04	1.74E+04	1.67E+04	2.25E+04	2.38E+04
Eu	5.94E+04	6.02E+04	8.13E+04	8.36E+04	1.99E+05	2.33E+05
Gd	4.60E+02	5.87E+02	6.07E+02	8.47E+02	4.66E+03	6.40E+03
Tb	3.37E+01	6.13E+01	3.68E+01	1.11E+02	9.59E+02	1.96E+03
Dy	7.76E-01	7.33E-01	6.03E-01	2.21E+00	4.68E+01	1.21E+02
Ho	2.93E-02	5.38E-02	4.53E-02	1.04E-01	6.12E+00	5.27E+01
Er	2.44E-02	4.48E-02	4.01E-02	8.62E-02	4.96E+00	5.78E+01
Tm	5.44E-04	1.01E-03	2.94E-03	7.18E-03	1.83E-01	3.18E+00
Yb	1.02E-04	1.79E-04	5.35E-04	1.47E-03	3.55E-02	5.75E-01
Lu	0.00E+00	3.22E-12	0.00E+00	0.00E+00	0.00E+00	8.69E-09

Adjustment for decay of radioactive fission products

Tables 1 and 3 were based on the yield immediately after a fission event. They do not include additional neutron capture during residency in the core or decay that would occur in between the time of ejection of the spent fuel from a reactor and its reprocessing. Most spent fuel, post-Carter administration, has been cooling for 40 years or fewer. Thus, additional decay will influence the yield when reprocessing spent fuel. To correct this, a 4% enriched LEU core of a 3800 MW_{th} BWR was considered. The data was acquired by inputting the typical burn up, 50 GWd/tHM, into the program ORIGEN-RA and the resulting atoms per L of spent fuel volume was the measured output (these numbers have been reported previously by Ganda).¹⁸ Table 4 gives this yield in total grams based on the ORIGEN output for spent fuel after the Bateman equation was applied as a first order approximation in terms of the time (10 years, 30 years, 50 years and 100 years) before reprocessing. Using Table 2, the total gross profit from each fission product was calculated and reported in Table 4. The most profitable radioactive isotopes are highlighted in yellow and those isotopes that are less radioactive than naturally occurring radioactive material of the corresponding element are highlighted green.

Table 4: Final discharge from a reactor after decaying for 10, 30, 50 or 100 years. The green highlighted total value is for the top 3 value isotopes that have a radioactivity equal to or less than the naturally occurring radioactivity (NORM) of an element. Yellow highlights are for other top grossing elements that are still more radioactive than is acceptable versus NORM. Tc and Pm were left out due to the lack of data on their value (see Table 2).

Time = 10 years

Element	Total (g)	Total value	NORM?	Ci/g	Stable?	Ci/gram	Acceptable vs NORM
---------	-----------	-------------	-------	------	---------	---------	--------------------

Ge	64.71	108.06	Y	2.14E-19	N	2.17E-18	FALSE
As	19.39	0.03	N	0	Y	0	TRUE
Se	8381.73	4.69	Y	3.70E-20	N	2.75E-19	FALSE
Br	3546.66	0.53	N	0	Y	0	TRUE
Kr	60531.48	756.64	N	0	N	13.99	FALSE
Rb	92204.22	224978.29	Y	2.38E-08	N	3.84E-08	FALSE
Sr	129566.60	974340.80	N	0	N	76.027	FALSE
Y	77730.17	102603.83	N	0	N	0	TRUE
Zr	632067.60	163073.44	Y	5.49E-18	N	15.585	FALSE
Nb	0.68	1.14	N	0	N	0.0312	FALSE
Mo	581685.46	459531.52	N	0	N	0	TRUE
Ru	394967.60	754388.11	N	0	N	0.2172	FALSE
Rh	74366.21	2295548.75	N	0	N	0	TRUE
Pd	251875.62	5754264.55	N	0	N	7.83E-05	FALSE
Ag	12758.53	7925.88	N	0	Y	0	TRUE
Cd	16254.74	8127.37	Y	5.06E-14	N	3.75E-16	TRUE
In	232.58	125.59	Y	6.76E-12	N	7.06E-12	FALSE
Sn	8519.13	71.22	N	0	N	0.00463	FALSE
Sb	1475.28	26.02	N	0	N	68.488	FALSE
Te	81777.66	19217.75	Y	1.21E-18	N	1.75E-09	FALSE
I	33950.72	1459.88	N	0	N	0.000136	FALSE
Xe	917473.75	1100968.50	Y	1.11E-19	N	5.118E-19	FALSE
Cs	433474.52	1593018.85	N	0	N	35.556	FALSE
Ba	319179.87	2425766.99	Y	5.73E-21	Y	0	TRUE
La	210886.48	1265318.88	Y	2.18E-11	Y	0	TRUE
Ce	415634.01	494604.47	N	0	N	0.0468	FALSE
Pr	192981.08	192981.08	N	0	N	0	TRUE
Nd	702718.64	902290.73	Y	2.58E-13	N	3.65E-13	FALSE
Sm	141986.10	116996.54	Y	3.37E-09	N	0.4382	FALSE
Eu	23361.01	610166.16	Y	2.25E-16	N	30.072	FALSE
Gd	25742.72	52643.86	Y	4.21E-14	N	9.83E-15	TRUE
Tb	418.12	2646.67	N	0	Y	0	TRUE
Dy	215.67	219.77	N	0	Y	0	TRUE
Ho	13.78	70.26	N	0	Y	0	TRUE
Er	4.72	47.66	N	0	Y	0	TRUE

Time = 30 years

Element	Total (g)	Total value	NORM?	Ci/g	Stable?	Ci/gram	Acceptable vs NORM
Ge	64.71	108.06	Y	2.14E-19	N	2.17E-18	FALSE
As	19.39	0.03	N	0.00E+00	Y	0.00E+00	TRUE
Se	8381.73	4.69	Y	3.70E-20	N	2.75E-19	FALSE

Br	3546.66	0.53	N	0.00E+00	Y	0.00E+00	TRUE
Kr	58964.90	737.06	N	0.00E+00	N	3.96E+00	FALSE
Rb	93770.78	228800.70	Y	2.38E-08	N	3.78E-08	FALSE
Sr	102326.05	769491.87	N	0.00E+00	N	5.95E+01	FALSE
Y	77730.17	102603.83	N	0.00E+00	N	0.00E+00	TRUE
Zr	659306.44	170101.06	Y	5.49E-18	N	9.23E+00	FALSE
Nb	1.80	3.02	N	0.00E+00	N	1.18E-02	FALSE
Mo	581685.46	459531.52	N	0.00E+00	N	0.00E+00	TRUE
Ru	394950.31	754355.10	N	0.00E+00	N	2.72E-07	FALSE
Rh	74366.21	2295548.75	N	0.00E+00	N	0.00E+00	TRUE
Pd	251901.44	5754854.38	N	0.00E+00	N	7.83E-05	FALSE
Ag	12758.61	7925.93	N	0.00E+00	Y	0.00E+00	TRUE
Cd	16254.74	8127.37	Y	5.06E-14	N	3.75E-16	TRUE
In	232.58	125.59	Y	6.76E-12	N	7.06E-12	FALSE
Sn	8518.94	71.22	N	0.00E+00	N	4.63E-03	FALSE
Sb	1378.89	24.32	N	0.00E+00	N	4.74E-01	FALSE
Te	81874.24	19240.45	Y	1.21E-18	N	2.76E-18	FALSE
I	33950.70	1459.88	N	0.00E+00	N	1.36E-04	FALSE
Xe	917473.78	1100968.53	Y	1.11E-19	N	5.12E-19	FALSE
Cs	371543.23	1365421.37	N	0.00E+00	N	2.44E+01	FALSE
Ba	381110.02	2896436.14	Y	5.73E-21	Y	0.00E+00	TRUE
La	210886.48	1265318.88	Y	2.18E-11	Y	0.00E+00	TRUE
Ce	415627.90	494597.20	N	0.00E+00	N	9.06E-10	FALSE
Pr	192981.08	192981.08	N	0.00E+00	N	0.00E+00	TRUE
Nd	702724.75	902298.57	Y	2.58E-13	N	3.65E-13	FALSE
Sm	143309.79	118087.27	Y	3.37E-09	N	3.71E-01	FALSE
Eu	21738.15	567778.71	Y	2.25E-16	N	5.67E+00	FALSE
Gd	27702.50	56651.61	Y	4.21E-14	N	9.14E-15	TRUE
Tb	418.12	2646.67	N	0.00E+00	Y	0.00E+00	TRUE
Dy	215.67	219.77	N	0.00E+00	Y	0.00E+00	TRUE
Ho	13.78	70.26	N	0.00E+00	Y	0.00E+00	TRUE
Er	4.72	47.66	N	0.00E+00	Y	0.00E+00	TRUE

Time = 50 years

Element	Total (g)	Total value	NORM?	Ci/g	Stable?	Ci/gram	Acceptable vs NORM
Ge	64.71	108.06	Y	2.14E-19	N	2.17E-18	FALSE
As	19.39	0.03	N	0.00E+00	Y	0.00E+00	TRUE
Se	8381.73	4.69	Y	3.70E-20	N	2.75E-19	FALSE
Br	3546.66	0.53	N	0.00E+00	Y	0.00E+00	TRUE
Kr	58532.97	731.66	N	0.00E+00	N	1.10E+00	FALSE
Rb	94202.71	229854.61	Y	2.38E-08	N	3.76E-08	FALSE

Sr	85492.82	642906.04	N	0.00E+00	N	4.40E+01	FALSE
Y	77730.17	102603.83	N	0.00E+00	N	0.00E+00	TRUE
Zr	676138.18	174443.65	Y	5.49E-18	N	5.56E+00	FALSE
Nb	2.91	4.89	N	0.00E+00	N	7.26E-03	FALSE
Mo	581685.46	459531.52	N	0.00E+00	N	0.00E+00	TRUE
Ru	394958.93	754371.55	N	0.00E+00	N	3.53E-13	FALSE
Rh	74366.21	2295548.75	N	0.00E+00	N	0.00E+00	TRUE
Pd	251901.36	5754852.51	N	0.00E+00	N	7.83E-05	FALSE
Ag	12758.69	7925.98	N	0.00E+00	Y	0.00E+00	TRUE
Cd	16254.74	8127.37	Y	5.06E-14	N	3.75E-16	TRUE
In	232.58	125.59	Y	6.76E-12	N	7.06E-12	FALSE
Sn	8518.74	71.22	N	0.00E+00	N	4.63E-03	FALSE
Sb	1378.27	24.31	N	0.00E+00	N	3.07E-03	FALSE
Te	81875.06	19240.64	Y	1.21E-18	N	2.76E-18	FALSE
I	33950.68	1459.88	N	0.00E+00	N	1.36E-04	FALSE
Xe	917473.80	1100968.56	Y	1.11E-19	N	5.12E-19	FALSE
Cs	332935.73	1223538.80	N	0.00E+00	N	1.72E+01	FALSE
Ba	419716.81	3189847.75	Y	5.73E-21	Y	0.00E+00	TRUE
La	210886.48	1265318.88	Y	2.18E-11	Y	0.00E+00	TRUE
Ce	415627.90	494597.20	N	0.00E+00	N	0.00E+00	TRUE
Pr	192981.08	192981.08	N	0.00E+00	N	0.00E+00	TRUE
Nd	702724.75	902298.57	Y	2.58E-13	N	3.65E-13	FALSE
Sm	143029.98	117856.70	Y	3.37E-09	N	3.18E-01	FALSE
Eu	21668.87	565969.31	Y	2.25E-16	N	1.09E+00	FALSE
Gd	28060.01	57382.72	Y	4.21E-14	N	9.02E-15	TRUE
Tb	418.12	2646.67	N	0.00E+00	Y	0.00E+00	TRUE
Dy	215.67	219.77	N	0.00E+00	Y	0.00E+00	TRUE
Ho	13.78	70.26	N	0.00E+00	Y	0.00E+00	TRUE
Er	4.72	47.66	N	0.00E+00	Y	0.00E+00	TRUE

Time = 100 yrs

Element	Total (g)	Total value	NORM?	Ci/g	Stable?	Ci/gram	Acceptable vs NORM
Ge	64.71	108.06	Y	2.14E-19	N	2.17E-18	FALSE
As	19.39	0.03	N	0.00E+00	Y	0.00E+00	TRUE
Se	8381.73	4.69	Y	3.70E-20	N	2.75E-19	FALSE
Br	3546.66	0.53	N	0.00E+00	Y	0.00E+00	TRUE
Kr	58375.11	729.69	N	0.00E+00	N	4.40E-02	FALSE
Rb	94360.57	230239.79	Y	2.38E-08	N	3.75E-08	FALSE
Sr	66438.96	499620.99	N	0.00E+00	N	1.70E+01	FALSE
Y	77730.17	102603.83	N	0.00E+00	N	0.00E+00	TRUE
Zr	695188.82	179358.72	Y	5.49E-18	N	1.62E+00	FALSE

Nb	5.71	9.59	N	0.00E+00	N	3.70E-03	FALSE
Mo	581685.46	459531.52	N	0.00E+00	N	0.00E+00	TRUE
Ru	394980.46	754412.68	N	0.00E+00	N	0.00E+00	TRUE
Rh	74366.21	2295548.75	N	0.00E+00	N	0.00E+00	TRUE
Pd	251901.15	5754847.85	N	0.00E+00	N	7.83E-05	FALSE
Ag	12758.90	7926.11	N	0.00E+00	Y	0.00E+00	TRUE
Cd	16254.74	8127.37	Y	5.06E-14	N	3.75E-16	TRUE
In	232.58	125.59	Y	6.76E-12	N	7.06E-12	FALSE
Sn	8518.26	71.21	N	0.00E+00	N	4.62E-03	FALSE
Sb	1378.26	24.31	N	0.00E+00	N	1.03E-08	FALSE
Te	81875.54	19240.75	Y	1.21E-18	N	2.76E-18	FALSE
I	33950.62	1459.88	N	0.00E+00	N	1.36E-04	FALSE
Xe	917473.86	1100968.63	Y	1.11E-19	N	5.12E-19	FALSE
Cs	287733.28	1057419.81	N	0.00E+00	N	6.32E+00	FALSE
Ba	464918.43	3533380.04	Y	5.73E-21	Y	0.00E+00	TRUE
La	210886.48	1265318.88	Y	2.18E-11	Y	0.00E+00	TRUE
Ce	415627.90	494597.20	N	0.00E+00	N	0.00E+00	TRUE
Pr	192981.08	192981.08	N	0.00E+00	N	0.00E+00	TRUE
Nd	702724.75	902298.57	Y	2.58E-13	N	3.65E-13	FALSE
Sm	142478.78	117402.51	Y	3.37E-09	N	2.16E-01	FALSE
Eu	22135.06	578145.56	Y	2.25E-16	N	1.89E-02	FALSE
Gd	28145.07	57556.66	Y	4.21E-14	N	8.99E-15	TRUE
Tb	418.12	2646.67	N	0.00E+00	Y	0.00E+00	TRUE
Dy	215.67	219.77	N	0.00E+00	Y	0.00E+00	TRUE
Ho	13.78	70.26	N	0.00E+00	Y	0.00E+00	TRUE
Er	4.72	47.66	N	0.00E+00	Y	0.00E+00	TRUE

The results in Table 4 showed that aside from Pd, the top three grossing isotopes were as radioactive as the naturally occurring composition of that element. This was important to note if industry were to buy the resulting fission products after reprocessing. Otherwise industry and the public are likely to reject the use of fission products as feed stock due to its radioactivity.

Based on the information from Table 4, the best reprocessing profit from the top three isotopes was between \$5,986,634.62 and \$7,094,247.67 for fission products below NORM. If the results included the above NORM Pd and left out La, the profit increased

to between \$10,475,580.29 and \$11,583,776.64. Many of the other top grossing elements were also above NORM as evident from Table 4, and if industry would not accept fission products that were above NORM levels of specific activity, then the stated numbers represented the cap on available gross profit.

Total recoverable profit for each scheme

Total profit for reprocessing would come from two major sources: reselling of fissile fuel recovered by COEX or UREX and the selling of fission products for industrial application. First, the possibility of selling recycled fissile elements that enough fissile material would be present in the spent fuel that, if recovered, could be sold for the price of fuel for a reactor.

The US EIA has cited prices in the range of \$ 40 million for replacing 1/3 of the core every 18 months.¹⁹ For the sake of continuity, the US EIA's fuel cost was adjusted to a price per year of \$27 million. Upon further investigation, the EIA's number was calculated for total fabricated fuel, and the product from our process would only be the coarse material in fabricated fuel.

In AREVA's estimate, the fissile atom oxide that goes into the fabricated fuel only accounts for 35% of the finished fuel assembly's cost. Thus it is more accurate to assume a return of 35% of the aforementioned \$27 million, or \$9.5 million.²⁰ While the price for metallic fuel was not as standardized, the IAEA reported that for France, the price was on par with the price of oxide fuel.²¹ Therefore, due to cost and the fact that the conversion factor was above 1, this work assumed that the same recovery can be realized for fast reactors as that of thermal reactors (\$9.5 million). However, in practice, this number was not absolute and was only used as a rough estimation.

The following six total possible profits from reprocessing were calculated using both the data from Table 3 for the three highest grossing fission products for each scenario and the information on waste and recovery of fissile atoms for new fuel assemblies:

- 1) Reprocessing fuel from one 1 GWth thermal reactor (4.5 mTHM/yr reprocessing) based on U-233: \$9.5 million in fissile material + \$4.31 million in selling top three grossing fission products – \$7.25 million for waste = \$6.56 million in yearly gross profit.
- 2) Reprocessing fuel from one 1 GWth fast reactor (2.85 mTHM/yr reprocessing) based on U-233: \$9.5 million in fissile material + \$4.13 million in selling top three grossing fission products – \$4.59 million from waste = \$9.04 million in yearly gross profit.
- 3) Reprocessing fuel from one 1 GWth thermal reactor (4.5 mTHM/yr reprocessing) based on U-235: \$9.5 million in fissile material + \$4.44 million in selling top three grossing fission products – \$7.25 million for waste = \$6.69 million in yearly gross profit.
- 4) Reprocessing fuel from one 1 GWth fast reactor (2.85 mTHM/yr reprocessing) based on U-235: \$9.5 million in fissile material + \$4.33 million in selling top three grossing fission products – \$4.59 million from waste = \$9.24 million in yearly gross profit.
- 5) Reprocessing fuel from one 1 GWth thermal reactor (4.5 mTHM/yr reprocessing) based on Pu-239: \$9.5 million in fissile material + \$6.82 million

in selling top three grossing fission products – \$7.25 million for waste = \$9.07 million in yearly gross profit.

- 6) Reprocessing fuel from one 1 GW_{th} fast reactors (2.85 mTHM/yr reprocessing) based on Pu-239: \$9.5 million in fissile material + \$6.62 million in selling top three grossing fission products – \$4.59 million from waste = \$11.52 million in yearly gross profit.

The gross profit from the U-235 thermal reactor can also be compared to the data from Table 4 (adjusted for a 1GW_{th} reactor), in which both the neutron capture and decay time before reprocessing is considered (i.e., 100-year decay time):

- 3') Reprocessing fuel from one 1 GW_{th} thermal reactor (4.5 mTHM/yr reprocessing) based on U-235: \$9.5 million in fissile material + \$3.86 million in selling top three grossing fission products (\$2.36 million for NORM elements) – \$7.25 million for waste = \$6.11 (\$4.61) million in yearly gross profit.

Conclusion and recommendations

The previous two sections showed that a small reprocessing plant with a capacity of 2.85 metric tons of heavy metal per year could have a maximum yearly gross profit of \$11.52 million. The highest estimates of small pilot plant reprocessing costs by Bunn *et al.*, \$25.80 billion total cost over 40 years for a 200 mTHM/yr plant (may include the estimate for cost of disposing of waste).¹ If the profit of a 2.85 mTHM/yr reprocessing plant were scaled to that of 200 mTHM/yr, assuming a linear scaling (which was on the higher cost estimate). The operation could realize a yearly profit of \$808 million or a 40-year total profit of \$32.3 billion, giving a net total profit of \$6.5 billion. This would be a payoff time of upfront capital costs of about 32 years, which is preferable when

compared to a U/PU recovery only reprocessing facility which would not turn a profit (\$-12 billion).

Given the above comparison, it would be a worthwhile venture to build and operate a reprocessing facility where the fissile isotopes, and top three grossing stable fission products are recovered and sold on the market. It is recommended that this business opportunity be studied in greater detail. While there was a profit in the current model, there were also many assumptions that need to be clarified and refined. It is also recommended that the profit and cost of recovering fission produced medical isotopes be further investigated. Due to the large need in the global market for medical isotopes, a larger net profit would be possible relative to selling fission products competing with mining and ore operations.

Future work

Future work will focus on reducing the number of assumptions made in this chapter. In doing so, a more accurate, informed, and usable model and data will aid in pursuing paths forward in reprocessing work.

An in-depth analysis will need to take place on the feasibility of using a reprocessing plant to recover medical isotopes in large quantities. Generally, medical isotopes exist only while the fuel is still too radioactive to facilitate processing. However, additional shielding and recovery schemes could be realized for such a venture.

Additionally, further investigation into numbers from outside sources will need to be carried out. For example, if the work by Bunn *et al.* already includes waste in the operations and maintenance cost of his 200 mTHM reprocessing plant, and if his capacity

and finance factors make sense (e.g. a 1.3 multiplication factor for engineering overhead), then this future work will have greater accuracy in future reports.

Acknowledgements

I would like to thank the Fuel Cycle Option campaign and Dr. Francesco Ganda for bringing me into this work. This work was carried out entirely on my personal time and is independent of Argonne National Laboratory and its funding sources.

This chapter was prepared under award #NRC-HQ-15-G-0036, from the Office of the Chief Human Capital Officer of the Nuclear Regulatory Commission. Any statements, findings, conclusions, and recommendations are those of the author and do not necessarily reflect the view of the Outreach and Recruitment Branch or the US Nuclear Regulatory Commission.

References

1. Bunn, M., Hui Zhang, Li Kang *The Cost of Reprocessing in China*. Cambridge, Mass.: Report for Project on Managing the Atom, Belfer Center for Science and International Affairs, Harvard Kennedy School,; January, 2016.
2. Choi, S.; Nam, H. O.; Ko, W. I., Environmental life cycle risk modeling of nuclear waste recycling systems. *Energy* **2016**, *112*, 836-851.
3. Sowell, T., *Basic Economics a common sense guide to the economy*. Basic Books: New York, 2014.
4. Hazlitt, H.; Forbes, S., *Economics in one lesson*. Laissez Faire Books: San Francisco, CA, 1996.
5. Friedman, M.; Savage, L. J.; Becker, G. S., *Milton Friedman on economics : selected papers*. University of Chicago Press: Chicago, 2007.
6. Friedman, M., *Money and economic development*. Praeger: New York, 1973.
7. Solbrekken, G. L.; Turner, K. K.; Govindarajan, S. G., High-Density, Low-Enriched Uranium-Based Target for Radioisotope Production. **2013**
8. *Homogeneous versus heterogeneous recycling of transuranics in fast nuclear reactors*; 2012.
9. Till, C. E.; Chang, Y. I., *Plentiful energy : the story of the integral fast reactor, the complex history of a simple reactor technology, with emphasis on its scientific basis for non-specialists*. Amazon Publishing: United States, 2011.
10. JENDL FP decay data file 2011 and fission yields data file 2011. Japan Atomic Energy Agency, 2012.
11. Lamarsh, J. R., *Introduction to nuclear engineering*. Addison-Wesley: Reading, Mass., 1983.
12. *Nuclear proliferation and civilian nuclear power. Report of the Nonproliferation Alternative Systems Assessment Program. Volume IX. Reactor and fuel cycle description*; DOE/NE-0001/9F; TRN: 80-011296 United States 10.2172/5413513 Department of Energy, Washington, DC (USA). Assistant Secretary for Nuclear Energy: 1980; Pages: 625.
13. Mohandas, K. S., Direct electrochemical conversion of metal oxides to metal by molten salt electrolysis: a review. *Mineral Processing and Extractive Metallurgy* **2013**, *122* (4), 195-212.

14. Choppin, G. R.; Choppin, G. R.; Liljenzin, J.-O.; Rydberg, J., *Radiochemistry and nuclear chemistry*. Butterworth-Heinemann: Woburn, MA, 2002.
15. Joly, P.; Boo, E. *ROADMAP: Actinide separation processes 2015*; SACSESS: 2016; p 77.
16. Chesna, J. C.; Gray, L. W. *Dissolution of uranium fuel tubes in nitric acid*; DP-1671; ON: DE84010928 United States; Du Pont de Nemours (E.I.) and Co., Aiken, SC (USA). Savannah River Lab.: 1984; Pages: 30.
17. de Almeida, V. F. *Plant-Level Modeling and Simulation of Used Nuclear Fuel Dissolution*; ORNL/TM--2012/375; Other: AF5805000; NENT005 United States 10.2172/1330507 ; Oak Ridge National Laboratory (ORNL), Oak Ridge, TN (United States): 2012; 76 p.
18. Ganda, F. *Physics of hydride fueled PWR*. Ph.D., University of California, Berkeley, Ann Arbor, 2008.
19. *Levelized Cost and Levelized Avoided Cost of New Generation Resources in the Annual Energy Outlook 2016* 2016.
20. Ganda, F.; Dixon, B., *NUCLEAR ENERGY SYSTEM COST MODELING*. ; Idaho National Laboratory (INL): 2012
21. Golan, S.; Leduc, J.; Nakagawa, H., *Liquid-metal fast reactors: Technical and economic status*. *IAEA BULLETIN* **1989**, 31.

Appendix B: Synthesis, Spectroscopy, Electrochemistry, and Coordination Chemistry of Substituted Phosphine Sulfides and Selenides[†]

[†]This appendix is based on a manuscript that was submitted to and accepted by

Polyhedron. The DOI is: 10.1016/j.poly.2015.07.008 and can be cited as:

Breshears, A. T.; Behrle, A. C.; Barnes, C. L.; Laber, C. H.; Baker, G. A.; Walensky, J.

R., Synthesis, spectroscopy, electrochemistry, and coordination chemistry of substituted phosphine sulfides and selenides. *Polyhedron* **2015**, *100*, 333-343.

Abstract

Phosphines and phosphine chalcogenides are important ligands for various metal systems, especially catalysts. Based on previously synthesized phosphine oxide ligands, described here are the synthesis and characterization of a series of compounds having the general formula, EPh_2Ar , $\text{E} = \text{S}, \text{Se}$; $\text{Ar} = 1\text{-naphthyl}, 9\text{-phenanthryl}, 9\text{-anthracenyl}, 1\text{-pyrenyl}$. Reaction of $\text{EPh}_2(9\text{-phenanthryl})$, $\text{E} = \text{S}, \text{Se}$, with HAuCl_4 yields $\text{ArPh}_2\text{PEAuCl}$. Similar to the phosphine oxide derivative, the anthracenyl compounds, $\text{EPh}_2(9\text{-anthracenyl})$, showed a nonplanar conformation within the anthracene ring as observed using X-ray crystallography. The difference in fluorescence spectra relative to the parent aryl species is attributed to this deformation. The deviation is probably due to steric strain within the phosphine ligand due to its position on the anthracenyl ring since DFT calculations suggest that the 1-anthracenyl ligand should be planar. Each compound has been characterized using ^1H , ^{13}C , ^{31}P , and (where applicable) ^{77}Se NMR, and IR spectroscopy, with structure determination by X-ray crystallography. Finally, the

electrochemistry of the unoxidized phosphines is reported, showing one-electron reductions in the polycyclic aromatic hydrocarbons.

Scope of Impact

This work advances the field of phosphine chalcogenide compounds by questioning and investigating the assumptions made in previous polyaromatic hydrocarbon substituent phosphine chalcogenides in literature. Previously, other investigators held that the red shift observed in the fluorescence spectra for many of these compounds was due to a complex interaction with gold or silver. However, in this investigation, data suggested that it was a bend in the polyaromatic hydrocarbon that produced this red shift.

Introduction

Phosphines are commonly employed as coordinating ligands to metal centers for varying their steric and electronic properties.¹⁻² Changing these parameters can exert a significant effect over the catalytic and redox chemistry of metal complexes. The use of phosphines has been indispensable for the first generations of the Grubbs,³ Wilkinson,⁴ and Heck catalysts.⁵⁻⁹ In recent years, various groups have investigated how changing substituents and steric bulk around phosphorus changes the ligand chemistry. These investigations have included heteroatomic polycyclic aromatic substituents,¹⁰ increased steric properties of phenyl groups,¹¹⁻¹³ and oxidation chemistry.¹⁴⁻¹⁵ In addition, sulfur and selenium-based ligands have become increasingly studied due to their relevance in medicine and biological systems.¹⁶⁻¹⁷

Previous work involving EPh_2Ar ($\text{E} = \text{S}, \text{Se}$; $\text{Ar} =$ polycyclic aromatic hydrocarbon) ligands is limited (Figure 1) and there are no examples for $\text{Ar} =$ phenanthryl or pyrenyl. Recently, our group examined the coordination chemistry of phosphine oxide ligands of

the form OPPh_2Ar (Ar = naphthyl, phenanthryl, anthracenyl, or pyrenyl) with uranyl nitrate, $\text{UO}_2(\text{NO}_3)_2$.¹⁸ One feature of these ligands is an unusual red-shift in the fluorescence spectrum for the anthracenyl-derivative. To probe this further, examination of sulfur and selenium analogs of those phosphine ligands and their coordination chemistry with Au(I) as well as their electrochemical and spectroscopic properties.

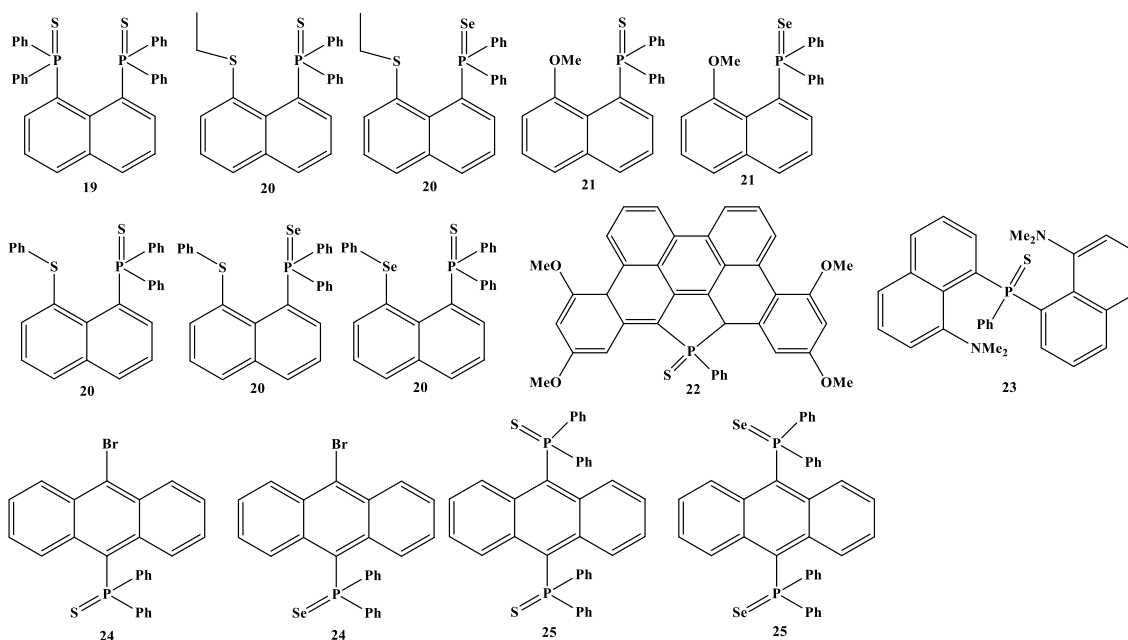


Figure 1: Examples of known triarylphosphine chalcogenide compounds. Numerals identify the literature references reporting the corresponding species.

Experimental

General considerations

All materials were purchased (Sigma-Aldrich, St. Louis, MO) at 95% purity or higher and used as received. Reactions were conducted in a Vacuum Atmosphere, Inc. nitrogen atmosphere dry box or using Schlenk line techniques. Gold(I) compounds were handled with exclusion of light unless otherwise specified. HAuCl_4 (Strem) was used as received. Phosphines were synthesized according to their literature procedures.^{18, 26-27} All solvents

used were purchased anhydrous, stored over activated 4 Å molecular sieves, and sparged with nitrogen prior to use. Benzene-*d*₆ (Cambridge Isotope Laboratories) was used as received. ¹H, ¹³C, and ³¹P NMR spectroscopy were obtained using a 250 MHz ARX, 300 MHz DRX, or 500 MHz DRX Bruker spectrometer. ¹H NMR spectrum resonances were referenced internally to the residual protio impurities at δ 5.32 ppm (CDHCl₂) or at δ 7.16 ppm (C₆D₅H). ¹³C NMR spectral resonances were referenced internally to the deuterated solvent peaks at δ 53.52 ppm (CD₂Cl₂) or δ 128.00 ppm (C₆D₆). ³¹P NMR spectra were referenced externally to 0.00 ppm with 85% H₃PO₄ in D₂O. ⁷⁷Se NMR spectra were externally referenced to 460.00 ppm with 1.0 M diphenyl diselenide in C₆D₆. Infrared spectra were recorded using KBr pellets on a Perkin-Elmer Spectrum One FT-IR spectrometer. Elemental analyses were performed by Atlantic Microlab, Inc. (Norcross, GA).

SPh₂(1-naphthyl), 1

A scintillation vial was charged with elemental sulfur (32 mg, 0.125 mmol) and a second scintillation vial was charged with PPh₂(C₁₀H₇) (312 mg, 1.00 mmol). Toluene (10 mL) and sulfur were added to the phosphine and stirred for 48 h. The solution was then filtered over Celite and the solvent removed *in vacuo* to yield **1** as a white solid (338 mg, 98%). ¹H NMR (C₆D₆, 500 MHz): δ 6.86 (dt, 1H, ³J_{H-H} = 7.5 Hz, ⁴J_{P-H} = 2.5 Hz, naph), 6.92-7.07 (m, 7H, naph and Ph), 7.14 (t, 1H, ³J_{H-H} = 4.5 Hz, naph), 7.25 (dd, 1H, ³J_{P-H} = 16.5, ³J_{H-H} = 8.5 Hz, naph), 7.50 (d, 1H, ³J_{H-H} = 8.5 Hz, naph), 7.56 (d, 1H, ³J_{H-H} = 8.5 Hz, naph) 7.94 (ddd, 4H, ³J_{P-H} = 13 Hz, ³J_{H-H} = 7 Hz, ⁴J_{H-H} = 1 Hz, Ph), 9.03 (d, 1H, ³J_{H-H} = 8.5 Hz, naph). ¹³C{¹H} NMR (C₆D₆, 125 MHz): δ 124.11 (s, naph), 125.34 (naph), 126.33 (naph), 126.59 (naph), 127.81 (Ph), 128.00 (naph), 128.26 (d, ²J_{P-C} = 14 Hz,

naph), 128.48 (naph), 128.98 (naph), 131.08 (Ph), 132.52 (d, $^2J_{P-C} = 10$ Hz, Ph), 133.62 (d, $^1J_{P-C} = 84$ Hz, Ph), 134.33 (d, $^1J_{P-C} = 106$ Hz, naph), 137.53 (naph). $^{31}P\{^1H\}$ NMR (C_6D_6 , 101 MHz): δ 42.00. IR (KBr, cm^{-1}): 3049 (m), 1591 (w), 1504 (m), 1478 (m), 1436 (s, C-P), 1390 (m), 1336 (m), 1313 (w), 1261 (w), 1179 (w), 1096 (s, C=C), 1026 (m), 1000 (w), 979 (w), 827 (m), 800 (s), 776 (s, C=C-H), 710 (s, P-C), 691 (s, P=S), 635 (s), 526 (s), 508 (s). Anal. Calc. for $C_{22}H_{17}PS$: C, 76.72%; H, 4.98%. Found: C, 76.82%; H, 5.26%.

SPh₂(9-phenanthryl), 2

A scintillation vial was charged with elemental sulfur (32 mg, 0.125 mmol) and a second scintillation vial was charged with $PPh_2(C_{14}H_9)$ (362 mg, 1.00 mmol). The synthesis followed the same approach as that for **1**, yielding **2** as a white solid (348 mg, 97%). 1H NMR (C_6D_6 , 500 MHz): δ 6.90-7.04 (m, 4H, phen and Ph), 7.08-7.19 (m, 4H, Ph), 7.22 (t, 1H, $^3J_{H-H} = 8$ Hz, phen), 7.61 (d, 1H, $^4J_{P-H} = 17.5$ Hz, phen), 8.00 (dd, 4H, $^3J_{H-H} = 8.5$ Hz, $^3J_{P-H} = 7$ Hz, Ph), 8.28 (d, 2H, $^3J_{H-H} = 8.5$ Hz, phen), 8.34 (d, 2H, $^3J_{H-H} = 8.5$ Hz, phen), 9.17 (d, 1H, $^3J_{H-H} = 8.5$ Hz, phen). $^{13}C\{^1H\}$ NMR (C_6D_6 , 125 MHz): δ 122.91 (phen), 123.35 (phen), 126.5 (phen), 126.80 (phen), 127.1(Ph), 127.28 (phen), 128.70 (d, $^4J_{P-C} = 12.5$ Hz, phen), 128.97 (phen), 129.12 (d, $^4J_{P-C} = 12.5$ Hz, phen), 130.22 (d, $^3J_{P-C} = 15$ Hz, Ph), 130.33 (d, $^4J_{P-C} = 22.5$ Hz, phen), 131.43 (d, $^4J_{P-C} = 3$ Hz, phen), 132.10 (phen), 132.34 (d, $^4J_{P-C} = 3$ Hz, phen), 133.90 (d, $^2J_{P-C} = 10$ Hz, Ph), 133.8 (d, $^1J_{P-C} = 84$ Hz, Ph), 135.92 (d, $^2J_{P-C} = 10$ Hz, phen), 136.2 (d, $^1J_{P-C} = 110$ Hz, phen). $^{31}P\{^1H\}$ NMR (C_6D_6 , 101 MHz): δ 42.85. IR (KBr, cm^{-1}): 2962 (m, =C-H), 1476 (w), 1448 (w), 1435 (s), 1385 (w), 1306 (w), 1261 (m), 1249 (w), 1158 (w), 1103 (s, C=C), 1023 (m), 952 (w), 903 (w), 859 (w), 803 (m), 773 (m), 750 (s), 716 (s, P-C), 691 (s, P=S), 652 (s), 599

(m), 558 (w), 518 (m). Anal. Calc. for C₂₆H₁₉PS: C, 79.16%; H, 4.85%. Found: C, 78.60%; H, 4.96%.

SPh₂(9-anthracenyl), 3

A scintillation vial was charged with elemental sulfur (32 mg, 0.125 mmol) and a second scintillation vial was charged with PPh₂(C₁₄H₉) (362 mg, 1.00 mmol). The reaction was then performed analogously to **1**, yielding **3** as a white solid (339 mg, 94%). ¹H NMR (C₆D₆, 500 MHz): δ 6.77 (t, 2H, ³J_{H-H} = 8 Hz, anth), 6.82-6.90 (m, 6H, Ph), 6.99 (t, 2 H, 7.5Hz, anth), 7.66 (d, 2H, ³J_{H-H} = 8.5, anth), 7.88-7.98 (m, 4H, Ph), 8.20 (s, 1H, anth), 8.37 (d, 2H, ³J_{H-H} = 9 Hz, anth). ¹³C{¹H} NMR (C₆D₆, 125 MHz): δ 124.41 (d, ²J_{P-C} = 87.5 Hz, anth), 125.39 (d, ³J_{P-C} = 34 Hz, anth), 125.66 (d, ³J_{P-C} = 34 Hz, anth), 126.67 (anth), 128.49 (anth), 129.20 (anth), 130.41 (d, ⁴J_{P-C} = 2.5 Hz, anth), 131.24 (d, ²J_{P-C} = 10 Hz, Ph), 131.80 (anth), 132.41 (Ph), 133.53 (d, ⁴J_{P-C} = 4 Hz, anth), 133.75 (d, ⁴J_{P-C} = 7.5 Hz, Ph) 133.88 (d, ⁴J_{P-C} = 5 Hz, anth), 133.92 (d, ⁴J_{P-C} = 5 Hz, anth), 138.25 (d, ¹J_{P-C} = 107.5 Hz, Ph), 138.5 (d, ²J_{P-C} = 81.25 Hz, anth). ³¹P{¹H} NMR (C₆D₆, 101 MHz): δ 34.37. IR (KBr, cm⁻¹): 3056 (w), 2960 (m, =C-H), 1700 (w), 1685 (w), 1653 (w), 1617 (w), 1540 (w), 1481 (m), 1437 (s, C=C), 1384 (m), 1261 (w), 1093 (s, C=C-H, plane bend), 1026 (m), 902 (m), 845 (w), 823 (m), 779 (m), 740 (s, P-C), 716 (m), 698 (s, P=S), 675 (w), 646 (w), 635 (w), 615 (w). Anal. Calc. for C₂₆H₁₉PS: C, 79.16%; H, 4.85%. Found: C, 79.14%; H, 5.16%.

SPh₂(1-pyrenyl), 4

A scintillation vial was charged with elemental sulfur (32 mg, 0.125 mmol) and a second scintillation vial was charged with PPh₂(C₁₆H₉) (388 mg, 1.00 mmol). The reaction was then performed analogously to **1**, yielding **4** as a pale yellow solid (410 mg, 98%). Low

solubility and overlapping protons made assignment of proton and carbon resonances in their respective NMR spectra unsuccessful. ^1H NMR (C_6D_6 , 500 MHz): δ 6.89-6.98 (m, 1H, pyr), 7.0-7.08 (m, 6H, Ph), 7.54-7.8 (m, 4H, pyr), 7.84 (d, 1H, $^3J_{\text{H-H}} = 7.5$ Hz, pyr), 7.91 (d, 1H, $^3J_{\text{H-H}} = 7.5$ Hz, pyr), 8.00-8.07 (m, 4H, Ph), 9.28 (d, 1H, $^3J_{\text{H-H}} = 9$ Hz, pyr). $^{13}\text{C}\{^1\text{H}\}$ NMR (C_6D_6 , 125 MHz): δ 123.87 (d, $^3J_{\text{P-C}} = 12.5$ Hz), 124.67, 125.24, 125.95 (d, $^3J_{\text{P-C}} = 12.5$ Hz), 126.06, 127.41 (d, $^4J_{\text{P-C}} = 5$ Hz), 128.67 (d, $^2J_{\text{P-C}} = 11.3$ Hz), 129.27, 129.73, 130.70 (d, $^3J_{\text{P-C}} = 12.5$ Hz), 131.18 (d, $^1J_{\text{P-C}} = 106$ Hz, Ph), 131.36 (d, $^4J_{\text{P-C}} = 2.5$ Hz, CH), 131.37 (d, $^1J_{\text{P-C}} = 20$ Hz), 132.96 (d, $^2J_{\text{P-C}} = 10$ Hz, CH), 133.29 (d, $^2J_{\text{P-C}} = 9$ Hz), 133.85 (d, $^3J_{\text{P-C}} = 7.5$ Hz), 133.89 (d, $^3J_{\text{P-C}} = 7.5$ Hz), 134.17, 134.24 (d, $^4J_{\text{P-C}} = 2.5$ Hz), 134.84, 137.83. $^{31}\text{P}\{^1\text{H}\}$ NMR (C_6D_6 , 101 MHz): δ 42.65. IR (KBr, cm^{-1}): 3431 (wb), 3148 (w), 2961 (w), 1578 (w), 1435 (s), 1384 (s, C=C-H), 1263 (w), 1207 (w), 1178 (w), 1098 (m), 1026 (w), 847 (w), 819 (w), 752 (m), 712 (s, P-C), 692 (m, P=S), 659 (m), 514 (w), 493 (w). Anal. Calc. for $\text{C}_{28}\text{H}_{19}\text{PS}$: C, 80.36%; H, 4.58%. Found: C, 80.34%; H, 4.71%.

SePPh₂(1-naphthyl), **5**

A scintillation vial was charged with elemental selenium (79 mg, 1.00 mmol). A second scintillation vial was charged with PPh₂(C₁₀H₇) (312 mg, 1.00 mmol) then dissolved in toluene (10 mL) and then transferred into the selenium scintillation vial and allowed to stir for 48 h. The solution was then filtered over Celite and the solvent was removed *in vacuo* yielding **5** as a white solid (377 mg, 96%). ^1H NMR (C_6D_6 , 500 MHz): δ 6.85 (dt, 1H, $^3J_{\text{H-H}} = 7.5$ Hz, $^4J_{\text{P-H}} = 2.5$ Hz, naph), 6.92-7.03 (m, 7H, naph and Ph), 7.06 (t, 1H, $^3J_{\text{H-H}} = 3.0$ Hz, naph), 7.22 (dd, 1H, $^3J_{\text{P-H}} = 16.5$, $^3J_{\text{H-H}} = 7.0$ Hz, naph), 7.49 (d, 1H, $^3J_{\text{H-H}} = 8.5$ Hz, naph), 7.54 (d, 1H, $^3J_{\text{H-H}} = 8.5$ Hz, naph) 7.97 (ddd, 4H, $^3J_{\text{P-H}} = 13.5$ Hz, $^3J_{\text{H-H}}$

= 8.5 Hz, $^4J_{\text{H-H}} = 1.5$ Hz, Ph), 9.04 (d, 1H, $^3J_{\text{H-H}} = 8.5$ Hz, naph). $^{13}\text{C}\{^1\text{H}\}$ NMR (C_6D_6 , 125 MHz): δ 124.22 (naph), 124.48 (d, $^3J_{\text{P-C}} = 13.8$ Hz, naph), 126.57 (naph), 126.72 (naph), 128.54 (d, $^3J_{\text{P-C}} = 9$ Hz, Ph), 131.14 (d, $^4J_{\text{P-C}} = 3$ Hz, Ph), 131.43 (d, $^4J_{\text{P-C}} = 3$ Hz, naph), 131.86 (naph), 132.5 (d, $^2J_{\text{P-C}} = 10$ Hz, Ph), 133.4 (d, $^1J_{\text{P-C}} = 88$ Hz, Ph), 133.38 (d, $^2J_{\text{P-C}} = 10$ Hz, naph) 134.7 (d, $^1J_{\text{P-C}} = 126$ Hz, naph), 137.82 (naph), 139.08 (naph). $^{31}\text{P}\{^1\text{H}\}$ NMR (C_6D_6 , 101 MHz): δ 31.85 (singlet with doublet satellites, $^1J_{\text{P-Se}} = 748$ Hz). $^{77}\text{Se}\{^1\text{H}\}$ NMR (C_6D_6 , 57 MHz): δ -252.71 (d, $^1J_{\text{P-Se}} = 748$ Hz). IR (KBr, cm^{-1}): 3050 (w), 2961 (w), 1591 (m), 1504 (m), 1477 (m), 1436 (s, C=C-H), 1390 (w), 1334 (w), 1312 (w), 1263 (m), 1181 (w), 1143 (w), 1095 (s, P-C), 1025 (m), 998 (m), 976 (w), 800 (s), 776 (s), 754 (m), 735 (m), 691 (s, P-C), 626 (m), 568 (s, P=Se), 529 (s), 504 (m). Anal. Calc. for $\text{C}_{22}\text{H}_{17}\text{PSe}$: C, 67.53%; H, 4.38%. Found: C, 66.19%; H, 4.51%.

SePPh₂(9-phenanthryl), **6**

A scintillation vial was charged with $\text{PPh}_2(\text{C}_{14}\text{H}_9)$ (362 mg, 1.00 mmol) in toluene (10 mL) and elemental selenium (79 mg, 1.00 mmol) was added. The reaction was then performed analogously to **5**, yielding **6** as a white solid (398 mg, 98% yield). ^1H NMR (C_6D_6 , 500 MHz): δ 6.92-7.02 (m, 4H, phen and Ph), 7.08-7.15 (m, 4H, Ph), 7.22 (t, 1H, $^3J_{\text{H-H}} = 8$ Hz, phen), 7.61 (d, 1H, $^4J_{\text{P-H}} = 17.5$ Hz, phen), 8.00 (dd, 4H, $^3J_{\text{H-H}} = 8.5$ Hz, $^3J_{\text{P-H}} = 7$ Hz, Ph), 8.28 (d, 2H, $^3J_{\text{H-H}} = 8.5$ Hz, phen), 8.34 (d, 2H, $^3J_{\text{H-H}} = 8.5$ Hz, phen), 9.19 (d, 1H, $^3J_{\text{H-H}} = 8.5$ Hz, phen). $^{13}\text{C}\{^1\text{H}\}$ NMR (C_6D_6 , 125 MHz): δ 122.81 (phen), 123.25 (phen), 126.53 (phen), 126.74 (phen), 127.12 (Ph), 127.35 (phen), 128.71 (d, $^4J_{\text{P-C}} = 12.5$ Hz, phen), 128.96 (phen), 130.05 (phen), 130.13 (d, $^3J_{\text{P-C}} = 7.5$ Hz, phen), 130.33 (d, $^3J_{\text{P-C}} = 15$ Hz, Ph), 130.43 (d, $^3J_{\text{P-C}} = 9$ Hz, phen), 131.46 (d, $^4J_{\text{P-C}} = 4$ Hz, phen), 131.63 (d, $^2J_{\text{P-C}} = 9$ Hz, Ph), 132.30 (d, $^4J_{\text{P-C}} = 3$ Hz, phen), 132.33 (d, $^1J_{\text{P-C}} = 75$, Ph), 133.51 (d, $^2J_{\text{P-C}}$

c = 11 Hz, Ph), 135.55 (d, $^2J_{P-C} = 9$ Hz, phen), 136.20 (d, $^1J_{P-C} = 108$ Hz, phen). $^{31}P\{^1H\}$ NMR (C_6D_6 , 101 MHz): δ 32.84 (singlet with doublet satellites, $^1J_{P-Se} = 748$ Hz). $^{77}Se\{^1H\}$ NMR (C_6D_6 , 57 MHz): δ -258.80 (d, $^1J_{P-Se} = 748$ Hz). IR (KBr, cm^{-1}): 3025 (w), 2963 (m), 1478 (w), 1448 (w), 1435 (s, C=C), 1385 (w), 1308 (w), 1261 (w), 1247 (w), 1181 (w), 1158 (w), 1099 (s, P-C), 1092 (s), 1024 (m), 999 (w), 951 (w), 902 (w), 801 (w), 772 (s), 750 (s), 713 (m), 691 (s, P-C), 623 (m), 567 (s, P=Se), 537 (s), 515 (s). Anal. Calc. for $C_{26}H_{19}PSe$: C, 70.75%; H, 4.34%. Found: C, 70.50%; H, 4.45%.

SePPh₂(9-anthracenyl), **7**

A scintillation vial was charged with elemental selenium (79 mg, 1.00 mmol) and a second scintillation vial was charged with PPh₂(C₁₄H₉) (362 mg, 1.00 mmol). The reaction was then performed analogously to **5**, yielding **7** as a white solid (374 mg, 92% yield). 1H NMR (C_6D_6 , 500 MHz): δ 6.77 (t, 2H, $^3J_{H-H} = 8$ Hz, anth), 6.80-6.87 (m, 6H, Ph), 7.13 (t, 2 H, 7.5 Hz, anth), 7.66 (d, 2H, $^3J_{H-H} = 8.5$, anth), 7.92-8.01 (m, 4H, Ph), 8.16 (s, 1H, anth), 8.36 (d, 2H, $^3J_{H-H} = 9$ Hz, anth). ^{13}C NMR (C_6D_6 , 125 MHz): δ 122.60 (d, $^2J_{P-C} = 78.5$ Hz, anth), 125.33 (d, $^3J_{P-C} = 23.75$ Hz, anth), 125.55 (d, $^3J_{P-C} = 9$ Hz, anth), 126.66 (s, anth), 128.49 (s, anth), 129.27 (s, anth), 130.41 (d, $^4J_{P-C} = 2.5$ Hz, anth), 131.24 (d, $^2J_{P-C} = 10$ Hz, Ph), 131.30 (s, anth), 132.41 (s, Ph), 133.53 (d, $^4J_{P-C} = 4$ Hz, anth), 133.75 (d, $^4J_{P-C} = 7.5$ Hz, Ph), 133.48 (d, $^4J_{P-C} = 5$ Hz, anth), 133.54 (d, $^4J_{P-C} = 6.25$ Hz, anth), 136.25 (d, $^1J_{P-C} = 107.5$ Hz, Ph), 136.71 (d, $^2J_{P-C} = 72.5$ Hz, anth). ^{31}P NMR (C_6D_6 , 101 MHz): δ 25.56 (singlet with doublet satellites, $^1J_{P-Se} = 752$ Hz). $^{77}Se\{^1H\}$ NMR (C_6D_6 , 57 MHz): δ -290.25 (d, $^1J_{P-Se} = 752$ Hz). IR (KBr, cm^{-1}): 3049 (w), 2956 (m), 2927 (m), 1616 (w), 1512 (w), 1480 (m), 1437 (s, C=C), 1384 (m), 1308 (w), 1262 (w), 1248 (w), 1178 (w), 1154 (w), 1092 (s), 1024 (m), 999 (w), 957 (w), 900 (m), 843

(w), 822 (m), 778 (m), 739 (s), 695 (s), 558 (m), 522 (s, P=Se), 515 (s). Anal. Calc. for $C_{26}H_{19}PSe$: C, 70.75%; H, 4.34%. Found: C, 71.17%; H, 4.55%.

SePPh₂(1-pyrenyl), 8

A scintillation vial was charged with elemental selenium (79 mg, 1.00 mmol) and a second scintillation vial was charged with PPh₂(C₁₆H₉) (388 mg, 1.00 mmol). The reaction was then performed analogously to **5**, yielding **8** as a green solid (402 mg, 96%). As with SPh₂Pyrenyl, low solubility and an overlapping proton spectrum made assignment of proton and carbon resonances in their respective NMR spectra unsuccessful. ¹H NMR (C₆D₆, 500 MHz): δ 6.77 (t, 1H, ³J_{H-H} = 8 Hz, pyr), 6.89-7.08(m, 6H, Ph), 7.50-7.89 (m, 5H, pyr), 7.80 (d, 1H, ³J_{H-H} = 7.5 Hz, pyr), 7.93 (d, 1H, ³J_{H-H} = 7.5 Hz, pyr), 8.04-8.11 (m, 4H, Ph), 9.29 (d, 1H, ³J_{H-H} = 10 Hz, pyr). ¹³C{¹H} NMR (C₆D₆, 125 MHz): δ 123.97 (d, *J*_{P-C} = 13.8 Hz), 124.67, 125.24, 125.95 (d, ³*J*_{P-C} = 12.5 Hz), 126.06, 127.49 (d, ⁴*J*_{P-C} = 5 Hz), 128.67 (d, ²*J*_{P-C} = 11.3 Hz, Ph), 129.28, 129.71, 130.46 (d, ⁵*J*_{P-C} = 2.5 Hz), 131.20 (d, ¹*J*_{P-C} = 106 Hz, Ph), 131.41 (d, ⁵*J*_{P-C} = 2.5 Hz), 131.81 (d, ²*J*_{P-C} = 11.3 Hz), 132.96 (d, ³*J*_{P-C} = 10 Hz), 133.28 (d, ⁴*J*_{P-C} = 4 Hz), 133.5 (d, ³*J*_{P-C} = 10 Hz), 133.55 (d, ³*J*_{P-C} = 10 Hz), 134.17, 136.46, 137.04, 137.83. ³¹P{¹H} NMR (C₆D₆, 101 MHz): δ 32.34 (singlet with doublet satellites, ¹*J*_{P-Se} = 746 Hz). ⁷⁷Se{¹H} NMR (C₆D₆; 57 MHz): δ -336.4 (d, ¹*J*_{Se-P} = 746 Hz). IR (KBr, cm⁻¹): 3046 (m), 2959 (m), 2926 (m), 2855 (w), 1577 (w), 1477 (w), 1457 (w), 1436 (s, C=C), 1384 (m), 1261 (m), 1208 (w), 1180 (w), 1099 (s), 1025 (m), 998 (w), 843 (s), 819 (m), 749 (m), 691 (s), 639 (w), 601 (m), 555 (s, P=Se), 514 (m). Anal. Calc. for $C_{28}H_{19}PSe$: C, 72.26%; H, 4.12%. Found: C, 71.91%; H, 4.51%.

[(9-phenanthryl)Ph₂PS]AuCl, 9

A scintillation vial was charged with 0.25 M H₂AuCl₄ (1.96 mL, 0.49 mmol) in air. A second scintillation vial was charged with **2** (396 mg, 1.00 mmol) and brought out of the glove box. The two were then added quickly to a Schlenk flask with a high flow rate of N₂ and dissolved in 50 mL of anhydrous ethanol that had been dried overnight over 4 Å molecular sieves. The reaction was stirred overnight to yield a brown solution. The reaction mixture was filtered over a medium-porosity ceramic frit. The white precipitate was washed with cold ethanol (2 × 5 ml) and extracted with methylene chloride (10 ml) and concentrated to yield **9** as colorless crystals (229 mg, 40%). ¹H NMR (C₆D₆, 300 MHz): δ 6.83-7.03 (m, 6H, Ph), 7.29-8.00 (m, 10H, Ph (4H) and phen (6H)), 8.31 (dd, 2H, ³J_{H-H} = 5.5 Hz, ³J_{H-H} = 4.5 Hz, phen), 8.70 (d, 1H, ³J_{H-H} = 4.5 Hz, phen). ¹³C{¹H} NMR (C₆D₆, 75 MHz): δ 122.98 (phen), 123.56 (phen), 127.15 (phen), 127.32 (phen), 127.40 (Ph), 128.28 (phen), 128.70 (d, ⁴J_{P-C} = 12.5 Hz, phen), 129.12 (phen), 129.37 (d, ⁴J_{P-C} = 12.5 Hz, phen), 130.22 (d, ³J_{P-C} = 15 Hz, Ph), 130.59 (d, ⁴J_{P-C} = 22.5 Hz, phen), 131.03 (d, ⁴J_{P-C} = 3 Hz, phen), 131.81 (s, phen), 132.32 (d, ⁴J_{P-C} = 3 Hz, phen), 132.52 (d, ²J_{P-C} = 10 Hz, Ph), 135.02 (d, ¹J_{P-C} = 84 Hz, Ph), 135.12 (d, ²J_{P-C} = 10 Hz, phen), 136.60 (d, ¹J_{P-C} = 110 Hz, phen). ³¹P{¹H} NMR (C₆D₆, 101 MHz): δ 27.1. IR (KBr, cm⁻¹) 3058 (m), 1527 (w), 1436 (s), 1384 (s), 1249 (m), 1185 (w), 1095 (s), 1051 (w), 998 (m), 953 (m), 899 (w), 742 (s), 716 (m), 686 (m), 622 (m), 586 (m), 556 (m), 512 (s, P-S), 482 (w). Anal. Calc. for C₂₆H₁₉PSAuCl: C, 45.71%; H, 3.14%. Found: C, 45.70%; H, 3.22%.

[(9-phenanthryl)Ph₂PSe]AuCl, 10

A scintillation vial was charged with 0.25 M H₂AuCl₄ (1.96 ml, 0.49 mmol) and a second scintillation vial was charged with **6** (444 mg, 1.00 mmol) then brought out of the glove box. The reaction and isolation of product were carried out in the same manner as **9**,

resulting in the isolation of **10**. The solvent was evaporated slowly to form colorless crystals (228 mg, 35%). Crystals suitable for X-ray crystallographic analysis were obtained from slow evaporation of 1:1 benzene and dichloromethane solution at room temperature. ^1H NMR (C_6D_6 , 300 MHz): δ 7.49 (t, 1H, $^3J_{\text{H-H}} = 7.8$ Hz, phen), 7.60-7.69 (m, 6H, Ph), 7.71-7.95 (m, 9H, phen and Ph), 8.64 (d, 1H, $^3J_{\text{H-H}} = 8.4$ Hz, phen), 8.87 (d, 1H, $^3J_{\text{H-H}} = 8.4$ Hz, phen), 8.94 (d, 1H, $^3J_{\text{H-H}} = 8.4$ Hz, phen). $^{13}\text{C}\{^1\text{H}\}$ NMR (C_6D_6 , 75 MHz): δ 122.82 (phen), 123.26 (phen), 123.60 (phen), 124.06 (phen), 126.81 (Ph), 127.28 (phen), 127.58 (d, $^4J_{\text{P-C}} = 12.5$ Hz, phen), 127.88 (phen), 128.20 (phen), 128.44 (d, $^3J_{\text{P-C}} = 7.5$ Hz, phen), 129.48 (d, $^3J_{\text{P-C}} = 15$ Hz, Ph), 129.54 (d, $^1J_{\text{P-C}} = 114$ Hz, phen), 130.30 (d, $^4J_{\text{P-C}} = 4$ Hz, phen), 130.40 (d, $^2J_{\text{P-C}} = 9$ Hz, Ph), 130.00 (d, $^4J_{\text{P-C}} = 3$ Hz, phen), 132.02 (d, $^1J_{\text{P-C}} = 75$ Hz, Ph), 132.42 (d, $^2J_{\text{P-C}} = 11$ Hz, Ph), 135.00 (d, $^2J_{\text{P-C}} = 9$ Hz, phen), 136.82 (d, $^1J_{\text{P-C}} = 108$ Hz, phen). $^{31}\text{P}\{^1\text{H}\}$ NMR (C_6D_6 , 101 MHz): δ 27.75 (singlet with doublet satellites, $^1J_{\text{P-Se}} = 410$ Hz). $^{77}\text{Se}\{^1\text{H}\}$ NMR (C_6D_6 , 57 MHz): 104.5 (d, $^1J_{\text{Se-P}} = 410$ Hz). IR (KBr, cm^{-1}): 2962 (m), 2925 (m), 2855 (w), 1481 (w), 1434 (m), 1384 (s), 1262 (m), 1100 (m), 1025 (m), 803 (m), 749 (m), 693 (w), 611 (w), 566 (w), 507 (w). Anal. Calc. for $\text{C}_{22}\text{H}_{19}\text{PSeAuCl}$: C, 46.35%; H, 2.84%. Found: C, 46.12%; H, 2.64%.

Electrochemistry

Cyclic voltammetry (CV) experiments were conducted using a CH Instruments (CHI) model 700D series workstation and the data were analyzed using CHI software version 12.05. All experiments were conducted inside a N_2 atmosphere glovebox with an electrochemical cell consisting of a 10-mL vial, glassy carbon electrode (3-mm diameter), a platinum wire counter electrode, and a silver wire plated with AgCl as a

quasi-reference electrode. The working electrode surfaces were polished prior to each set of experiments and were periodically replaced to prevent buildup of oxidized or reduced products on the electrode surfaces. Solutions employed during CV studies ranged from 1.0 to 1.5 mM in analyte concentration and contained 100 mM [ⁿBu₄N][PF₆] as supporting electrolyte. Potentials were reported versus Fc/Fc⁺, which was added as an internal standard for calibration at the end of each experiment. All data were collected in a positive-feedback iR compensation mode to minimize uncompensated resistance in the solution cells. The THF solution cell resistances were measured prior to each run to ensure resistances were approximately 1500 Ω or less.

Single crystal X-ray diffraction experiments

The selected single crystal was mounted on a nylon cryoloop using viscous hydrocarbon oil. X-ray data collection was performed at 173(2) K. The X-ray data were collected on a Bruker CCD diffractometer with monochromated Mo-K α radiation ($\lambda = 0.71073 \text{ \AA}$). The data collection and processing utilized Bruker Apex2 suite of programs.²⁸ The structures were solved using direct methods and refined by full-matrix least-squares methods on F^2 using Bruker SHELX-97 program.²⁹ All non-hydrogen atoms were refined with anisotropic displacement parameters. All hydrogen atoms were added on idealized positions and not allowed to vary. Thermal ellipsoid plots were prepared by using X-seed³⁰ with 50% of probability displacements for non-hydrogen atoms. The crystal parameters for **1-8** are highlighted in Table 1, and **9-10** are highlighted in Table 2.

Table 1: X-ray crystallographic data for complexes **1-8**.

	1	2	3	4	5	6	7	8
CCDC Deposit Number	1057597	1057598	1057596	1057599	1057594	1057593	1057592	1057595
Empirical Formula	C ₂₂ H ₁₇ PS•0.5(C ₇ H ₈)	C ₂₆ H ₁₉ PS	C ₂₆ H ₁₉ PS	C ₂₈ H ₁₉ PS	C ₂₂ H ₁₇ PSe•0.5(C ₇ H ₈)	C ₂₆ H ₁₉ PSe	C ₂₆ H ₁₉ PSe•0.5(C ₇ H ₈)	C ₂₈ H ₁₉ PSe
Formula weight (g/mol)	389.95	394.44	394.44	418.46	437.35	441.34	467.88	465.36
Crystal Habit, color	Prism, Colorless	Plate, Colorless	Plate, Colorless	Plate, Pale yellow	Prism, Colorless	Plate, Colorless	Block, Colorless	Plate, Pale green
Temperature (K)	173(2)	173(2)	173(2)	173(2)	173(2)	173(2)	173(2)	173(2)
Space group	<i>C2/c</i>	<i>P2₁/n</i>	<i>P-1</i>	<i>P-1</i>	<i>P2₁/c</i>	<i>P2₁/n</i>	<i>P-1</i>	<i>P-1</i>
Crystal system	<i>Monoclinic C</i>	<i>Monoclinic P</i>	<i>Triclinic P</i>	<i>Triclinic P</i>	<i>Monoclinic P</i>	<i>Monoclinic P</i>	<i>Triclinic P</i>	<i>Triclinic P</i>
Volume (Å ³)	4100.2(15)	1993.2(3)	1995.0(13)	1057.82(19)	4165.1 (13)	1998.10(10)	2159.5(19)	1056.28(3)
<i>a</i> (Å)	11.570(2)	13.4383(12)	10.234(4)	9.200(11)	11.555(2)	13.5233(4)	12.566(6)	9.2015(2)
<i>b</i> (Å)	14.878(3)	9.2261(9)	12.379(4)	10.553(13)	15.173(3)	9.1692(3)	12.864(6)	10.6136(2)
<i>c</i> (Å)	24.459(5)	16.0765(15)	17.407(6)	12.337(15)	24.382 (4)	16.1177(4)	16.340(8)	12.4204(2)
α (°)	90.0	90.0	101.530(5)	66.615(16)	90.0	90.0	92.376(7)	65.547(1)
β (°)	103.143(2)	90.423(1)	91.073(5)	74.640(17)	103.010(2)	91.224(1)	112.045(6)	73.595(1)
γ (°)	90.0	90.0	111.838(3)	80.613(18)	90.0	90.0	114.796(6)	79.512(1)
Z	8	4	4	2	8	4	4	2
Calculated density (Mg/m ³)	1.263	1.314	1.314	1.314	1.395	1.467	1.439	1.463
Absorption coefficient (mm ⁻¹)	0.24	0.25	0.25	0.24	1.89	3.35	1.83	3.2
Final R indices [I > 2 σ (I)]	R1 = 0.035 wR2 = 0.100	R1 = 0.043 wR2 = 0.100	R1 = 0.039 wR2 = 0.091	R1 = 0.053 wR2 = 0.136	R1 = 0.045 wR2 = 0.176	R1 = 0.032 wR2 = 0.089	R1 = 0.068 wR2 = 0.193	R1 = 0.024 wR2 = 0.063

Table 2: X-ray crystallographic data for complexes **9** and **10**.

	9	10
CCDC Deposit Number	1057591	1057590

Empirical Formula	C ₂₆ H ₁₉ AuCIPS	C ₂₆ H ₁₉ AuCIPSe•C ₆ H ₆
Formula weight (g/mol)	626.86	751.87
Crystal Habit, color	Prism, Colorless	Prim, Colorless
Temperature (K)	173(2)	173(2)
Space group	Monoclinic	Triclinic
Crystal system	<i>P2₁/c</i>	<i>P-1</i>
Volume (Å ³)	4422.8	1381.5
<i>a</i> (Å)	16.0492(15)	9.788(2)
<i>b</i> (Å)	18.1088(16)	12.054(3)
<i>c</i> (Å)	15.7268(15)	12.466(3)
<i>α</i> (°)	90	79.177(2)
<i>β</i> (°)	104.618(1)	75.285(2)
<i>γ</i> (°)	90	79.037(2)
<i>Z</i>	8	2
Calculated density (Mg/m ³)	1.883	1.807
Absorption coefficient (mm ⁻¹)	6.95	6.82
Final R indices [<i>I</i> > 2σ(<i>I</i>)]	R1 = 0.032 wR2 = 0.063	R1 = 0.035 wR2 = 0.080

Computational details

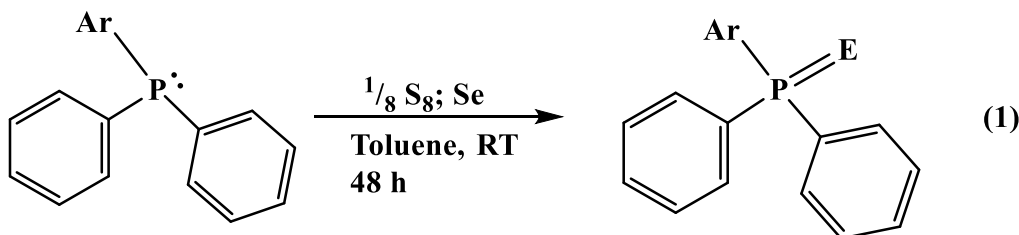
The electronic structures of complexes **1-8** and their unoxidized structures were examined using the Gaussian09 suite of software³¹ at the B3LYP³² (Becke-3³³ exchange and Lee-Yang-Parr³⁴ correlation functional) level of theory. Full geometry optimizations were performed and stationary points were determined to be global minima using analytical frequency calculations. The Pople double- ζ quality basis set, 6-31G(d,p),^{35,36}

was used for all atoms. NCIS(1) values were calculated as described previously,¹⁰ using Gaussview to place the ghost atom 1 Å above or below the centroid of the ring.

Results and Discussion

Synthesis

The phosphine ligands, PPh₂Ar, Ar = C₁₀H₇ (1-naphthyl), C₁₄H₉ (9-phenanthryl), C₁₄H₉ (9-anthracenyl), and C₁₆H₉ (1-pyrenyl), were synthesized as previously reported^{18, 26-27} and oxidized with either an eighth of an equivalent of elemental sulfur or one equivalent of selenium to produce the corresponding E=PPh₂Ar complexes, eq 1, E = S, Se. Coordination of EPPH₂(9-phenanthryl) to Au(I) was achieved by reaction of two equivalents of EPPH₂Ar with HAuCl₄ to yield (Ph₂ArPE)AuCl, E = S, **9**; Se, **10**. No attempt to determine the byproducts of the reactions with auric acid was pursued but similar reactivity has been reported previously.³⁷



- E = S; Ar = 1-naphthyl, **1**
- E = S; Ar = 9-phenanthryl, **2**
- E = S; Ar = 9-anthracenyl, **3**
- E = S; Ar = 1-pyrenyl, **4**
- E = Se; Ar = 1-naphthyl, **5**
- E = Se; Ar = 9-phenanthryl, **6**
- E = Se; Ar = 9-anthracenyl, **7**
- E = Se; Ar = 1-pyrenyl, **8**

Spectroscopy

Each reaction was monitored by ^{31}P NMR spectroscopy. Upon oxidation, a general shift downfield of the resonance from the unoxidized product was observed, Table 3. The difference between **2** and Au complex, **9**, was ~ 15 ppm, while **6** and Au complex, **10**, differed by 5 ppm. Interestingly, there is no correlation between the ^{31}P NMR chemical shifts and the size of the aryl ring. However, for $\text{S}=\text{PPh}_2\text{Ar}$, **3**, $\text{Se}=\text{PPh}_2\text{Ar}$, **7**, $\text{Ar} = 9$ -anthracenyl, the ^{31}P NMR resonances are shifted up field at 34.4 and 25.6 ppm, respectively, when compared to the unoxidized phosphine. This deviation of complexes **3** and **7** could be due to loss of planarity (described later), which then creates an up field shift in the ^{31}P NMR spectra due to relatively greater σ - than π -bonding between phosphorus and the aryl ipso carbon. Different electronic factors on the phosphine have been known to influence the ^{31}P NMR spectrum.³⁸ However, a strong correlation between the aromatic substituent on the phosphine and the shift of the ^{77}Se NMR resonance, Table 4, was observed for compounds **5-8**: increasing the electron withdrawing ability of the polycyclic aromatic hydrocarbon leads to an up field shift of the ^{77}Se NMR resonance.

Table 3: ^{31}P NMR chemical shifts for **1-10**.

Compound	^{31}P NMR Chemical Shift (ppm)
1	42.0
2	42.8
3	34.4
4	42.7
5	31.8
6	32.8
7	25.6
8	32.3
9	27.1
10	27.8

Table 4: ^{77}Se NMR spectroscopy resonances for Se containing compounds, **5-8** and **10**.

Compound	^{77}Se NMR chemical resonance (ppm)	$^{77}\text{Se} - ^{31}\text{P}$ coupling (Hz)
5	-252.71	748
6	-258.80	748
7	-290.25	752
8	-336.40	746
10	104.50	410

Both **5** and **6** show ^{77}Se resonances very close to that of triphenylphosphine selenide (-262 ppm),³⁹ while those for **7** and **8** are significantly upfield from **5** and **6**. Finally, as to be expected, ^{77}Se NMR spectroscopy of **10** shows a large shift downfield with a significant decrease in Se-P coupling which denotes the weakening of the Se-P bond from selenium donating electron density to gold.

Each reaction was monitored by IR spectroscopy for the P-Se or the P-S stretching frequencies, Table 5. The same trends for the NMR spectroscopy also apply to those observed in the IR spectroscopy: 1) There is no correlation between ring size and P-E (E = S, Se) stretching frequency and 2) the frequency appears at a lower wave number when coordinated to Au(I).

Table 5: IR stretching frequency (cm⁻¹) complexes **1-10**.

Bond stretching frequency (cm ⁻¹)	1, E = S	2, E = S	3, E = S	4, E = S	5, E = Se	6, E = Se	7, E = Se	8, E = Se	9, E = S	10, E = Se
$\nu(\text{P}=\text{E})_{\text{asym}}$	691	691	698	692	568	569	522	555	512	Not observed

Optical Spectroscopy

The electronic absorbance spectra for the phosphine sulfides and selenides dissolved in toluene are provided in Figure 2 and agree with the absorbance profiles expected for the parent aryl phosphine compounds.¹⁸ The corresponding fluorescence emission spectra are shown alongside. As observed earlier for the corresponding phosphine oxides, the order of the emission intensities for the phosphine sulfides (selenides) is **4(8) > 3(7) >> 2(6) >> 1(5)**.

As shown in Figure 2A, the absorbance profiles for the naphthyl phosphine complexes **1** and **5** show a relatively narrow absorbance in the 275 nm to 360 nm range, with a maximum absorbance near 290 nm. The phenanthryl species **2** and **6** display absorption maxima at 281 nm, however, **6** shows a broader spectrum relative to its sulfur counterpart, with a “tail” extending from 320 to 375 nm (Figure 2B). The pyrenyl phosphine sulfide (**4**) and selenide (**8**) results, shown in Figure 2C, display the typical vibrational features expected for unsubstituted pyrene monomer. The fact that well-defined vibrational peaks (i.e., peaks I, II, IV, and V) can still be observed for the pyrene substituted at the 1-position is unusual.⁴⁰⁻⁴¹ Indeed, the analogous pyrenyl phosphine oxide studied previously¹⁸ showed an emission profile more typical of 1-substituted pyrenyl compounds (i.e., two well-resolved monomeric bands near 375 nm and 400 nm).

The relative fluorescence intensity of the sulfide analog (**4**) was twice that of the selenide analog (**8**), for an identical absorbance at the excitation wavelength (325 nm). This is a general trend observed for all the aryl phosphines studied here.

When excited at 310 nm, complexes **3** and **7** show vibronic emission similar to conventional anthracene monomer, displaying peaks near 380, 402, 430, and 450 nm, Figure 3. When the excitation wavelength was red shifted to 410 nm, the emission observed from the anthracenyl phosphine sulfide and selenide ligands became structureless and was red-shifted by some 50 nm relative to typical anthracene monomer emission, a result mirroring that seen with the anthracenyl phosphine oxide earlier.^{18, 42}

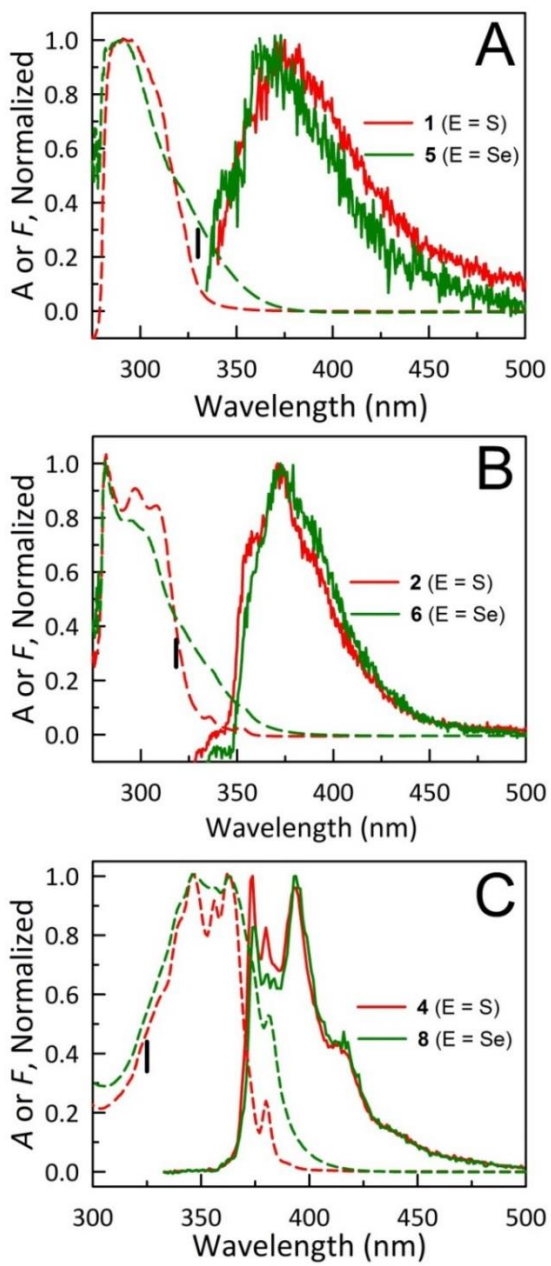


Figure 2: Normalized absorbance (broken profiles) and fluorescence emission (solid curves) spectra of (A) **1** and **5**, (B), **2** and **6**, and (C) **4** and **8**. The vertical bars within each panel indicate the excitation wavelengths employed to generate the emission spectra shown.

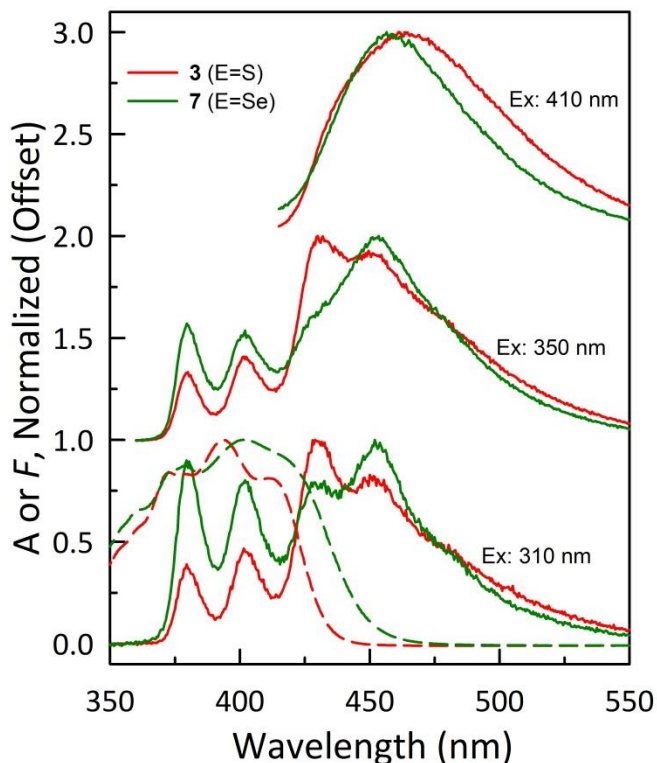


Figure 3: Normalized absorbance spectra (broken profiles) and fluorescence emission spectra (solid profiles) of the anthracenyl phosphine complexes **3** (red, S) and **7** (green, Se) measured in toluene. The emission spectra collected at different excitation wavelengths are offset vertically for clarity. Proceeding from top to bottom, the excitation wavelength decreases in the order 410 nm, 350 nm, and 310 nm.

Electrochemistry of Phosphine Complexes

Electrochemical experiments were investigated for phosphine compounds PPh_2Ar : Ar = 1-naphthyl, 9-phenanthryl, 9-anthracenyl, and 1-pyrenyl, at room temperature in THF. All the phosphine compounds displayed a one-electron irreversible oxidation wave at positive potentials relative to Fc/Fc^+ that can be attributed to the oxidation of phosphine, Figure 4. Substitution of the various polycyclic aromatic hydrocarbon (PAH) groups did not affect the oxidation potential of phosphine and the irreversible wave was independent

of scan rates. These results are consistent with previously published reports describing the electrochemical irreversible oxidation of PPh_3 .⁴²⁻⁴³

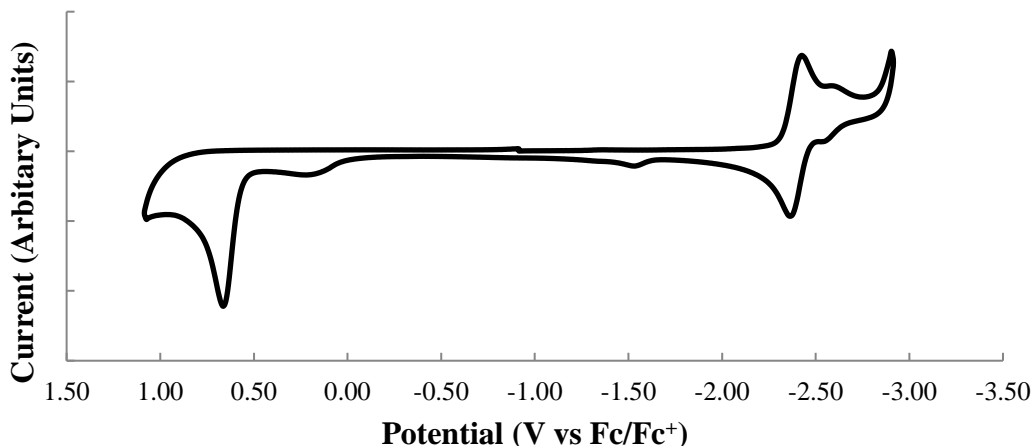


Figure 4: Representative cyclic voltammogram of PPh_2Ar , Ar = 1-pyrenyl, displaying irreversible one-electron oxidation wave at a positive potential with scan rate at 250 mVs^{-1} .

Table 6 shows the redox potentials for the PPh_2Ar (Ar = C_{10}H_7 (naphthyl), C_{14}H_9 (phenanthrenyl), C_{14}H_9 (anthracenyl), and C_{16}H_9 (pyrenyl)) compounds. All the $E_{1/2}$ values of the PPh_2Ar compounds compare well to the free PAH $E_{1/2}$ values previously reported.⁴⁴⁻⁴⁵ The $E_{1/2}$ values of the PPh_2Ar compounds indicate that reduction potentials of the PAH are reversible and there is no significant steric crowding, electron donation or removal to shift the reduction potential cathodically or anodically. Figure 5 is a representative cyclic voltammogram of $\text{PPh}_2(1\text{-pyrenyl})$ compounds showing scan rate dependence of reversible reduction of the PAH with return oxidation.

Table 6: Reduction potentials (V vs Fc/Fc⁺) of PPh₂Ar, Ar = C₁₀H₇ (naphthyl), C₁₄H₉ (phenanthrenyl), C₁₄H₉ (anthracenyl), and C₁₆H₉ (pyrenyl), at room temperature in THF.

PPh ₂ Ar	$E_{1/2}$ vs. Fc/Fc ⁺
1-naphthyl	(-3.10) ^a
9-phenanthrenyl	-2.73, (-2.89) ^a
9-anthracenyl	-2.43, -2.23, (-2.37) ^a
1-pyrenyl	-2.38, (-2.40) ^a

^aValues in parentheses represent $E_{1/2}$ potentials of the free alternate aromatic hydrocarbon.

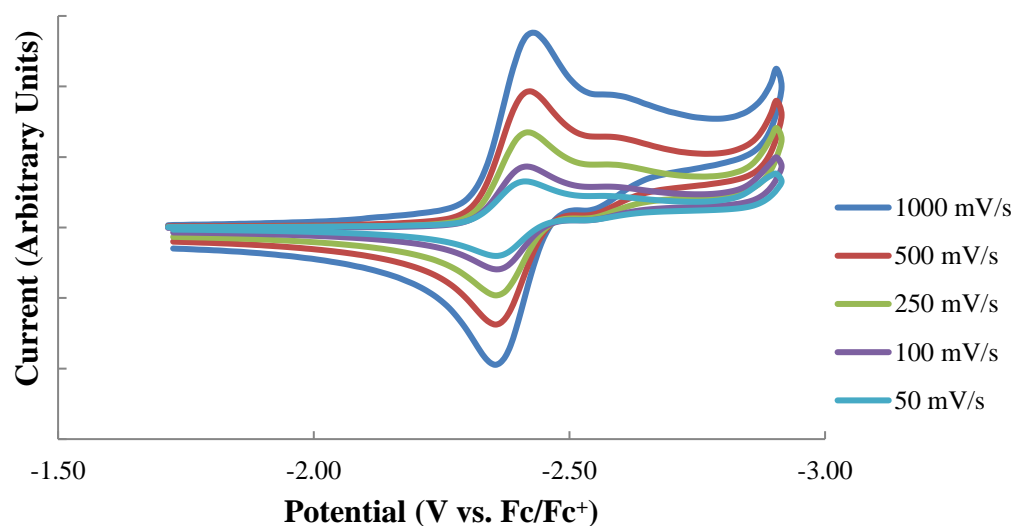


Figure 5: Representative cyclic voltammogram of PPh₂Ar, Ar = 1-pyrenyl, displaying reversible one electron reduction of pyrene with scan rate dependence in THF.

X-ray Crystallographic analysis

Upon a search of the Cambridge Crystallographic Database Center, CCDC, the only arylphosphine chalcogenides were the triphenylphosphine chalcogenides. To complement the database, the phosphine sulfide compounds of **1-4** were examined and their bond distances and angles are recorded in Table 7.

Table 7: Selected bonds lengths and angles of complexes **1-4**.

Bond distance (Å)/angle (°)	1	2	3	4	Ph₃PS
P1-S1	1.9856(2)	1.9573(7)	1.9535(14)	1.959(3)	1.9528(9)
P1-C (Phenyl)	1.8213(15)	1.8167(18)	1.825(3)	1.817(6)	1.8218(17)
P1-C (PAH)	1.8151(14)	1.8212(18)	1.828(3)	1.815(6)	-
S-P-C (Phenyl) average	112.88	113.22	112.75	112.86	113.09
S-P-C (PAH)	113.82(5)	113.09(6)	116.12(11)	115.3(2)	-

Compound **1** has a sulfur phosphorus bond length ~ 0.03 Å longer than that of the other sulfide complexes, **2-4**, including the triphenylphosphine sulfide with a bond length of 1.9528(9) Å.⁴⁶ All other structural features are comparable to triphenylphosphine sulfide. For compounds **5-8**, the bond distances for the four selenide compounds are highlighted in Table 8 and show very similar bond distances and angles to Ph₃PSe.⁴⁷ The bond lengths and the bond angles of compounds **9** and **10** are highlighted in Table 9. The structural data for **9** and **10** compare well with previously reported gold(I) phosphine sulfide and selenide adduct complexes.⁴⁸

Table 8: Selected bonds lengths and angles of complexes **5-8**.

Bond distance (Å)/angle (°)	5	6	7	8	Ph₃PSe
P1-Se1	2.1194(2)	2.1104(13)	2.1045(19)	2.1186(4)	2.106(1)
P1-C (Phenyl)	1.8186(2)	1.824(5)	1.825(6)	1.8168(17)	1.826(13)
P1-C (PAH)	1.8198(2)	1.814(6)	1.815(6)	1.8214(16)	-
Se-P-C (Phenyl) average	113.34	113.43	114.59	112.50	113.13(8)
Se-P-C (PAH)	111.76	112.89(17)	113.1(2)	114.90(5)	-

Table 9: Selected bonds lengths and angles of complexes **9** and **10**.

Bond distance (Å)/angle (°)	9	10	Ph ₃ PS-AuCl	Ph ₃ PSe-AuCl
Au1-Cl1	2.2824(12)	2.284(4)	2.285(6)	2.277(6)
Au1-E1 (E = S or Se)	2.2744(12)	2.3829(19)	2.285(5)	2.371(2)
P1-E1 (E = S or Se)	2.0256(16)	2.176(4)	2.017(8)	2.187
E1-Au1-Cl1	177.08(4)	177.25(12)	175.84(18)	178.6(1)
P1-E1-Au1	100.85(6)	92.71(12)	105.6(3)	100.1(1)

The crystal structures for **1-4** and **5-8** are shown in Figures 6-9, respective of their polyaromatic substituent. Interestingly, as seen in the oxide complex, the anthracenyl derivatives, **3** and **7**, show deviation from planarity in the anthracene ring. These deviations are small, 3° and 5°, and compare well with the 3° twist of OPPh₂(9-anthacenyl).¹⁸ The crystal structures of **9** and **10** are featured in Figures 10 and 11, respectively, highlighting the coordination motif of chalcogenide to gold metal center.

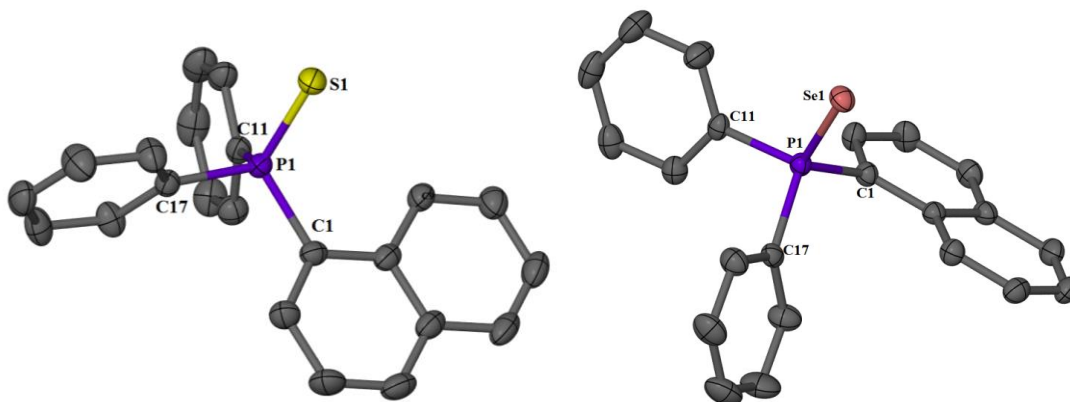


Figure 6: Thermal ellipsoid plot of **1** (left) and **5** (right) shown at the 50% probability level. Hydrogen atoms and solvent molecules have been removed for clarity.

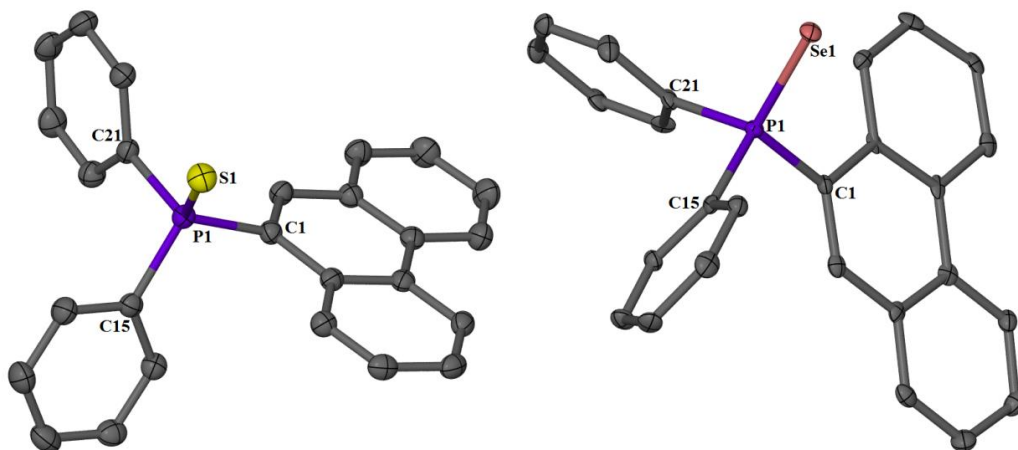


Figure 7: Thermal ellipsoid plot of **2** (left) and **6** (right) shown at the 50% probability level. Hydrogen atoms and solvent molecules have been removed for clarity.

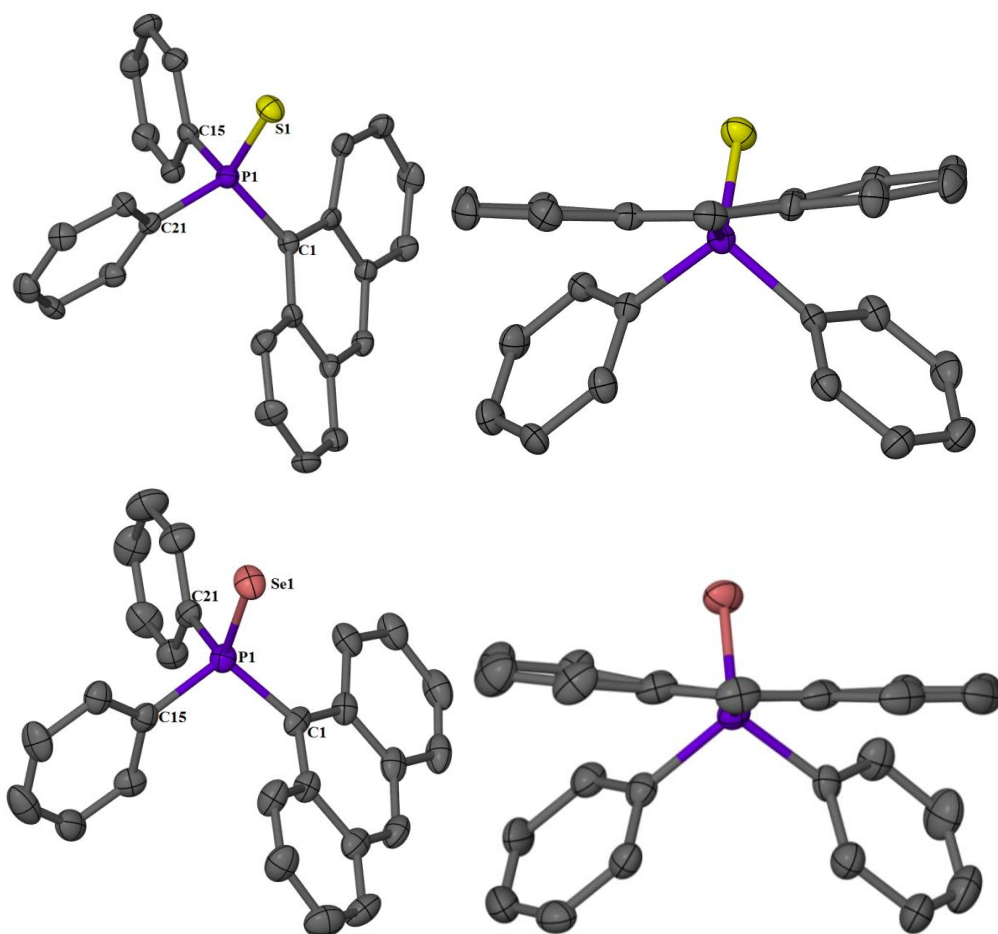


Figure 8: Thermal ellipsoid plot of **3** (top-left) and **7** (bottom-left) shown at the 50% probability level. Hydrogen atoms and other independent molecule have been removed for clarity. (top-right) **3** oriented to show the 3°-degree bend in the anthracenyl ring, while (bottom-right) **5** oriented to show the 5°-degree bend in the anthracenyl ring.

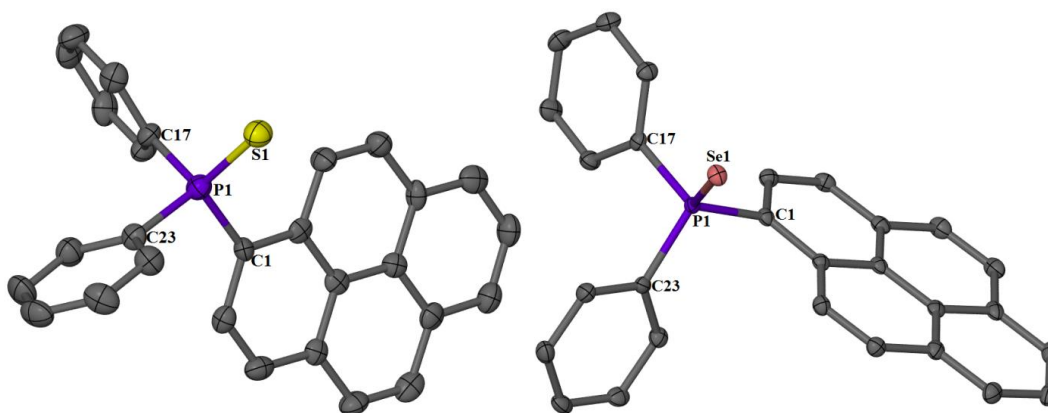


Figure 9: Thermal ellipsoid plot of **4** (left) and **8** (right) shown at the 50% probability level. Hydrogen atoms have been removed for clarity.

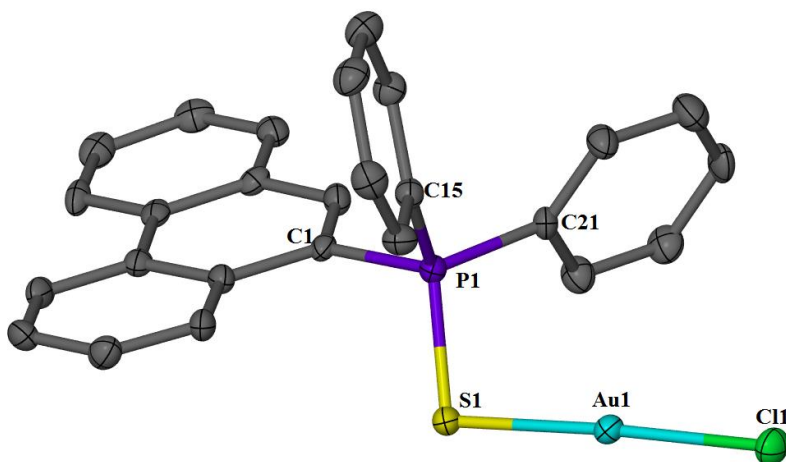


Figure 10: Thermal ellipsoid plot of **9** at 50% probability level. Hydrogen atoms and other independent molecule in the unit cell have been removed for clarity.

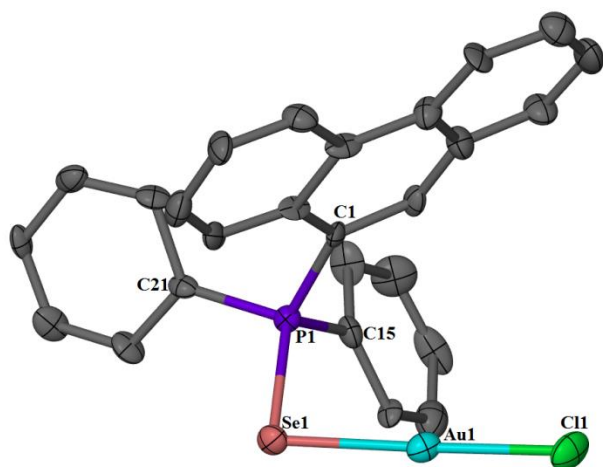


Figure 11: Thermal ellipsoid of **10** at 50% probability level. Hydrogen atoms, solvent molecules and other independent molecules in the unit cell have been removed for clarity.

Literature precedent for bent polycyclic aromatic hydrocarbons

Evidence from **3** and **7** by fluorescence spectroscopy and X-ray crystallography gave reason to search pre-existing structures and scrutinize if other polycyclic aromatic structures also had a nonplanar motif. Our search was narrowed to complexes that only contained P(V) since the structures of PPh₂Ar did not show any obvious strain in the ring system. This was assumed to be the case because the ring systems were either not large enough to cause more steric pressure than phenyl as in the case of naphthyl,^{13, 49-51} or the orientation of the aromatic group in space was away from the other rings like phenanthrenyl⁵²⁻⁵³ and pyrene.^{8, 54} Upon examining the P(V) compounds with anthracenyl ligands, all structures with a chalcogenide contained a deviation from planarity. The deviation in the anthracenyl system is presumably due to the increased steric demand around the phosphine and the steric pressure that a new substituent caused. Table 10 highlights some of those structures and the deviation from planarity caused in the

anthracenyl system. None of the referenced structures in Table 10 brought attention to the fact that the anthracene ring showed bending.

Table 10: Complexes with a 9-anthracenyl (anth) substituent on a triarylphosphine and the deviation from planarity that is observed in the anthracene ring in that compound.

Complex	CCDC Number	Deviation from planarity ^o (dihedral angle)*	Reference
Eu(hfac) ₃ [OPPh ₂ (anth)] ₂	902262	10.2	7
9,10-[OPPh ₂] ₂ (anth)	189388	3.6**	25
9,10-[SPPH ₂] ₂ (anth)	19389	4.3**	25
9,10-[SePPh ₂] ₂ (anth)	19390	4.1**	25
OPPh ₂ (10-Br-anth)	610421	7.0	55
SPPH ₂ (10-Br-anth)	610422	12.1	55
SePPh ₂ (10-Br-anth)	610423	12.1	55
Ph ₂ anthracenyl PO	1005323	10	18
3		2.6	This work
7		5.0	This work

* When multiple anthracenyl moieties are present, the average is given.

**The major deviations are with C9 and C10 being out of the plane of the anthracene ring.

Only a few reports that included phosphorus ligands highlighted anthracenyl deviating from planarity.⁴⁷⁻⁵² In one case, a Au(III) phosphorus complex, 3[Au(9,10-bis(diphenylphosphino)anthracene)], the fluorescence spectrum red-shifted and broadening was described as being due to excimer formation which are not observed in the compounds described here.⁵⁶

DFT calculations

Due to the change in fluorescence spectra of **3** and **7**, the previously reported OPPh₂(9-anthracenyl),¹⁸ and the crystallographic evidence supporting a bent anthracenyl

substituent, an investigation of the molecular structures of **1-8** was initiated to elucidate if the same geometric steric constraints were present in the gas phase. The optimized structures had the same bond lengths and angles as that of the crystal structures (within 0.01 Å). Upon examination of the optimized structures of **3** and **7**, it was observed that there was still a bent motif of the anthracene ring at 3.2° and 3° radial curve, respectively. This suggests that not all the nonplanarity of the crystal structures of **3** and **7** are due to crystal packing forces as seen in Figure 12. However, NICS(1) calculations revealed that this deviation from planarity does not significantly change the aromaticity of the anthracene ring (Figure 13).

Due to the ring bend and the red shift of the fluorescence spectra, both would indicate partial loss of planarity within the anthracenyl ring of **3** and **7**. It was then hypothesized that if there was loss of planarity that it would be reflected in NICS(1) calculations of the ligands which describes the induced field by the π system of the electronic structure. The results showed no major deviation in the NICS values for **1**, **2**, **4-6**, and **8**, when compared with that of previously recorded values using the same basis set and level of theory, see Figure 13. However, upon inspection of **3** and **7**, the shielding values for the outer rings do differ by 1 to 2. The NICS values are still negative, indicative of an aromatic ring system, but show a nontrivial deviation from the P(III) compounds. This supports the theory that added steric effects could disturb some of the ring current by disrupting π orbital overlap. The overall effects are the observed phenomenon of substituent deviation from planarity, change in aromatic shielding, and the red shift in the fluorescence emission spectra.

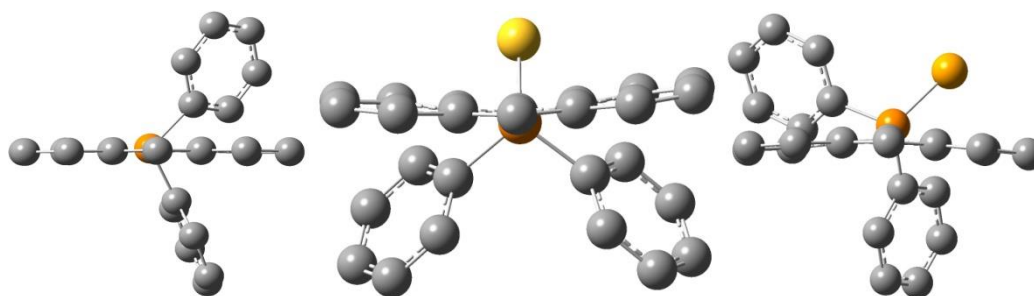


Figure 12: Comparison of the anthracenyl strain in the optimized structures of left, unoxidized diphenylanthracenylphosphine; center, **3**; right, **7**.

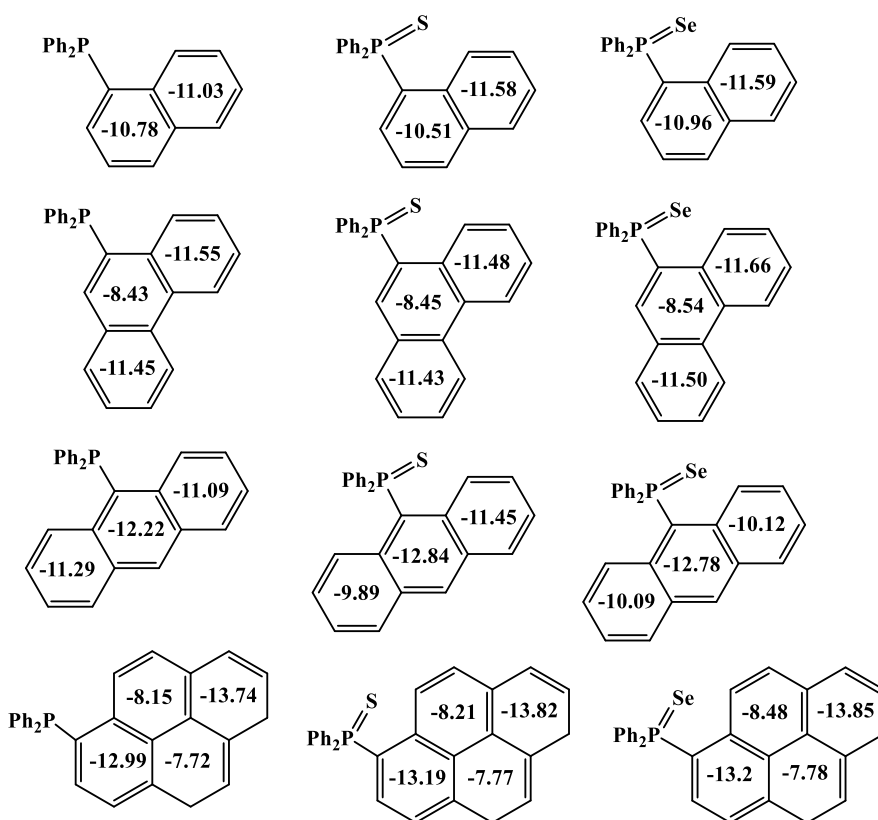


Figure 13: NICS(1) values of unoxidized and oxidized phosphines, **1-8**.

Further examination was conducted to observe if anthracenyl was the only aromatic substituent that would undergo bending. Systems of diphenylphosphine with 9-tetracenyl, 1-anthracenyl, 10-pentacenyl, and 9-anthanthrenyl, as well as their oxides to determine if bending was reserved only for 9-anthracenyl were calculated. In the series,

1-anthracenyl and its oxides did not show deviation from planarity. This is due to the 1 position allowing for the polycyclic aromatic hydrocarbon substituent to rotate away from the phenyl groups on the phosphorus to alleviate steric pressure. While the 9-tetracenyl, 10-pentacenyl, and 9-anthanthrenyl showed deviation from planarity to the same degree as that of the 9-anthracenyl substituent, the 9 and 10 position in each case does not allow the PAH to rotate away from the phenyl groups.

Conclusions

This work focuses on synthesizing phosphine sulfide and selenide complexes with two phenyl groups and a polycyclic aromatic hydrocarbon: 1-naphthyl, 9-phenanthryl, 9-anthracenyl, and 1-pyrenyl. These compounds have been characterized using ^1H , ^{13}C , and ^{31}P NMR, IR, and fluorescence spectroscopy. Their structures were determined by single crystal X-ray diffraction analysis and the electrochemistry of the parent phosphines were examined by cyclic voltammetry. One-electron reduction waves are observed for all but the naphthyl derivative. Reaction of $\text{EPPh}_2(\text{9-phenanthryl})$, $\text{E} = \text{S, Se}$, with auric acid produces the Au(I) products, $[(\text{phen})\text{Ph}_2\text{PE}]\text{AuCl}$. As shown in the solid-state, the anthracenyl-substituted derivative was found to have unusual bending, not observed with the naphthyl, phenanthryl, or pyrenyl derivatives. In analogy to the phosphine oxide, $\text{EPPh}_2(\text{9-anthracenyl})$, showed loss of fine structure in the fluorescence spectra, was red-shifted and accompanied by an increase in the quantum yield. DFT calculations confirmed the bending of the anthracenyl ring occurs in the gas phase and provides evidence for this being a sterically induced buckling of the ring and this is not observed in compounds without similar coordination of anthracenyl to the phosphorus atom.

Acknowledgments

Special thanks to Dr. Andrew Behrle for completing the electrochemistry experiments. As well as, Charles Laber and Dr. Gary Baker for their work on the fluorescence spectroscopy. I would also like to thank Dr. Paul Sharp for insightful discussions, Dr. Charles Barnes for assistance with x-ray crystallography and Dr. Wei Wycoff for assistance with NMR spectroscopy.

References

1. Tolman, C. A., Phosphorus ligand exchange equilibriums on zerovalent nickel. Dominant role for steric effects. *J. Am. Chem. Soc.* **1970**, *92* (10), 2956-2965.
2. Tolman, C. A.; Seidel, W. C.; Gosser, L. W., Formation of three-coordinate nickel(0) complexes by phosphorus ligand dissociation from NiL₄. *J. Am. Chem. Soc.* **1974**, *96* (1), 53-60.
3. Trnka, T. M.; Grubbs, R. H., The Development of L₂X₂RuCHR Olefin Metathesis Catalysts: An Organometallic Success Story. *Acc. Chem. Res.* **2000**, *34* (1), 18-29.
4. Osborn, J. A.; Jardine, F. H.; Young, J. F.; Wilkinson, G., The preparation and properties of tris(triphenylphosphine)halogenorhodium(I) and some reactions thereof including catalytic homogeneous hydrogenation of olefins and acetylenes and their derivatives. *J. Chem. Soc. A* **1966**, 1711-1732.
5. Heck, R. F., Mechanism of arylation and carbomethoxylation of olefins with organopalladium compounds. *J. Am. Chem. Soc.* **1969**, *91* (24), 6707-6714.
6. Coulson, D. R.; Satek, L. C.; Grim, S. O., Tetrakis (Triphenylphosphine) Palladium (0). In *Inorg. Synth.*, John Wiley & Sons, Inc.: 2007; pp 121-124.
7. Xu, H.-B.; Jiao, P.-C.; Kang, B.; Deng, J.-G.; Zhang, Y., Walkable Dual Emissions. *Sci. Rep.* **2013**, *3*.
8. Hu, J.; Nguyen, M.-H.; Yip, J. H. K., Metallacyclophanes of 1,6-Bis(diphenylphosphino)pyrene: Excimeric Emission and Effect of Oxygen on Stability of the Rings. *Inorg. Chem.* **2011**, *50* (16), 7429-7439.
9. Lin, R.; Yip, J. H. K., Self-Assembly, Structures, and Solution Dynamics of Emissive Silver Metallacycles and Helices. *Inorg. Chem.* **2006**, *45* (11), 4423-4430.
10. Bailey, J. A.; Ploeger, M.; Pringle, P. G., Mono-, Di-, and Triborylphosphine Analogues of Triarylphosphines. *Inorg. Chem.* **2014**, *53* (14), 7763.
11. Bullock, J. P.; Bond, A. M.; Boeré, R. T.; Gietz, T. M.; Roemmele, T. L.; Seagrave, S. D.; Masuda, J. D.; Parvez, M., Synthesis, Characterization, and Electrochemical Studies of PPh₃-n(dipp)_n (dipp = 2,6-Diisopropylphenyl): Steric and Electronic Effects on the Chemical and Electrochemical Oxidation of a Homologous Series of Triarylphosphines and the Reactivities of the Corresponding Phosphoniumyl Radical Cations. *J. Am. Chem. Soc.* **2013**, *135* (30), 11205-11215.
12. Herbst-Irmer, R.; Henn, J.; Holstein, J. J.; Hübschle, C. B.; Dittrich, B.; Stern, D.; Kratzert, D.; Stalke, D., Anharmonic Motion in Experimental Charge Density Investigations. *J. Phys. Chem. A* **2012**, *117* (3), 633-641.

13. Davis, W. L.; Muller, A., Tris(naphthalen-1-yl)phosphane chloroform hemisolvate. *Acta Cryst. E* **2012**, *68* (12), o3484.
14. Pop, A.; Silvestru, A.; Gimeno, M. C.; Laguna, A.; Kulcsar, M.; Arca, M.; Lippolis, V.; Pintus, A., New group 11 complexes with metal-selenium bonds of methyldiphenylphosphane selenide: a solid state, solution and theoretical investigation. *Dalton Trans.* **2011**, *40* (46), 12479-12490.
15. Tiedemann, M. A.; Mandell, C. L.; Chan, B. C.; Nataro, C., X-ray structures and oxidative electrochemistry of phosphine sulfides and phosphine selenides. *Inorg. Chim. Acta* **422** (2014), 193.
16. Manindar, K.; Abdur, R.; Julianne, C.-W.; Zhen, H., Biochemistry of Nucleic Acids Functionalized with Sulfur, Selenium, and Tellurium: Roles of the Single-Atom Substitution. In *Biochalcogen Chemistry: The Biological Chemistry of Sulfur, Selenium, and Tellurium*, Am. Chem. Soc.: **2013**; *1152*, pp 89-126.
17. Stadtman, T. C., Selenium Biochemistry: Proteins containing selenium are essential components of certain bacterial and mammalian enzyme systems. *Science* **1974**, *183* (4128), 915-922.
18. Breshears, A. T.; Barnes, C. L.; Wagle, D. V.; Baker, G. A.; Takase, M. K.; Walensky, J. R., Structure and spectroscopy of uranyl and thorium complexes with substituted phosphine oxide ligands. *Radiochim. Acta*, **2015**; *103*, p 49.
19. Karaçar, A.; Freytag, M.; Thönnessen, H.; Omelanczuk, J.; Jones, P. G.; Bartsch, R.; Schmutzler, R., Oxidation reactions of 1,8-bis(phosphino)naphthalenes: syntheses and molecular structures of bis(phosphine oxides) and of a bis(phosphine sulfide). *Heteroat. Chem.* **2001**, *12* (2), 102-113.
20. Knight, F. R.; Fuller, A. L.; Bühl, M.; Slawin, A. M. Z.; Woollins, J. D., Sterically Crowded peri-Substituted Naphthalene Phosphines and their PV Derivatives. *Chem. Euro. J.* **2010**, *16* (25), 7617-7634.
21. Knight, F. R.; Fuller, A. L.; Slawin, A. M. Z.; Derek Woollins, J., Preparation and compounds of (8-methoxynaphth-1-yl)diphenylphosphine. *Polyhedron* **2010**, *29* (7), 1849-1853.
22. Bouit, P.-A.; Escande, A.; Szűcs, R.; Szieberth, D.; Lescop, C.; Nyulászi, L.; Hissler, M.; Réau, R., Dibenzophosphapentaphenes: Exploiting P Chemistry for Gap Fine-Tuning and Coordination-Driven Assembly of Planar Polycyclic Aromatic Hydrocarbons. *J. Am. Chem. Soc.* **2012**, *134* (15), 6524-6527.
23. Chauhan, M.; Chuit, C.; Corriu, R. J. P.; Reyé, C.; Declercq, J.-P.; Dubourg, A., Crystallographic evidence of hexacoordination at phosphorus via intramolecular

- coordination of donor groups on phosphane and phosphane sulphide. *J. Organomet. Chem.* **1996**, 510 (1–2), 173-179.
24. Schwab, G. S., D.; Leusser, D.; Stalke, D., Syntheses and Structures of 9-Bromo-10-diphenylphosphanyl anthracene. *Z. Naturforsch. B.* **2007**, (62), 711-716.
25. Fei, Z.; Kocher, N.; Mohrschladt, C. J.; Ihmels, H.; Stalke, D., Single Crystals of the Disubstituted Anthracene 9,10-(Ph₂P=S)₂C₁₄H₈ Selectively and Reversibly Detect Toluene by Solid-State Fluorescence Emission. *Angew. Chem. Int. Ed.* **2003**, 42 (7), 783-787.
26. Tefteller, W.; Zingaro, R. A.; Isbell, A. F., Phosphines and Phosphine Sulfides Containing Highly Condensed Aromatic Groups. *J. Chem. Eng. Data* **1965**, 10 (3), 301-302.
27. Arrigo, L. M.; Galenas, M.; Bassil, D. B.; Tucker, S. A.; Kannan, R.; Katti, K. V.; Barnes, C. L.; Jurisson, S. S., Fluorescent phosphinimine as possible precursor to an anionic and fluorescent sensor for Tc-99. *Radiochim. Acta* **2008**, 96 (12), 835-844.
28. Apex II suite, B. A. L., 2006, Madison, WS.
29. Sheldrick, G., A short history of SHELX. *Acta Cryst. A* **2008**, 64 (1), 112-122.
30. Barbour, L. J., X-Seed – A Software Tool for Supramolecular Crystallography. *J. Supramol. Chem.*, **2001**, 1, 189-191.
31. Frisch, M. J.; Trucks, G. W.; Schlegel, H. B.; Scuseria, G. E.; Robb, M. A.; Cheeseman, J. R.; Scalmani, G.; Barone, V.; Mennucci, B.; Petersson, G. A.; Nakatsuji, H.; Caricato, M.; Li, X.; Hratchian, H. P.; Izmaylov, A. F.; Bloino, J.; Zheng, G.; Sonnenberg, J. L.; Hada, M.; Ehara, M.; Toyota, K.; Fukuda, R.; Hasegawa, J.; Ishida, M.; Nakajima, T.; Honda, Y.; Kitao, O.; Nakai, H.; Vreven, T.; Montgomery Jr., J. A.; Peralta, J. E.; Ogliaro, F.; Bearpark, M. J.; Heyd, J.; Brothers, E. N.; Kudin, K. N.; Staroverov, V. N.; Kobayashi, R.; Normand, J.; Raghavachari, K.; Rendell, A. P.; Burant, J. C.; Iyengar, S. S.; Tomasi, J.; Cossi, M.; Rega, N.; Millam, N. J.; Klene, M.; Knox, J. E.; Cross, J. B.; Bakken, V.; Adamo, C.; Jaramillo, J.; Gomperts, R.; Stratmann, R. E.; Yazyev, O.; Austin, A. J.; Cammi, R.; Pomelli, C.; Ochterski, J. W.; Martin, R. L.; Morokuma, K.; Zakrzewski, V. G.; Voth, G. A.; Salvador, P.; Dannenberg, J. J.; Dapprich, S.; Daniels, A. D.; Farkas, Ö.; Foresman, J. B.; Ortiz, J. V.; Cioslowski, J.; Fox, D. J. *Gaussian 09*, Gaussian, Inc.: Wallingford, CT, USA, 2009.
32. Stephens, P. J.; Devlin, F. J.; Chabalowski, C. F.; Frisch, M. J., Ab Initio Calculation of Vibrational Absorption and Circular Dichroism Spectra Using Density Functional Force Fields. *J. Phys. Chem.* **1994**, 98 (45), 11623-11627.
33. Becke, A. D., Density-functional thermochemistry. III. The role of exact exchange. *J. Chem. Phys.* **1993**, 98 (7), 5648-5652.

34. Lee, C.; Yang, W.; Parr, R. G., Development of the Colle-Salvetti correlation-energy formula into a functional of the electron density. *Phys. Rev. B* **1988**, *37* (2), 785-789.
35. Hariharan, P. C.; Pople, J. A., The influence of polarization functions on molecular orbital hydrogenation energies. *Theor. Chim. Acta* **1973**, *28* (3), 213-222.
36. Francl, M. M.; Pietro, W. J.; Hehre, W. J.; Binkley, J. S.; Gordon, M. S.; DeFrees, D. J.; Pople, J. A., Self-consistent molecular orbital methods. XXIII. A polarization-type basis set for second-row elements. *J. Chem. Phys.* **1982**, *77* (7), 3654-3665.
37. Ahmad, S.; Isab, A.; Perzanowski, H.; Hussain, M. S.; Akhtar, M. N., Gold(I) complexes with tertiary phosphine sulfide ligands. *Transition Met. Chem.* **2002**, *27* (2), 177-183.
38. Mann, B. E., The carbon-13 and phosphorus-31 nuclear magnetic resonance spectra of some tertiary phosphines. *J. Chem. Soc., Perkin Trans. 2* **1972**, (1), 30-34.
39. Dean, P. A. W., Nuclear magnetic resonance studies of the solvation of phosphorus(V) selenides, 1,2-bis(diphenylphosphino)ethane, and tris(dimethylamino)phosphine telluride by sulfur dioxide. *Can. J. Chem.* **1979**, *57* (7), 754-761.
40. Winnik, F. M., Photophysics of preassociated pyrenes in aqueous polymer solutions and in other organized media. *Chem. Rev.* **1993**, *93* (2), 587-614.
41. Kane, M. A.; Baker, G. A.; Pandey, S.; Maziarz, E. P.; Hoth, D. C.; Bright, F. V., Effects of Added CO₂ on the Conformation of Pyrene End-Labeled Poly(dimethylsiloxane) Dissolved in Liquid Toluene. *J. Phys. Chem. B* **2000**, *104* (35), 8585-8591.
42. Ohmori, H.; Nakai, S.; Masui, M., Anodic oxidation of organophosphorus compounds. Part 1. Anodic alkylamination of triphenylphosphine. *J. Chem. Soc., Perkin Trans. 1* **1978**, (11), 1333-1335.
43. Schiavon, G.; Zecchin, S.; Cogoni, G.; Bontempelli, G., Anodic oxidation of triphenylphosphine at a platinum electrode in acetonitrile medium. *J. Electroanal. Chem. Interfac. Electrochem.* **1973**, *48* (3), 425-431.
44. Parker, V. D., Energetics of electrode reactions. II. The relationship between redox potentials, ionization potentials, electron affinities, and solvation energies of aromatic hydrocarbons. *J. Am. Chem. Soc.* **1976**, *98* (1), 98-103.
45. Connelly, N. G.; Geiger, W. E., Chemical Redox Agents for Organometallic Chemistry. *Chem. Rev.* **1996**, *96* (2), 877-910.

46. Ziemer, B.; Rabis, A.; Steinberger, H.-U., Triclinic polymorphs of triphenylphosphine and triphenylphosphine sulfide. *Acta Cryst. C* **2000**, *56* (2), e58-e59.
47. Coddling, P. W.; Kerr, K. A., Triphenylphosphine selenide. *Acta Cryst. B* **1979**, *35* (5), 1261-1263.
48. Sakhawat Hussain, M., Gold(I)-selenium bond: synthesis and x-ray structure of chloro(triphenylphosphine selenide)gold(I). *J. Crystallogr. Spectrosc. Res.* **1986**, *16* (1), 91-99.
49. Allen, D. V.; Venkataraman, D., Copper-Catalyzed Synthesis of Unsymmetrical Triarylphosphines†. *JOC* **2003**, *68* (11), 4590-4593.
50. Kabir, S. E.; Ahmed, F.; Ghosh, S.; Hassan, M. R.; Islam, M. S.; Sharmin, A.; Tocher, D. A.; Haworth, D. T.; Lindeman, S. V.; Siddiquee, T. A.; Bennett, D. W.; Hardcastle, K. I., Reactions of rhenium and manganese carbonyl complexes with 1,8-bis(diphenylphosphino)naphthalene: Ligand chelation, C–H and C–P bond-cleavage reactions. *J. Organomet. Chem.* **2008**, *693* (16), 2657-2665.
51. Meijboom, R., trans-Carbonylchloridobis[tris(naphthalen-1-yl)phosphane- κ P]rhodium(I) acetone trisolvate. *Acta Cryst. E* **2011**, *67* (10), m1438.
52. Osawa, M.; Hoshino, M.; Akita, M.; Wada, T., Synthesis and Characterization of Phenanthrylphosphine Gold Complex: Observation of Au-Induced Blue-Green Phosphorescence at Room Temperature. *Inorg. Chem.* **2005**, *44* (5), 1157-1159.
53. Osawa, M.; Hoshino, M.; Wada, T.; Araki, Y.; Ito, O., Phosphorous atom induced intramolecular charge transfer fluorescence in 9-diphenylphosphinophenanthrene. *Chem. Phys. Lett.* **2006**, *427* (4–6), 338-342.
54. Hu, J.; Yip, J. H. K.; Ma, D.-L.; Wong, K.-Y.; Chung, W.-H., Switching on the Phosphorescence of Pyrene by Cycloplatination. *Organometallics* **2008**, *28* (1), 51-59.
55. Schwab, G. S., D.; Leusser, D.; Stalke, D., Syntheses and Structures of 9-Bromo-10-diphenylphosphanyl anthracene and its oxidation products. *Z. Naturfor.* **2007**, *62b*, 711.
56. Yip, J. H. K.; Prabhavathy, J., A Luminescent Gold Ring That Flips Like Cyclohexane. *Angew. Chem. Int. Ed.* **2001**, *40* (11), 2159-2162.

VITA

Andrew Thomas Breshears was born 1988 in Moscow, Idaho, to parents Richard and Mary Ann Breshears. He grew up in the Tri-Cities, Washington, attending Southridge High School and graduating as a part of the 2006 class.

From 2006 to 2010, he attended the University of Idaho. During this time, he did research for his advisors Drs. Thomas Bitterwolf and I. Frances Cheng, while conducting research at Pacific Northwest National Laboratory (PNNL) during breaks under the direction of Dr. James Szecsody. In the Fall of 2010, Andrew received a Bachelor's of Science in Chemistry. He then started a two year Post-Bachelors research assistant position with Drs. Lucas Sweet and Shane Pepper.

In the Spring of 2013, Andrew left PNNL to pursue a Ph.D. in chemistry at the University of Missouri, under the direction of Dr. Justin Walensky. After completing his candidacy exam, Andrew was awarded a Lab Graduate Fellowship with Argonne National Lab under Dr. Artum Gelis. After working between the two labs on multiple projects, Andrew is defending his thesis in the spring of 2017.